Contribution to Integral Equation Techniques for Solving Electromagnetic Problems

THÈSE N^{O} 4771 (2010)

PRÉSENTÉE LE 24 SEPTEMBRE 2010

À LA FACULTÉ SCIENCES ET TECHNIQUES DE L'INGÉNIEUR
LABORATOIRE D'ÉLECTROMAGNÉTISME ET ACOUSTIQUE
SECTION DE GÉNIE ÉLECTRIQUE ET ÉLECTRONIQUE

ÉCOLE POLYTECHNIQUE FÉDÉRALE DE LAUSANNE

POUR L'OBTENTION DU GRADE DE DOCTEUR ÈS SCIENCES

PAR

Sergio LÓPEZ PEÑA

acceptée sur proposition du jury:

Prof. L. Thévenaz, président du jury
Prof. J. R. Mosig , directeur de thèse
Prof. F. Rachidi-Haeri, rapporteur
J. M. Rius Casals, rapporteur
Dr I. Stevanovic, rapporteur

ÉCOLE POLYTECHNIQUE
FÉDÉRALE DE LAUSANNE

Lausanne, EPFL
2010

Abstract

Surface Mixed Potential Integral Equation (MPIE) formulations together with the Method of Moments (MoM) are widely used to solve electromagnetic problems. An accurate evaluation of the Green functions (GF) associated to the integral equation and of the coupling integrals needed to fill the MoM matrix are the cornerstone steps in the implementation of integral equation algorithms. This thesis is mainly focused on these two topics.

The main intended application of our MPIE-MoM formulation is the analysis of enclosed structures, with the shield being materialized by rectangular cavities with perfect conducting (PEC) walls. GFs for rectangular cavities constitute a classic research topic, where there is still a lot of room for improvements. In this area, three main original results are presented in this thesis. Firstly, the exponential convergence of the modal series is ensured via a sophisticated coordinate permutation method. In second place, a study which allows setting the relationship between cavity resonances, excited modes and GF components' singularities, is fully developed. Finally, a novel hybrid method, to compute the GF static part is introduced. This method combines in a new original way both, the modal and image expansions of the cavity GFs.

The discretization of the MPIE via the method of moments leads to a matrix equation. In the Galerkin version of the MoM, the matrix elements are given by four-dimensional integrals over source and observer surface domains of the GFs multiplied by some basis and test functions. These so-called coupling integrals invoke the integration of the GF singularity, which in the MPIE case is of the weak type (*1/R*). The accurate integration of this singularity is a very challenging topic, which has been tackled following many different strategies. Here, the closed analytical expressions of the 4D integral over rectangular domains of this singularity are presented. The problem related to the integration of the GF singularity on arbitrary shaped domains is solved through a hybrid numerical-analytical technique based on an original integral transformation and using by the first time double exponential (DE) numerical integration rules.

The thesis concludes with several numerical examples and benchmarks of practical interest. They ascertain the validity of strategies, concepts and results of this thesis and they strongly hint to the development of future competitive computer tools.

Key words: numerical methods, integral equations, method of moments, green function, singular integrals.

Résumé

Les formulations en équations intégrales de surface aux potentiels mélangés (MPIE) se combinent usuellement avec la méthode des moments (MoM) pour pouvoir résoudre une large variété de problèmes électromagnétiques. Une évaluation précise des fonctions de Green (GFs) associées à l'équation intégrale et le calcul des intégrales de couplage nécessaires pour remplir la matrice des moments sont les deux étapes-clé dans toute implémentation d'un algorithme de résolution d'équations intégrales. Cette thèse se concentre essentiellement sur ces deux sujets.

L'application principale prévue pour notre formulation MPIE-MoM est l'analyse de structurées blindées, le blindage étant matérialisé comme des cavités rectangulaires aux parois parfaitement conductrices. Les fonctions de Green pour ces cavités constituent un sujet classique de recherche dans lequel beaucoup d'améliorations sont encore possibles. Dans cette optique, trois résultats originaux sont présentés dans cette thèse. Tout d'abord, on garantit une convergence de type exponentiel aux séries décrivant les fonctions de Green, grâce à une méthode sophistiqué de transformation et permutation de coordonnées. Puis, on propose une étude exhaustive des relations entre les résonances de la cavité, les modes excités et les singularités des différentes fonctions de Green. Finalement, on introduit une nouvelle méthode hybride pour le calcul des parties statiques, combinant d'une nouvelle façon les expansions en images et en modes des fonctions de Green de la cavité.

La discretisation de la MPIE à travers une méthode des moments mène à une équation matricielle. Dans la variante de Galerkin dans la MoM, les éléments de la matrice de moments sont donnés par des intégrales quadri-dimensionelles sur des domaines surfaciques associés aux points source et observateur. L'intégrand est constitué par la fonction de Green pertinente multiplié par des fonctions de base et de test. Ces entités appelées intégrales de couplage demandent l'intégration des singularités des fonctions de Green qui, dans le cas MPIE sont du type faible ($1/R$). Une évaluation précise est très délicate et plusieurs stratégies sont possibles. Ici, on présente un traitement original et exhaustif de l'intégrale 4D dans le cas de domaines rectangulaires. Dans le cas des domaines de forme arbitraire, le problème est résolu avec une technique hybride analytico-numérique, qui s'appuie dans un changement de variables nouveau et utilise pour la première fois une quadrature numérique de type exponentiel double.

La thèse conclut avec plusieurs exemples et tests numériques d'intérêt pratique. Ils permettent de vérifier la validité des concepts, stratégies et résultats de cette thèse. En même temps elles indiquent clairement le chemin pour le développement de futurs logiciels compétitifs.

Mots clés: méthodes numériques, equation intégrale, méthode des moments, fonction de green, intégrales singulières.

Acknowledgements

First of all, I would like to acknowledge all the LEMA people I have had the pleasure of sharing my time with. All of them were helpful during the last years. Among all of them Eden Sorolla and Roberto Torres supported and listened to me in the very bad moments, either professional or personal. Over all, a great thanks to Roberto for his constant advice and his invaluable help in the most critical situations during the development of this manuscript. Also, a great thanks to Michael Mattes and Athanasios Polimeridis for support and very interesting scientific discussions. Jean François, I will never forget you (a real Swiss), it was wonderful working with you during POLARIS. Anja, thanks for your the constant correction of my French. I cannot forget Eulalia, the laboratory would really collapse without her.

I have specially to acknowledge to my thesis advisor Juan Ramón Mosig. I have always admired either great scientist or great leaders who take care of his people. Juan you have both, I have always felt supported under your supervision and for me you will always be more than a boss. In the same direction, I would like to render thanks to Juan Manuel Rius for putting his trust in me and supporting my candidature to LEMA. I do not want to forget all my educators, specially Luis Aguayo, thanks to him I love science and I took some agility in doing integrals.

I would also like to acknowledge all the people outside LEMA in Lausanne who help me a lot specially at the beginning. Antonio, now you are not between as but I know you would be proud of me.

Finally, I cannot forget my parents, which have always support me in this adventure. Thanks mum for being the strongest of the family and thanks dad for having always taken care on me in the old-fashioned way.

Table of Contents

1 Introduction 1
1.1 Thesis Outline 2
1.2 Original Contributions 3

2 Principles 5
2.1 Introduction 5
2.2 The MPIE and the Lorentz's Gauge 6
2.3 The Method of Moments 10
References 12

3 Potential Cavity Green Functions 13
3.1 Introduction 13
3.2 The Green Function as Image Series 14
3.3 The Green Function as 2D Modal Series 18
3.3.1 The Infinite Parallel Plate Waveguide GF in the Spectral Domain 19
3.3.2 The Cavity GF as a 2D series in the Spatial Domain 21
3.3.3 GF Permutations in the Spatial Domain 26
3.4 Images-Modes GF Hybrid Representation 30
3.5 GF Evaluation Techniques Comparative Study 33
3.6 Full Wave Characterization of Potential Cavity GFs 37
3.6.1 Degenerate Modes 37
3.6.2 GF Modal Study 40
3.6.3 Numerical Example 41
3.7 Novel Method to Evaluate Static Potential Cavity GFs 44
3.7.1 Mathematical Formulation 44
3.7.2 Physical Interpretation 46
3.7.3 Implementation 47
3.7.4 Numerical Results 49

3.8 Conclusions 51
References 53

4 Multidimensional Singular Integrals 55
4.1 Introduction 55
4.2 The MPIE-MoM Interaction Integrals 56
4.2.1 The Scalar Potential GF Contribution 58
4.2.2 The Vector Potential GF Contribution 59
4.3 Topological Classification of MSI 61
4.4 Review of techniques to solve MSI 63
4.5 Analytical 4D Weakly MSI over Rectangular Flat Domains 66
4.5.1 Coplanar Source and Observer cells 68
4.5.2 Source and Observer cells Located at Parallel Planes 71
4.5.3 Source and Observer cells Located at Orthogonal Planes 75
4.6 Hybrid Analytic-Numeric 4D Weakly MSI over Arbitrary Flat Polygons 84
4.6.1 Alternative Analytical Approach to Evaluate the 2D Potential Integral 85
4.6.2 Features of the Endpoint Singularities in the Potential Derivatives 90
4.6.3 Numerical Integration of the 2D Observer Integral via DE Rules 93
4.7 Conclusions 98
References 100

5 Applications 103
5.1 Introduction 103
5.2 Static Problems 104
5.2.1 Performance of 2D GC-DE rules within a SIE-MoM Framework 104
5.2.2 Numerical Static Potential GFs 106
5.3 Impact of PEC Enclosures in the EM Response of Shielded Structures 108
5.3.1 The Coupled Strips Antenna in Free Space 109
5.3.2 The Coupled Strips Antenna inside a Cavity 111
5.4 Analysis of Combline Type Shielded Structures 115
5.4.1 Single Combline Resonator Study 116
5.4.2 Combline Filter Study 130
5.5 Conclusions 134
References 136

6 Thesis Assessment 139

CV 141

List of publications 143

1 Introduction

"It is not knowledge, but the act of learning, not possession but the act of getting there, which grants the greatest enjoyment."

Carl. F. Gauss

"Plans are nothing; planning is everything."

Dwight D. Eisenhower

Nowadays, numerical methods are widely used in many engineering areas, as for instance mechanical, civil, aeronautical or in our case electrical engineering. They have helped many engineers to solve efficiently the problems and challenges, which are inherent to their work, since a huge number of analyses and studies can be performed with the help of computers. This has also helped to reduce considerably the economic cost typically associated to trial and error procedures. Usually, a researcher on numerical modeling aspires to find the method, which can solve any generic problem. Unfortunately, this is still an open problem. According to the type of problem one method can be more suitable than others, for instance finite element methods (FEM) [1]-[2] are typically used for the analysis of 3D enclosed structures, but they exhibit less performance than other methods when simulating for instance open problems or planar structures. In this case, the discretization of integral equations (IE) via the method of moments (MoM) is the most performing technique. Ideally, it would be desirable to attain the same performance when simulating 3D structures via an IE-MoM strategy than when dealing with planar ones. Nowadays, it exists an active research activity in this direction for this reason.

The author of this thesis has been considerably involved in the aforementioned research activities within the framework of an European Space Agency (ESA) project, whose goal is the development of a proof of concept code (POC) able to show the capabilities of the IE-MoM strategy when simulating shielded structures especially when the gaps between the enclosed objects are very small. Specifically, these structures are combline resonators, which are built by means of cavities that enclose 3D objects, like posts, for example. The results and formulations which will be presented in this thesis have been mainly obtained during the development of this project. Besides, the author of this thesis has been also involved in another ESA project, which has been developed in the framework of antenna design.

IE implementations call for an accurate evaluation of the corresponding Green functions (GF). The calculation of these GFs is a rather complicated problem, which may require to deal

with elaborated mathematical concepts. In our case, the required rectangular cavity GFs have to model basically three phenomena. In first place, the boundary conditions (BC) at the cavity walls have to be properly represented. Secondly, a good model of the sharp cavity resonances has to be achieved. Finally, a perfect model of the spatial singularity, inherent to the GFs is required. Depending on the type of IE utilized, the GF can exhibit either strong or weakly singular behavior. IEs formulated in terms of fields lead to strong singular GF, whereas formulations via potentials produce weak singular GF. The elements of the MoM are indistinctly referred as coupling or interaction integrals, which require the integration of these singular GFs. Therefore, if formulations in terms of fields are used, the accurate evaluation of strong singularities is thus needed. However, this problem is tempered if an IE formulated via potentials as the mixed potential integral equation (MPIE) is used.

In this thesis, the problems associated to the formulation of the GFs linked to the MPIE, as well the integration of its weak singularity, are addressed in detail. Several solutions to compute accurately cavity GFs are proposed. On its turn, the closed expression of the integral of GF the singularity has been attained in several situations of interest. When the full analytical solution is not found, the singular integral is evaluated through a hybrid numeric-analytical method based on the direct exponential (DE) formula. It is illustrated how this method overwhelms classical schemas based on Gaussian rules. All these aspects are applied to the resolution of several electromagnetic problems, which are presented at the end of this thesis.

1.1 Thesis Outline.

In general, chapters and sections are referred uniformly in this thesis: §1 is chapter 1 and §1.1 is section 1.1. §2-§5 contain detailed introduction, conclusion and list of references.

§2 is devoted to provide a brief description of the theoretical and physical aspects involved in this thesis. Basically, the IE procedure is described, as well as the MPIE integral equation and the MoM.

In §3 several techniques to compute cavity GFs are exhaustively described and compared, targeting for the solution which better behaves in terms of boundary (BC) and singularity representation, as well as sharp resonance model. These techniques are based on image expansions, modal series and hybrids of both. Solutions to guarantee an exponential convergence rate in the modal series in all the possible cases are provided. A detailed study of the frequency response of the resulting GF is also presented. Finally, a method to efficiently compute static cavity GFs is proposed.

§4 addresses in detail the problem related to the integration of the GF singularity within a Galerkin-MoM framework. The cases where this integral represents a real challenging problem are described. Also, a detailed explanation of the techniques commonly used to tackle these singular integrals is given. Closed analytical formulas for the integration of the potential GFs spatial singularities as well as hybrid numeric-analytical methods are proposed.

Finally, in §5 the results obtained in §3 and §4 are used to solve several IE problems. Static problems, as for example the numerical computation of static cavity GFs are dealt with. An interesting analysis of the behavior of highly coupled structures is presented. In the final part of

this chapter, the MPIE-MoM strategy is used to simulate several types of combline-like structures.

The thesis report is concluded with a general assessment of the presented work §6.

1.2 Original Contributions.

The original contributions of this thesis are summarized as follows:

- In §3, a coordinate permutation method is applied to the modal series associated to the potential GFs, so that exponential convergence is ensured. The relationship between GF components, resonant frequency and excited cavity mode is set via a rigorous modal classification. Finally, a novel hybrid method to compute the static cavity GF is presented. This method is based on a hybrid representation through image and modal expansions
- Original closed formulas for the 4D integrals of the potential GF singularity over rectangular domains are reported in §4. On its turn, the 2D integral of this GF over arbitrarily oriented flat polygons is analytically calculated through a novel integral transformation. The resulting expression is numerically integrated via numerical rules based on the DE formula instead of using classical Gaussian rules, so that the accuracy in the integration is enhanced.
- In §5 the aforesaid hybrid-numeric analytic schema is applied within an IE-MoM framework. Also in §5, the appearance of anomalous “lump” in the frequency response of highly coupled structures is highlighted. The potential relationship between this lump and a transmission zero, which appears also in the frequency response of the same structure shielded by a cavity, has been analyzed and established.

References

[1] T. Itoh, ed., *Numerical Techniques for Microwave and Millimeter- Wave Passive Structures*. New York: Wiley, 1989.

[2] P. P. Silvester and R. L. Ferrari, *Finite Elements for Electrical Engineers*. Cambridge: Cambridge Univ. Press, 2 ed., 1990.

.

2 Principles

"Politics is for the moment.
An equation is for the eternity."
A. Einstein

"Short words are best and
the old words when short are best of all."
Winston Churchill

2.1 Introduction

This chapter is devoted to describe briefly the theoretical context, within which this thesis has been developed. Although, the concepts exhibited here are well known, it is considered worth to give a mere description of them in order to set the physical and mathematical background of this work.

The thesis has been developed in the framework of integral equations (IE) [1]-[3], which are inferred from the Maxwell through the use of equivalence principles [4]. These IEs are discretized through the Method of Moments [5], so that the IE is transformed into a linear system of equations, whose solution are the equivalent sources defined in the structure under study via the aforesaid equivalence principles. Here, only surface equivalent sources are considered, so that surface integral equations (SIE) are solved. Finally, measurable quantities, as for example S parameters, are derived from this solution. The joint use of the IE and the MoM, is commonly known as IE-MoM strategy, whose implementation follows the next steps:

- *Discretization of the geometry*: The problem under study is subdivided in small domains that are used to define a set of functions called *basis functions*, which expand the equivalent sources in the structure under study.
- *Construction of the GF*: Physically, these GFs are either potentials or fields associated to a point sources. One of the most relevant aspects of these GFs is that they are singular, where the source is located. If the IE is set in terms of potentials the GF exhibit a weak singular behavior. On the contrary, if the IE is formulated via fields, then a strong singular behavior is attained. Either fields or potentials are expressed in integral form through the convolution of these GFs with the equivalent sources.

- *Filling the MoM matrix*: This step requires the evaluation of the aforesaid GF and the computation of the coupling integrals. The accurate evaluation of these integrals is real challenging problem, inasmuch as the singularity of the GF has to be integrated. Formulations through fields enhance this issue, whereas IE equation sets in terms of potential mitigate the problem.
- *Definition of an excitation vector*: The field which excites the structure under study has to be modeled somehow. There exist several techniques in literature to model this excitation field. Here when required, a well known δ-gap model [6]-[9] will be used.
- *Solving the matrix equation*: The aforesaid MoM matrix is inverted and multiplied times the excitation vector to produce the targeted equivalent sources. Although, this thesis is not developed in the context associated to this step, it has to be mentioned that the matrix inversion can represent a very challenging problem, since there are situations where the inversion of huge matrices has to be broached. There are many researchers which concentrate their effort to solve efficiently this step.
- *Recovering equivalent circuit or system parameters of the structure*: In function of the problem, the values of the sources, which are obtained after solving the system, are use to produce impedances, admittances, S parameters, radiation diagrams, etc…

The procedure described above is commonly known as *IE-MoM chain*. In this thesis this procedure is mainly used with the Mixed Potential Integral Equation (MPIE), which is utilized to infer the electric equivalent surface sources. One of the main advantages of this IE is that its related potential GFs exhibit weak singular behavior, which tempers considerably the calculus of the coupling integrals to fill in the MoM matrix. Among the steps forming the IE-MoM chain, the framework of this thesis embraces mainly the construction of these potential GFs and the computation of their related coupling integrals or interaction integrals. These problems are respectively treated in detail in §3 and §4.

2.2 The MPIE and the Lorentz's Gauge

The MPIE is a well known IE [10]-[13], which is commonly used to solve a wide range of EM problems. Nevertheless, it is considered worth to presents its formal mathematical development here, since there are intermediate steps (mainly the ones involving the gauge choice), which will have relevant implications in future chapters.

IEs connect the EM fields across the boundary conditions (BC) that relate these fields in some region. Only perfect electric PEC surfaces as region and only electric fields are considered in this thesis. Therefore, the BC for this sort of fields on a PEC surface is only required [14].

$$\hat{\mathbf{n}} \times \mathbf{E}^{\mathbf{t}} = \hat{\mathbf{n}} \times (\mathbf{E}^{\mathbf{e}} + \mathbf{E}) = 0 \tag{2.1}$$

$\hat{\mathbf{n}}$ is the normal vector to the PEC surface, $\mathbf{E}^{\mathbf{t}}$ is the total electric field. This field is the superposition of the excitation field $\mathbf{E}^{\mathbf{e}}$ and the scattered field $\mathbf{E}$. This field will be expressed in

terms of the magnetic potential vector **A** and the scalar potential *V*. with the help of the Maxwell equations:

$$\nabla \times \mathbf{B} = \mu \mathbf{J} + j\omega\mu\varepsilon \mathbf{E}, \tag{2.2}$$

$$\nabla \times \mathbf{E} = -j\omega \mathbf{B}, \tag{2.3}$$

$$\nabla \bullet \mathbf{E} = q_s / \varepsilon, \tag{2.4}$$

$$\nabla \bullet \mathbf{B} = 0, \tag{2.5}$$

where $\mathbf{E}$ and $\mathbf{B}$, are respectively electric and magnetic induction fields, ω is the angular frequency and, $\mathbf{J}$ and q_s the electric sources, these sources being respectively the electric current and electric charge density, which are related via the continuity equation, $q_s = -\nabla \bullet \mathbf{J} / j\omega$. Also in (2.2)-(2.5), ε and μ are respectively the permittivity and the permeability of the medium, which will be considered the vacuum along this entire thesis. $\mathbf{B}$ can be defined as the curl of a vector, since the divergence of the curl is 0, thereby $\mathbf{B} = \nabla \times \mathbf{A}$, with $\mathbf{A}$ the magnetic potential vector. If this expression of $\mathbf{B}$ is used in (2.3), then $\nabla \times (\mathbf{E} + j\omega \mathbf{A}) = 0$, which implies

$$\mathbf{E} = -j\omega \mathbf{A} - \nabla V \tag{2.6}$$

since the curl of the gradient is 0. This equation expresses the electric field **E** in terms of the vector potential $\mathbf{A}$ and the scalar potential *V*. As consequence of replacing $\mathbf{B} = \nabla \times \mathbf{A}$ and (2.6) in (2.2) and then using the identity $\nabla \times \nabla \times \mathbf{F} = \nabla \nabla \cdot \mathbf{F} - \nabla^2 \mathbf{F}$ ($\mathbf{F}$ a vector function)

$$\nabla^2 \mathbf{A} + \omega^2 \mu\varepsilon \mathbf{A} - \nabla \left[\nabla \bullet \mathbf{A} + j\omega\mu\varepsilon V \right] = -\mu \mathbf{J} \tag{2.7}$$

is found. Similarly,

$$\nabla^2 V + j\omega \nabla \bullet \mathbf{A} = -\frac{q_s}{\varepsilon} \tag{2.8}$$

is obtained, by using (2.6) in (2.4) and applying $\nabla \cdot \nabla f = \nabla^2 f$ (f a scalar function). Expression (2.7) and (2.8) are a coupled system of differential equations, whose solutions are the potentials. The $\nabla \bullet \mathbf{A}$ can be freely defined, the Coulomb gauge $\nabla \bullet \mathbf{A} = 0$ or the Lorentz's gauge $\nabla \bullet \mathbf{A} = -j\omega\mu\varepsilon V$ being the most common choices. This work is developed in the framework of the Lorentz's gauge, whose usage respectively in (2.7) and (2.8) leads to Helmholtz's equations for **A** and *V* are attained, which are of the form:

$$\nabla^2 \mathbf{A} + \omega^2 \mu\varepsilon \mathbf{A} = -\mu \mathbf{J} \tag{2.9}$$

$$\nabla^2 V + \omega^2 \mu\varepsilon V = -\frac{q_s}{\varepsilon}. \tag{2.10}$$

If, in (2.9) and (2.10), **J** and q_s are respectively replaced by the point current dyad $\bar{\bar{\mathbf{I}}}\delta$ and δ, with δ a Dirac delta, then

$$\nabla^2\bar{\bar{\mathbf{G}}}_{\mathbf{A}} + \omega^2\mu\varepsilon\bar{\bar{\mathbf{G}}}_{\mathbf{A}} = -\mu\bar{\bar{\mathbf{I}}}\delta \tag{2.11}$$

$$\nabla^2 G_V + \omega^2\mu\varepsilon G_V = -\frac{\delta}{\varepsilon} \tag{2.12}$$

where, $\bar{\bar{\mathbf{G}}}_{\mathbf{A}}$ are G_V are respectively the Green functions (GF) linked to the potential vector and to the scalar potential *V*. It is well known, that the usage of the Lorentz's gauge to derive (2.11) and (2.12) implies that $\bar{\bar{\mathbf{G}}}_{\mathbf{A}}$ is of diagonal form [15]-[16] with components G_A^{xx}, G_A^{yy} and G_A^{zz}, provided that the problem is being solved in the vacuum, which is the case in these thesis. These components represent the potential of a point current, which is respectively directed in *x, y* or *z*, whereas G_V is the potential produced by a point charge. Chapter §3 is devoted to the detailed study of these GFs obtained via the Lorentz's gauge for empty rectangular cavity problems. Other interesting consequence of the gauge choice in this kind of problems, is the existence of cavity resonances in all the components of $\bar{\bar{\mathbf{G}}}_{\mathbf{A}}$, as well as in G_V. On the contrary, if the Coulomb gauge is utilized only $\bar{\bar{\mathbf{G}}}_{\mathbf{A}}$ exhibits resonances, whereas G_V boils down to a static potential. Besides with this gauge, $\bar{\bar{\mathbf{G}}}_{\mathbf{A}}$ is a full dyadic [17]. The convolution of **J** and q_s respectively with (2.11) and (2.12) leads to

$$\nabla^2\bar{\bar{\mathbf{G}}}_{\mathbf{A}} \otimes \mathbf{J} + \omega^2\mu\varepsilon\bar{\bar{\mathbf{G}}}_{\mathbf{A}} \otimes \mathbf{J} = -\mu\mathbf{J} \tag{2.13}$$

$$\nabla^2 G_V \otimes \rho + \omega^2\mu\varepsilon G_V \otimes q_s = -\frac{q_s}{\varepsilon}. \tag{2.14}$$

It can be inferred from (2.13) and (2.9) that $\mathbf{A} = \bar{\bar{\mathbf{G}}}_{\mathbf{A}} \otimes \mathbf{J}$, and analogously, it is deduced from (2.14) and (2.10) that $V = G_V \otimes q_s$. The usage of these expressions in (2.6) leads to

$$\mathbf{E} = -j\omega\bar{\bar{\mathbf{G}}}_{\mathbf{A}} \otimes \mathbf{J} - \nabla\left[G_V \otimes q_s\right], \tag{2.15}$$

which, Finally, if (2.15) is used in (2.1)replaced by $\mathbf{E}^{\mathbf{s}}$ in the MPIE is found:

$$\mathbf{n}\times\mathbf{E}^{\mathbf{e}} = \mathbf{n}\times\left(j\omega\bar{\bar{\mathbf{G}}}_{\mathbf{A}} \otimes \mathbf{J} + \nabla\left[G_V \otimes q_s\right]\right), \tag{2.16}$$

which through the continuity equation is transformed in

$$\mathbf{n}\times\mathbf{E}^{\mathbf{e}} = \mathbf{n}\times\left(j\omega\bar{\bar{\mathbf{G}}}_{\mathbf{A}} \otimes \mathbf{J} + \frac{j}{\omega}\nabla\left[G_V \otimes \left(\nabla\bullet\mathbf{J}\right)\right]\right). \tag{2.17}$$

As a matter of completeness this procedure is graphically summarized in Fig. 2.1

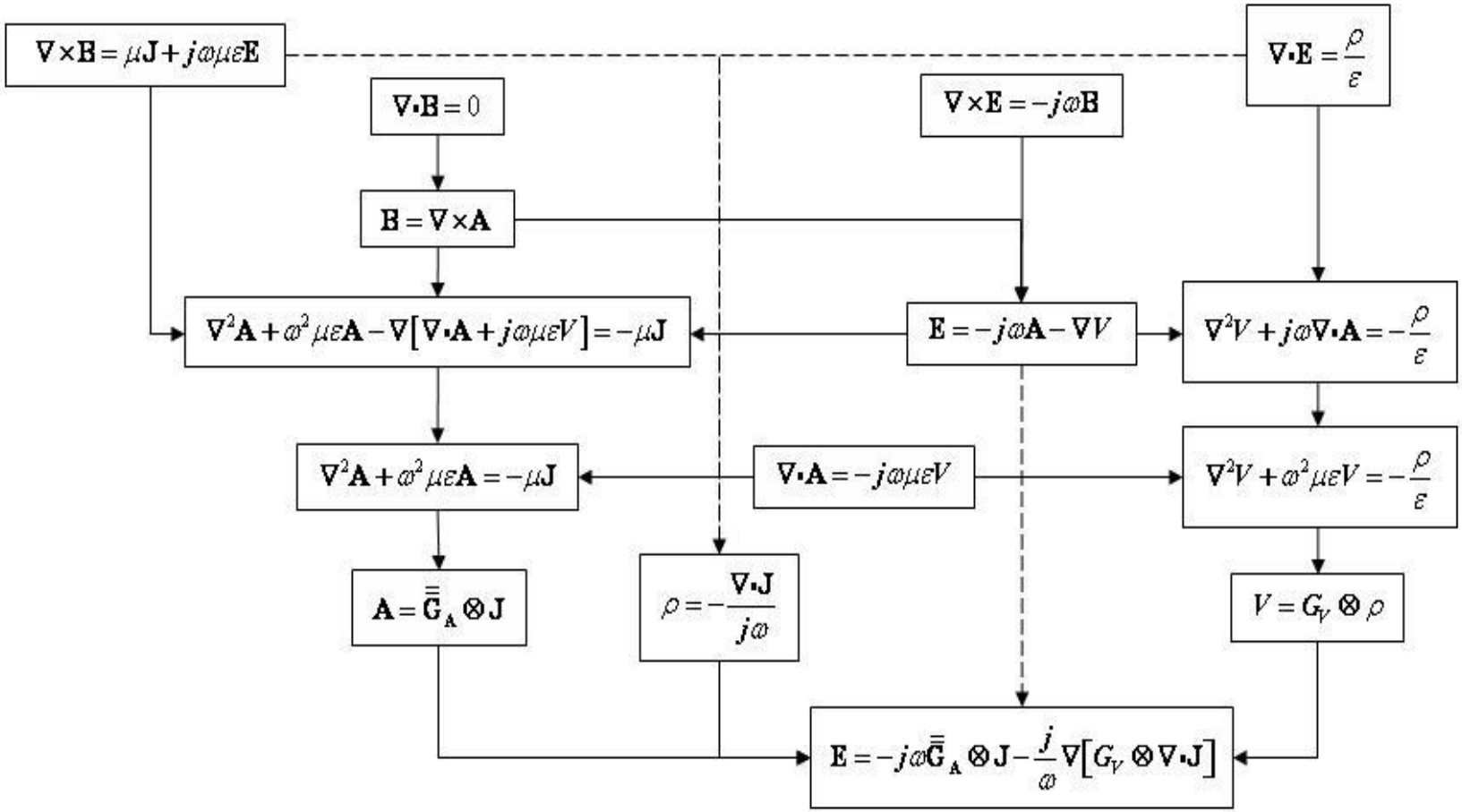

Fig. 2.1 *Flow Chart to obtain the MPIE.*

2.3 The Method of Moments.

The MoM have also been widely applied to solve numerically (2.17). As aforementioned, the method transforms the MPIE in a linear system of equations. In the section, this discretization process of the MPIE via the MoM is briefly described. On its turn, the aspects, which will be of relevance in next chapters, will be indicated.

The first step to apply MoM is to express the surface current density **J** in (2.17) as an expansion in terms of *N* basis functions $\mathbf{b_n}$ as

$$\mathbf{J} \simeq \sum_{n=1}^{N} \alpha_n \mathbf{b}_n \,. \tag{2.18}$$

Here, subdomain basis functions, mainly classical rooftops, which are described in detail in §4.2, are used. In (2.18), the α_i coefficients, are the unknowns of the aforesaid linear system. An approximation of the excitation field $\mathbf{E^e}$ is found if (2.18) is used in (2.17), thereby

$$\mathbf{E^e} \simeq \mathbf{E^e_N} = \sum_{n=1}^{N} \alpha_n \left[j\omega \bar{\bar{\mathbf{G}}}_{\mathbf{A}} \otimes \mathbf{b}_n + \frac{j}{\omega} \nabla \left[G_V \otimes \nabla \bullet \mathbf{b}_n \right] \right]. \tag{2.19}$$

They key step in the MoM consist on minimizing the relative error $e_r = \mathbf{E^e} - \mathbf{E^e_N}$ by making 0 the projection of e_r over a space of *M* test functions $\mathbf{c_m}$, namely the inner product $\langle \mathbf{c_m}, \mathbf{e_r} \rangle = 0$ for $m = 1..M$. If a Galerkin method [5] is used to perform this projection, which is the case in this work, then the set of test function and the set of basis functions are the same. As consequence the MPIE is finally transformed in a linear system of the form

$$\left\langle \mathbf{b}_m, \mathbf{E^e} \right\rangle = \sum_{n=1}^{N} \alpha_i \left[j\omega \left\langle \mathbf{b}_m, \bar{\bar{\mathbf{G}}}_{\mathbf{A}} \otimes \mathbf{b}_n \right\rangle + \frac{j}{\omega} \left\langle \mathbf{b}_m, \nabla \left[G_V \otimes \nabla \bullet \mathbf{b}_n \right] \right\rangle \right] \quad m = 1..M \,, \tag{2.20}$$

which can be expressed as $\mathbf{d} = \underline{\bar{\mathbf{Z}}}\boldsymbol{\alpha}$ with $\underline{\bar{\mathbf{Z}}}$ the impedance matrix, **d** the excitation vector and $\boldsymbol{\alpha}$ the targeted vector of unknowns. The aforesaid inner product is defined in integral form [18], so that (2.20) can be written as

$$\int_S \mathbf{b}_m \mathbf{E^e} dS = \sum_{n=1}^{N} \alpha_i \left[j\omega \int_S \mathbf{b}_m \left(\bar{\bar{\mathbf{G}}}_{\mathbf{A}} \otimes \mathbf{b}_n \right) dS + \frac{j}{\omega} \int_S \left(\mathbf{b}_m, \nabla \left[G_V \otimes \nabla \bullet \mathbf{b}_n \right] \right) \right], \tag{2.21}$$

noticeably for $m = 1..M$. All the integrals in (2.21) are performed over the test function definition domain *S*. On the one hand, the integrals on the right side of (2.21) require the multidimensional integration of the GFs bounded to the MPIE, which is a very challenging problem, since the singularity inherent to this GFs has to be integrated, §4 being totally devoted to the analytical

integration of this singularity. In second place, the excitation field $\mathbf{E}^{e}$, which when required, is defined through a classical δ-gap generator in the MPIE-MoM simulations presented in this thesis (§5) has to be integrated. This does not represent any major problem in this thesis, inasmuch as the utilized basis functions here make this integral to boil down to a constant.

References

[1] J. R. Mautz and R. F. Harrington. E-field and combined-field solutions for conducting bodies of revolution. AEU, 32:157–164, 1978.

[2] A. J. Poggio and E. K. Miller. Integral equation solutions of three-dimensional scattering problems. In: R. Mittra, editor. Computer techniques for electromagnetics. Oxford, UK: Pergamon Press, 1973.

[3] A. F. Peterson, S. L. Ray, and R. Mittra, *Computational methods for electromagnetics*. New York: IEEE Press, 1998.

[4] R. F. Harrington, *Time Harmonic Electromagnetic Fields*. USA: McGraw-Hill, 1961.

[5] R. F. Harrington, *Field Computation by Moment Methods*. Piscataway: IEEE Press, 1992.

[6] J. W. R. Cox, "Some limitations of realistic driving sources in moment method calculations," in Proc. *ICAP*, York, Apr. 1991.

[7] G. P. Junker, A. A. Kishk and A. W. Glisson, "A novel delta gap source model for center fed cylindrical dipoles," *IEEE Trans. Antennas Propag*., vol. 43, no. 5, pp. 537–540, May. 1995.

[8] G. V. Eleftheriades and J. R. Mosig, "On the network characterization of planar passive circuits using the method of moments," *IEEE Trans. Microw. Theory Tech*., vol. 44, no. 3, pp. 438–445, Mar. 1996.

[9] R. Rodrígues-Berral, F. Mesa and D. R. Jackson, "A high-frequency circuit model for the gap excitation of a microstrip line," *IEEE Trans. Microw. Theory Tech.*, vol. 54, no. 12, pp. 4100–4110, Mar. 1996.

[10] K. A. Michalski, "The mixed-potential electric field integral equation for objects in layered media," Arch. Elek. Ubertragung., vol. 39, no. 5, pp. 317–322, 1985.

[11] J. R. Mosig, "Arbitrarily shaped microstrip structures and their analysis with a mixed potential integral equation," *IEEE Trans. Microw. Theory Tech.*, vol. 36, no. 2, pp. 314–323, Feb. 1988.

[12] J. R. Mosig, R. C. Hall, and F. E. Gardiol, *Numerical analysis of microstrip patch antennas. in Handbook of Microstrip Antennas,* London: James and Hall, Eds. 1989.

[13] K. A. Michalski and J. R. Mosig, "Multilayered media Green's functions in integral equation formulations," *IEEE Trans. Antennas Propag.*, vol. 45, no. 3, pp. 508–519, Mar. 1997.

[14] C. A. Balanis, *Advanced Engineering Electromagnetics*. USA: John Wiley and Sons, 1989.

[15] R.E Collin, *Field of Guided Waves*. New York: McGraw-Hill, 1960.

[16] Jean Van Bladel, *Electromagnetic Fields*, USA: Springer-Verlag, 1985.

[17] G. Conciauro, M. Gugliemi and R. Sorrentino, *Advanced Modal Analysis*. Chichester: John Wiley & Sons, 2000.

[18] A. Cardama, L. Jofre, J. M. Rius, J. Romeu and S. Blanch, *Antenas*. Barcelona: Edicions UPC, 1998.

.

3 Potential Cavity Green Functions

"I walk away with fright and horror from the gloomy evil of functions without derivatives."

Charles Hermite

"There is a time to take counsel of your fears, and there is a time to never listen to any fear"

George S. Patton

3.1 Introduction

The studies and results presented in this chapter have been mostly performed in the framework of the scientific activities of a European Spatial Agency (ESA) project, addressed to study the EM behavior of shielded structures. An empty rectangular cavity with perfectly conducting walls PEC is considered as a metallic enclosure. As mentioned in §2, it is assumed that the excitation of this enclosure is modeled with electric currents. Alike, the shielded items are also modeled via equivalent electric currents. The whole system is analyzed through the discretization of the Mixed Potential Integral Equation (MPIE) via the Method of Moments (MoM). This implies that the Green functions (GF) associated to the MPIE have to be obtained. The needed Green functions depend on the nature of both the enclosed structure and the excitation. Therefore, only Green functions relating electric currents to electric fields are needed here. Besides, only the GFs related to the magnetic potential vector **A** and to the scalar electric potential V, which are respectively $\overline{\overline{\mathbf{G}}}_{\mathbf{A}}$ and G_V, are required, since the MPIE is utilized. These GFs are calculated by within Lorentz gauge framework (§2.2), which implies basically two facts. On the one hand, $\overline{\overline{\mathbf{G}}}_{\mathbf{A}}$ is diagonal with components G_A^{xx}, G_A^{yy} and G_A^{zz}. In second place, both these components as well as G_V have resonances corresponding to the allowed modes of the cavity.

In the first part of this chapter, several techniques to develop these Green functions are studied and confronted. The studied techniques are basically based on image expansions, modal series and hybridizations of both. The behavior of the analytical expressions obtained with these techniques is studied, paying special attention to discern what is the best strategy to properly model the sharp cavity resonances, the boundary conditions (BC) at the cavity walls and the *1/R*

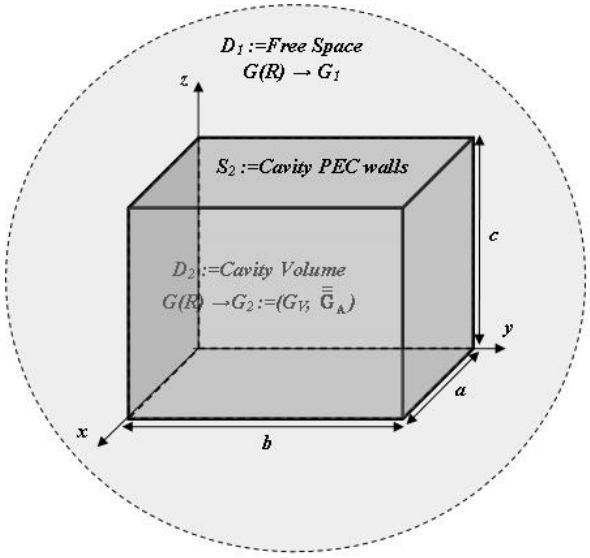

Fig. 3.1 *The cavity walls isolate a region from the free space. This region is the cavity, whose dimensions are respectively a, b, c in x, y, z. Using the method of images the cavity Green function can be obtained from the free space Green functions.*

singularity inherent to potential GFs, which appears when source point $\mathbf{r}' = (x', y', z')$ and observer point $\mathbf{r} = (x, y, z)$ are the same.

The detailed study of G_V, G_A^{xx}, G_A^{yy} and G_A^{zz} reveals that the relationship between type of Green's function, existence of resonances and eventual modal degeneracy is very complex. In the second part of this chapter, this relationship is understood through a rigorous classification scheme of the allowed modes within a rectangular PEC cavity. This scheme allows determining a priori which modal resonances are to be present in each type of Green's function by linking these resonances to classical cavity modes.

Finally, an hybrid acceleration algorithm for the computation of the static potential Green's functions of a rectangular cavity is proposed. Similarly to Ewald's method [1]-[7] it combines the series expansions in terms of images and modes. The main particularity with respect to Ewald resides in the fact that it does not need the evaluation of a non-algebraic function such as the complementary error function (erfc). Indeed, the method only requires the computation of eight images and of several modal series corresponding to bigger cavities, which can be efficiently performed. Numerical results are provided to verify the feasibility of the algorithm, which appears as a promising alternative to the existing methods in literature.

3.2 The Green Function as Image Series

The method of images is one of the most widely known and well documented methods to calculate a GF. As previously introduced, this calculus boils down to solve a boundary value problem (BVP), which consists of a differential equation defined in domain D_2 and its related BC

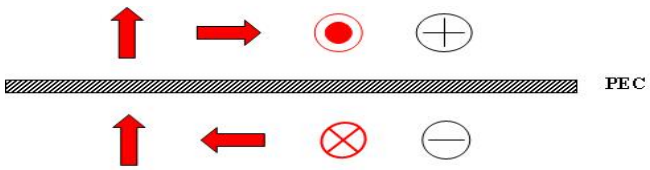

Fig. 3.2 *Mirroring sources in front of a PEC wall.*

defined over the boundary S_2 enclosing D_2. The method of images consist of removing, totally or partially the boundary S_2, thus enlarging the original domain D_2 to a larger (and in principle geometrically simpler) domain D_1 with a new boundary S_1. This is usually achieved by introducing some additional sources. In a nutshell the method of images simplifies the BCs of a BVP by increasing the complexity of the inhomogeneous (source) term in the differential equation. This scenario is illustrated for the case of a PEC rectangular cavity in Fig. 3.1, where D_1 represents the free space (FS), whereas D_2 is the volume enclosed by the surface of the cavity walls S_2, in which the BC linked to the problem are defined. Therefore as aforesaid, the cavity GF G_2 can be derived from G_1, which in this case is the FS GF.

As explained in §2, potential GFs, which are obtained via the Lorentz's gauge, are used. Besides, only electric sources are considered in this chapter. Consequently, the FS potential GFs of interest here are: on the one hand, the FS scalar potential GF

$$G_{VFS} = \frac{1}{4\pi\varepsilon} G(R); \tag{3.1}$$

and on the other hand, the vector potential GF

$$\bar{\bar{G}}_{AFS} = \begin{bmatrix} G_{AFS}^{xx} & 0 & 0 \\ 0 & G_{AFS}^{yy} & 0 \\ 0 & 0 & G_{AFS}^{yy} \end{bmatrix} = \frac{\mu}{4\pi} G(R) \begin{bmatrix} 1 & 0 & 0 \\ 0 & 1 & 0 \\ 0 & 0 & 1 \end{bmatrix} \tag{3.2}$$

In (3.1) and (3.2), $G(R) = e^{-jkR}/R$ with $R = \sqrt{(x-x')^2 + (y-y')^2 + (z-z')^2}$ and k the wave number. Although, these expression are very well known, they are given here as matter of completeness. Physically, expression (3.1) is the potential produced by a point charge in FS, while in (3.2) G_{AFS}^{xx}, G_{AFS}^{yy} and G_{AFS}^{zz} are respectively the potentials produced by point currents directed in $\hat{x}$, $\hat{y}$, and $\hat{z}$. Noticeably, the potential of any set of point charges in the free space is obtained from (3.1), by simply adding the potential produced by each element, and analogously, the same procedure applies in the obtaining of the potential of any set of point current distribution in free space from (3.2).

The targeted empty cavity GFs are G_V and $\bar{\bar{G}}_A$, which are also obtained through the Lorentz's gauge, thereby $\bar{\bar{G}}_A$ is also of diagonal from with components G_A^{xx}, G_A^{yy} and G_A^{zz}. The physical meanings of these components and G_V are respectively the potentials produced by point currents,

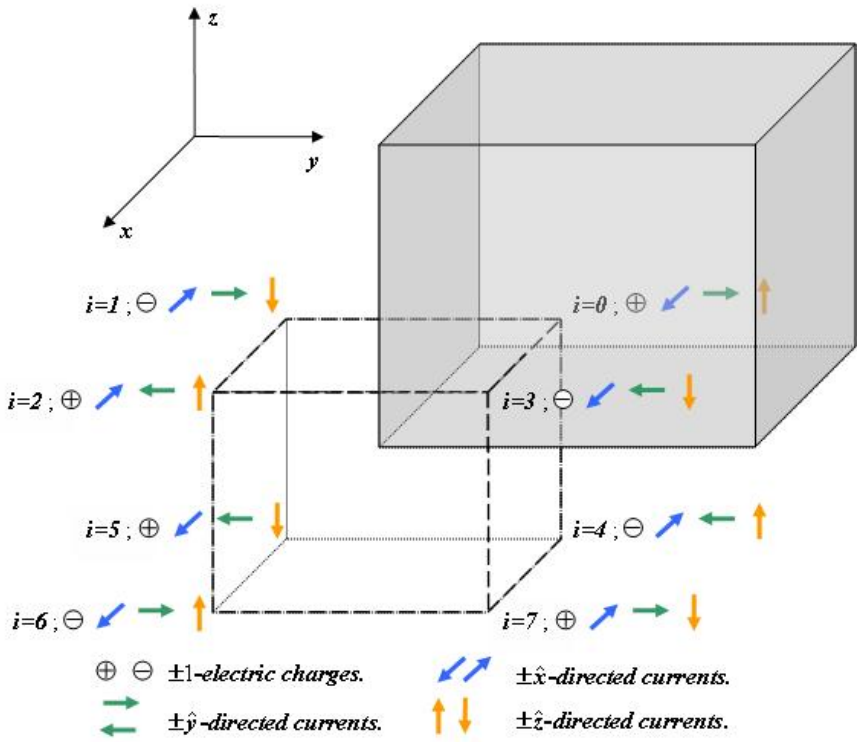

Fig. 3.3 *The basic image set (BIS) for the needed point sources.*

which are shielded by the rectangular cavity, directed in $\hat{x}$, $\hat{y}$, and $\hat{z}$, and the potential produced by a point charge also enclosed within the rectangular enclosure. These potentials should satisfy the BC at the cavity walls, which as aforesaid are assumed to be PEC. G_V fulfills Dirichlet BC in all the directions *x*, *y* and *z*, whereas G_A^{hh} satisfies Neumann BC in the *h* direction, with *h* any of either *x*, *y* or *z* and Dirichlet BC in the other two. A description of these BC is provided in §3.3, since this section describes merely the procedure to obtain the cavity GF via the image method.

The first step to apply the image method consists of inferring an infinite set of sources outside the cavity from a source shielded by the cavity itself. This source will be named as *original source*, while the external distribution will be denoted as *image sources*. Even though, the way to mirror electric charges and currents in front of a PEC wall is very well known, the basic principle is illustrated in Fig. 3.2. Commonly, the *original source* is mirrored to obtain a preliminary finite basic image set (BIS) of sources [7]. The four possible BIS are illustrated in Fig. 3.3 for both punctual currents directed in $\hat{x}$, $\hat{y}$, and $\hat{z}$,and a point charge. In this figure, the index *i=0* refers to the original source, while *i*=(*1, 2, 3, 4, 5, 6, 7*) points to the mirrored ones. In table 3.1, the position of these BIS sources, assuming that the cavity starts at the coordinate origin and the shielded volume is in the first octant, is provided. Also in this table, the values Q_i of a BIS of charges and A_i^{hh} ($h \in \{x, y, z\}$) of a BIS of point currents either directed in $\hat{x}$, $\hat{y}$, or $\hat{z}$, are exhibit. The infinite set of sources is derived from the BIS by simply shifting the positions in

BIS PARAMETERS								
i	**Position**	X_i	Y_i	Z_i	Q_i	A_i^{xx}	A_i^{yy}	A_i^{zz}
0	*(+x',+y',+z')*	$x-x'$	$y-y'$	$z-z'$	+1	+1	+1	+1
1	*(+x', –y',+z')*	$x-x'$	$y+y'$	$z-z'$	–1	–1	+1	–1
2	*(–x', –y',+z')*	$x+x'$	$y+y'$	$z-z'$	+1	–1	–1	+1
3	*(–x',+y',+z')*	$x+x'$	$y-y'$	$z-z'$	–1	+1	–1	–1
4	*(+x',+y', –z')*	$x-x'$	$y-y'$	$z+z'$	–1	–1	–1	+1
5	*(+x', –y', –z')*	$x-x'$	$y+y'$	$z+z'$	+1	+1	–1	–1
6	*(–x', –y', –z')*	$x+x'$	$y+y'$	$z+z'$	–1	+1	+1	+1
7	*(–x', +y', –z')*	$x+x'$	$y-y'$	$z+z'$	+1	–1	+1	–1

Table 3.1 *BIS variables values.*

table 3.1 by *(2ma, 2nb, 2pc)*, with (*m, n, p*) integer numbers. A enlightening example in 2D, which is exhibits how this infinite set is generated is provided in the next section.

The second step consists of removing the cavity, so that all the sources are now in FS. Namely, the boundary is replaced by an infinite set of sources. The potentials associated to the resulting infinite set of sources in FS are obtained by using the FS GFs (3.1) and (3.2), and they are the tackled cavity GF. This is done by firstly calculating the potentials of the BIS, which are of the form

$$P_V(X_i,Y_i,Z_i)=\frac{1}{4\pi\varepsilon}\sum_{i=0}^{7}Q_i\frac{e^{-jk\sqrt{X_i^2+Y_i^2+Z_i^2}}}{\sqrt{X_i^2+Y_i^2+Z_i^2}} \tag{3.3}$$

$$P_A^{hh}(X_i,Y_i,Z_i)=\frac{\mu}{4\pi}\sum_{i=0}^{7}A_i^{hh}\frac{e^{-jk\sqrt{X_i^2+Y_i^2+Z_i^2}}}{\sqrt{X_i^2+Y_i^2+Z_i^2}}, \tag{3.4}$$

with X_i, Y_i and Z_i defined in table 3.1 is obtained. Expressions, (3.3) and (3.4) are respectively, the BIS potential for point charges and for point currents directed in *h*, with $h\in\{x,y,z\}$. Finally as before, this potentials are simply shifted by *(2ma, 2nb, 2pc)*, with *m*, *n* and *p* integer numbers to obtain the targeted cavity GFs, which are of the form:

$$G_V=\frac{1}{4\pi\varepsilon}\sum_{m,n,p}\sum_{i=0}^{7}Q_i\frac{e^{-jkR_{i,mnp}}}{R_{i,mnp}} \tag{3.5}$$

$$G_A^{hh}=\frac{\mu}{4\pi}\sum_{m,n,p}\sum_{i=0}^{7}A_i^{hh}\frac{e^{-jkR_{i,mnp}}}{R_{i,mnp}} \tag{3.6}$$

with $R_{i,mnp}=\sqrt{(X_i+2ma)^2+(Y_i+2nb)^2+(Z_i+2pc)^2}$

It can be generically said that, by using method of images, a Green function G_2 associated to a region D_2, which boundary is defined by S_2, can be inferred from a Green function G_1 bounded to a region D_1 that contains D_2. Therefore, the direct solution of the BVP with BC defined on S_2 can be avoided. This is done by replacing S_2 by a set of sources whose potentials or fields are obtained from G_1. This potential simulates the boundary condition in S_2 and fulfills the differential equation inside D_2. This can be done even in cases where both regions have different parameters by properly weighting the images. Unfortunately, the method of images can be only applied for a reduced number of problems. Mostly geometries are not friendly enough to obtain the set of sources that avoids broaching the direct solution of the BVP. Luckily here, the cavity walls allow us an easy mirroring to find out this set.

3.3 The Green Function as 2D Modal Series

Here, a cavity is considered as an empty volume of the space enclosed by a PEC surface without any electromagnetic excitation. This system has a natural set of resonance frequencies of the form [8]:

$$f_i = \frac{k_i}{2\pi\sqrt{\varepsilon\mu}} \tag{3.7}$$

where f_i is the i^{th} resonant frequency of the system associated to the wave number k_i. According to [8] the electromagnetic field in the vicinity of f_i can be expressed by electric and or magnetic eigenvectors. These eigenvectors are the resonant modes of the cavity and they represent the patterns of the field at the resonance frequencies. If the cavity is a cuboid, then the resonance frequencies linked to the modes are of the form:

$$f_i = f_{mnl} = \frac{1}{2\pi\sqrt{\varepsilon\mu}}\sqrt{\left(\frac{m\pi}{a}\right)^2 + \left(\frac{n\pi}{b}\right)^2 + \left(\frac{l\pi}{c}\right)^2} \tag{3.8}$$

where a, b and c are respectively the cavity dimensions in x, y and z. The analytical expressions of the cavity TE_{mnl} and TM_{mnl} modes are inferred from [8] and shown in table 2.1. In the same table, the conditions the indices m, n and l have to fulfill are given as well. The modes exhibit in table 2.1 fulfill the BC on the cavity walls

Several ways of obtaining the cavity GFs as modal expansions based on the expressions in table 2.1 can be found in literature. Although, the resulting formulas are rather simple, the procedure to obtain them can be quite complicated, since it involves very sophisticated mathematical concepts [8]-[13].

Classically, cavity GFs can be expressed as 3D modal series [11], which exhibits slow quadratic convergence. Nevertheless, the convergence of this 3D expansions can be enhanced be summing the series in one dimension ([11] and [14]), which can be arbitrarily chosen between x, y and z. Consequently, a reduced 2D series exhibiting a faster exponential convergence rate associated to this reduced dimension is achieved. Different strategies can be employed to obtain

RECTANGULAR CAVITY MODES		
	TE_{mnl}	TM_{mnl}
Electric Field	$E=\frac{1}{\chi_{mn}}\sqrt{\frac{2\cdot\varepsilon_m\cdot\varepsilon_n}{a\cdot b\cdot c}}\cdot\left(E_x\hat{x}+E_y\hat{y}+E_z\hat{z}\right)$	$E=\frac{-2}{\chi_{mn}\cdot k_{mnl}}\sqrt{\frac{\varepsilon_l}{a\cdot b\cdot c}}\cdot\left(E_x\hat{x}+E_y\hat{y}+E_z\hat{z}\right)$
E_x	$\frac{n\cdot\pi}{b}\cdot\cos(\frac{m\cdot\pi\cdot x}{a})\sin(\frac{n\cdot\pi\cdot y}{b})\sin(\frac{l\cdot\pi\cdot z}{c})$	$\frac{ml\pi^2}{a\cdot c}\cdot\cos(\frac{m\cdot\pi\cdot x}{a})\sin(\frac{n\cdot\pi\cdot y}{b})\sin(\frac{l\cdot\pi\cdot z}{c})$
E_y	$-\frac{m\cdot\pi}{a}\cdot\sin(\frac{m\cdot\pi\cdot x}{a})\cos(\frac{n\cdot\pi\cdot y}{b})\sin(\frac{l\cdot\pi\cdot z}{c})$	$\frac{nl\pi^2}{b\cdot c}\cdot\sin(\frac{m\cdot\pi\cdot x}{a})\cos(\frac{n\cdot\pi\cdot y}{b})\sin(\frac{l\cdot\pi\cdot z}{c})$
E_z	0	$-\chi_{mn}^2\cdot\sin(\frac{m\cdot\pi\cdot x}{a})\sin(\frac{n\cdot\pi\cdot y}{b})\cos(\frac{l\cdot\pi\cdot z}{c})$
Magnetic Field	$H=\frac{1}{\chi_{mn}\cdot k_{mnl}}\sqrt{\frac{2\cdot\varepsilon_m\cdot\varepsilon_n}{a\cdot b\cdot c}}\cdot\left(H_x\hat{x}+H_y\hat{y}+H_z\hat{z}\right)$	$H=\frac{2}{\chi_{mn}}\sqrt{\frac{\varepsilon_l}{a\cdot b\cdot c}}\cdot\left(H_x\hat{x}+H_y\hat{y}+H_z\hat{z}\right)$
H_x	$\frac{ml\pi^2}{a\cdot c}\cdot\sin(\frac{m\cdot\pi\cdot x}{a})\cos(\frac{n\cdot\pi\cdot y}{b})\cos(\frac{l\cdot\pi\cdot z}{c})$	$\frac{n\cdot\pi}{b}\cdot\sin(\frac{m\cdot\pi\cdot x}{a})\cos(\frac{n\cdot\pi\cdot y}{b})\cos(\frac{l\cdot\pi\cdot z}{c})$
H_y	$\frac{nl\pi^2}{b\cdot c}\cdot\cos(\frac{m\cdot\pi\cdot x}{a})\sin(\frac{n\cdot\pi\cdot y}{b})\cos(\frac{l\cdot\pi\cdot z}{c})$	$-\frac{m\cdot\pi}{a}\cdot\cos(\frac{m\cdot\pi\cdot x}{a})\sin(\frac{n\cdot\pi\cdot y}{b})\cos(\frac{l\cdot\pi\cdot z}{c})$
H_z	$-\chi_{mn}^2\cdot\cos(\frac{m\cdot\pi\cdot x}{a})\cos(\frac{n\cdot\pi\cdot y}{b})\sin(\frac{l\cdot\pi\cdot z}{c})$	0
Allowed indices	$\left[\{m,n\}\neq\{0,0\};l\neq 0\right]$	$\left[m\neq 0;n\neq 0\right]$
Common factors	$\chi_{mn}^2=\left(\frac{m\cdot\pi}{a}\right)^2+\left(\frac{n\cdot\pi}{b}\right)^2\quad k_{mnl}^2=\left(\frac{m\cdot\pi}{a}\right)^2+\left(\frac{n\cdot\pi}{b}\right)^2+\left(\frac{l\cdot\pi}{c}\right)^2\quad \varepsilon_p=\begin{cases}1 & p=0\\ 2 & p\neq 0\end{cases}\quad p=\{m,n,l\}$	

Table. 3.2 *Mathematical expressions for the modes of a PEC rectangular cavity.*

this 2D series. For instance in [11], the mathematical relations in [15] are utilized in the 3D sum. In this section, a very simple method to obtain straightforwardly this 2D reduced series without losing mathematical strictness is presented. Basically, the 2D modal expansion is attained after applying image theory and the Poisson summation formula to a short-circuited infinite parallel plate waveguide.

3.3.1 The Infinite Parallel Plate Waveguide GF in the Spectral Domain

An infinite parallel plate (PP) waveguide consists of two infinite PEC plates separate by the distance D_w as it is depicted in Fig. 3.4 within the Cartesian framework (u,v,w). The potential Green functions related to this structure are also calculated using the Lorentz gauge. Thus $\overline{\overline{\mathbf{G}}}_{\mathbf{A}}$ is of diagonal form:

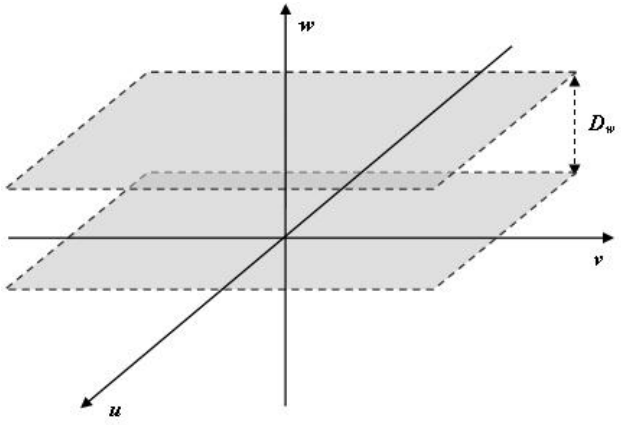

Fig. 3.4 *The infinite parallel plate waveguide consist of two PEC infinite plates separated by the distance D_w.*

$$\bar{\bar{\mathbf{G}}}_{\mathbf{A}} = \begin{bmatrix} \tilde{G}_A^{uu} & 0 & 0 \\ 0 & \tilde{G}_A^{vv} & 0 \\ 0 & 0 & \tilde{G}_A^{ww} \end{bmatrix} \tag{3.9}$$

The mathematical expressions of the components of $\bar{\bar{\mathbf{G}}}_{\mathbf{A}}$ as well as G_V in the spectral domain can be derived from the 1D Helmholtz equation

$$\left[\frac{\partial^2}{\partial w^2} - u_s^2 \right] \cdot \tilde{\Phi}(w, w', k_\rho) = -C \cdot \delta(w - w') \tag{3.10}$$

with $u_s^2 = k_\rho^2 - k^2$ the Sommerfeld parameter, which is linked to the wave number k and the cutoff wave number of the waveguide k_ρ^2. Also in (3.10), $\tilde{\Phi}(w, w', k_\rho)$ is the targeted solution, which can be any of $\tilde{G}_{VPP}$, $\tilde{G}_{APP}^{uu}$, $\tilde{G}_{APP}^{vv}$ or $\tilde{G}_{APP}^{ww}$ depending on the role of point source distribution δ, which is placed between the two plates. On the one hand, If δ is physically an electrical charge and as consequence $C=1/\varepsilon$, then $\tilde{G}_{VPP}$ is obtained by solving (3.10) with Dirichlet BC

$$\tilde{\Phi}(w = 0) = \tilde{\Phi}(w = D_w) = 0 \tag{3.11}$$

on the plates of the waveguide. Namely, the potential should vanish on these plates, albeit the use of a constant different of 0 is also possible in (3.11). On the other hand, $\tilde{G}_{APP}^{uu}$, $\tilde{G}_{APP}^{vv}$ or $\tilde{G}_{APP}^{ww}$, are respectively attained for δ representing an electric current, whose flowing direction is linked either to $\hat{\mathbf{u}}$, $\hat{\mathbf{v}}$ or $\hat{\mathbf{w}}$. In these cases, equation (3.10) is solved with $C=\mu$ by using Dirichlet BC (3.11) for current's directions associated to $\hat{\mathbf{u}}$ or $\hat{\mathbf{v}}$, while Neumann BC

$$-\frac{\partial\tilde{\Phi}(w=0)}{\partial w}=\frac{\partial\tilde{\Phi}(w=D_w)}{\partial w}=0, \tag{3.12}$$

that's to say continuity of the potentials on the plates of the PP waveguide, are needed if the current's direction is $\hat{\mathbf{w}}$. The mathematical procedure to solve (3.10) is described in detail in [16]. After applying this procedure, the resulting solutions of of (3.10) for Dirichlet BC and for Neumann BC are respectively

$$\tilde{\Phi}_D(w,w',k_\rho)=C\frac{\sinh\left[u_s\cdot(D_w-w_>)\right]\cdot\sinh\left[u_s\cdot w_<\right]}{u_s\cdot\sinh(u_s\cdot D_w)} \tag{3.13}$$

$$\tilde{\Phi}_N(w,w',k_\rho)=C\frac{\cosh\left[u_s\cdot(D_w-w_>)\right]\cdot\cosh\left[u_s\cdot w_<\right]}{u_s\cdot\sinh(u_s\cdot D_w)} \tag{3.14}$$

where $w_>$ = max(w,w') and $w_<$ = min(w,w'). The expression of the desired GFs are inferred from (3.13) and (3.14) as $\tilde{G}^{uu}_{APP}(w,w',k_\rho)=\tilde{G}^{vv}_{APP}(w,w',k_\rho)=\mu\cdot\tilde{\Phi}_D$, $\tilde{G}^{ww}_{APP}(w,w',k_\rho)=\mu\cdot\tilde{\Phi}_N$ $\tilde{G}_{VPP}(w,w',k_\rho)=\tilde{\Phi}_D/\varepsilon$. The most relevant aspect, which have been described in this section are summarized in table 3.3.

3.3.2 The Cavity GF as a 2D series in the Spatial Domain

This subsection is devoted to describe the process to derive the cavity GFs in the spatial domain from the PP waveguide GFs previously provided in the spectral domain. Basically, the image method and the Poisson sum will be utilized to attain the desire GFs.

In first place, the cavity is built from the infinite PP waveguide by simply short-circuiting this waveguide with an empty PEC rectangular prism without lids, as it is shown in Fig. 3.5. This prism is in fact a rectangular waveguide section, with dimensions D_u and D_v respectively in u and v directions. The volume within the prism walls and bounded by the PP waveguide plates is the rectangular cavity, whose dimensions are D_u×D_v×D_w. This new scenario is ideal to apply image theory, since the PEC walls of the prism can be replaced by an infinite distribution of point sources, which is parallel to the plane UV and is exemplarily illustrated (a portion of it) in Fig. 3.6. As explained in §3.2, the total potential associated to the infinite distribution is the tackled GF, which is calculated by simply adding the potentials produced by each one of the point sources, that, on its turn, are shifted versions of the PP waveguide GFs in the spatial domain (u,v). In this domain, the expression of the PP waveguide GFs simply boil down to the double inverse Fourier transform of $\tilde{G}_{VPP}$, $\tilde{G}^{uu}_{APP}$, $\tilde{G}^{vv}_{APP}$ and $\tilde{G}^{ww}_{APP}$, which are

$$G_{VPP}(u,v,w,u',v',w')=\frac{1}{2\pi^2}\int_{-\infty}^{\infty}\int\tilde{G}_{VPP}\cdot e^{jk_u(u-u')}\cdot e^{jk_v(v-v')}dk_u dk_v \tag{3.15}$$

$$G^{hh}_{APP}(u,v,w,u',v',w')=\frac{1}{2\pi^2}\int_{-\infty}^{\infty}\int\tilde{G}^{hh}_{APP}\cdot e^{jk_u(u-u')}\cdot e^{jk_v(v-v')}dk_u dk_v \tag{3.16}$$

<table>
<tr><th colspan="5">INFINITE PARALLEL PLATE WAVEGUIDE GREEN FUNCTION SUMMARY</th></tr>
<tr><td>Differential Equation</td><td colspan="4">$$\left[\frac{\partial^2}{\partial w^2}-u_s^2\right]\cdot\tilde{\Phi}(w,w',k_\rho)=-C\cdot\delta(w-w')$$</td></tr>
<tr><td rowspan="2">δ</td><td>Point charge</td><td>Point current
$\hat{\mathbf{u}}$-directed</td><td>Point current
$\hat{\mathbf{v}}$-directed</td><td>Point current
$\hat{\mathbf{w}}$-directed</td></tr>
<tr><td> 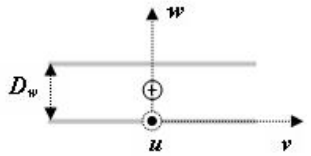
</td><td> 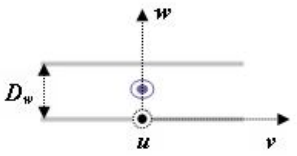
</td><td> 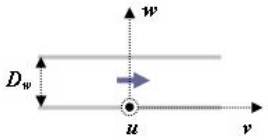
</td><td> 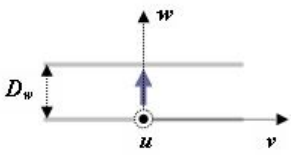
</td></tr>
<tr><td>C</td><td>$1/\varepsilon$</td><td colspan="3">μ</td></tr>
<tr><td rowspan="2">BC</td><td colspan="2">Dirichlet</td><td colspan="2">Neumann</td></tr>
<tr><td colspan="2">$$\tilde{\Phi}(w=0)=\tilde{\Phi}(w=D_w)=0$$</td><td colspan="2">$$-\frac{\partial\tilde{\Phi}(w=0)}{\partial w}=\frac{\partial\tilde{\Phi}(w=D_w)}{\partial w}=0$$</td></tr>
<tr><td>Solution</td><td colspan="2">$$\tilde{\Phi}_D(w,w',k_\rho)=\frac{\sinh\left[u_s\cdot(D_w-w_>)\right]\cdot\sinh\left[u_s\cdot w_<\right]}{u_s\cdot\sinh(u_s\cdot D_w)}$$</td><td colspan="2">$$\tilde{\Phi}_N(w,w',k_\rho)=\frac{\cosh\left[u_s\cdot(D_w-w_>)\right]\cdot\cosh\left[u_s\cdot w_<\right]}{u_s\cdot\sinh(D_w\cdot d)}$$</td></tr>
<tr><td rowspan="2">Related GF component</td><td rowspan="2">$\tilde{G}_{VPP}$</td><td>G^{uu}_{APP}</td><td>G^{vv}_{APP}</td><td>G^{ww}_{APP}</td></tr>
<tr><td colspan="3">$\bar{\bar{\mathbf{G}}}_{APP}$</td></tr>
<tr><td>Potential Green functions</td><td>$$\frac{\sinh\left[u_s\cdot(D_w-w_>)\right]\cdot\sinh\left[u_s\cdot w_<\right]}{\varepsilon\cdot u_s\cdot\sinh(u_s\cdot D_w)}$$</td><td colspan="3">$$\frac{\mu}{u_s\cdot\sinh(u_s\cdot D_w)}\begin{bmatrix}\sinh\left[u_s\cdot(D_w-w_>)\right]\cdot\sinh\left[u_s\cdot w_<\right] & 0 & 0\\ 0 & \sinh\left[u_s\cdot(D_w-w_>)\right]\cdot\sinh\left[u_s\cdot w_<\right] & 0\\ 0 & 0 & \cosh\left[u_s\cdot(D_w-w_>)\right]\cdot\cosh\left[u_s\cdot w_<\right]\end{bmatrix}$$</td></tr>
</table>

Table. 3.3 *PP Waveguide GF formulation summary.*

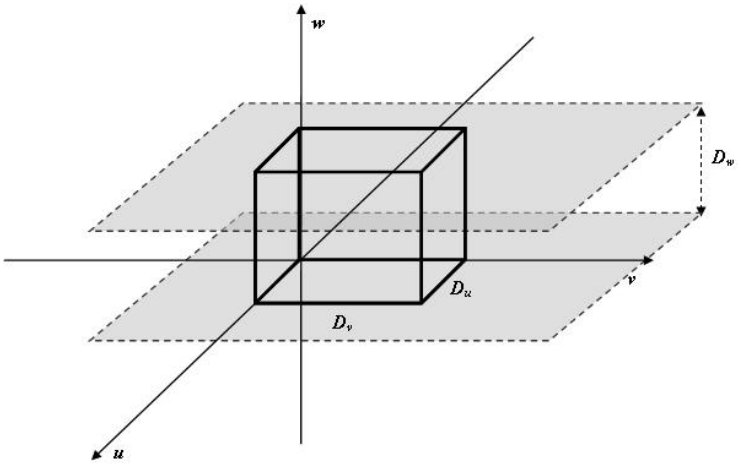

Fig. 3.5 *Short-circuit of the infinite parallel plate waveguide with an empty rectangular prism without lids of dimensions D_uxD_v. This prism can be understood as a section of a rectangular PEC waveguide.*

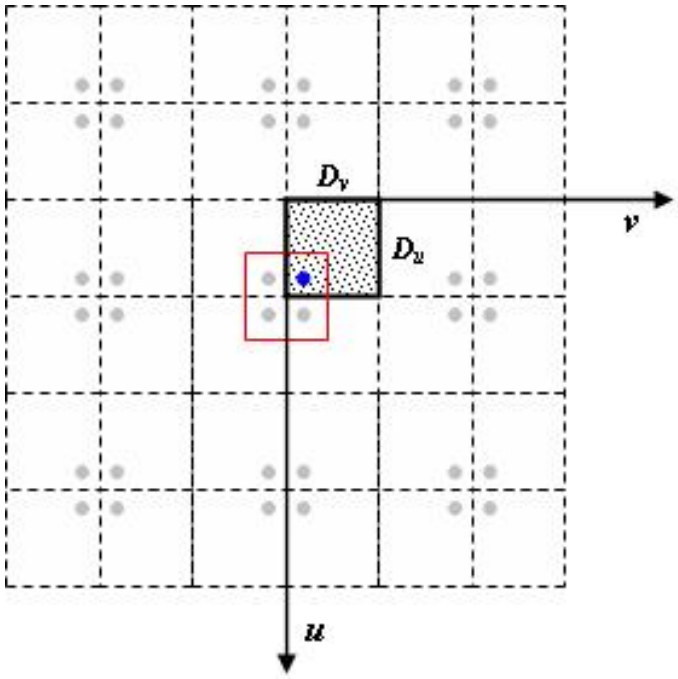

Fig. 3.6 *Distribution of the original (blue) and the image sources (grey) in the plane (u,v). The BIS related to the system is framed in red.*

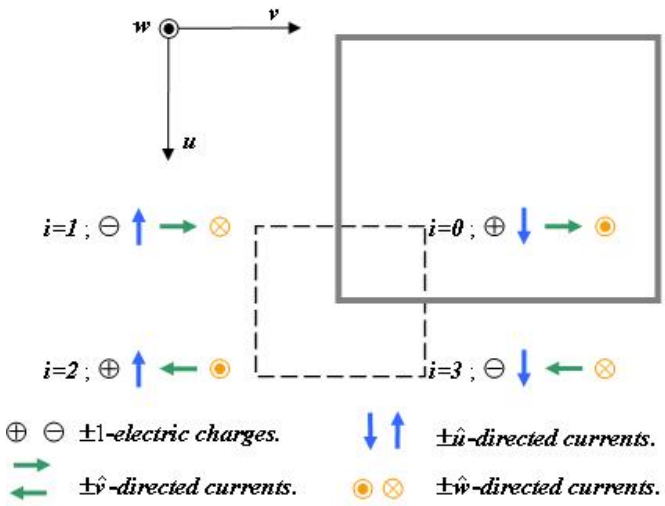

Fig. 3.7 *BIS applied to the parallel plate waveguide Green functions to obtain the cavity potential Green functions.*

($h \in \{u, v, w\}$), insomuch as $k_\rho^2 = k_u^2 + k_v^2$, with $k_u = p \cdot \pi / D_u$ and $k_v = q \cdot \pi / D_v$, in the framework illustrated in Fig. 3.5. Similarly to the 3D case, a 2D BIS is defined to apply the image method. This BIS is highlighted in Fig. 3.6 and described in detail in Fig. 3.7. In this figure, the index *i= 0* denotes the original source, while *i = (1, 2, 3)* points to the image sources. The values Q_i of the point charges, A_i^{uu}, A_i^{vv} and A_i^{ww} of the point currents, which are respectively directed in $\hat{\mathbf{u}}$, $\hat{\mathbf{v}}$ and $\hat{\mathbf{w}}$, as well as the positions (U_i, V_i) of all these sources are shown in table 3.4. The potentials associated to this BIS are inferred from (3.15) and (3.16) as

$$V_{BIS}(U_i, V_i) = \sum_{i=0}^{3} Q_i \cdot G_{VPP}(U_i, V_i) \tag{3.17}$$

$$A_{BIS}^{hh}(U_i, V_i) = \sum_{i=0}^{3} A_i^{hh} \cdot G_{APP}^{hh}(U_i, V_i)\,. \tag{3.18}$$

The desired cavity GFs in the spatial domain are obtained from (3.17) and (3.18) by simply adding the shifted versions of these expressions with regard to (U_i, V_i) by $(2mD_u,\ 2nD_v)$. Therefore,

$$G_V = \sum_{p,q} \sum_{i=0}^{3} Q_i \cdot G_{VPP}(U_i + 2pD_u, V_i + 2qD_v) \tag{3.19}$$

$$G_A^{hh} = \sum_{p,q} \sum_{i=0}^{3} A_i^{hh} \cdot G_{APP}^{hh}(U_i + 2pD_u, V_i + 2qD_v)\,, \tag{3.20}$$

which, after using the Poisson summation formula in 2D

BIS CHARACTERISTICS							
i	***Position***	U_i	V_i	Q_i	A_i^{uu}	A_i^{vv}	A_i^{ww}
0	*(+u',+v')*	$u-u'$	$v-v'$	+1	+1	+1	+1
1	*(–u', +v')*	$u-u'$	$v+v'$	–1	+1	–1	–1
2	*(–u', –v')*	$u+u'$	$v+v'$	+1	–1	–1	+1
3	*(+u', –v')*	$u+u'$	$v-v'$	–1	–1	+1	–1

Table 3.4 2D *BIS variables values*.

$$\sum_{p,q} G(U+2pD_u, U+2qD_v) = \frac{1}{4\cdot D_u\cdot D_v}\sum_{p,q}\tilde{G}(k_u,k_v)\cdot e^{jUk_u}\cdot e^{jVk_v}, \tag{3.21}$$

are transformed in

$$G_V = \frac{1}{4\cdot D_u\cdot D_v}\sum_{p,q}\tilde{G}_{VPP}\cdot\sum_{i=0}^{3}Q_i\cdot e^{jk_uU_i}e^{jk_vV_i} \tag{3.22}$$

$$G_A^{hh} = \frac{1}{4\cdot D_u\cdot D_v}\sum_{p,q}\tilde{G}_{APP}^{hh}\cdot\sum_{i=0}^{3}A_i^{ss}\cdot e^{jk_uU_i}e^{jk_vV_i} \tag{3.23}$$

Notice that the Poisson summation formula (3.21) sets basically that the sum of certain periodical discrete samples of a function *G* can be found from the Fourier series expansion of *G*. Two additional steps remain to obtain the expressions of the cavity GFs as 2D modal series. In first place, expressions (3.22) and (3.23) are written as a cosine expansion, namely

$$G_V = \frac{1}{4\cdot D_u\cdot D_v}\sum_{p,q=0}^{\infty}\varepsilon_p\varepsilon_q\tilde{G}_{VPP}\sum_{i=0}^{3}Q_i\cdot\cos(k_uU_i)\cdot\cos(k_vV_i) \tag{3.24}$$

$$G_A^{hh} = \frac{1}{4\cdot D_u\cdot D_v}\sum_{p,q=0}^{\infty}\varepsilon_p\varepsilon_q\tilde{G}_{APP}^{ss}\sum_{i=0}^{3}A_i^{ss}\cdot\cos(k_uU_i)\cdot\cos(k_vV_i), \tag{3.25}$$

where $\varepsilon_{p,q}$ is 1 for *p,q*=0 and 2 otherwise. Secondly, G_V and the components of $\bar{\bar{\mathbf{G}}}_{\mathbf{A}}$ are inferred from (3.24) and (3.25) after some basic algebraic manipulations, which involve the values exhibit in table 3.4 and the trigonometric relations in [17], as

$$G_V = \frac{4}{D_u\cdot D_v\cdot\varepsilon}\sum_{p,q=1}^{\infty}\tilde{\Phi}_D\cdot S(k_u,u,u')\cdot S(k_v,v,v') \tag{3.26}$$

$$G_A^{uu} = \frac{2\mu}{D_u\cdot D_v}\left[\sum_{q=1}^{\infty}\tilde{\Phi}_D\cdot S(k_v,v,v') + 2\sum_{p,q=1}^{\infty}\tilde{\Phi}_D\cdot C(k_u,u,u')\cdot S(k_v,v,v')\right] \tag{3.27}$$

$$G_A^{vv} = \frac{2\mu}{D_u \cdot D_v}\left[\sum_{p=1}^{\infty} \tilde{\Phi}_D \cdot S\left(k_u,u,u'\right) + 2\sum_{p,q=1}^{\infty} \tilde{\Phi}_D \cdot S\left(k_u,u,u'\right)\cdot C\left(k_v,v,v'\right)\right] \quad (3.28)$$

$$G_A^{ww} = \frac{4\mu}{D_u \cdot D_v}\sum_{p,q=1}^{\infty} \tilde{\Phi}_N \cdot S\left(k_u,u,u'\right)\cdot S\left(k_v,v,v'\right), \quad (3.29)$$

with the functions $S\left(k_u,u,u'\right)=\sin(k_u u)\cdot\sin(k_u u')$, $S\left(k_v,v,v'\right)=\sin(k_v v)\cdot\sin(k_v v')$, $C\left(k_u,u,u'\right)=\cos(k_u u)\cdot\cos(k_u u')$ and $C\left(k_v,v,v'\right)=\cos(k_v v)\cdot\cos(k_v v')$. Notice that in (3.26)-(3.29) all the vanishing terms produced by $S\left(0,u,u'\right)=S\left(0,v,v'\right)=0$ have been eliminated, and the terms involving $C\left(0,u,u'\right)=C\left(0,v,v'\right)=0$ have been grouped into a 1D series. Noticeably, this improves the efficiency of the series, since the number of terms to be computed smaller, and moreover the computation of $\varepsilon_{p,q}$ is avoided, as well.

3.3.3 GF Permutations in the Spatial Domain

Although, expressions (3.26)-(3.29) allow a more efficient evaluation of the GFs than classical 3D modal series expansions, these 2D series are not devoid of drawbacks. The fast exponential convergence rate in (3.26)-(3.29) is only guaranteed in the *w* dimension, which can be easily ascertained via an expansion in terms of exponentials of (3.13) and (3.14) [18], whereas in the other coordinates (*u, v*) the 2D series exhibits poor convergence. This fact can be empirically inferred from the observation of the isolines of G_V in the *UV* plane and G_A^{vv} in the *UW* plane, which are respectively represented in of Fig. 3.8a and Fig. 3.8b. Here, it can be observed that the isolines behave unphysicaly in the dimensions, where the 2D series does not exhibit the aforesaid exponential convergence rate. In this subsection, the convergence problems inherent to expressions (3.26)-(3.29) are solved, being the followed strategy to attain this objective described in three steps. As a result of this process, the final expression of the rectangular cavity GFs as a 2D modal expansion are provided in the Cartesian frame (*x, y, z*).

In first place, a new auxiliary Cartesian frame (*r, s, t*) is introduced, so that (3.26)-(3.29) can be obtained from the expressions

$$G_{VD} = \frac{4}{D_r D_s \varepsilon}\sum_{i,j=1}^{\infty} \tilde{\Phi}_D(t,t')\cdot S\left(k_r,r,r'\right)\cdot S\left(k_r,s,s'\right) \quad (3.30)$$

$$G_{AN} = \frac{4\mu}{D_r D_s}\sum_{i,j=1}^{\infty} \tilde{\Phi}_N(t,t')\cdot S\left(k_r,r,r'\right)\cdot S\left(k_r,s,s'\right) \quad (3.31)$$

$$G_{AD} = \frac{2\mu}{D_r D_s}\left[\sum_{j=1}^{\infty} \tilde{\Phi}_D(t,t')\cdot S\left(k_r,s,s'\right) + 2\sum_{i,j=1} \tilde{\Phi}_D(t,t')\cdot C\left(k_r,r,r'\right)\cdot S\left(k_r,s,s'\right)\right], \quad (3.32)$$

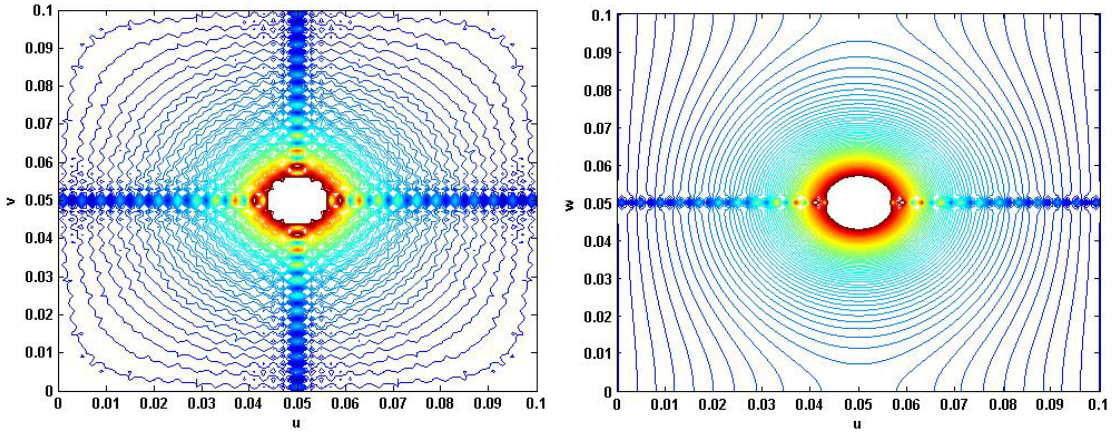

a) **b)**

Fig. 3.8 *Impact of the poor convergence on the isolines of a)* G_V *in the plane UV b) of* G_A^{ww} *in the plane UW.*

GREEN FUNCTIONS	D_R	D_S	D_T	R	S	T	K_R	K_S	I	J	FORMULA TO USE
G_V	D_u	D_v	D_w	u	v	w	k_u	k_v	p	q	G_{VD}
G_A^{uu}	D_u	D_v	D_w	u	v	w	k_u	k_v	p	q	G_{AD}
G_A^{vv}	D_v	D_u	D_w	v	u	w	k_v	k_u	q	p	G_{AD}
G_A^{ww}	D_u	D_v	D_w	u	v	w	k_u	k_v	p	q	G_{AN}

Table 3.5 *Mapping from (r, s, t) to (u, v, w).*

which are defined in this new frame with $k_r = i \cdot \pi / D_r$ and $k_s = j \cdot \pi / D_s$, with the help of table 3.5, that sets a map between (*r*, *s*, *t*) and (*u*, *v*, *w*). Expression (3.30) satisfies Dirichlet BC in all the directions, whereas (3.31) fulfill respectively Dirichlet BC in *r* and *s* directions and Neumann BC in *t* directions. On the other hand, (3.32) satisfy Neumann BC in *r*, while in *t* and *s* it fulfils Dirichlet BC. The coordinate map in table 3.5 is set, so that, the BC associated to (3.26)-(3.29) are properly recovered from (3.30)-(3.32).

Secondly, the three possible sets $\left\{G_V, G_A^{xx}, G_A^{yy}, G_A^{zz}\right\}$, which exhibit exponential convergence either in *z*, in *x* or in *y*, are generated by simply recovering the expressions, which result of setting either (*u*=*x*, *v*=*y*, *w*=*z*), (*u*=*y*, *v*=*z*, *w*=*x*) or (*u*=*z*, *v*=*x*, *w*=*y*) in (3.26)-(3.29). This is equivalent to apply the procedure described in §3.3.1 and §3.3.2 respectively for a *PP* waveguide, which is parallel either to the plane, *XY*, *YZ* or *ZX*. These facts as well as the resulting expressions are presented in table 3.6.

CAVITY GEOMETRY	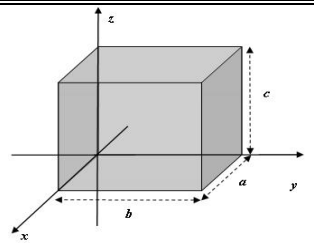		
Possible Starting PP Waveguides Mapped in the (*u*, *v*, *w*) Coordinate System	***XY Plane***	***YZ Plane***	***XZ Plane***
	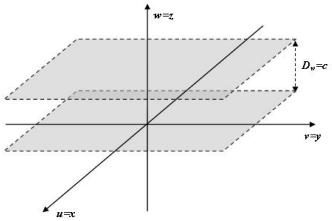	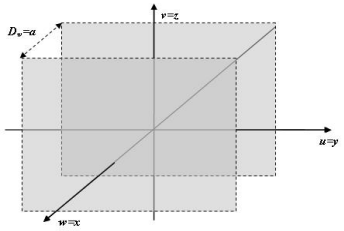	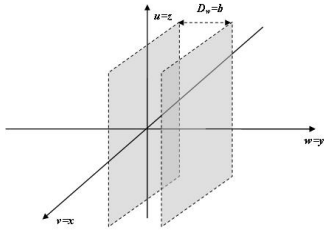
G_V	$G_{VD}=\frac{4}{ab\varepsilon}\sum_{m,n=1}\tilde{\Phi}_D(z,z')S(k_x,x,x')S(k_y,y,y')$	$G_{VD}=\frac{4}{bc\varepsilon}\sum_{n,p=1}\tilde{\Phi}_D(x,x')S(k_y,y,y')S(k_z,z,z')$	$G_{VD}=\frac{4}{ac\varepsilon}\sum_{m,p=1}\tilde{\Phi}_D(y,y')S(k_x,x,x')S(k_z,z,z')$
G_A^{xx}	$G_A^{xx}=\frac{2\mu}{ab}\left[\sum_{n=1}^{\infty}\tilde{\Phi}_D(z,z')S(k_y,y,y')+2\sum_{m,n=1}\tilde{\Phi}_D(z,z')C(k_x,x,x')S(k_y,y,y')\right]$	$G_A^{zz}=\frac{4\mu}{bc}\sum_{n,p=1}\tilde{\Phi}_N(x,x')S(k_y,y,y')S(k_z,z,z')$	$G_A^{xx}=\frac{2\mu}{ac}\left[\sum_{p=1}^{\infty}\tilde{\Phi}_D(y,y')S(k_z,z,z')+2\sum_{m,p=1}\tilde{\Phi}_D(y,y')C(k_x,x,x')S(k_z,z,z')\right]$
G_A^{yy}	$G_A^{yy}=\frac{2\mu}{ab}\left[\sum_{m=1}^{\infty}\tilde{\Phi}_D(z,z')S(k_x,x,x')+2\sum_{m,n=1}\tilde{\Phi}_D(z,z')S(k_x,x,x')C(k_y,y,y')\right]$	$G_A^{yy}=\frac{2\mu}{bc}\left[\sum_{p=1}^{\infty}\tilde{\Phi}_D(x,x')S(k_z,z,z')+2\sum_{n,p=1}\tilde{\Phi}_D(x,x')C(k_y,y,y')S(k_z,z,z')\right]$	$G_A^{zz}=\frac{4\mu}{ac}\sum_{m,p=1}\tilde{\Phi}_N(y,y')S(k_x,x,x')S(k_z,z,z')$
G_A^{zz}	$G_A^{zz}=\frac{4\mu}{ab}\sum_{m,n=1}\tilde{\Phi}_N(z,z')S(k_x,x,x')S(k_y,y,y')$	$G_A^{zz}=\frac{2\mu}{bc}\left[\sum_{n=1}^{\infty}\tilde{\Phi}_D(x,x')S(k_y,y,y')+2\sum_{n,p=1}\tilde{\Phi}_D(x,x')S(k_y,y,y')C(k_z,z,z')\right]$	$G_A^{yy}=\frac{2\mu}{bc}\left[\sum_{m=1}^{\infty}\tilde{\Phi}_D(y,y')S(k_x,x,x')+2\sum_{m,p=1}\tilde{\Phi}_D(y,y')S(k_x,x,x')C(k_z,z,z')\right]$

Table. 3.6 *Possible rectangular cavity GFs in function of the starting PP waveguide.*

G_V MAPPING											
P_c	D_r	D_s	D_t	r	s	t	k_r	k_s	i	j	G_V
$\|(x-x')\|$	b	c	a	y	z	x	k_y	k_z	n	p	G_{VD}
$\|(y-y')\|$	c	a	b	z	x	y	k_z	k_x	p	m	G_{VD}
$\|(z-z')\|$	a	b	c	x	y	z	k_x	k_y	m	n	G_{VD}

Table 3.7 *Mapping from (r, s, t) to (x, y, z) for G_V.*

G_A^{XX} MAPPING											
P_c	D_r	D_s	D_t	r	s	t	k_r	k_s	i	j	G_A^{xx}
$\|(x-x')\|$	b	c	a	y	z	x	k_y	k_z	n	p	G_{AN}
$\|(y-y')\|$	a	c	b	x	z	y	k_x	k_z	m	p	G_{AD}
$\|(z-z')\|$	a	b	c	x	y	z	k_x	k_y	m	n	G_{AD}

Table 3.8 *Mapping from (r, s, t) to (x, y, z) for G_A^{xx}.*

G_A^{YY} MAPPING											
P_c	D_r	D_s	D_t	r	s	t	k_r	k_s	i	j	G_A^{yy}
$\|(x-x')\|$	b	c	a	y	z	x	k_y	k_z	n	p	G_{AD}
$\|(y-y')\|$	c	a	b	z	x	y	k_z	k_x	p	m	G_{AN}
$\|(z-z')\|$	b	a	c	y	x	z	k_y	k_x	n	m	G_{AD}

Table 3.9 *Mapping from (r, s, t) to (x, y, z) for G_A^{yy}.*

G_A^{ZZ} MAPPING											
P_c	D_r	D_s	D_t	r	s	t	k_r	k_s	i	j	G_A^{zz}
$\|(x-x')\|$	c	b	a	z	y	x	k_z	k_y	p	n	G_{AD}
$\|(y-y')\|$	c	a	b	z	x	y	k_z	k_x	p	m	G_{AD}
$\|(z-z')\|$	a	b	c	x	y	z	k_x	k_y	m	n	G_{AN}

Table 3.10 *Mapping from (r, s, t) to (x, y, z) for G_A^{zz}.*

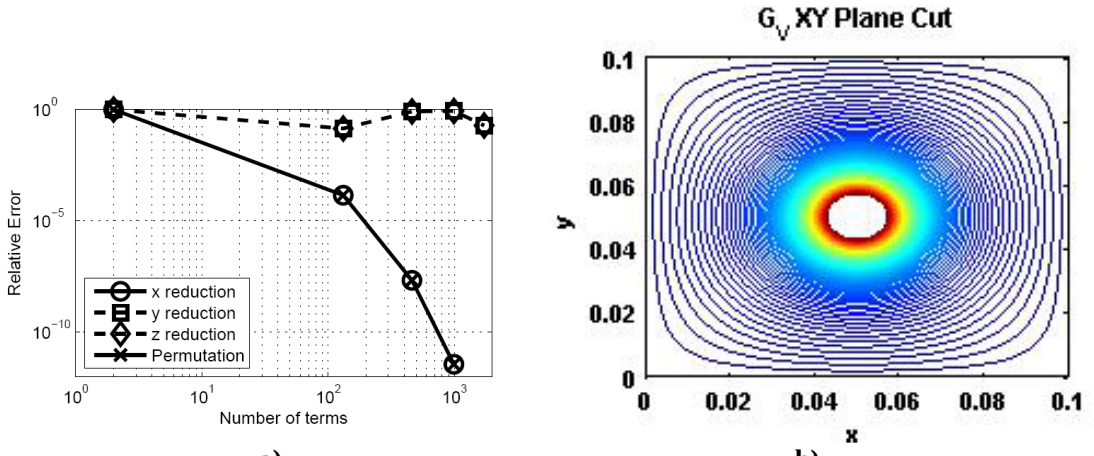

a) **b)**

Fig. 3.9 *a) Convergence of* G_A^{xx} *b) Isolines of GV, when calculating it through the presented permutation.*

Finally, a convergence criterion to make the right choice among the three existing different possibilities for each one of the GFs G_V, G_A^{xx}, G_A^{yy} and G_A^{zz} exhibit in table 3.6, so that the exponential convergence rate is guaranteed, is established. As aforementioned, the exponential convergence rate in is only achieved in the *w* dimension within the Cartesian (*u*, *v*, *w*) framework. Besides, the bigger $|w-w'|$ is, the faster exponential convergence rate is, which can also be deduced from the expansion in terms of exponentials of (3.13) and (3.14) [18]. As consequence, the appropriate GF expression will be chosen in the (*x*, *y*, *z*) Cartesian frame in function of $P_c = \max\left[\left|(x-x')\right|,\left|(y-y')\right|,\left|(z-z')\right|\right]$. The final expressions, of G_V, G_A^{xx}, G_A^{yy} and G_A^{zz} in this frame can be respectively derived from table 3.7-table 3.10 with the help of (3.30)-(3.32). In Fig. 3.9a, the convergence of G_A^{xx} for a case where $P_c = \left|(x-x')\right|$ is exemplarily shown. In this figure, the convergence of the three possible modal series for G_A^{xx} is exhibit. As expected, the GF computed with the permutation algorithm described in this subsection follows automatically the best possible choice. The well behavior of the isolines attained via the presented permutation is also shown, as a matter or completeness for the case of G_V, in Fig. 3.9b.

3.4 Images-Modes GF Hybrid Representation

The mathematical expressions of the GFs in the spatial domain have to fulfill mainly two basic properties. In first place, a perfect representation of the BC on the cavity walls has to be attained. On the other hand, the GFs spatial singular behavior has to be properly modeled. Within the framework of potential GFs, this behavior is of the type $1/R$ and it is especially important when $\mathbf{r}$ and $\mathbf{r}'$ are very close or even the same, the value of the GF being infinite in this case.

Modal expansions achieve a perfect representation of the BC on the cavity walls, inasmuch as they are inferred from the cavity modes, which fulfill the BC by themselves. However, they do not model properly the singular behavior, since a huge number of modes is required to evaluate the series when $\mathbf{r}$ and $\mathbf{r}'$ are very close, this number being infinite when $\mathbf{r} = \mathbf{r}'$. On the contrary, image expansions obtain perfect model of the $1/R$, in so much as the mathematical expression of

this singularity, which boils down to the FS static GF, appears explicitly on the GF formulation (§3.2). Nonetheless, it is well known that image expansions exhibit a low convergence rate when it is evaluated aloof of the singularity.

GF expressions, which achieve a good representation of both the BC and the $1/R$ singular behavior, can be obtained by applying a Kummer's transform [19]-[20]. Basically, the GFs are expressed as the sum of a static part G_{Stat} and a dynamic part G_{Dyn} ([21]-[23]), so that $G = G_{Dyn} + G_{Stat}$. The expression of G_{Dyn} is obtained by subtracting all the terms *k*=0 (static terms) from the 2D modal expansions in §3.3, so that $G_{Dyn} = G - G(k=0)$. This static contribution is recovered in G through G_{Stat}, which is expressed as an 3D image series. The expressions of G_{Dyn} for G_V, G_A^{xx}, G_A^{yy} and G_A^{zz} are also obtained through the usage of table 3.7-table 3.10 and with the help of (3.30)-(3.32), but replacing $\tilde{\Phi}_D$ and $\tilde{\Phi}_N$ respectively by $\tilde{\Phi}_{Ddyn}$ and $\tilde{\Phi}_{Ndyn}$ in these formulas. On its turn, $\tilde{\Phi}_{Ddyn}$ and $\tilde{\Phi}_{Ndyn}$ are respectively calculated from (3.13) and (3.14) as $\tilde{\Phi}_{Ddyn} = \tilde{\Phi}_D - \tilde{\Phi}_D(k=0)$ and $\tilde{\Phi}_{Ndyn} = \tilde{\Phi}_N - \tilde{\Phi}_N(k=0)$. On the other hand, the usage of table 3.1 together with (3.5) and (3.6) for $k=0$ provides the forms of G_{Stat} for G_V, G_A^{xx}, G_A^{yy} and G_A^{zz}. The final expressions of these GFs, which result after applying this procedure, are provided in explicit form:

$$G_V = \frac{1}{4\pi\varepsilon}\sum_{m=-M}^{M}\sum_{n=-N}^{N}\sum_{p=-P}^{P}\sum_{i=0}^{7} Q_i \frac{1}{\sqrt{(X_i+2ma)^2+(Y_i+2nb)^2+(Z_i+2pc)^2}} + \\ + \begin{cases} \dfrac{4}{bc\varepsilon}\displaystyle\sum_{n=1}^{N}\sum_{p=1}^{P}\tilde{\Phi}_D(x,x')S(k_y,y,y')S(k_y,z,z') & P_c = |x-x'| \\ \dfrac{4}{ca\varepsilon}\displaystyle\sum_{p=1}^{P}\sum_{m=1}^{M}\tilde{\Phi}_D(y,y')S(k_z,z,z')S(k_x,x,x') & P_c = |y-y'| \\ \dfrac{4}{ab\varepsilon}\displaystyle\sum_{m=1}^{M}\sum_{n=1}^{N}\tilde{\Phi}_D(z,z')S(k_x,x,x')S(k_y,y,y') & P_c = |z-z'| \end{cases} \qquad (3.33)$$

$$G_A^{xx}=\frac{\mu}{4\pi}\sum_{m=-M}^{M}\sum_{n=-N}^{N}\sum_{p=-P}^{P}\sum_{i=0}^{7}A_i^{xx}\frac{1}{\sqrt{(X_i+2ma)^2+(Y_i+2nb)^2+(Z_i+2pc)^2}}+$$
$$+\begin{cases}\dfrac{4\mu}{bc}\sum_{n=1}^{N}\sum_{p=1}^{P}\tilde{\Phi}_N(x,x')S(k_y,y,y')S(k_z,z,z') & P_c=|x-x'|\\ \dfrac{2\mu}{ca}\sum_{p=1}^{P}\tilde{\Phi}_D(y,y')S(k_z,z,z')+ & \\ \quad+\dfrac{4\mu}{ca}\sum_{m=1}^{M}\sum_{p=1}^{P}\tilde{\Phi}_D(y,y')C(k_x,x,x')S(k_z,z,z') & P_c=|y-y'|\\ \dfrac{2\mu}{ab}\sum_{n=1}^{N}\tilde{\Phi}_D(z,z')S(k_y,y,y')+ & \\ \quad+\dfrac{4\mu}{ab}\sum_{m=1}^{M}\sum_{n=1}^{N}\tilde{\Phi}_D(z,z')C(k_x,x,x')S(k_y,y,y') & P_c=|z-z'|\end{cases} \tag{3.34}$$

$$G_A^{yy}=\frac{\mu}{4\pi}\sum_{m=-M}^{M}\sum_{n=-N}^{N}\sum_{p=-P}^{P}\sum_{i=0}^{7}A_i^{yy}\frac{1}{\sqrt{(X_i+2ma)^2+(Y_i+2nb)^2+(Z_i+2pc)^2}}+$$
$$+\begin{cases}\dfrac{2\mu}{bc}\sum_{n=1}^{N}\tilde{\Phi}_D(x,x')S(k_z,z,z')+ & \\ \quad+\dfrac{4\mu}{bc}\sum_{n=1}^{N}\sum_{p=1}^{P}\tilde{\Phi}_D(x,x')C(k_y,y,y')S(k_z,z,z') & P_c=|x-x'|\\ \dfrac{4\mu}{bc}\sum_{p=1}^{P}\sum_{m=1}^{M}\tilde{\Phi}_N(y,y')S(k_y,z,z')S(k_x,x,x') & P_c=|y-y'|\\ \dfrac{2\mu}{ab}\sum_{m=1}^{M}\tilde{\Phi}_D(z,z')S(k_x,x,x')+ & \\ \quad+\dfrac{4\mu}{ab}\sum_{n=0}^{N}\sum_{m=0}^{M}\tilde{\Phi}_D(z,z')C(k_y,y,y')S(k_x,x,x') & P_c=|z-z'|\end{cases} \tag{3.35}$$

$$G_A^{zz} = \frac{\mu}{4\pi}\sum_{m=-M}^{M}\sum_{n=-N}^{N}\sum_{p=-P}^{P}\sum_{i=0}^{7} A_i^{zz}\frac{1}{\sqrt{(X_i+2ma)^2+(Y_i+2nb)^2+(Z_i+2pc)^2}} + \\ + \begin{cases} \dfrac{2\mu}{bc}\sum_{n=1}^{N}\tilde{\Phi}_D(x,x')S(k_y,y,y') + \\ \quad + \dfrac{4\mu}{bc}\sum_{p=1}^{P}\sum_{n=1}^{N}\tilde{\Phi}_D(x,x')C(k_y,z,z')S(k_y,y,y') \qquad P_c = |x-x'| \\ \dfrac{2\mu}{ca}\sum_{m=1}^{M}\tilde{\Phi}_D(y,y')S(k_x,x,x') + \\ \quad + \dfrac{4\mu}{ca}\sum_{p=1}^{P}\sum_{m=1}^{M}\tilde{\Phi}_D(y,y')C(k_z,z,z')S(k_x,x,x') \qquad P_c = |y-y'| \\ \quad \dfrac{4\mu}{ab}\sum_{m=1}^{M}\sum_{n=1}^{N}\tilde{\Phi}_N(z,z')S(k_x,x,x')S(k_y,y,y') \qquad P_c = |z-z'| \end{cases} \tag{3.36}$$

In these GFs, the contribution of the image series is more important when $\mathbf{r}$ and $\mathbf{r}'$ are close, whereas when these points are far away the modal series is dominant. Therefore, it can be easily inferred that both a good representation of both the BC and the $1/R$ singular behavior will be attained.

3.5 GF Evaluation Techniques Comparative Study

This section is devoted to compare the techniques, which have been described in the previous sections, to implement the potential cavity GF. Namely, the 3D image series (§3.2), the 2D modal expansion (§3.3) and the hybrid representation as the sum of a dynamic part and a static part (§3.4, which will be denoted as *static part extraction* technique in this section, will be contrasted through their study in both in space and frequency.

In Fig. 3.10-Fig. 3.13 the comparison between the aforementioned techniques in the spatial domain is respectively exhibit for G_V, G_A^{xx}, G_A^{yy} and G_A^{zz}, which are associated to a cuboid of 100 mm per dimension. The simulation frequency and source point $\mathbf{r}'$ have been respectively set to 3.82 GHz and (20, 25, 50) mm. The field point $\mathbf{r}$ has been swept in three directions, which are respectively parallel to the axis *x, y* and *z*, each sweep starting in one wall of the cavity, ending at the opposite side and containing $\mathbf{r}' = (0.02, 0.025, 0.05)$. The free space static is also depicted in these figures to better discern the technique that best models the *1/R* singular behavior inherent to the potential GFs. The comparison for G_V is presented in Fig. 3.10, where Fig. 3.10a, Fig. 3.10b and Fig. 3.10c are the GF cuts along directions, which as aforesaid are respectively parallel to the axis *x, y* and *z*. It can be appraised in these figures that only modal expansion and static part extraction techniques fulfill the Dirichlet boundary conditions, which are required on the cavity walls. In the case of G_A^{xx} (Fig. 3.11), the three strategies are able of representing the Neumann BC required in the *x* direction, which can be observed in Fig. 3.11a. Nevertheless, the Dirichlet BC required in y (Fig. 3.11b) and *z* (Fig. 3.11c) directions are only achieved by the modal expansion and the static part extraction techniques. The same happens in the case of G_A^{yy} (Fig. 3.12), where

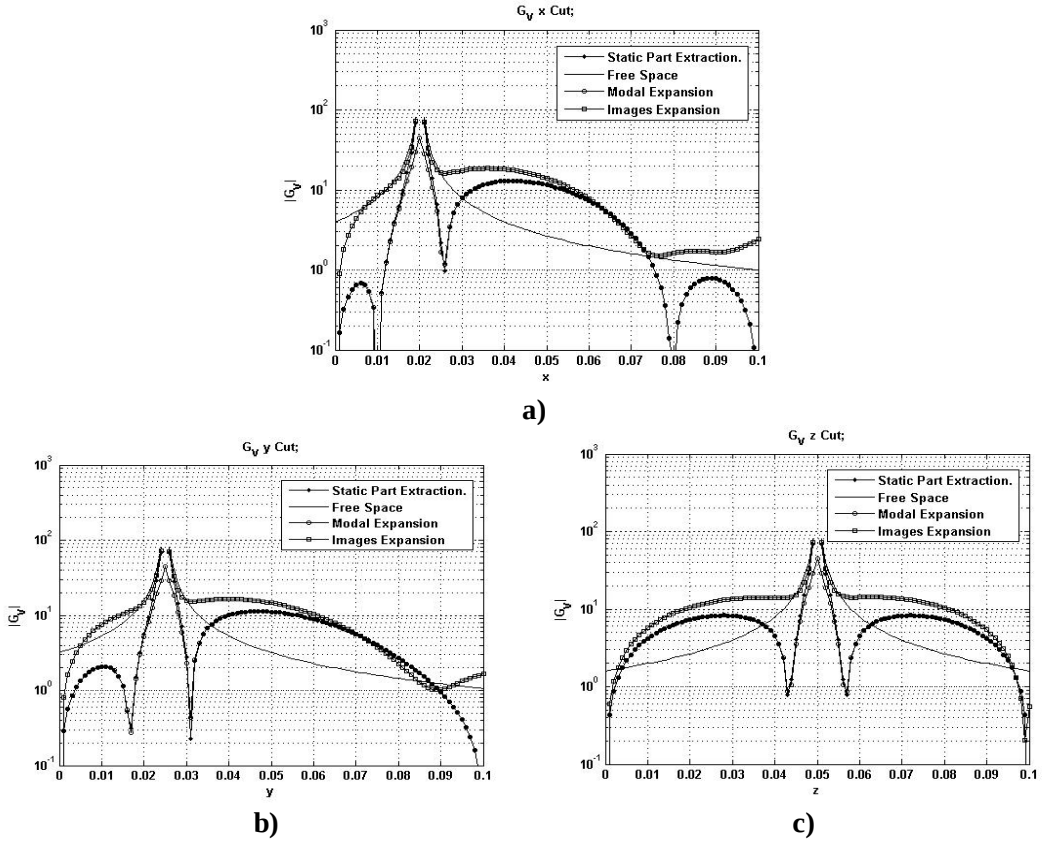

Fig 3.10 *Comparison of techniques for G_V. a) Cut along x, b) Cut along y and c) Cut along z.*

only these two strategies fulfill the Dirichlet BC in *x* (Fig. 3.12a) and in *z* (Fig. 3.12c) directions, whereas in the *y* (Fig. 3.12b) direction all techniques can represent the Neumann BC. Similarly in Fig. 3.13 for G_A^{zz}, The required Dirichlet BC along *x* (Fig. 3.13a) and *y* (Fig. 3.13b) are only attained by modals and singularity extraction techniques, while all the strategies can represent Neumann BC along *z* (Fig. 3.13c). In all these figures (Fig. 3.10-Fig.3.13), it can be observed that the images series and the static part extraction technique represent perfectly the spatial singular behavior. Two facts can be said on this matter. On the one hand, these two strategies show the sharpest variation in the neighborhood of the spatial singularity ($\mathbf{r}=\mathbf{r}'$), they even match the FS space curve in this neighborhood. In second place, this spatial singularity is perfectly represented, which can be appreciated in all these figures via the discontinuity in the curves appearing when $\mathbf{r}=\mathbf{r}'$. On the contrary, the modal expansion is not as sharper as the other two techniques in the neighborhood of the singularity. Moreover, this technique has a bounded value when $\mathbf{r}=\mathbf{r}'$. A huge number of series terms would be needed to improve the spatial singularity model when using a modal expansion.

The comparison between the image method, the 2D modal expansion and the static part extraction technique in frequency is exhibited in Fig. 3.14a, Fig. 3.14b, Fig. 3.14c and Fig. 3.14c, respectively for G_V, G_A^{xx}, G_A^{yy} and G_A^{zz}. These figures are also related to a cuboid of 100 mm per dimension. Source and field points are respectively set to (85.7, 57.1, 71.4) mm and (80, 60, 40)

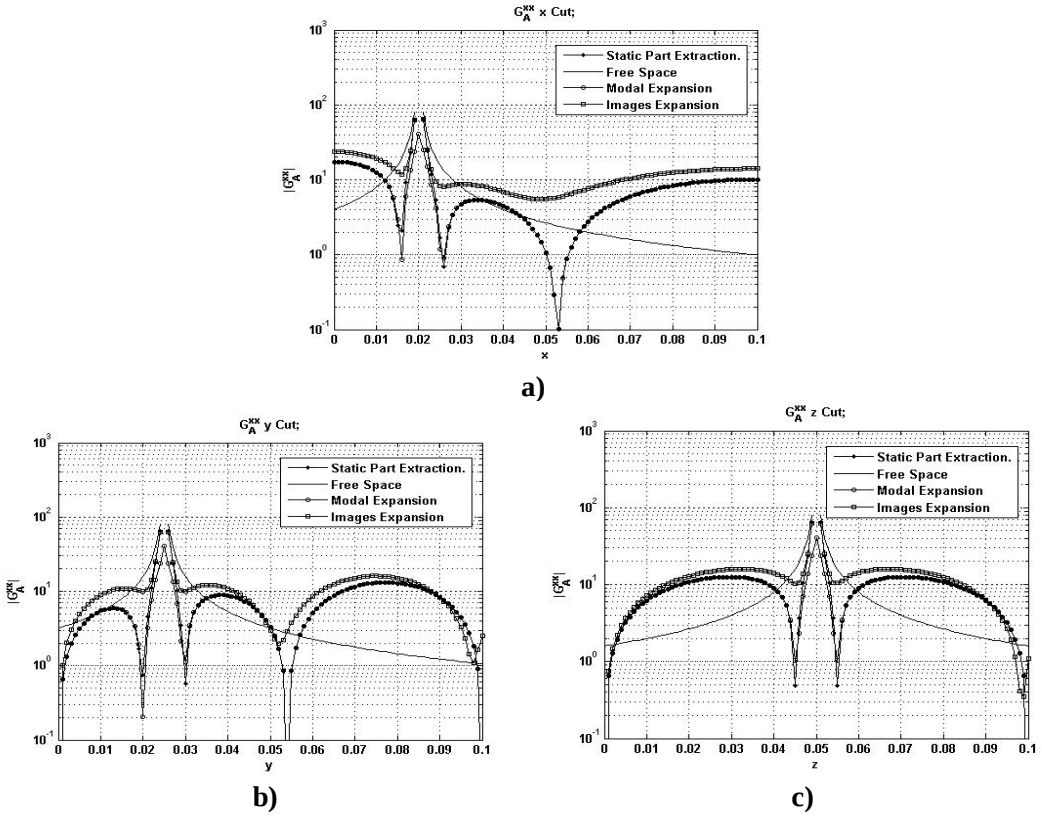

Fig 3.11 *Comparison of techniques for G_A^{xx}. a) Cut along x, b) Cut along y and c) Cut along z.*

mm. In frequency a sharp model of the cavity resonances is required, which is only obtained by the modal expansion and the static part extraction techniques, as it can be observed in Fig. 3.14 for G_V.

The most outstanding aspects inferred from Fig.3.10-Fig.3.14 are summarized in table 3.11. It is easily deduced from this table that, among exhibited techniques to implement the cavity GFs, the best one is the static part extraction, in as much as both the BC and the GF singular behavior are correctly represented.

GREEN FUNCTION IMPLEMENTING TECHNIQUE	**MODEL OF THE**		
	Spatial Singularity	**Boundary Conditions**	**Sharp Cavity Resonances**
Images Expansion	*Good*	*Bad*	*Bad*
Modal Expansion	*Bad*	*Good*	*Good*
Static Part Extraction	*Good*	*Good*	*Good*

Table 3.11 *Summary on the GF computation techniques comparison.*

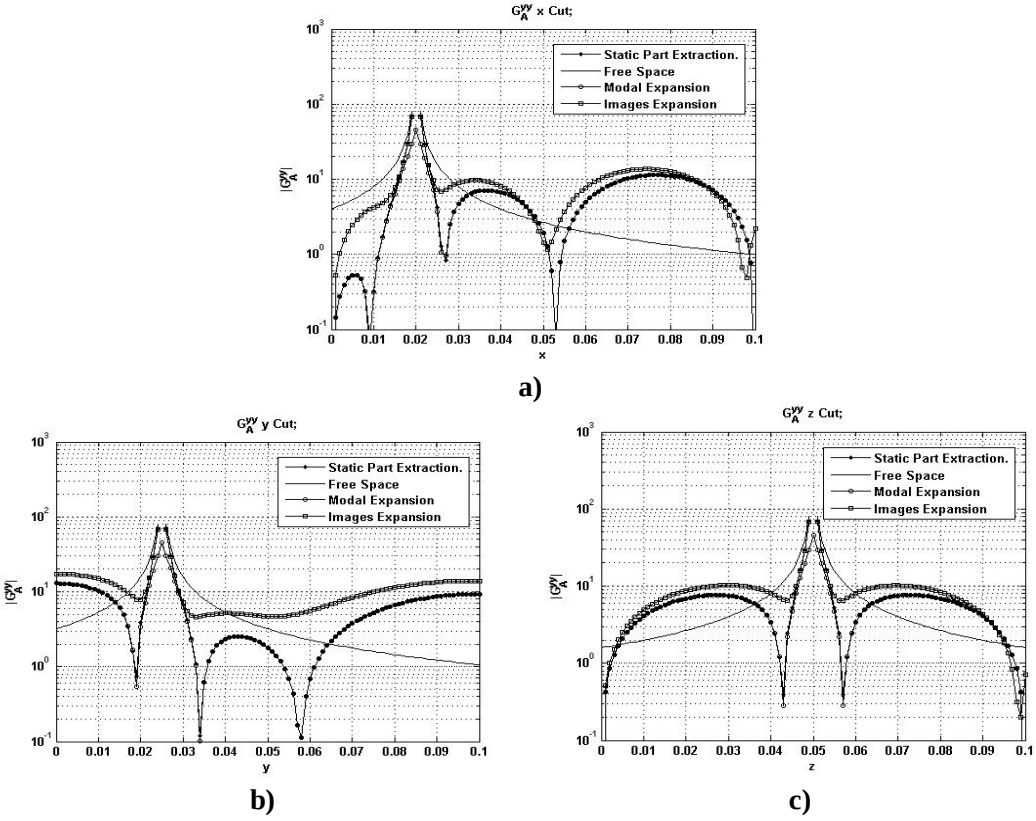

Fig 3.12 *Comparison of techniques for G_A^{yy}. a) Cut along x, b) Cut along y and c) Cut along z.*

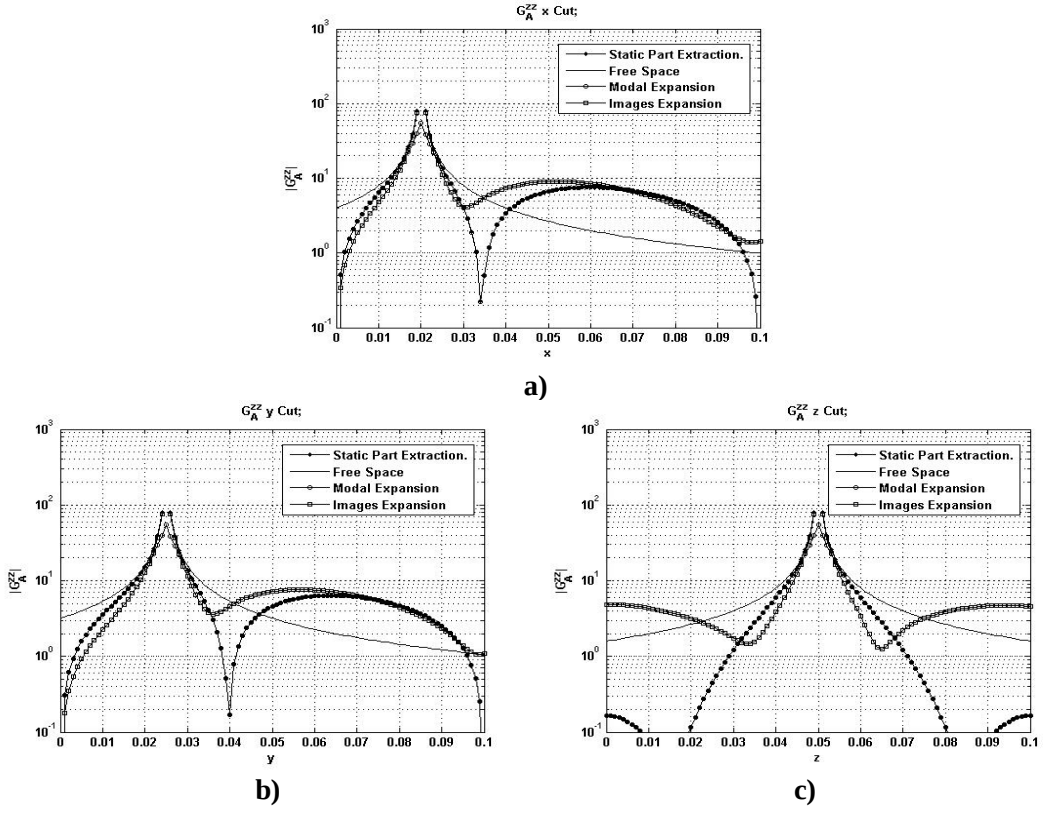

Fig 3.13 *Comparison of techniques for G_A^{zz}. a) Cut along x, b) Cut along y and c) Cut along z.*

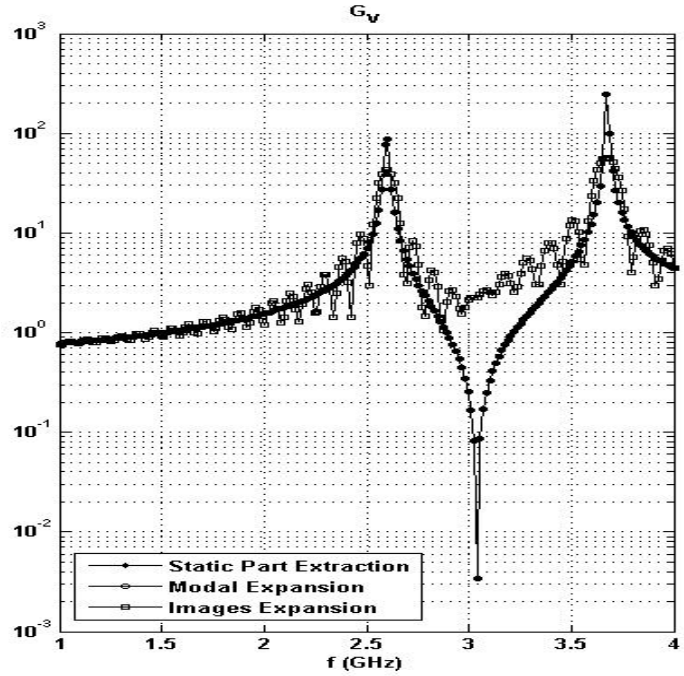

Fig 3.14 $|G_V|$ *in frequency.*

3.6 Full Wave Characterization of Potential Cavity GFs

In addition to have a sharp model of the cavity resonances, the GFs have to correctly detect all these resonances. Here, the GFs are obtained by using the Lorentz gauge. As consequence of the gauge choice all the GF components G_V, G_A^{xx}, G_A^{yy} and G_A^{zz} exhibit resonances. The detailed study of these GFs reveals that the relationship between any potential GF component and the existence of resonances including the eventual modal degeneracy is not evident. In section, this relationship will be described theoretically. To do this a classification of cavity modes according to their degeneracy is proposed. Then these modes are identified inside the expressions of the GFs. So that, the relationship between GF component, resonance frequency and excited mode can be theoretically predicted a priori. This prediction will be verified through numerical experiments to show the proper behavior of the GFs (3.33)-(3.36). The knowledge of these phenomena allows setting an efficient verification method to check the behavior of the potential cavity GFs.

3.6.1 Degenerate Modes.

The mathematical expressions of the modes of a rectangular cavity is given in table 3.2. A degenerate mode shares the same cavity resonant frequency (3.8) with other modes. Namely, this frequency may be obtained by different values of the indices *m*, *n* and *l*. It is very difficult to know the number of modes sharing a frequency. This depends on the dimensions of the cavity. For a given rectangular cavity the following modal classification, which to best of our knowledge is original, can be set:

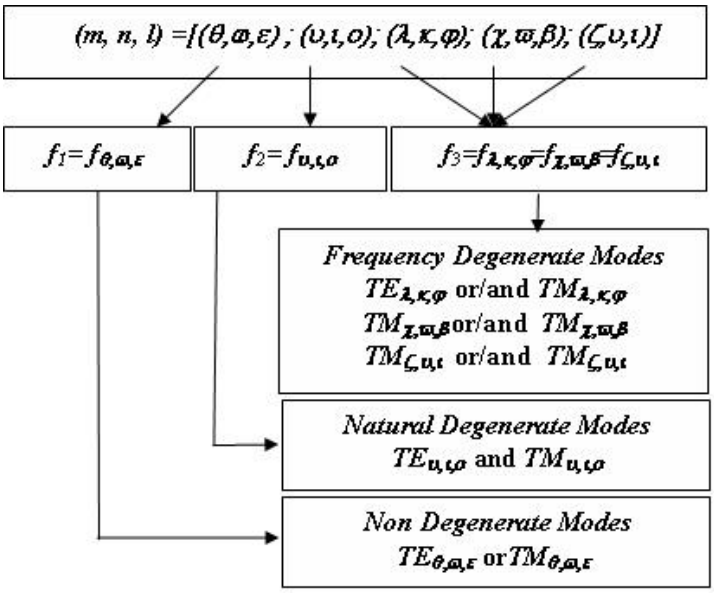

Fig 3.15 *Relationship between indices, frequencies and type of mode. At least any of* θ, ω or ε is 0.

- ***Non-degenerate modes***: They are modes whose frequency f_{mnl} is generated through a unique combination of *m*, *n*, and *l*. Therefore, they can be only related to TE_{0nl}, TE_{m0l}, or TM_{mn0} modes.
- ***Natural-degenerate modes:*** They appear when f_{mnl} is generated by a single combination of indices $m\neq0$, $n\neq0$ and $l\neq0$. In this case one mode TE_{mnl} and one mode TM_{mnl} are excited.
- ***Frequency-degenerate modes:*** They have a resonant frequency f_{mnl} which is obtained by several valid combinations of *m*, *n*, and *l*: for example when the modes $TE_{\alpha\beta\chi}$, $TM_{\alpha\beta\chi}$, $TE_{0\delta\varepsilon}$ and $TM_{\phi\gamma0}$ have the same frequency.

In Fig. 3.15, it is shown a scheme of this classification for a finite set of combinations. It has to be pointed out, that this classification is not universal, since it depends on the cavity dimensions. For example, modes classified as frequency degenerated for a given cavity may be classified as non-degenerate or natural-degenerate for another rectangular enclosure.

It is very difficult to link a resonant frequency with a Green function component when working in an environment dense in degenerate modes, since the same frequency can be shared by several modes. Consequently, the same frequency can appear in several Green function components. Here, it is desired to work in a context where the modes can be classified either as non-degenerate or natural-degenerate. Therefore, for each frequency f_{mnl} exist one and only one combination of indices *m, n* and *l* able to produce it. We will call a cavity that fulfills this property *canonical rectangular resonator*. In this resonator, all the modes TE_{0nl}, TE_{m0l}, or TM_{mn0} are non-degenerate and all the modes TE_{mnl}, TM_{mnl} ($m\neq0$, $n\neq0$, $l\neq0$) are natural degenerate. Then,

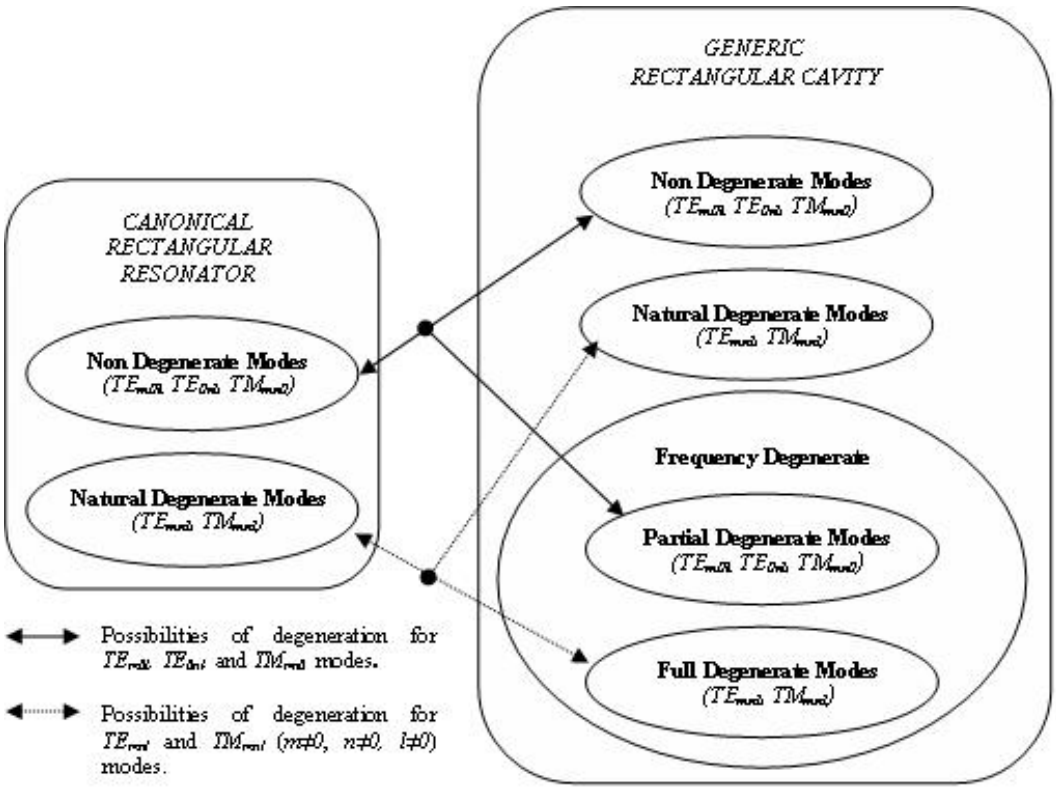

Fig 3.16 *Generic modal classification and its relation to a canonical rectangular resonator classification.*

the resonant frequencies can be easily related to G_A^{xx}, G_A^{yy}, G_A^{zz}, or G_V. The frequency degenerate modes in relation to a canonical rectangular resonator can be classified as:

- ***Partial degenerate modes:*** They are non degenerate modes in a canonical rectangular resonator. For example if for a given cavity the modes $TE_{\alpha\beta\chi}$, $TM_{\alpha\beta\chi}$, $TE_{0\delta\varepsilon}$ and $TM_{\phi\gamma0}$ are frequency degenerate, then the modes $TE_{0\delta\varepsilon}$ and $TM_{\phi\gamma0}$ are non-degenerate in a canonical rectangular resonator.
- ***Full degenerate modes:*** They appear as natural degenerate modes in a canonical rectangular resonator. For example when the modes $TE_{\alpha\beta\chi}$, $TM_{\alpha\beta\chi}$, $TE_{0\delta\varepsilon}$ and $TM_{\phi\gamma0}$ have the same frequency in a given resonator, the modes $TE_{\alpha\beta\chi}$ and $TM_{\alpha\beta\chi}$, are natural degenerate in a canonical rectangular resonator.

The whole modal classification is shown in Fig. 3.16, where the different sets of modes, which can appear in a generic rectangular cavity, can be observed. The relation of these sets to the sets in a canonical rectangular resonator is also shown.

3.6.2 GF Modal Study

In this subsection a the spectral study of the potential cavity GFs is implemented. The resonating phenomena of G_A^{xx}, G_A^{yy}, G_A^{zz}, and G_V will be characterized. On this matter the relation between a part and/or the type of Green's function, existence of resonances and eventual modal degeneracy will be described. Knowing this, An easier, faster and more efficient analysis and evaluation of the Green functions can be performed.

The relationship between the GFs, their related resonances and the eventual modal degeneracy is not evident from the expressions of G_A^{xx}, G_A^{yy}, G_A^{zz}, and G_V described in §3.3 and §3.4, where 2D modal expansions are used. Nevertheless, if the identities in [15] are applied to the formulas in 2D modal expressions without extracting the static part (§3.3), then G_V, G_A^{xx}, G_A^{yy} and G_A^{zz}, are expanded in form of a 3D modal series which are of the form

$$G_V = \frac{8}{abc\varepsilon}\sum_{m=1}^{M}\sum_{n=1}^{N}\sum_{l=1}^{L}\frac{1}{k_x^2+k_y^2+k_z^2-k^2}S\left(k_x,x,x'\right)\cdot S\left(k_x,y,y'\right)S\left(k_x,z,z'\right) \tag{3.37}$$

$$\begin{aligned} G_A^{xx} = {} & \frac{4\mu}{abc}\sum_{n=1}^{N}\sum_{l=1}^{L}\frac{1}{k_y^2+k_z^2-k^2}S\left(k_x,y,y'\right)\cdot S\left(k_x,z,z'\right)+ \\ & +\frac{8\mu}{abc}\sum_{m=1}^{M}\sum_{n=1}^{N}\sum_{l=1}^{L}\frac{1}{k_x^2+k_y^2+k_z^2-k^2}C\left(k_x,x,x'\right)\cdot S\left(k_x,y,y'\right)\cdot S\left(k_x,z,z'\right) \end{aligned} \tag{3.38}$$

$$\begin{aligned} G_A^{yy} = {} & \frac{4\mu}{abc}\sum_{m=1}^{M}\sum_{l=1}^{L}\frac{1}{k_x^2+k_z^2-k^2}S\left(k_x,x,x'\right)\cdot S\left(k_x,z,z'\right)+ \\ & +\frac{8\mu}{abc}\sum_{m=1}^{M}\sum_{n=1}^{N}\sum_{l=1}^{L}\frac{1}{k_x^2+k_y^2+k_z^2-k^2}S\left(k_x,x,x'\right)\cdot C\left(k_x,y,y'\right)\cdot S\left(k_x,z,z'\right) \end{aligned} \tag{3.39}$$

$$\begin{aligned} G_A^{zz} = {} & \frac{4\cdot\mu}{abc}\sum_{m=1}^{M}\sum_{n=1}^{N}\frac{1}{k_x^2+k_y^2-k^2}S\left(k_x,x,x'\right)S\left(k_x,y,y'\right)+ \\ & +\frac{8\mu}{abc}\sum_{m=1}^{M}\sum_{n=1}^{N}\sum_{l=1}^{L}\frac{1}{k_x^2+k_y^2+k_z^2-k^2}S\left(k_x,x,x'\right)S\left(k_x,y,y'\right)\cdot C\left(k_x,z,z'\right) \end{aligned} \tag{3.40}$$

Although as aforementioned, these 3D modal series exhibit poor converge, they are useful to identify easily the resonances in G_A^{xx}, G_A^{yy}, G_A^{zz}, and G_V as well as the modal degeneracy. (3.38)-(3.40) show that G_A^{xx}, G_A^{yy} and G_A^{zz} expressed as the sum of two terms. The first term has the form of double series. For these series, the possible resonances of G_A^{xx}, G_A^{yy} and G_A^{zz} appear respectively when

$$k = \sqrt{k_y^2+k_z^2} = \sqrt{\left(\frac{n\pi}{b}\right)^2+\left(\frac{l\pi}{c}\right)^2} \tag{3.41}$$

$$k = \sqrt{k_x^2 + k_z^2} = \sqrt{\left(\frac{m\pi}{a}\right)^2 + \left(\frac{l\pi}{c}\right)^2} \tag{3.42}$$

$$k = \sqrt{k_x^2 + k_y^2} = \sqrt{\left(\frac{m\pi}{a}\right)^2 + \left(\frac{n\pi}{b}\right)^2} \tag{3.43}$$

Equation (3.41) shows that the resulting frequencies are linked to TE_{0nl} modes for G_A^{xx}. For G_A^{yy} it can be concluded from (3.42) that the resonances are bound to TE_{m0l} modes. Finally from (3.43) it is observed that for G_A^{zz} the excited modes are to be TM_{mn0}. It is easily inferred that all the modes connected to (3.41)-(3.43) are either non-degenerate modes or partial degenerate modes. Because of this fact the double sums in (3.38)-(3.40) will be referred as *Low Degenerate Green's Function Part* and they will be represented as G_{ALD}^{hh}, where *h* can be *x*, *y* or *z*. The second part in (3.38)-(3.40) has the form of a triple series. Here the possible resonances appear for all the dyadic components when

$$k = \sqrt{k_x^2 + k_y^2 + k_z^2} = \sqrt{\left(\frac{m\pi}{a}\right)^2 + \left(\frac{n\pi}{b}\right)^2 + \left(\frac{l\pi}{c}\right)^2} \tag{3.44}$$

The resulting frequencies from (3.44) are related to either natural degenerate modes or full degenerate modes. Due to this the triple sums in (3.38)-(3.40) will be called *High Degenerate Green's Function Part* and they will be represented as G_{AHD}^{hh}. Thus G_A^{hh} where *h* is *x*, *y* or *z* can be expressed as:

$$G_A^{hh} = G_{ALD}^{hh} + G_{AHD}^{hh} \tag{3.45}$$

Related to G_V the direct inspection of (3.37) allows to conclude that the possible resonances are just as for G_{AHD}^{hh}. Consequently the excited modes are to be natural degenerate modes or full degenerate modes as well.

Table 3.12 summarizes the links between G_A^{xx}, G_A^{yy}, G_A^{zz}, and G_V, the resonating frequencies and their eventual modal degeneracy. As a matter of completeness, it is worth of mentioning that when the wave number is close to (3.41)-(3.44) the series (3.37)-(3.40) have a dominant term strongly linked with a cavity resonance, and the resulting field will be very similar to the cavity mode. On the contrary, in the limiting case k=0, none resonance's is specially privileged, the resultant field, being a static mode.

3.6.3 Numerical Example

In this section the behavior of the empty rectangular PEC cavity potential GFs is verified via a simple numerical experience, which consists of doing theoretical prediction describing the resonance and mode distributions between the Green functions components by using the knowledge in table 3.12. Then, the expressions for the Green functions given in §3.4 will be

G_V	***FREQUENCY/MODE***		***MODE TYPE.***	
	f_{mnl} TE_{mnl}; TM_{mnl} $m\neq0,n\neq0,l\neq0$		Natural or Full degenerate	
$\bar{\bar{G}}_A$	G_{ALD}^{hh}		G_{AHD}^{hh}	
	frequency/ mode	***Mode type.***	***frequency/ mode***	***Mode type.***
G_A^{xx}	f_{0nl} TE_{0nl} $n\neq0,l\neq0$	Non or Partial degenerate	f_{mnl} TE_{mnl}; TM_{mnl} $m\neq0,n\neq0,l\neq0$	Natural or Full degenerate
G_A^{yy}	f_{m0l} TE_{m0l} $m\neq0,l\neq0$	Non or Partial degenerate	f_{mnl} TE_{mnl}; TM_{mnl} $m\neq0,n\neq0,l\neq0$	Natural or Full degenerate
G_A^{zz}	f_{mn0} TM_{mn0} $m\neq0,n\neq0$	Non or Partial degenerate	f_{mnl} TE_{mnl}; TM_{mnl} $m\neq0,n\neq0,l\neq0$	Natural or Full degenerate

Table 3.12 *GF Modal study summary.*

simulated. The reader is reminded that these formulas describe the Green function as the sum of a dynamic part and a static part. The dynamic part was expressed as a double series of short-circuited waveguide modes, while the static part was represented by a triple sum of images. Finally, the agreement between the theoretical prediction and the obtained results is checked.

The aforesaid numerical experiment is performed in the framework of a PEC rectangular cavity with dimensions $a=\sqrt[4]{3\cdot10^{-4}}$, $b=\sqrt[4]{5\cdot10^{-4}}$ and $c=\sqrt[4]{7\cdot10^{-5}}$, which avoids any degeneracy in the modes (except for natural ones, obviously). In table 3.13, the relation between the expected resonances, their related modes and their linked Green function components is predicted for this resonator in the range 1-3 GHz. In this table, it can be observed that the combinations (*m*, *n*, *l*) and the resulting frequency f_{mnl} is univocal in the frequency band. Here, it can be also observed that the resonances are linked either to non-degenerate or natural-degenerate modes. Therefore, in the range 1-3 GHz the cavity acts as a canonical rectangular resonator. This is the best resonator choice to perform this experiment since the frequencies and its related modes can be clearly identified in the potential cavity Green functions. Fig. 3.17 shows that the theoretical predictions in table 3.13 are fulfilled. In Fig.3.17a, it is observed that, in G_v, only the frequencies and the related natural degenerate modes with $m\neq0$, $n\neq0$ and $l\neq0$ are found. Fig. 3.17b-Fig. 3.17d show that these frequencies and these modes are also found in G_A^{xx}, G_A^{yy} and G_A^{zz}. This is the consequence of their high degenerate Green's function part. The frequencies f_{0nl} related to TE_{0nl} modes only appear in G_A^{xx}, as it is observed in Fig. 3.17b. On the other hand, Fig. 3.17c shows that in G_A^{yy} only the frequencies f_{m0l} associated with modes TE_{m0l} appear. Finally, in G_A^{zz} appear the frequencies f_{mn0} and its related modes TM_{mn0} as it can be seen in Fig. 3.17d. All the modes TE_{0nl}, TE_{m0l}, and TM_{mn0} are non degenerate modes and they are related to the low degenerate Green's function part.

$f_{mnl}\,(GHz)_{MNL}$	MODES	MODE TYPE	EXPECTED IN
1.51831	TM_{110}	Non degenerate	G_A^{zz}
1.92237	TE_{011}	Non degenerate	G_A^{xx}
1.99707	TE_{101}	Non degenerate	G_A^{yy}
2.23485	TE_{111} ; TM_{111}	Natural degenerate	G_V; G_A^{xx}; G_A^{yy}; G_A^{zz}
2.30737	TM_{120}	Non degenerate	G_A^{zz}
2.49046	TM_{210}	Non degenerate	G_A^{zz}
2.59117	TE_{021}	Non degenerate	G_A^{xx}
2.80810	TE_{201}	Non degenerate	G_A^{yy}
2.83076	TE_{121}, TM_{121}	Natural degenerate	G_V; G_A^{xx}; G_A^{yy}; G_A^{zz}
2.98189	TE_{211}, TM_{211}	Natural degenerate	G_V; G_A^{xx}; G_A^{yy}; G_A^{zz}

Table 3.13 *Numerical experiments predictions.*

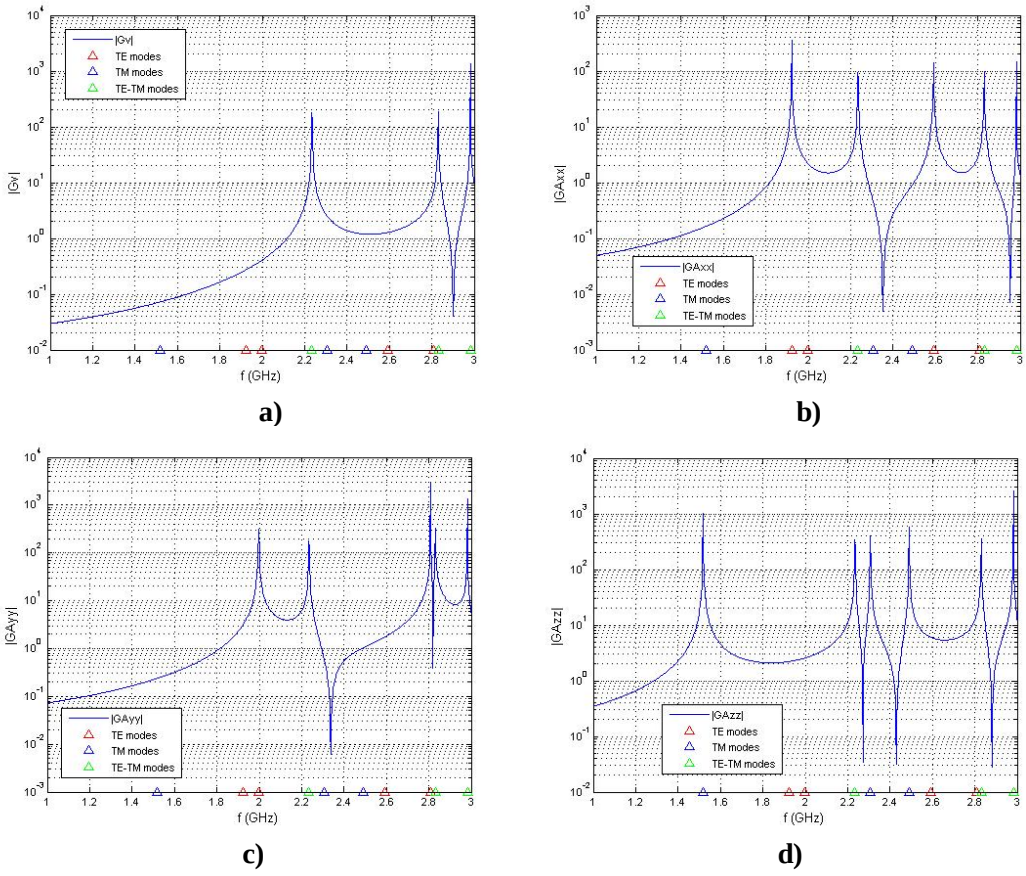

Fig 3.17 Resonances and related modes in a) G_V, *b)* G_A^{xx},*c)* G_A^{yy} *and d)* G_A^{zz}.

3.7 Novel Method to Evaluate Static Potential Cavity GFs

The original method presented in this section is based on an idea introduced by J. M. Tamayo, PhD. student from the Polytechnic University of Catalonia (UPC), during his stay at LEMA/EPFL. The author of this thesis participated in this successful EPFL-UPC collaboration and was instrumental in the numerical implementation of the procedure.

As it has been seen in previous sections, in the case of rectangular cavities, the Green function can be expressed as a triple infinite series of cavity modes or images. Both series have their advantages and disadvantages. While the modal series satisfies the boundary condition and converges fast for far-interactions, it is unable to catch the singular behavior of the GF when source and observer are close. On the other hand, the image series works best in the latter case, but converges slowly if source and observer are far away.

Due to their slow convergence these triple infinite series used to be accelerated. For this, various techniques can be found in literature [24]-[30], that are often general approaches not taking into account the physics behind the problem.

Another approach is Ewald's technique [1]-[7], which is one of the most used ones in the framework of Cartesian coordinates due to its high efficiency and precision. It is based on a hybridization of both, modal and images series developments combining the "best" of them. Unfortunately, the terms in the images part inside Ewald's method requires the evaluation of the complementary error function (*erfc*), which is computationally expensive, mainly for complex arguments, thus frequency dependent problems. To mitigate this problem, the GF could be also split into a static and dynamic part using Kummer's transform, just like in §3.4. But still, the static part contains the evaluation of the *erfc* with real-valued arguments. In this context of hybrid acceleration techniques, we propose another combination of modal and image series, whose terms only need the evaluation of algebraic expressions.

The method presented here applies to the computation of the static GF, which is split into a modal and image series part. Different to Ewald's method, the image part boils down to a single evaluation of a finite sum containing only algebraic expressions. The modal part is most efficiently computed using the technique proposed in §3.3. Similar to Ewald's technique, the proposed method combines the best of the aforementioned series, i.e. images and modes.

3.7.1 Mathematical Formulation

The 3D image expansion of the GF static part, which has been used in the expressions (3.33)-(3.36) (§3.4), is considered as starting point here. A generic mathematical formula for this expression is provided here as a matter of clearness. This expression is of the form

$$G = \frac{1}{4\pi} \sum_{m,n,p} \sum_{i=0}^{7} \frac{S_i}{R_{i,mnp}}, \tag{3.46}$$

with $S_i \in \left\{ Q_i, A_i^{hh} \right\}$, whose value can be obtained from table 3.1. As exhibited in §3.2 (3.46) can be expressed as 3D repletion of a BIS potential, which here will be denoted as *P*, as

$$G = \sum_{m,n,p} P\left(x + 2ma, y + 2nb, z + 2pc\right) \tag{3.47}$$

with (a, b, c) the dimensions of the cavity and

$$P\left(x, y, z\right) = \frac{1}{4\pi} \sum_{i=0}^{7} \frac{S_i}{\sqrt{X_i^2 + Y_i^2 + Z_i^2}}, \tag{3.48}$$

where X_i, Y_i and Z_i are also defined in table 3.1.

The proposed method is outlined at the example of a 1D periodic series, which is split into a sum of series. Therefore the function under study now is

$$G_{1D} = \sum_{m} P_{1D}\left(x + 2ma\right), \tag{3.49}$$

which is a periodic repetition of a function of one variable P_{1D} with a period 2a, typical for a parallel plate configuration. It can be subdivided into two new series of double period 4a considering the two basic terms x and x+2a as follows.

$$G_{1D} = \sum_{m} \left[P_{1D}\left(x + 4ma\right) + P_{1D}\left(x + 2a + 4ma\right) \right] \tag{3.50}$$

Two series $\psi_{01D}^{(L)}$ and $\psi_{11D}^{(L)}$, so that $G_{1D} = \psi_{01D}^{(L)} + \psi_{11D}^{(L)}$, are defined. Te first series is now equivalent to the original one but with period 4a instead of 2a, so we can apply again the same kind of subdivision, keeping the other series as it is. We can proceed in this manner, always subdividing the first series into two new series of double period with respect to he previous one, obtaining after L iterations, the following expression:

$$G_{1D} = \psi_{01D}^{(L)} + \sum_{l=1}^{L} \psi_{11D}^{(l)} \tag{3.51}$$

where the functions involved are

$$\psi_{01D}^{(L)} = \sum_{m} P_{1D}\left(x + 2^{L+1} ma\right) \tag{3.52}$$

$$\psi_{11D}^{(l)} = \sum_{m} P_{1D}\left(x + 2^{l} a + 2^{l+1} ma\right) \tag{3.53}$$

Equation (3.51) holds for every natural number L. As consequence, the limit when L tends to infinity of the aforementioned equation can be calculated as

$$G_{1D} = \lim_{L\to\infty} \psi_{01D}^{(L)} + \sum_{l=1}^{\infty} \psi_{11D}^{(l)} \tag{3.54}$$

Interchanging limit and summation in the first term of the last expression, the only term remaining is the one with m=0, as all the others would represent the evaluation of the function at P_{1D} at $\pm\infty$. But this function tends to zero for large numbers. Hence,

$$\lim_{L\to\infty} \psi_{01D}^{(L)} = P_{1D}\left(x\right) \tag{3.55}$$

yielding finally the following decomposition:

$$G_{1D} = P_{1D}\left(x\right) + \sum_{l=1}^{\infty} \psi_{11D}^{(l)} \tag{3.56}$$

Summarizing, the original periodic series, has been subdivided into one single function and a sum of periodic series with periods $2^{l+1}a$. After applying a similar procedure in the 3D case, the original series is subdivided as follows

$$G = \frac{1}{4\pi} \sum_{i=0}^{7} \frac{S_i}{\sqrt{X_i^2 + Y_i^2 + Z_i^2}} + \sum_{l=1}^{\infty} \sum_{i=1}^{7} S_i \, \psi_i^{(l)} \tag{3.57}$$

with

$$\psi_i^{(l)} = \sum_{m,n,p} P\left[X_i^{(l)} + 2m\left(2^l a\right), Y_i^{(l)} + 2n\left(2^l b\right), Z_i^{(l)} + 2p\left(2^l c\right) \right] \tag{3.58}$$

where the values of $X_i^{(l)}, Y_i^{(l)}, Z_i^{(l)}$ are obtained from table 3.14. Now, the single function evaluation is transformed into the evaluation of the eight terms in the BIS and for each level l seven series with periods $\left(2^{l+1}a, 2^{l+1}b, 2^{l+1}c\right)$ are obtained instead of one single series.

3.7.2 Physical Interpretation

For the sake of simplicity, a 2D case of the algorithm is considered in this subsection. The inclusion of the third dimension is immediate. The complete set of images of a cavity problem can be subdivided into four disjoint groups of images as shown in Fig. 3.18, where the different sets are represented with different gray tones.

The key point resides in the fact that each subset (points of same gray tones) can in turn be interpreted as the images of a point inside a bigger cavity of double size (light gray cavity in Fig. 3.18) containing the original smaller cavity (dark gray in Fig. 3.18). A schematic representation

i	$X_i^{(l)}$	$Y_i^{(l)}$	$Z_i^{(l)}$	$x_i^{(l)}$	$y_i^{(l)}$	$z_i^{(l)}$
0	x	y	z	x	y	z
1	x	y	$z+2^{l-1}c$	x	y	$2^{l-1}c$-z
2	x	$y+2^{l-1}b$	z	x	$2^{l-1}b$-y	z
3	x	$y+2^{l-1}b$	$z+2^{l-1}c$	x	$2^{l-1}b$-y	2^{l-1}-z
4	$x+2^{l-1}a$	y	z	$2^{l-1}a$-x	y	z
5	$x+2^{l-1}a$	y	$z+2^{l-1}c$	$2^{l-1}a$-x	y	$2^{l-1}c$-z
6	$x+2^{l-1}a$	$y+2^{l-1}b$	z	$2^{l-1}a$-x	$2^{l-1}b$-y	z
7	$x+2^{l-1}a$	$y+2^{l-1}b$	$z+2^{l-1}c$	$2^{l-1}a$-x	$2^{l-1}b$-y	$2^{l-1}c$-z

Table 3.14 *Initial points* $X_i^{(l)}$, $Y_i^{(l)}$ *and* $Z_i^{(l)}$ *in the periodic repetition series* $\psi_i^{(l)}$ *in (3.58).* $x_i^{(l)}$, $y_i^{(l)}$ *and* $z_i^{(l)}$ *are the new observation poins inside the bigger cavity problems, equivalents to the periodic series subdivision.*

of this decomposition is shown in Fig. 3.19, where the original problem (small cavity) is equivalent to the sum of contributions coming from the bigger cavities. Note that the problems $\psi_1^{(l+1)}$, $\psi_2^{(l+1)}$ and $\psi_3^{(l+1)}$ in the same figure can be considered as far interactions, and therefore can be efficiently computed via a 2D modal series following the techniques explained §3.3.3. The remaining first problem $\psi_0^{(l+1)}$ is again a near interaction but now inside a bigger cavity. This problem can be subdivided again in the same manner, whereas the others are directly computed using the modal series representation.

This process can be repeated infinitely until we have for each level *l* three cavities the sizes of which are 2^l times the original cavity size, respectively, and a remaining problem of infinite dimension. This consists of an infinite space containing the original source plus the BIS. Hence, the solution of the last problem will be the BIS of the original problem.

Finally, the problem is solved using a BIS plus the contribution of an infinite set of problems with source and observation points progressively further away with increasing cavity size. It means that the contribution of these problems to the final sum decreases very quickly when we go to bigger cavities, and only the series up to a certain level *l=L* actually need to be computed.

Regarding the connection with the last section, it can be easily proved that each $\psi_i^{(l+1)}$ in the periodic series subdivision is the solution to the cavity problem with dimensions $\left(2^l a, 2^l b, 2^l c\right)$, with the source point at (x', y', z') and the field point at $\left(x_i^{(l)}, y_i^{(l)}, z_i^{(l)}\right)$ as defined in table 3.14, where (a, b, c) are the original dimensions of the cavity and (x', y', z') and (x, y, z) are the original source and field points. Note that the points $\left(x_i^{(l)}, y_i^{(l)}, z_i^{(l)}\right)$ are not exactly the $\left(X_i^{(l)}, Y_i^{(l)}, Z_i^{(l)}\right)$ as in (3.58), because we need the image corresponding to the new, bigger cavity.

3.7.3 Implementation

Without loss of generality, it is assumed that the replicated point in the series images is the one closest to the walls and that it is included in the octant closest to the origin. The other cases are outlined at the end of this section explaining how to transform them to the basic situation. It is also assumed source and field points are not very far away from each other. This is the case

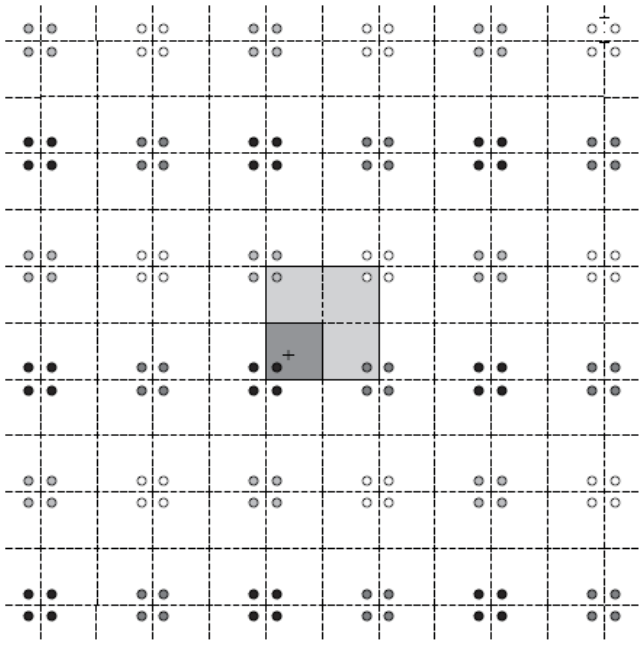

Fig 3.18 *Images distribution between the different problems. The whole set of circles represent the images of the black source point inside the small cavity in the center (1x1 squares filled with dark gray). The different gray tones of the images stand for the set of images produced by each of the images in the new bigger cavity (2x2 squares filled with soft gray).*

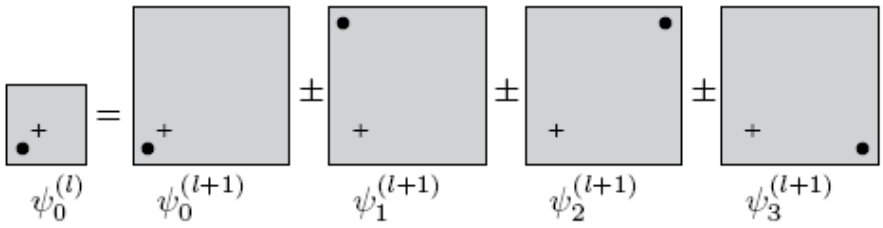

Fig 3.19. *Subdivision of the 0th cavity problem at level l, $\psi_i^{(0)}$ into the sum of four new double sized cavity problems at level $l + 1$. Although it is a 2D representation for a better understandability. The 3D cavity is subdivided into eight cavity problems instead of four. The signs depend on the potential we are dealing with.*

where this method will work efficiently. For large distances it is better to go directly to a 2D modal series.

Following the aforementioned procedure, the contribution of the remaining problem $\psi_0^{(\infty)}$, which boils simply down to (3.48) is firstly computed Secondly, the value of each series $\psi_i^{(l)}$ is computed by using a 2D reduced modal series truncated after $M^{(l)}$ modes. These series can indeed be computed utilizing modes because they are still periodic series or because they belong actually to other cavity problems. Note that the new problems have a larger relative distance

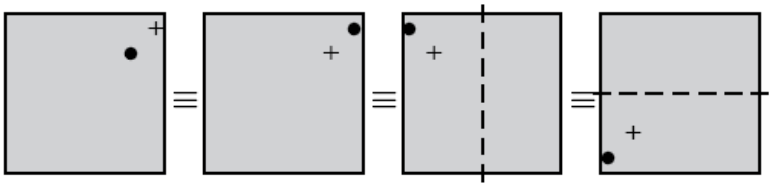

Fig 3.20. *Equivalent problems, showing the kind of transformation, which can be done without affecting the GF result.*

between source and observation point with respect to the cavity size. It means that when l grows, the value of $\psi_i^{(l)}$ decays exponentially, implying that a small number of levels is sufficient to achieve a desired relative error. Furthermore, at each level l a decreasing number of modes is needed, as it will be shown in §3.7.4. When the relation between the distance from source point to observation point and the cavity size is larger than a certain value, still to be determined, the original problem is directly computed by using a 2D reduced modal series.

In order to achieve the aforementioned configuration, there are different transformations, which can be performed without affecting the result: source and field points can be interchanged; symmetries can be performed from any coordinate plane passing through the center of the cavity. Playing with these two properties, it is straightforward to set the samples in the proper way. It is necessary because it is need to be sure that the BIS, which is being kept (remember BIS is defined always done from the origin), is the one where all the replicas are closest to the walls.

To clarify this preprocessing an example is exhibited in Fig. 3.20. This figure starts with an original source and observation points configuration (left of Fig. 3.20). Different transformations are applied in order to reach the final configuration (right of Fig. 3.20) to which the algorithm is applied. In the first step, source and observation points are interchanged because it is needed that the field point is closer to the walls. Secondly, symmetry with respect to the vertical line crossing the center is performed. Finally, symmetry with respect to the horizontal line crossing the center is used, yielding the desired configuration. Note these kind of transformations need to be applied only when source and observation point are close to each other.

3.7.4 Numerical Results

To show the feasibility of the method we have chosen a rectangular cavity of dimensions 1m×1m×1m and observation and source points at $\mathbf{r}$ = (0.5, 0.5, 0.5)m and $\mathbf{r}'$ = (0.51, 0.5, 0.5)m, respectively. This is a case where the points are close to each other with respect to the cavity size (1%). As they are placed in the center of the cavity, it can be considered the worst case for the hybrid method we have presented here because source and observation points in the new bigger cavities are placed the closest they can.

To have a good reference we have pushed Ewald's and the method presented here to the limits until having an agreement up to a relative error of 10^{-15}. The considered reference solution equals: $G_{Aref}^{xx} = 7.83996277902221$. As both Ewald and the method presented here have a steep convergence of the series elements, they can reach the machine precision (see Fig.3.21).

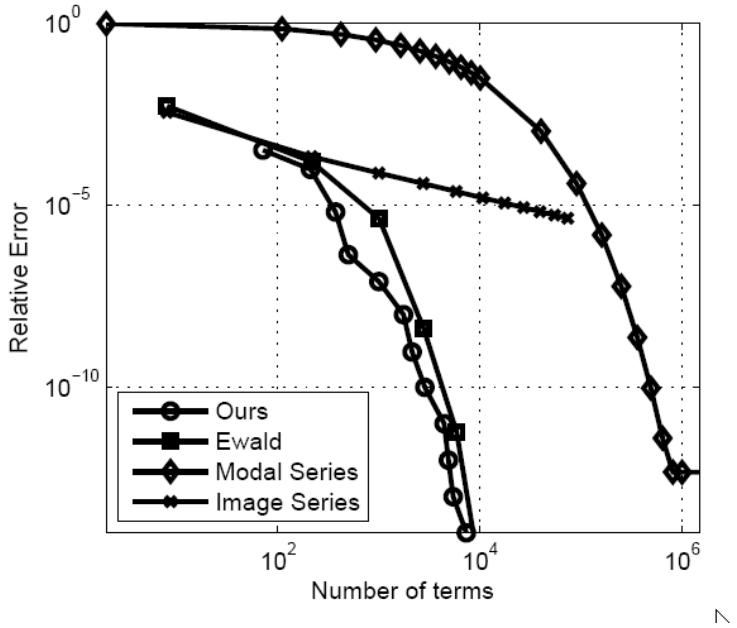

Fig 3.21. *Comparison of the evolution of the relative error with the total number of computed terms in the series for the different methods.*

However, as the terms in the modal series reduce slowly, it is more affected by round off errors and only a relative error of about 10^{-13} is achievable as shown in the same figure.

Fig. 3.21 shows the comparison between our approach and the three most used methods in literature. Ewald results have been obtained with the commonly used value for the parameter E [5]-[6]

$$E = \left(\pi^2 \frac{\frac{1}{a^2} + \frac{1}{b^2} + \frac{1}{c^2}}{a^2 + b^2 + c^2} \right)^{1/4} \tag{3.59}$$

considered somehow optimum in general. On the contrary, in the hybrid method presented here, as there is not a systematic procedure to obtain the number of modes at each level yet, these numbers have been optimized for this particular case in order to have an idea of the power of the method. Hence, the comparison is not completely fair but it shows the theoretical behavior. The optimal number of modes found for the same case to have a relative error of 10^{-15} are $7{\cdot}21^2$, $7{\cdot}14^2$, $7{\cdot}12^2$, $7{\cdot}11^2$, $7{\cdot}9^2$, $7{\cdot}8^2$, $7{\cdot}6^2$, $7{\cdot}5^2$ and $7{\cdot}3^2$ respectively for levels 1, 2, 3, 4, 5, 6, 7, 8, 9. As expected the number of modes is decreasing with increasing level l, and it is zero beyond a certain maximum level.

The results of Fig. 3.21 have been obtained for the distance between source and observer mentioned at the beginning of his section. If it is further increased the curves associated with

Ewald's and our method move further right in Fig. 3.21, meaning a larger number of summation terms are necessary, whereas the modal series curve moves left, becoming more efficient. This means beyond a certain distance between source and observer the 2D modal series will be more efficient than Ewald or the method presented here. When the distance is maintained but the two points are closer to the walls or a corner, the curve of our method moves to the left, improving the efficiency. This behavior confirms that the worst case of the method presented here occurs when source and observation point are located in the cavity center. Even in this case, the convergence of the method presented here is comparable to Ewald, which is one of the most popular techniques to compute GFs efficiently.

3.8 Conclusions

In this chapter, three techniques to evaluate the potential cavity GFs have been presented and studied. These GF, have been expressed as image series expansions in §3.2, whereas in §3.3 a modal expansion is used to calculate them. Finally, a hybrid representation, which consist of expressing the GF dynamic and static parts respectively as modal and image expansions, has been presented in §3.4. The three strategies have been compared in section §3.5, the hybrid approach being the technique, which better represent the sharp cavity resonances, the boundary conditions at the cavity walls and the *1/R* singularity. Basically, this strategy takes the best of the modal expansions techniques and the image series representations. On the one hand, all the spectral information is concentrated in the GF dynamic part, where the singularity in frequency inherent to the cavity resonances appears explicitly. In second place, this part is based on the cavity modes mathematical expressions, which satisfy by themselves the BC at the cavity walls. In the Green function static part the static type *1/R* singularity appears explicitly, inasmuch as it is inferred as an image expansion, so that a perfect model of the singular behavior when source and field points are very close or even the same is attained. A single representation as image series would satisfy the BC only at the limit, while an infinite number of modes would be needed to represent the singularity if a single modal expansion is used.

In §3.6, the relationship between any potential GF component and the corresponding cavity resonances including the eventual modal degeneracy has been provided. To describe the eventual modal degeneracy a modal classification has been proposed. It has been shown that the Green functions related to $\bar{\bar{\mathbf{G}}}_{\mathbf{A}}$ can be expressed as the sum of two parts, G_{ALD}^{hh} and G_{AHD}^{hh}. G_{ALD}^{hh} is related to all the modes TE_{0nl}, TE_{m0l}, or TM_{mn0}. It has been shown that the modes TE_{0nl} are linked to G_A^{xx}, the modes TE_{m0l}, are bound to G_A^{yy} and the modes TM_{mn0} are related to G_A^{zz}. These modes are either non-degenerate or partial degenerate. On the other hand in G_{AHD}^{hh}, just like in G_V, all the frequencies are related to degenerate modes. Even if their associated frequency is unique, a mode TE_{mnl} and a mode TM_{mnl} ($m\neq0$, $n\neq0$, $l\neq0$) will both appear. This knowledge allows a faster and more efficient evaluation and analysis of the GFs. This study has been implemented using the Lorentz gauge but a similar analysis can be performed for other gauge conditions.

In §3.7, a novel technique to compute the static part of the potential GFs inside a rectangular cavity has been presented. Similar to the Ewald acceleration method, it hybridizes images and modal series representations, extracting the best of them. The main particularity resides in the fact that it can be physically interpreted as the decomposition of the original cavity problem into

bigger cavity problems with better convergence rates. Furthermore, the images part in the method presented in §3.7 is completely algebraic and does not need the evaluation of another function as the complementary error function (erfc) in Ewald's method. A complete theoretical analysis has been introduced, based upon the decomposition of periodic series into a sum of series with larger periods. The numerical results presented here highlight the proposed method as a good alternative to compute potential cavity GFs. The optimum choice of the different parameters inside the algorithm still remains open, mainly the number of levels and the number of modes per level and the limiting relative distance which decides whether the GF is better directly computed using a 2D reduced modal series or the proposed method. Still, the main interesting point is that in the proposed method the image part is completely algebraic ($1/R$) in opposition to Ewald's method, which needs the evaluation of the complementary error function (*erfc*). If the further goal of computing the MoM matrix elements in the framework of integral equations is considered, both Ewald and the proposed method have the advantage that the modal part is analytically integrable. However, a great advantage of our approach is that, opposite to Ewald's, the static part is easier and faster to compute and it can be analytically integrated in most of the integral required in a MoM approach, as it will be seen in the next chapter. The presented method in §3.7 and the coordinate permutation technique in §3.3 haven published in a journal paper.

References

[1] P.P. Ewald, “Die berechnung optischer und elektrostatischen gitterpotentiale,” *Ann. der Phys.* 64 (1921) 253-287, Transalted by A. Cornell, Atomics International Library, 1964.

[2] M.-J. Park, J. Park, S. Nam, “Efficient calculation of the Green’s function for the rectangular cavity,” *IEEE Microwave Guided Wave Lett.* 8(3)(1998) 124-126.

[3] V.G. Papanicolao, “Ewald’s method revisited: rapidly convergent series representations of certain Green’s functions,” *J. Comp. Anal. Appl.* vol. 1, (1) (1999) 105-114.

[4] F. Marliani, A. Ciccolella, “Computationally efficient expressions of the dyadic Green’s function for rectangular enclosures,” *Progr. Electromagnet. Res.*, PIER 31 (2001) 195-223.

[5] A. Kustepeli and A.Q. Martin, “On the splitting parameter in the ewald method,” *IEEE Trans. on Microwave and Guided Wave Letters*, vol. 10, No. 5, May 2000.

[6] I. Stevanović, “Modelling challenges in computational electromagnetics: large planar multilayered structures and finite-thickness irises,” PhD. dissertation in ´Ecole Polytechnique Fédéerale de Lausanne, 2005.

[7] A. Borji and S. Sfavi-Naeini, “Rapid Calculation of the green’s function in a rectangular enclosure with application to conductor loaded cavity resonators,” *IEEE Trans. Microw. Theory and Techn.*, vol. 52, no. 7, pp. 762-765, Jul. 2004.

[8] G. Conciauro, M. Gugliemi and R. Sorrentino, *Advanced Modal Analysis*. Chichester: John Wiley & Sons, 2000.

[9] I. Stakgold, Boundary Value Problems of Mathematical Physics vols. I-II. USA: SIAM, 2000.

[10] Y. Rahmat-Samii, “On the question of computation of the dyadic green’s function at the source Region in waveguides and cavities,” *IEEE Trans. Microw. Theory and Techn.,* vol. 23, no. 9, pp. 762-765, Sep. 1975.

[11] C-T. Tai, P. Rozenfeld, “Different representations of dyadic green’s functions for rectangular cavity,” *IEEE Trans. Microw. Theory and Techn.,* vol. 24, no. 9, pp. 597-601, Sep. 1976.

[12] D. I. Wu, D. C. Chang, “A hybrid representation of the green’s function in an overmoded rectangular cavity,” *IEEE Trans. Microw. Theory and Techn.,* vol. 36, no. 9, pp. 762-765, Sep. 1988.

[13] L. W. Li, P. S. Kooi, M. S. Leong, T. S. Yeo, and S. L. Ho, “On the eigenfunction expansion of electromagnetic dyadic green’s functions in rectangular cavities and waveguides,” *IEEE Trans. Microw. Theory and Techn.*, vol. 43, no. 3, pp. 700-702, Mar. 1995.

[14] P. M. Morse and H. Feshbach, *Methods of Theoretical Physics*, part II. New York: McGraw-Hill, 1953, pp. 1849-1851.

[15] R.E Collin, *Field of Guided Waves*. New York: McGraw-Hill, 1960.

[16] C. A. Balanis, *Advanced Engineering Electromagnetics*. USA: John Wiley and Sons, 1989.

[17] M. Abramowitz and I. A. Stegun, Handbook of Mathematical Functions. New York: Dover, 1970.

[18] J.P. Estienne, “Full wave MoM Analysis & tricks for EM interactions inside a rectangular cavity (Part 1: Green’s functions & the out-of singularity zone),” in *Proc. 1st European Conference on Antennas and Propagation*, Nice, Nov. 2006, pp. 1-5.

[19] K. Knopp, *Theory and Application of Infinite Series*. New York: Dover, 1990.

[20] F.J.P. Soler, F.D.Q. Pereira, D.C. Rebenaque, A.A. Melcon, J.R. Mosig, "A novel efficient technique for the calculation of green's function in rectangular waveguides based on accelerated series decomposition,", *IEEE Trans. Antennas Popag.*, vol. 56, no 10, pp. 3260-3270, Oct. 2008.

[21] A. Q. Howard, Fr., "On the longitudinal component of the green's function dyadic," Proc. IEEE, vol. 62, no. 12, pp. 1704-1705, Dec. 1974.

[22] A.Q. Howard, Jr., and D. B. Seidel, "Singularity extraction in kernel functions in closed region problems," Radio Science, vol. 13, no. 3, pp. 425-429, May-Jun. 1978.

[23] J. Wang, "On the dyadic green's functions for a rectangular cavity with special consideration to their application in the source region," in Proc. APS-1979, pp. 421-424, 1979.

[24] G.V. Eleftheriades, J.R. Mosig, M. Guglielmi, "A fast integral equation technique for shielded planar circuits defined on nonuniform meshes," *Microwave Theory and Techniques, IEEE Transactions on* , vol.44, no.12, pp.2293-2296, Dec 1996.

[25] G. Valerio, P. Baccarelli, P. Burghignoli, and A. Galli, "Comparative analysis of acceleration techniques for 2-D and 3-D Greens functions in periodic structures along one and two directions," *IEEE Trans. Microw. Theory Tech.*, vol. 55, pp. 16301643, Jun. 2007.

[26] S. Singh, W. F. Richards, J. R. Zinecker, and D. R. Wilton, "Accelerating the convergence of series representing the free space periodic Greens functions," *IEEE Trans. Antennas Propag.*, vol. 38, pp. 1958-1962, Dec. 1990.

[27] D. Shanks, "Non linear transformations of divergent and slowly convergent sequences," *J. Math. Phys.*, 34:1-42, 1995.

[28] D. Levin, "Development of non-linear transformations for improving convergence of sequences," *Ins. J. Comput. Math.*, B3:371-388, 1973.

[29] Herbert H.H. Homeier, "Scalar Levin-type sequence transformations," *Journal of Computational and Applied Mathematics* 122 (2000) 81-147.

[30] M. Bressan and G. Conciauro, "Rapidly converging expressions for dyadic Green's functions of two-dimensional resonators of circular and rectangular cross-section," *Alta frequenza (Special issue on Applied Electromagnetics)*, vol. 52, no. 3, pp. 188-190, 1983.

4 Multidimensional Singular Integrals

"If you are stuck with a calculus problem and not know what to do, try to integrate by parts or change of variables."

Jerry Kazdan

"Divide and Conquer."

Julius Caesar

4.1 Introduction

Nowadays, surface integral equation (SIE) formulations are commonly used to solve a wide range of electromagnetic problems. As explained in (§2.1), SIEs can be set either in terms of fields or in terms of potentials. Both cases call for the multidimensional integration of the GFs associated to the SIE when utilizing the MoM to discretize the equation. As shown in the previous chapter, GFs exhibit a singular behavior when source and observation points are very close. Consequently, the accurate evaluation of multidimensional singular integrals (MSI) is needed in order to fill the MoM matrix. A formulation through fields magnifies this issue, since the computation of strongly singular and hypersingular integrals is required. Nevertheless, the problem is mitigated if potential formulations are utilized, inasmuch as the integration of weakly singular potential GFs is only needed.

This thesis is developed in the framework of potential formulations, so that only the integration of the aforementioned weakly singular potential GFs is needed. As shown in chapter (§3.4) within a full-wave MPIE context, the weak singularity inherent to these GFs is of the free-space static potential type. This is the same sort of singularity found in, both electrostatic and magnetostatic, free space potential IEs, whose associated GF is only the free-space static potential GF. The accurate integration of the singularity associated to this GF is a very challenging problem, which has been faced by many researchers. Generally, the direct numerical evaluation of the MSI within the region of the singularity is full of inconveniences, so that commonly, analytical techniques are used either to direct integrate this singularity or to alleviate the singular behavior of the integrand.

In this chapter, a detailed study of weakly 4D Multidimensional Singular Integrals (MSI), whose integrand exhibit the aforesaid free-space static potential singularity, is presented. The organization of the chapter is as follows. Firstly, the framework, mainly linked to the MoM,

where the weakly 4D MSI appear, is illustrated. Secondly, some techniques to solve MSI are briefly described. Thirdly, the original full analytical solution of these weakly 4D MSI is presented for some cases of interest. Finally, a hybrid analytical and numerical technique to solve weakly 4D MSI, which is based on an original integral transformation and numerical techniques especially tailored to integrate endpoint singular functions, is presented. Obviously, this technique applies in the cases, where the full analytical solution of the MSI is not possible.

4.2 The MPIE-MoM Interaction Integrals

As mentioned in (§2.3), the MoM transforms the IE into a linear system of equation, whose associated matrix is called the impedance matrix $\underline{\underline{\mathbf{Z}}}$. The elements z_{mn} of this matrix can be referred to as interaction or coupling integrals. If a Galerkin schema, which is undoubtedly the most popular version of MoM, is used to discretize the MPIE, then the interaction integrals can be expressed as $z_{mn} = v_{mn} + a_{mn}$ [1] with

$$v_{mn} = \int_{S_m} \mathbf{b}_m \cdot \nabla \left[\int_{S_n} G_V q_s dS' \right] dS \tag{4.1}$$

$$a_{mn} = j\omega \int_{S_m} \mathbf{b}_m \int_{S_n} \underline{\underline{\mathbf{G}}}_{\mathbf{A}} \mathbf{b}_n dS' dS\,, \tag{4.2}$$

provided that only electric equivalent currents $\mathbf{J}$ are assumed in the structure under study. In (4.1) and (4.2), $\mathbf{b}$ are the basis functions used to expand these equivalent currents (§2.3). Commonly, the expansion of $\mathbf{J}$ is set trough the employ of subsectional basis functions [2], which invokes the subdivision of the analyzed structure's surface into elementary domains (patches or cells). These patches are employed to create the definition domain S of the basis function, so that $\mathbf{b}$ represents an elementary current enclosed by S. Also in (4.1) and (4.2), $\underline{\underline{\mathbf{G}}}_{\mathbf{A}}$ and G_V are the GFs respectively related to the vector potential and the scalar potential (§2.2). Therefore, the physical meanings of the inner integrals in a_{mn} and v_{mn} are respectively the potential vector, which is produced by a current $\mathbf{b}_n$ enclosed by the source domain S_n, and the scalar potential created by the charge $q_s = -\nabla \cdot \mathbf{b}_n / j\omega$, which is also confined in S_n and bounded to $\mathbf{b}_n$. This is the reason why these integrals are also referred as *potential integrals*. As consequence, the sum of the inner integral in a_{mn} with the gradient of the inner integral in v_{mn} boils down to the electric field produced by $\mathbf{b}_n$. Within a Galerkin framework, this field should be integrated over the observer domain S_m, which is performed by means of the observer integral. This integral is the outer integral in (4.1), which boils down to the dot product between the aforesaid potentials and the test function $\mathbf{b}_m$, which is the same as the basis function but defined over S_m. Namely, z_{mn} is the weighted average associated the field confined by the observer domain, $\mathbf{b}_n$ representing the weights to perform this average.

In this thesis linear varying constant divergence basis functions are only considered. Specifically, the equivalent sources are mainly expanded through rooftop basis functions $\mathbf{T}$ [3]. As shown in Fig. 4.1a, two adjacent rectangular patches S^1 and S^2 are needed to define the rooftop's domain $S = S^1 \cup S^2$. Although in a generic case S^1 and S^2 can be arbitrarily oriented,

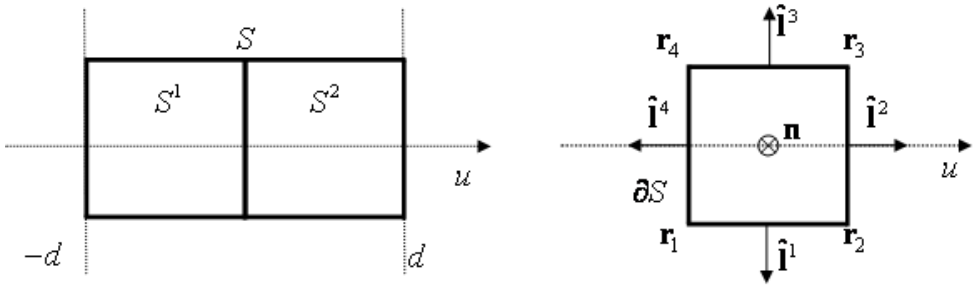

a) **b)**

Fig. 4.1 *a) Rooftop domain definition and b) single patch features.*

here it is assumed, without lost of generality and as matter of mathematical simplicity, that both patches are coplanar, being S limited between $-d$ and d along the longitudinal coordinate u, as also depicted in Fig. 4.1a. Each one of these patches is determined by the four nodes $\mathbf{r}_i$ (i=1:4) forming its boundary ∂S, the vectors $\hat{\mathbf{l}}^i$, which are orthogonal to the edges of ∂S in the plane containing the patch, and the vector $\mathbf{n}$ perpendicular to the surface enclosed by ∂S, as it can be appraised in Fig. 4.1b. $\mathbf{T}$ is defined over S as follows

$$\mathbf{T}(u) = \left(1 - \frac{|u|}{d}\right)\hat{\mathbf{u}}, \quad -d < u < d, \tag{4.3}$$

which represents a linear varying elementary current in u, that rises from $-d$, reach maximum value of 1 in the border between cells, so that the current continuity between patches is guaranteed, and finally, starts decaying till d, where it vanishes (two equal patches are assumed as a matter of mathematical simplicity). Noticeably, $\mathbf{T}$ exhibits no variation along the transversal coordinate to u. The charge associated to this current is expressed through the pulse doublet Π as

$$q_s = -\frac{\nabla \mathbf{T}(u)}{j\omega} = \frac{\Pi(u)}{j\omega d} = \frac{\operatorname{sgn}(u)}{j\omega d} \quad -d < u < d, \tag{4.4}$$

which represents negative and positive charges distributed respectively distributed over S^1 and S^2. The most relevant mathematical and physical features of $\mathbf{T}$ and its related charge q_s are summarized in table 4.1.

As consequence of (4.3) and (4.4), the interaction integrals (4.1) and (4.2) can be expressed as

$$v_{mn} = \frac{1}{j\omega d}\sum_{p=1}^{2}\sum_{q=1}^{2}\left\{\int_{S_m^p} \mathbf{T}_m \cdot \nabla\left[\int_{S_n^q} G_V \Pi(u)\, dS_n^q\right] dS_m^p\right\} \tag{4.5}$$

	CURRENT T	CHARGE $q_s = -\nabla \cdot \mathbf{T}/j\omega$
3D View	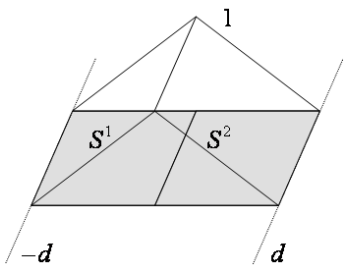	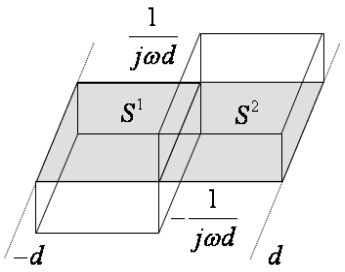
Surface Source Distribution	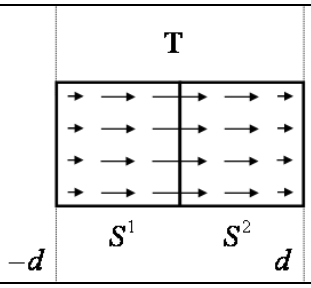	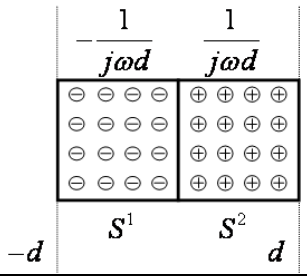
Longitudinal Cut	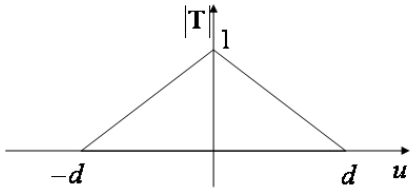	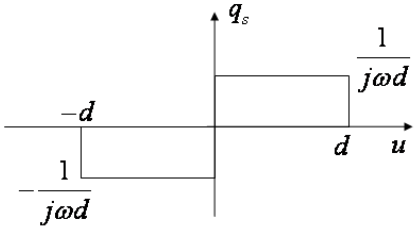

Table 4.1 *Physical and mathematical features of rooftop basis function.*

$$a_{mn} = j\omega \sum_{p=1}^{2}\sum_{q=1}^{2}\left\{\int_{S_m^p} \mathbf{T}_m \cdot \left[\int_{S_n^q} \bar{\bar{\mathbf{G}}}_{\mathbf{A}} \mathbf{T}_n dS_n^q\right] dS_m^p\right\}, \tag{4.6}$$

so that v_{mn} and a_{mn} can be directly calculated from the isolate interactions between the patches S_n^q (q=1:2) which form the n source rooftop domain $S_n = S_n^1 \cup S_n^2$, and the patches S_m^p (p=1:2), which set m rooftop observer domain $S_m = S_m^1 \cup S_m^2$. Some mathematical aspects related to the calculation of (4.5) and (4.6) are described in the two next subsections. It has to be pointed out that, even though all the mathematical developments and approximations presented in this section are particularized for the specific case of the rooftop, the same applies to other basis function fulfilling the same properties, as for instance RWG basis functions [4]. Namely, low order linear varying basis functions whose divergence is constant within their entire definition domain.

4.2.1 The Scalar Potential GF Contribution

The contribution to the interaction integral z_{mn} related to the scalar potential GF can be written as

$$v_{mn} = \frac{1}{j\omega d}\sum_{p=1}^{2}\sum_{q=1}^{2}(-1)^q \left\{\int_{S_m^p} \mathbf{T}_m \cdot \nabla\left[\int_{S_n^q} G_V dS_n^q\right] dS_m^p\right\}, \tag{4.7}$$

since Π in (4.4) is simply $\Pi(u)=\mathrm{sgn}(u)$ for $-d<u<d$ and 0 otherwise. Expression (4.7) can be further simplified though application of the vector identity $\mathbf{F}\nabla f=\nabla\cdot(f\mathbf{F})-f\nabla\cdot\mathbf{F}$ to the outer integrals ($\mathbf{F}=\mathbf{T}_m$ and f the gradient of the inner integral), and then the divergence theorem in the plane [5] to the resulting expression, so that

$$v_{mn}=\frac{1}{j\omega d}\sum_{p=1}^{2}\sum_{q=1}^{2}(-1)^q\left\{\sum_{i=1}^{4}\int_{l_m^{(p,i)}}\mathbf{T}_m\left[\int_{S_n^q}G_V dS_n^q\right]\hat{\mathbf{l}}_m^{(p,i)}dl_m^{(p,i)}+\right.$$
$$\left.+\frac{(-1)^p}{d}\int_{S_m^p}\int_{S_n^q}G_V dS_n^q dS_m^p\right\} \tag{4.8}$$

with $l_m^{(p,i)}$ the i edge (i=1:4) of the patch p (p=1:2) of the rooftop m, and $\hat{\mathbf{l}}_m^{(p,i)}$ the orthogonal vector to this edge as shown in Fig. 4.1b ($\hat{\mathbf{l}}^i$) for a generic patch. Therefore, it is clearly inferred with the help of this figure, (4.3) and Fig. 4.1a, that the sum of line integrals integral in (4.8) vanishes, insomuch as $\mathbf{T}_m\cdot\hat{\mathbf{l}}_m^{(1,4)}=\mathbf{T}_m\cdot\hat{\mathbf{l}}_m^{(2,2)}=0$ (the rooftop is 0 at $u=\pm d$), $\mathbf{T}_m\cdot\hat{\mathbf{l}}_m^{(p,1)}=\mathbf{T}_m\cdot\hat{\mathbf{l}}_m^{(p,3)}=0$ ($\hat{\mathbf{u}}\,||\,\hat{\mathbf{l}}_m^{(p,1)}\,||\,\hat{\mathbf{l}}_m^{(p,1)}$ for both p=1 and p=2) and $\mathbf{T}_m\cdot\hat{\mathbf{l}}_m^{(1,2)}=-\mathbf{T}_m\cdot\hat{\mathbf{l}}_m^{(2,4)}$. Therefore,

$$v_{mn}=\frac{1}{j\omega d^2}\sum_{p=1}^{2}\sum_{q=1}^{2}(-1)^{(p+q)}\int_{S_m^p}\int_{S_n^q}G_V dS_n^q dS_m^p\,, \tag{4.9}$$

which is really advantageous, since it only invokes the integration of G_V over the surface of the patches meshing the structure under study. Physically, the inner integral in (4.9) represent the scalar potentials by a uniform charge distribution over a rectangular patch, whereas the outer integral is the total amount of this potential within a rectangle.

4.2.2 The Vector Potential GF Contribution

The contribution a_{mn} (4.6) of the vector potential GF to the interaction integral z_{mn} can not be easily simplified, so that a priori, the integration of a function involving $\bar{\bar{\mathbf{G}}}_{\mathbf{A}}$ and the linear variations of $\mathbf{T}_n$ and $\mathbf{T}_m$ should be performed. As shown in Fig. 4.2a, this issue could be commonly tempered by expanding the rooftop as a sum, along the longitudinal coordinate ρ, of shifted pulses [6], which are obtained from $P(u)=1$ for $-1/2<u<1/2$ and 0 otherwise. As consequence (4.3) can be expressed as

$$\mathbf{T}(u)\simeq\sum_{i=1}^{I}A_i P\left(\frac{u+u_i^c}{\Delta_i}\right)\hat{\mathbf{u}}\,, \tag{4.10}$$

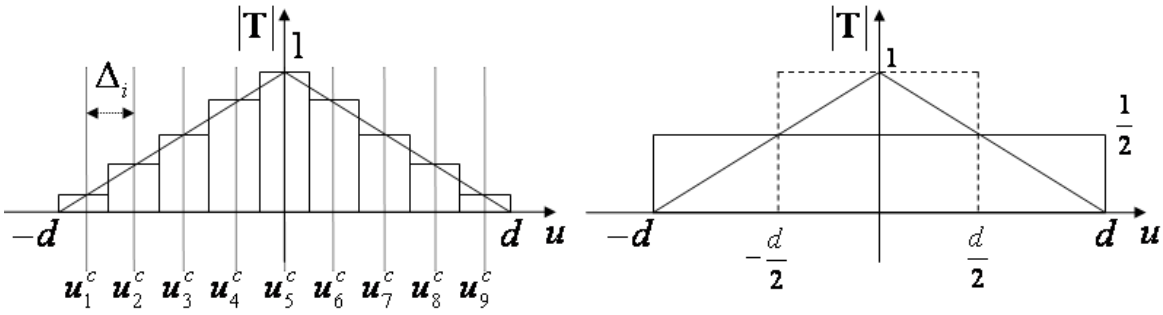

Fig. 4.2 *a) Expansion of rooftop a series of pulses b) and two possibilities to express the rooftop as a single pulse.*

where I is the number of pulses, within S^1 and S^2, $A_i = \left(1 - \left|u_i^c\right| / d\right)$, $\Delta_i = 2d/I$ and $u_i^c = -d + (2i-1)\Delta_i/2$ are respectively the amplitude, the length and the center of each pulse. Consequently (4.6) becomes

$$a_{mn} = j\omega \sum_{i=1}^{I} \sum_{k=1}^{I} \frac{1}{A_i A_k} \left\{ \int_{S_m^i} \hat{\mathbf{u}}_m \left[\int_{S_n^k} \hat{\mathbf{u}}_n \bar{\bar{\mathbf{G}}}_{\mathbf{A}} dS_n^{qk} \right] dS_m^{pi} \right\}, \tag{4.11}$$

where S_m^i and S_n^k are respectively the portion of S_m embraced by the pulse *i* and the portion of S_n comprised in the pulse *k*. Even though this approximation produce accurate results, its computation can be inefficient, since I^2 subinteractions are needed to obtain the total interaction between two patches. However, it is well known that coarser expansions of $\mathbf{T}$ in terms of pulses do not represents a significant lack of accuracy, provided that the current moments associated respectively to $\mathbf{T}$ and to its pulse expansion are the same as in the case of (4.10). Namely, the volume enclosed by the rooftop is equal to the volume housed by the pulses. Therefore, it can be considered that a single pulse, which confines the same volume as the rooftop, is enough to approximate $\mathbf{T}$. Among the several possibilities to obtain this pulse, two ways are exemplarily illustrated in Fig. 4.2b. On the one hand, it can be appraised in this figure that a single pulse of the same height as the rooftop can be utilized (Fig. 4.2b dashed line), so that $\mathbf{T}(u) \simeq P[u/d]\hat{\mathbf{u}}$ for $-d/2 < u < d/2$ and 0 otherwise, so that the new integration domain boils simply down to a rectangle centered at $d = 0$ and measuring d along u. Although, this is a valid strategy easily implementable over rectangular domains, its extrapolation to basis function defined over other patch geometries can result in integration domains, which can considerably complicate the integration of the GFs. Nevertheless on the other hand, as also depicted in Fig. 4.2b, this lack of flexibility can be solved if the rooftop is approximated by a pulse, which also confining the same volume as $\mathbf{T}$, embraces the entire rooftop's definition domain S. Therefore, $\mathbf{T}(u) \simeq P[u/2d]\hat{\mathbf{u}}/2$ for $-d < u < d$ and 0 otherwise, which corresponds to the sum of the two pulses that result of setting $I = 2$ in (4.10). As consequence, and heeding that the current flow between the two patches forming the rooftop can change of direction (always keeping the continuity), not as it has been assumed until this moment for coplanar patches, a_{mn} can be written as

$$a_{mn} = \frac{j\omega}{4}\sum_{p=1}^{2}\sum_{q=1}^{2}\left\{\int_{S_m^p}\hat{\mathbf{u}}_m^p\left[\int_{S_n^q}\hat{\mathbf{u}}_n^q\bar{\bar{\mathbf{G}}}_{\mathbf{A}}dS_n^q\right]dS_m^p\right\}, \tag{4.12}$$

where $\hat{\mathbf{u}}_m^p$ and $\hat{\mathbf{u}}_n^q$ set the direction of the current flow respectively in the patch *p* of the rooftop *m* and in the patch *q* of the rooftop *n*. In chapter §5, it is shown that this approximation is enough to produce accurate MoM results. Similarly to (4.9), the inner integral in (4.12) represent physically the vector potential associated to an uniform current. On its turn this vector potential is projected over $\hat{\mathbf{u}}_m^p$, so that the outer integral in (4.12) is total amount of this projection inside a rectangle. In some particular cases (4.12) can be further simplified, as for instance when $\hat{\mathbf{u}}_m^1 = \hat{\mathbf{u}}_m^2$, where the sum in *p* can be avoided, so that the outer integral can be directly performed over the whole definition domain of the rooftop *m* S_m. The same applies for $\hat{\mathbf{u}}_n^1 = \hat{\mathbf{u}}_n^2$, which implies that the inner integral can be directly set over S_n (definition domain of the rooftop *n*). At best, two surface integrals, respectively over S_n and over S_m, are only needed when $\left(\hat{\mathbf{u}}_m^1 = \hat{\mathbf{u}}_m^2\right) \| \left(\hat{\mathbf{u}}_n^1 = \hat{\mathbf{u}}_n^2\right)$.

4.3 Topological Classification of MSI

In the previous section, it has been evinced that, the interaction integrals within a Galerkin framework are simply built on basic interactions between cells describing the geometry under study. Provided that, potential formulations together with linear varying divergence constant basis functions are used. Also as aforementioned, two patches are involved in the computation of this basic interaction. On the one hand, the inner integral in (4.9) and (4.12) is performed over the patch where the source is defined and physically means a potential produce by a uniform source. So that in the following, as commonly done in the literature related to the topic, this integral will be referred as *source integral*, whereas the integration domain will be denoted as S' and referred as *source patch* or *source cell*. On the other hand, the outer integrals in (4.9) and (4.12), are connected to the potentials observed in a region of the space. Therefore, also as usually done in previous works associated to the subject, this integral will be referred as *observer integral*, while its integration domain will be represented by S and called *observer patch* or *observer cell*.

As introduced at the beginning of this chapter and shown in §3.4, the closer source $\mathbf{r}'$ and observation $\mathbf{r}$ points are, the more intense the singular behavior of the GFs to integrate is. This implies, that the difficulties associated to the computation of MSI are magnified when source and observer patches adjacent or coincident, which is a real challenge that has been faced by several researchers. According to the relative position of these domains, MSI can be topologically classified as singular or near singular. Specifically, since this thesis is developed in the context of potential GFs exhibiting at $1/R$ ($R = |\mathbf{r} - \mathbf{r}'|$) weak singularity, this topological classification can be set as *weak singular* and *weak near singular*. On the one hand, weak singular situations appear when source and observer domains are the same (*self case*) or share an edge or a vertex. On the other hand, weak near singular cases arise when source and observer cells are very close but their boundaries are totally separated. The rest of possible interaction will be referred as *smooth*.

SOURCE AND OBSERVER ROOFTOP DOMAINS	INTERACTION TYPE				
	Weakly Singular			Weakly Near Singular	Smooth
	Self	Adjacent	Vertex		
	$S'_A S_A$ $S'_B S_B$	$S'_A S_B$ $S'_B S_A$	-	-	-
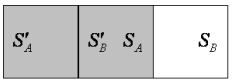	$S'_B S_A$	$S'_A S_A$ $S'_B S_B$	-	-	$S'_A S_B$
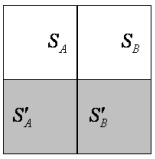	-	$S'_A S_A$ $S'_B S_B$	$S'_A S_B$ $S'_B S_A$	-	-
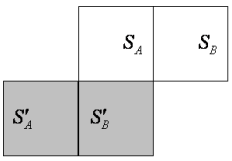	-	$S'_B S_A$	$S'_A S_A$ $S'_B S_B$	-	$S'_A S_B$
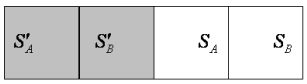	-	$S'_B S_A$		-	$S'_A S_A$ $S'_A S_B$ $S'_B S_B$
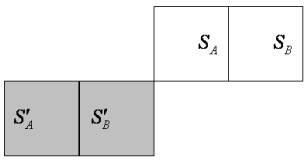	-	-	$S'_B S_A$	-	$S'_A S_A$ $S'_A S_B$ $S'_B S_B$
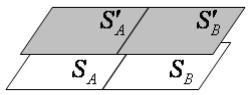	-	-	-	$S'_A S_A$ $S'_B S_B$	$S'_A S_B$ $S'_B S_A$
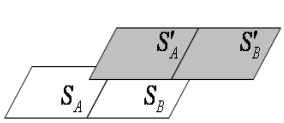	-	-	-	$S'_A S_B$	$S'_A S_A$ $S'_B S_A$ $S'_B S_B$

Table 4.2 *Some possible weakly singular, weakly near singular and smooth situations in function of the position of of source and observer rooftop's domains.*

In EM problems tackled by means of a SIE-MoM strategy these scenarios appear when the definition domain of the utilized basis functions intercept, share an edge or a vertex or are very close. Several situations for the specific case of the rooftop, where weak singular, weak near singular and regular situations appear, are shown in table 4.2.

As introduced at the beginning of the chapter, a direct numerical approach to solve the MSI within the singular region implies a lot of inconveniences. Firstly, the usage of well-behaved rules tailored to integrate smooth functions, as for instance Gauss-Legendre quadratures, either requires an unacceptable computational effort or fails when source and observer domains intercept. Nevertheless, these problems can be partially alleviated with some analytical preprocessing, which consists basically of cancelling the singularity to increase the smoothness of the integrand. Secondly, classical rules addressed to integrate functions with endpoint singularities, as for example Gauss-Jacobi quadratures, can only efficiently treat a limited set of singularities, within which $1/R$ is not. Finally although, double exponential quadratures, which will be of relevance in section §4.6, can deal with a wide range of endpoint singularities (including $1/R$), this quadrature is not devoid of analytical preprocessing in order to make the integrand to be endpoint singular in the self case. Besides, it has to be kept in mind that an accurate multidimensional integration is desired, which can imply an increment of computational cost if numerical rules are used. Therefore, the obtention or the use of the analytical expressions of weakly singular MSI appearing in the MoM matrix is highly recommended whenever possible, at least in the weak singular and weak near singular cases described in this section. If this is not feasible, then the MSI should be analytically integrated in as much dimensions as possible.

4.4 Review of techniques to solve MSI

The accurate evaluation of weakly MSI is a problem, which has been deeply studied by the EM community. The most challenging cases have been broached in the framework of free space GFs, mainly within the antenna community. In this community the techniques to solve MSI are classified as *direct evaluation*, *singularity cancelation*, and *singularity subtraction*. Although as above-mentioned, these techniques have been applied to free space GFs, they can be easily extrapolated to any similarly behaved GF. In the following a brief description of these techniques, which are strongly linked to the mathematical expression of the GF, is provided.

Firstly, direct evaluation techniques tackle the direct analytical integration of the GF. Its recent development [7]-[8] within the context of free space potential GFs has constituted a considerable breakthrough, since the analytical integration of these GFs together with RWG basis functions has been performed in several dimensions for the most challenging cases, which have been described in the previous section. On the one hand, the analytical expression of potential integral over the source path has been obtained for the self case [7] and for the adjacent case [8]. Even in the self situation, one dimension is analytically integrated over the observer patch. On the other hand, for the common vertex situation one dimension of the potential integral is analytically performed. The leftover dimensions can be numerically integrated without major inconveniences in all the cases. However, in problems involving other GFs, a direct evaluation strategy can not be the best choice, as for instance in a cavity problem, where the GF is expressed as infinite sum of

modes. Although, the full analytical integration of the potential GF is possible in this case, when source and observer points are very close a huge number of modes are needed to have a good representation of the singularity, as shown in section §3.5, so that a modal expansion including a lot of terms has to be integrated, which can be inefficient in weakly singular cases. Direct evaluation techniques can be considered if the cavity potential GF is calculated as an image expansion, but as also exhibited in section §3.5, but the image series does not match perfectly the boundary conditions at cavity walls.

Secondly, singularity cancellation techniques eliminate the singularity of the GF via an integral transformation. These techniques, which were introduced in [9], have been successfully applied by several authors [10]-[20]. As in the case of direct evaluation, its use in cavity problems requires a potential GF expanded as image series.

Finally, singularity subtraction techniques [21]-[26] express the GF as the sum of two parts, so that obviously, the associated MSI are also split in two parts, which are respectively called *regular* and *singular*. On the one hand, the regular part only invokes the integration of smooth varying terms of the GF, which can be numerically done without relevant problems. Although this is the usual strategy when free-space GFs are being integrated, it has to be pointed out that there are scenarios where this integration can be analytically performed. One of these cases is the cavity GF dynamic part presented in section §3.4, whose related multidimensional integrals can be fully done though analytical techniques. On the other hand, the singular part calls for the MSI of the singularity of the GF, which is done analytically in as much as dimensions as possible, at least in the weakly and near singular cases presented in the previous section. As also shown in section §3.4 for the GF static part, whose associated integral is an example of singular part, the best possible representation of the singular behavior requires the singularity's explicit mathematical expression to appear in the GF. In potential formulations, this expression is simply the static potential GF $1/R$ (up to the constant $1/(4\pi\varepsilon_0)$). Namely, weakly MSI of the static potential GF are commonly inherent to this singular part in IE problems set in terms of potentials, as for example in a free space problem, where the integration of this GF is only invoked, or in cavity problems, where shifted versions of the static potential GF need to be integrated. Generally, this GF can be always extracted and treated severally, thus the contribution $z_{mn}^{stc} = v_{mn}^{stc} + a_{mn}^{stc}$ of the static potential GF to the MPIE-MoM interaction integral, can be inferred from (4.9) and (4.12) as

$$z_{mn}^{stc} = j\omega \sum_{p=1}^{2}\sum_{q=1}^{2}\left[\frac{\left(\hat{\boldsymbol{\rho}}_m^p \underline{\underline{\mathbf{C}}} \hat{\boldsymbol{\rho}}_n^q\right)}{4} + \frac{A(-1)^{(p+q+1)}}{(\omega d)^2}\right]\int_{S_m^p}\int_{S_n^q}\frac{1}{R}dS_n^q dS_m^p\,, \tag{4.13}$$

where $\underline{\underline{\mathbf{C}}}$ is a matrix of constants, which are determined in accordance with the problem is being solved, for instance in a free-space problem involving potential Lorentz's gauge potential GFs $\underline{\underline{\mathbf{C}}}$ would be the eye matrix. In (4.13) , A is also a constant depending on the problem. Obviously linear varying constant divergence basis functions are assumed. Notice, that the MSI of the free space static potential GF needed are exactly the same as the interaction integrals required when solving a potential SIE-MoM problem, either electrostatic or magnetostatic, over the same structure under study with pulse basis functions, which are defined over the patches describing

REFERENCE	PATCH SHAPE	POTENTIAL INTEGRAL	OBSERVER INTEGRAL				
			Weakly Singular			Weakly Near Singular	Smooth
			Self	Adjacent	Vertex		
[21]	Generic Polygon	Analytic	Numeric				
[22]	Triangle	Analytic	Numeric				
[23]	Triangle	Analytic	Analytic	Numeric			
[24]	Triangle	Analytic	Analytic	Numeric			
[13]	Triangle	Analytic	Numeric				
[25]	Triangle	Analytic	Numeric				

Table 4.3. *Static MSI state of the art.*

the surface of this structure. Therefore, it can be considered that a singularity subtraction strategy basically extracts a static problem from a complete full-wave situation, the static problem being treated separately.

This thesis is concentrated in the framework of singularity subtraction techniques, since they still represents the most flexible technique to broach the interaction integrals appearing in a wide range of EM problems solved by means of a MPIE-MoM strategy. In the following, only the aforesaid singular part of the interaction integral will be studied, in as much as the regular part does not represent major problems. Specifically, the weakly MSI of the static GF will be only treated which, as easily deduced from (4.13), are 4D MSI that can be generically expressed as

$$I^{stc} = \int_S \left[\int_{S'} \frac{1}{R} dS' \right] dS , \tag{4.14}$$

where the inner integral (potential integral) physically represents the static potential produced by a charge uniformly distributed over the source patch S', whereas the outer integral is simply the quantity of this potential embraced by the observer path S. Several researchers have broached the analytical evaluation of the weakly MSI (4.14). Attained achievements in previous relevant works in this direction for the cases of interest described in section §4.3, are chronologically presented in table 4.3, which is by no means fully complete.

As it can be appreciated in table, the full analytical solution of (4.14) in a generic situation is still not provided. The study of these weakly MSI has been mainly oriented to classical meshes based on triangles, where the full analytical solution is only available for the weakly singular self case, being adjacent, vertex, near and smooth scenarios numerically solved. This is not even the case of mesh schemas based on other patch shapes of obvious interest like rectangles [1], quadrangles [27]-[29] or generic polygons, where only the analytical solution of the potential integral can be derived from [21], while the observer integral is also performed through numerical techniques in all the cases. Besides, the numerical integration over the observer patch is not devoid of drawbacks, inasmuch as standard Gaussian quadratures, which are tailored to efficiently integrate smooth functions, are commonly utilized. As it will be evinced in section §4.6.2, although the analytical expression of the potential integral is a continuous function, its derivatives exhibit endpoint singularities in the boundary of the source patch, so that the usage of Gaussian rules to numerically integrate this expression on the observer patch leads to lacks of

precision. These drawbacks appear especially in weakly singular and near singular situations, where the endpoint singular behavior of the derivatives of the analytical potential integral is magnified. Noticeably, full analytical expressions of the 4D weakly MSI are always devoid of these inconveniences.

In this thesis, three contributions are described in the following sections of this chapter in the framework of the accurate evaluation of the weakly MSI (4.14). Firstly, the original analytical expressions of the 4D MSI (4.14) over rectangular domains for several scenarios of interest are presented. These scenarios involve weakly singular self, adjacent and vertex situations, as well as near singular and smooth cases. Secondly, the 2D MSI potential integral in (4.14) is analytically solved for arbitrarily oriented flat generic polygonal patches through an original technique, based on an original integral transformation and leading directly to a result equivalent to the one in [21]. Thirdly, the observer integral linked to this potential is numerically performed via double exponential based rules, which are specially addressed to integrate functions exhibiting endpoint singularities in the derivatives. Therefore, the drawbacks, which are derived from the usage of standard Gaussian quadratures to perform the numerical integration over the observer patch, are greatly mitigated.

4.5 Analytical 4D Weakly MSI over Rectangular Flat Domains

This section is devoted to present the attainments obtained during the development of this thesis in the framework of the analytical computation of static 4D weakly MSI. Novel full analytical solutions for expression (4.14) will be presented. The formulas reported in this section embrace all the possible weakly singular, weakly near singular and smooth scenarios described in section §4.3 in some specific cases of interest, when using rectangular cells.

As above-mentioned rectangular cells are only considered for the geometry of source and observer patches here. All the analytical expressions exhibited in next subsections are obtained, without loss of generality, by considering the source patch S' located in a parallel plane to the XY plane, the cell's edges being parallel either to the x axis or to the y axis. Consequently, the coordinates of the source patch vertices can be explicitly expressed as $\mathbf{r_1'}=(x_1',y_1',z_s')$, $\mathbf{r_2'}=(x_1',y_2',z_s')$, $\mathbf{r_3'}=(x_2',y_2',z_s')$ and $\mathbf{r_4'}=(x_2',y_1',z_s')$, thereby (4.14) can be written as

$$I^{stc}=\int_S\left[\int_{y_1'}^{y_2'}\int_{x_1'}^{x_2'}\frac{dx'dy'}{\sqrt{(x-x')^2+(y-y')^2+(z-z_s')^2}}\right]dS \tag{4.15}$$

The aforesaid specific cases of interest, where the closed form of (4.15) has been reached, are associated to observer rectangular patches S, such that the edges of S' and the edges of S are either parallel or orthogonal two by two. This leads to three particular expressions for (4.15) which have been analytically found. Firstly, in the case source and observer patches are coplanar, thus $\mathbf{r_1}=(x_1,y_1,z_s')$, $\mathbf{r_2}=(x_1,y_2,z_s')$, $\mathbf{r_3}=(x_2,y_2,z_s')$ and $\mathbf{r_4}=(x_2,y_1,z_s')$ are the vertices of S, expression (4.15) boils down to

$$I_{cp}^{stc}=\int_{y_1}^{y_2}\int_{x_1}^{x_2}\left[\int_{y_1'}^{y_2'}\int_{x_1'}^{x_2'}\frac{dx'dy'}{\sqrt{\left(x-x'\right)^2+\left(y-y'\right)^2}}\right]dxdy\,. \tag{4.16}$$

Secondly, if S' and S are in parallel planes, that's to say the $\mathbf{r_1}=(x_1,y_1,z_o)$, $\mathbf{r_2}=(x_1,y_2,z_o)$, $\mathbf{r_3}=(x_2,y_2,z_o)$ and $\mathbf{r_4}=(x_2,y_1,z_o)$ with $d=\left|z_s'-z_o\right|$ the distance between both planes, then (4.15) becomes

$$I_{pl}^{stc}=\int_{y_1}^{y_2}\int_{x_1}^{x_2}\left[\int_{y_1'}^{y_2'}\int_{x_1'}^{x_2'}\frac{dx'dy'}{\sqrt{\left(x-x'\right)^2+\left(y-y'\right)^2+d^2}}\right]dxdy\,. \tag{4.17}$$

Finally, the observer patch can be located in a plane orthogonal to the source patches plane. Also without loss of generality, this plane is assumed to be the *XZ* plane, being S at $y=y_o$. Therefore, $\mathbf{r_1}=(x_1,y_o,z_1)$, $\mathbf{r_2}=(x_1,y_o,z_2)$, $\mathbf{r_3}=(x_2,y_o,z_2)$ and $\mathbf{r_4}=(x_2,y_o,z_1)$ set the observer patch, and consequently (4.15) is written as

$$I_{oth}^{stc}=\int_{z_1}^{z_2}\int_{x_1}^{x_2}\left[\int_{y_1'}^{y_2'}\int_{x_1'}^{x_2'}\frac{dx'dy'}{\sqrt{\left(x-x'\right)^2+\left(y_o-y'\right)^2+\left(z-z_s'\right)^2}}\right]dxdz\,. \tag{4.18}$$

In Fig. 4.3, the coplanar, parallel and orthogonal situations, which are related to (4.16), (4.17) and (4.18), are respectively depicted in Fig. 4.3a, Fig. 4.3b and Fig. 4.3c. It has to be remarked that the closed analytical expressions provided in the following subsections, can be easily generalized to arbitrary orientations of the source patch. Simply, an auxiliary cartesian frame (α,β,γ), whose related unitary vectors are inferred from the edges of the source patch has to be introduced, so that both source and observer cell's vertices are expressed in new frame through a simple change of basis from (x,y,z) to (α,β,γ). In the new frame, α, β and γ plays respectively the role of *x, y* and *z*. Notice also that expressions (4.16)-(4.18) consider also cases where S' and S intercept partially, the source patch encloses totally the observer patch or vice versa. Namely, the analytical expressions provided in the next subsections can be also useful when macrobasis basis functions [30] are used.

Anyone, who has ever been involved in the search of the closed form of any MSI, is undoubtedly aware of the enormous analytical effort required to attain the solution of the MSI (whether it exists). Nowadays, despite the appearance of mathematical softwares like MAPLE™ or MATHEMATICA™, whose use together with the classical tables [31]-[32] partially tempers the aforesaid effort, the analytical resolution of a MSI is a very challenging and difficult task, which is broached by many researchers. Among the problems to face during the analytical process to find the closed form of the MSI, two are worth mentioning. On the one hand, although mathematic computer-aided tools are essential, the results provided from them can be not concise enough, quite complicated and not very enlightening in some practical situations. On the other

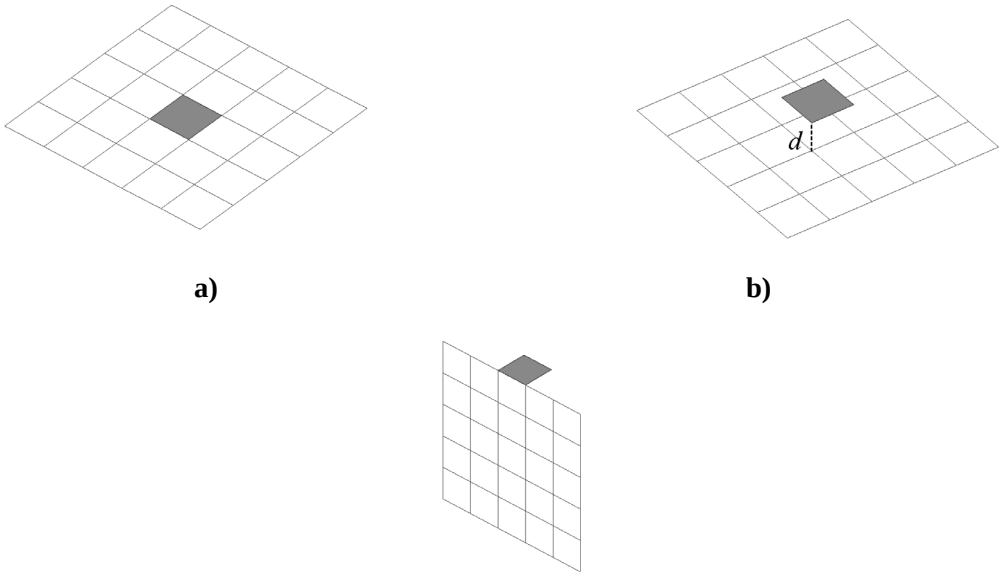

Fig. 4.3 *Some of Specific cases of interest, for which the MSI have been analytically solved: a) Coplanar cells b) Parallel cells c) Orthogonal cells In all the figures the grey cell is the source patch.*

hand in other cases, these tools are not able to provide a solution, which can be neither found in the tables. Therefore within this MSI framework, the researcher is constantly forced to look for integral transformations and to use mathematical ruses in order to alleviate the complexity of the expressions to integrate, so that, at best, the resulting integral can be easily either found in tables or dealt with computer-aided tools. In the subsections, the most relevant mathematical aspects involved in the search of the analytical closed form of the 4D MSI (4.16)-(4.18) are described.

4.5.1 Coplanar Source and Observer cells

Here the full analytical solution of I_{cp}^{stc} (4.16) is provided. The inner integral in this expression

$$V^{cp}(x,y)=\int_{y_1'}^{y_2'}\int_{x_1'}^{x_2'}\frac{dx'dy'}{\sqrt{(x-x')^2+(y-y')^2}}, \tag{4.19}$$

represents physically the potential in the *XY* plane (up to the constant $1/(4\pi\varepsilon_0)$) produced by a surface charge density of 1 C/m^2 uniformly distributed over the source rectangle, which is confined in the *XY* plane. The closed expression of the 4D integral I_{cp}^{stc}, which is needed within a Galerkin framework, requires the knowledge of the analytical form of V^{cp}, in order to integrate it over the observer patch. This analytical form is a well known result and can be derived from literature [21]. However, not all the possible mathematical expressions of V^{cp} mitigate the effort

required to perform the analytical integration over the observer patch. Here, the applied analytical procedure results in a expression for V^{cp}, which alleviates considerably the analytical obtaining of I_{cp}^{stc}. The procedure starts with the transformation $u = x - x'$, $v = y - y'$, whose associated Jacobian is 1, and leads to

$$\begin{aligned} V^{cp}(x,y) &= \int_{v_1(y)}^{v_2(y)} \int_{u_1(x)}^{u_2(x)} \frac{du dv}{\sqrt{u^2+v^2}} = \sum_{n=1}^{2} (-1)^n \int_{v_1(y)}^{v_2(y)} \sinh^{-1}\left(\frac{u_n(x)}{v}\right) dv \\ &= \sum_{n=1}^{2} (-1)^n \sum_{m=1}^{2} (-1)^m \left[v_m(y) \sinh^{-1}\left(\frac{u_n(x)}{v_m(y)}\right) + u_n(x) \sinh^{-1}\left(\frac{v_m(y)}{u_n(x)}\right) \right] \\ &= \sum_{m=1}^{2} \sum_{n=1}^{2} (-1)^{m+n} \left[f^{cp}\left(v_m(y), u_n(x)\right) + f_n^{cp}\left(u_n(x), v_m(y)\right) \right] \end{aligned} \quad (4.20)$$

where $u_n(x) = |x - x_n'|$, $v_m(y) = |y - y_m'|$ (m=1:2, n=1:2) and, obviously $f_n^{cp}(\alpha,\beta) = \alpha \sinh^{-1}(\beta/\alpha)$. The integral regarding v is solved in three steps: firstly, the change of variables $t = u_n/v$ is applied to the integrand; secondly, the resulting expression is integrated by parts; thirdly, the expression 2.266 in [31] is used to solve the remaining primitive after the integration by parts procedure.

It is clearly inferred from (4.20), that the final analytical form of I_{cp}^{stc} only invokes the computation of the *primitive* $F^{cp}(\alpha,\beta)$ linked to $f_n^{cp}(\alpha,\beta)$. Fortunately, in this case, the symbolic tool MAPLE ™ provides a concise and enlightening enough expression for this primitive, which is of the form

$$\begin{aligned} F^{cp}(\alpha,\beta) &= \iint f^{cp}(\alpha,\beta) d\alpha d\beta \\ &= \frac{1}{2}\left[\alpha^2 \beta \sinh^{-1}\left(\frac{\beta}{\alpha}\right) + \frac{1}{3}\left(\beta^2 - 2\alpha^2\right)\sqrt{\alpha^2+\beta^2} \right] \end{aligned} \quad (4.21)$$

and boils down to $F^{cp}(\alpha,\beta) = \beta^3/6$ for $\alpha = 0$ (this is easily proven by applying the Hôpital rule to (4.21) when $\alpha \to 0$). The employ of (4.21) in (4.20) provides the targeted integral of $V^{cp}(x,y)$ over the observer patch, which can be expressed as:

$$I_{cp}^{stc} = \sum_{m=1}^{2} \sum_{n=1}^{2} \sum_{p=1}^{2} \sum_{q=1}^{2} (-1)^{m+n+p+q} \left\{ F^{cp}\left[v_m(y_q), u_n(x_p) \right] + F^{cp}\left[u_n(x_p), v_m(y_q) \right] \right\} \quad (4.22)$$

The analytical expression of I_{cp}^{stc} presented here is ascertained by qualitatively comparing it to the results produced by the full numerical integration of (4.19) through the usage of Gaussian rules. A singularity cancelation technique based on a polar coordinate transformation, which will be described in detail in section §4.6.1, is employed to eliminate the $1/R$ singularity inherent to the integrand. The relative error between full analytical and full numerical solutions with regard to the normalized distance between the source cell center (X_c,Y_c) and the observer cell center (X,Y) is shown in Fig. 4.4a, Fig. 4.4b, Fig. 4.4c and Fig. 4.4d, respectively for 2, 4, 8 and 16

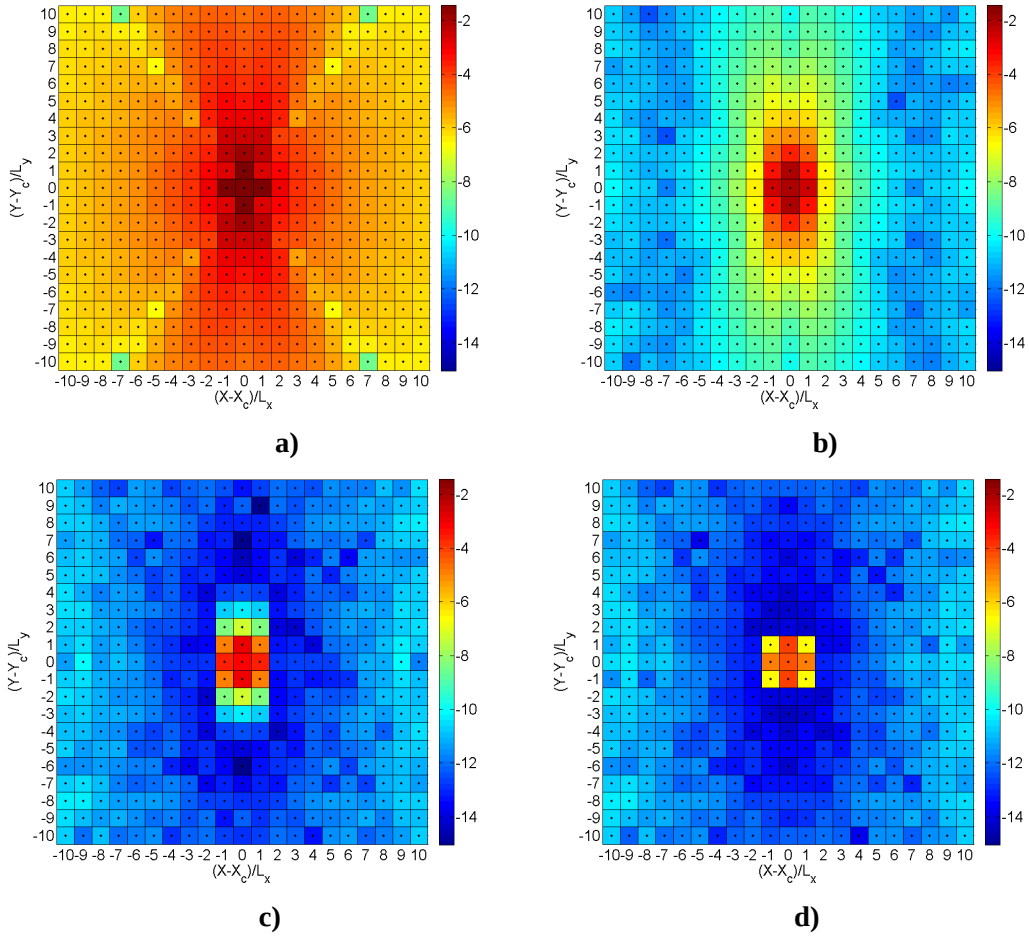

Fig 4.4 *Relative error between the analytic solution for the coplanar cell situation (4.22) and the full numerical solution of (4.16), which is calculated with a) 2 b), 4 c), 8 and d) 16 integration points per dimensions.*

integration abscissas in the numerical approach. The source cell is located in the center of the *XY* plane and measures L_x=1 x L_y=1/3 m. The observer cells are generated by dividing a plate, which is also centered at the origin of the *XY* plane, in 21x21 observer patches of the same size as the source cell. It can be clearly appraised in Fig. 4.4, that the bigger the number of integration points is, the closer analytical and numerical solutions are. As expected, in all the weakly singular cases (self, adjacent and vertex), the committed relative error is bigger, what happens basically for two reasons. On the one hand, the number of integration abscissas is not enough to achieve an accurate solution in these cases. At this point, this does not represent a problem, insomuch as the objective is not to obtain an accurate numerical integration, but verify the attained analytical solution. On the other hand, the observer integral invokes the integration of the potential produced by a uniform surface charge distribution. Namely, a function, which exhibit endpoint singular derivatives in the contour of the source cell, has to be integrated. As it will be shown in detail in section §4.6 this causes lacks of accuracy when using Gaussian rules, since they are not tailored to integrate these sort of functions.

4.5.2 Source and Observer cells Located at Parallel Planes.

In this subsection the closed form of the 4D integral I_{pl}^{stc} (4.17) is provided. In this expression the inner integral

$$V^{pl}(x,y)=\int_{y_1'}^{y_2'}\int_{x_1'}^{x_2'}\frac{dx'dy'}{\sqrt{(x-x')^2+(y-y')^2+d^2}} \tag{4.23}$$

physically represents the potential (except for the constant $1/(4\pi\varepsilon_0)$) produced by a uniform 1 C/m^2 surface charge distribution, which is confined in a rectangle housed in the *XY* plane, in a plane, which is parallel to this plane, being *d* the distance between both planes. The obtaining of the closed form I_{pl}^{stc} invokes the integration of the analytical solution of (4.23) over the observer patch. This analytical solution is calculated by starting, as in the previous subsection, with variable transformation $u=x-x'$, $v=y-y'$. Therefore

$$\begin{aligned}V^{pl}(x,y)&=\int_{v_1(y)}^{v_2(y)}\int_{u_1(x)}^{u_2(x)}\frac{dudv}{\sqrt{u^2+v^2+d^2}}=\sum_{n=1}^{2}(-1)^n\int_{v_1(y)}^{v_2(y)}\sinh^{-1}\left(\frac{u_n(x)}{\sqrt{v^2+d^2}}\right)dv\\&=\sum_{m=1}^{2}\sum_{n=1}^{2}(-1)^{m+n}\left[P_1^{pl}(u_n(x),v_m(y))\right]\end{aligned} \tag{4.24}$$

which requires the close form of the primitive P_1^{pl}. This closed form is found by firstly employing the change of variable $t=u_n(x)/\sqrt{v^2+d^2}$, which lead to

$$P_1^{pl}(u_n(x),v)=\int\sinh^{-1}\left(\frac{u_n(x)}{\sqrt{v^2+d^2}}\right)dv=\int\frac{-u_n(x)\sinh^{-1}(t)}{t^2\sqrt{1-At^2}}dt \tag{4.25}$$

with $A=\left[d/u_n(x)\right]^2$. The primitive in (4.25) is calculated by parts with $f(t)=-u_n(x)\sinh^{-1}(t)$, $f'(t)=-u_n(x)/\sqrt{1+t^2}$, $g'(t)=1/\left(t^2\sqrt{1-At^2}\right)$, which lead to $g(t)=-\sqrt{1-At^2}/t$ with the help of 342.1 in [32], so that.

$$P_1^{pl}(u_n(x),v)=\frac{u_n(x)\sinh^{-1}(t)\sqrt{1-At^2}}{t}-\int\frac{u_n(x)}{t}\sqrt{\frac{1-At^2}{1+t^2}}dt \tag{4.26}$$

The closed form of the primitive in (4.26) can be derived from the result provided by MAPLE™ after applying some algebra, thereby

$$V^{pl}(x,y)=\sum_{m=1}^{2}\sum_{n=1}^{2}(-1)^{m+n}\left\{f^{pl}\left[u_n(x),v_m(y)\right]+g^{pl}\left[u_n(x),v_m(y)\right]\right. \\ \left.-h^{pl}\left[u_n(x),v_m(y)\right]\right\} \quad (4.27)$$

where

$$f^{pl}\left[u_n(x),v_m(y)\right]=v_m(y)\sinh^{-1}\left(\frac{u_n(x)}{V_m(y)}\right)$$
$$g^{pl}\left[u_n(x),v_m(y)\right]=u_n(x)\tanh^{-1}\left(\frac{v_m(y)}{B_{mn}(x,y)}\right) \quad (4.28)$$
$$h^{pl}\left[u_n(x),v_m(y)\right]=d\tan^{-1}\left(\frac{u_n(x)v(y)}{dB_{mn}(x,y)}\right)$$

with $B_{mn}(x,y)=\sqrt{v_m^2(y)+u_n^2(x)+d^2}$ $V_m(y)=\sqrt{v_m^2(y)+d^2}$. The final expression of I_{pl}^{stc} is obtained by integrating f^{pl} g^{pl} and h^{pl} over the observer patch. In the following, the analytical steps involved in these three integrals are briefly. Firstly,

$$F^{pl}=\int_{u_n(x_1)}^{u_n(x_2)}\int_{v_m(y_1)}^{v_m(y_2)}f^{pl}\left[u_n(x),v_m(y)\right]dv_m du_n \quad (4.29)$$

whose inner integral is solved via the transformation $t=u_n(x)/V_m(y)$, is broached. The solution of the resulting expression after this transformation can be obtained from 731.3 in [32], thereby

$$F^{pl}=\sum_{p=1}^{2}(-1)^p\int_{u_n(x_1)}^{u_n(x_2)}\left[\frac{V_m^2(y)}{2}\sinh^{-1}\left(\frac{u_n(x)}{V_m(y)}\right)+\frac{u_n(x)B_{mn}(x,y_p)}{2}\right]du_n. \quad (4.30)$$

The leftover integral can be fortunately performed with MAPLE^{TM}, so that

$$F^{pl}=\frac{1}{2}\sum_{q=1}^{2}\sum_{p=1}^{2}(-1)^{p+q}\left[V_m^2(y_p)u_n(x_q)\sinh^{-1}\left(\frac{u_n(x_q)}{V_m(y_p)}\right)\right. \\ \left.+\frac{u_n^2(x_q)-2V_m^2(y_p)}{3}B_{mn}(x_q,y_p)\right] \quad (4.31)$$

Secondly, the inner integral in the integral over the observer patch of g_n^{pl}

$$G^{pl}=\int_{u_n(x_1)}^{u_n(x_2)}\int_{v_m(y_1)}^{v_m(y_2)}g^{pl}\left[u_n(x),v_m(y)\right]dv_m du_n \quad (4.32)$$

is found by means of the transformation $t = v_m(y)/B_{mn}(x,y)$, which produces a result also easily handled by MAPLE™, which after some algebra becomes

$$G^{pl} = \sum_{p=1}^{2}(-1)^p \int_{u_n(x_1)}^{u_n(x_2)} \left[u_n(x) v_m(y_p) \tanh^{-1}\left(\frac{v_m(y_p)}{B_{mn}(x,y_p)} \right) + u_n(x) B_{mn}(x,y_p) \right] du_n \tag{4.33}$$

The hyperbolic arctangent term in (4.33) can is also integrated with the transformation $t = v_m(y_p)/B_{mn}(x,y)$, which lead to 735.3 in [32], whereas the remaining term is straightforward. As consequence,

$$G^{pl} = \frac{1}{2}\sum_{q=1}^{2}\sum_{p=1}^{2}(-1)^{p+q} \left[v_m(y_p) U_n(x) \tanh^{-1}\left(\frac{v_m(y_p)}{B_{mn}(x_q,y_p)} \right) - \frac{\left(v_m^2(y_p) - 2U_n(x)\right)}{3} B_{mn}(x_q,y_p) \right] \tag{4.34}$$

with $U_n(x) = u_n^2(x) + d^2$. Thirdly, the integral over the observer patch of h_n^{pl}, which is of the form

$$H^{pl} = \int_{v_m(y_1)}^{v_m(y_2)} \int_{u_n(x_1)}^{u_n(x_2)} h^{pl}\left[u_n(x), v_m(y)\right] du_n dv_m \,, \tag{4.35}$$

is tackled. In the first place the transformation $t = u_n(x)v(y)/\left[dB_{mn}(x,y)\right]$ is applied to the inner integral, so that (4.35) becomes

$$H^{pl} = \int_{v_n(x_1)}^{v_n(x_2)} \frac{v_m^2(y) V_m(y)}{d^2} \left[\int_{u_n(x_1)}^{u_n(x_2)} \frac{\tan^{-1}(t)\,dt}{\sqrt{\frac{v_m^2(y)}{d^2} - t^2}} \right] dv_n \tag{4.36}$$

On its turn, the inner integral in (4.36) is solved by parts with $f(t) = \tan^{-1}(t)$, $f'(t) = 1/(1+t^2)$, $g'(t) = 1/\sqrt{v_m^2(y)/d^2 - t^2}^{\,3}$, which lead to $g(t) = td^2/\left[v_m^2(y)\sqrt{v_m^2(y)/d^2 - t^2}\right]$ (320.03 [32]). The leftover integral resulting of the integration by parts procedure can be easily handled by MAPLE™, so that

$$H^{pl}=\sum_{q=1}^{2}(-1)^{q}\int_{v_m(y_1)}^{v_m(y_2)}\left[u_n\left(x_q\right)\tan^{-1}\left(\frac{u_n\left(x_q\right)v_m\left(y\right)}{d^2B_{mn}\left(x_q,y\right)}\right)+d\tanh^{-1}\left(\frac{v_m\left(y\right)}{B_{mn}\left(x_q,y\right)}\right)\right]dv_m \tag{4.37}$$

The obtaining of the analytical solution of (4.37) is considerably easy, inasmuch as integral of the trigonometric arctangent term is the same as the inner integral in (4.35) but regarding *v*, whereas the hyperbolic term contribution can be also obtained without major problems from the result provided by MAPLE™. Therefore,

$$H^{pl}=\frac{1}{2}\sum_{q=1}^{2}\sum_{p=1}^{2}(-1)^{p+q}\left[v_m\left(y_p\right)u_n\left(x_q\right)\tan^{-1}\left(\frac{v_m\left(y_p\right)u_n\left(x_q\right)}{dB_{mn}\left(x_q,y_p\right)}\right)+u_n\left(x_q\right)d\tanh^{-1}\left(\frac{u_n\left(x_q\right)}{B_{mn}\left(x_q,y_p\right)}\right)+v_n\left(y_p\right)d\tanh^{-1}\left(\frac{v_m\left(y_p\right)}{B_{mn}\left(x_q,y_p\right)}\right)-dB_{mn}\left(x_q,y_p\right)\right] \tag{4.38}$$

Finally, the closed expression of I_{pl}^{stc} is set through a (4.31), (4.34) and (4.38) as

$$I_{pl}^{stc}=\sum_{m=1}^{2}\sum_{n=1}^{2}(-1)^{m+n}\left\{F^{pl}+G^{pl}+H^{pl}\right\} \tag{4.39}$$

This expression is verified in a similar way as for the coplanar case exhibit in the previous subsection. Namely, a qualitative comparison between (4.39) and the full numerical solution is performed. On the contrary, no special treatment is applied to the numerical integration, since I_{pl}^{stc} corresponds basically to weakly near singular scenarios, where the GF singularity can be, a priori, numerically integrated. The relative error between full analytical and full numerical solutions with regard to the normalized distance between the source cell center (X_c,Y_c) and the observer cell center (X,Y) is shown in Fig 4.5a, Fig 4.5b, Fig 4.5c and Fig 4.5d, respectively for 2, 4, 8 and 16 integration abscissas in the numerical approach. The source cell is located in the center of the *XY* plane and measures L_x=1 x L_y=1/3 m. The observer cells are generated by dividing a plate, which is also centered at the (0,0,*d*=0.001) plane, in 21x21 observer patches of the same size as the source cell. It is appreciated in Fig 4.5, that the bigger the number of integration points is, the closer analytical and numerical solutions are, as for the coplanar case. In the vicinity of the source cell, the committed relative error is bigger than in the rest of the plane, being the reasons associated to this fact the same as for the coplanar case. The reader is reminded that at this point, only a qualitative verification is targeted, so that showing the convergence of the

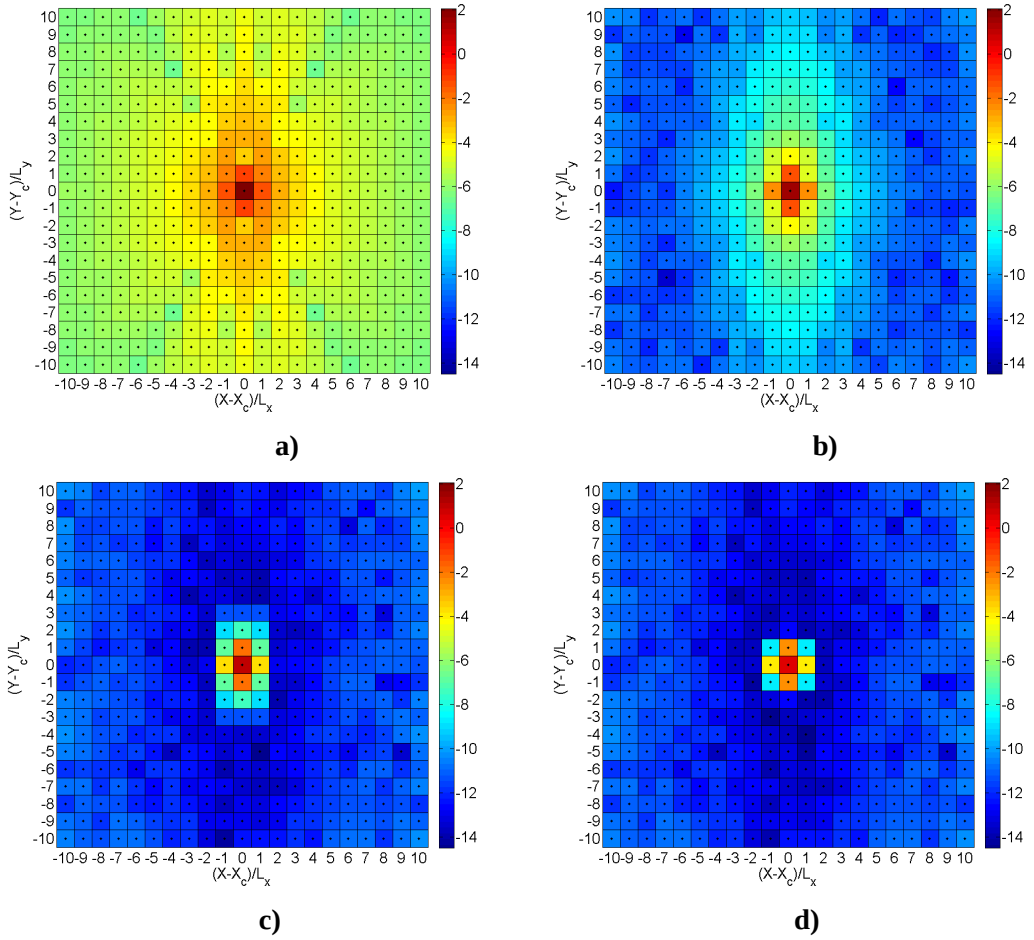

Fig 4.5 *Relative error between the analytic solution for the parallel cell situation (4.39) and the full numerical solution of (4.17), which is calculated with a) 2 b), 4 c), 8 and d) 16 integration points per dimensions. The observer plane is located at d=1 mm from the source cell.*

numerical solution to the analytical one is considered enough. More conclusive experiments are shown in section §4.6.3 and in chapter §5.

4.5.3 Source and Observer cells Located at Orthogonal Planes.

Here the closed solution of I_{oth}^{stc} (4.18) is presented. The physical meaning of the inner integral

$$V^{oth}(x,z)=\int_{y_1'}^{y_2'}\int_{x_1'}^{x_2'}\frac{dx'dy'}{\sqrt{(x-x')^2+(y_o-y')^2+(z-z_s')^2}}, \tag{4.40}$$

in this case to the potential (except for the constant $1/(4\pi\varepsilon_0)$) in a plane parallel to *XZ* plane and located at a distance y_o of this plane produced by a uniform 1 C/m^2 surface charge distribution,

which is enclosed by a rectangle lying on parallel plane to the *XY* plane and placed at distance z_s' of the *XY* plane. The analytical solution of (4.40) is straightforward, since it can be easily deduced from the solution associated to the parallel plane case $V^{pl}(x,y)$. If the transformation, $u = x - x'$, $w = y - y'$ is used and $v = z - z_s'$. Therefore, (4.40) can be written as

$$V^{oth}(x,z) = \int_{w_1}^{w_2} \int_{u_1}^{u_2} \frac{dudw}{\sqrt{u^2 + w^2 + v^2}}, \tag{4.41}$$

which is formally the same as (4.23) (after applying the transformation $u = x - x'$, $v = y - y'$ used in sections §4.5.1 and §4.5.2) but *v* plays the role of *d*. Therefore, (4.41) can be expressed as

$$\begin{aligned} V^{oth}(x,z) = \sum_{m=1}^{2}\sum_{n=1}^{2}(-1)^{m+n} \Big\{ & f^{pl}\left[u_n(x), v(z), w_m(y_o)\right] \\ & + g^{pl}\left[u_n(x), v(z), w_m(y_o)\right] - h^{pl}\left[u_n(x), v(z), w_m(y_o)\right]\Big\} \end{aligned} \tag{4.42}$$

with $w_m(y_o) = y_o - y_m'$, which will be a constant in the outer integral, and

$$\begin{aligned} f^{oth}\left[u_n(x), v(z)\right] &= v(z)\sinh^{-1}\left(\frac{u_n(x)}{V(z)}\right) \\ g^{oth}\left[u_n(x), v(z)\right] &= u_n(z)\tanh^{-1}\left(\frac{w_m(y_o)}{B_n(x,z)}\right) \\ h^{oth}\left[u_n(x), v(z)\right] &= v(z)\tan^{-1}\left(\frac{u_n(x)w_m(y_o)}{v(z)B_n(x,z)}\right) \end{aligned}, \tag{4.43}$$

with $B_n(x,z) = \sqrt{v^2(y) + u_n^2(x) + w_m^2(y_o)}$ $V(z) = \sqrt{v^2(z) + w_m^2(y_o)}$. Similarly to the previous section, the main aspects involved in the integration of f^{oth} g^{oth} and h^{oth} over the observer patch to attain the closed form of I_{oth}^{stc} will be briefly described in the following. Firstly, the double surface integral of f^{oth}

$$F^{oth} = \int_{v(z_1)}^{v(z_2)} \int_{u_n(x_1)}^{u_n(x_2)} f^{oth}\left[u_n(x), v(z)\right] du_n dv \tag{4.44}$$

is tackled. The inner integral is straightforward with MAPLE™, which provides a solution that leads to

$$F^{oth} = w_m(y_o)\sum_{q=1}^{2}(-1)^q \int_{v(z_1)}^{v(z_2)} \left[u_n(x_q)\sinh^{-1}\left(\frac{u_n(x_q)}{V(z)}\right) - B_n(x_q, z)\right] dv. \tag{4.45}$$

The hyperbolic arcsine term contribution in the outer integral can be easily built with the help of (4.27), since formally it invokes the same primitive (4.25), while the remaining term can be set with the help of expression 2.271 in [31]. As consequence

$$F^{oth} = w_m(y_o)\sum_{q=1}^{2}\sum_{p=1}^{2}(-1)^{p+q}\left[V^2(z_p)u_n(x_q)\sinh^{-1}\left(\frac{u_n(x_q)}{V(z_p)}\right)\right.$$
$$+u_n^2(x_q)\tanh^{-1}\left(\frac{v(z_p)}{V(z_p)}\right)-w_m(y_o)u_n(x_q)\tan^{-1}\left(\frac{u_n(x_q)v(z_p)}{w_m(y_o)V(z_p)}\right) \qquad (4.46)$$
$$\left.-\frac{v(z_p)}{2}B_n(x_q,z_p)-\frac{\left(u_n^2(x_q)+w_m^2(y_o)\right)}{2}\ln\left(v(z_p)+B_n(x_q,z_p)\right)\right]$$

In second place, the integral over the observer patch of g^{oth} is tackled

$$G^{oth} = \int_{v(z_1)}^{v(z_2)}\int_{u_n(x_1)}^{u_n(x_2)} g^{oth}\left[u_n(x),v(z)\right]du_n dv \qquad (4.47)$$

whose inner integral can be solved through the variable transformation $t = w_m(y_o)/B_n(x,z)$, which leads to expression . Therefore,

$$G^{oth} = \frac{1}{2}\sum_{q=1}^{2}(-1)^q\int_{v(z_1)}^{v(z_2)}\left[\left(u_q^2(x_q)+v^2(z)\right)\tanh^{-1}\left(\frac{w_m(y_o)}{B_n(x_q,z)}\right)\right. \qquad (4.48)$$
$$\left.-w_m(y_o)B_n(x_q,z)\right]dv$$

The contribution, of B_n is also obtained from 2.271 in [31], while the integral involving the hyperbolic arctangent is split in two parts in order to simplify further calculations. These two parts invoke for the calculation of the primitives $P_1^{oth}(z)$ and $P_2^{oth}(z)$, thus after some algebra,

$$G^{oth} = \frac{1}{2}\sum_{p=1}^{2}\sum_{q=1}^{2}(-1)^{p+q}\left\{P_1^{oth}(z_p)+u_n^2(x_q)P_2^{oth}(z_p)\right.$$
$$\left.+\frac{w_m(y_o)}{2}\left[v(z_p)B_n(x_q,z_p)+\left(u_n^2(x_q)+w_m^2(y_o)\right)\ln\left(v(z_p)+B_n(x_q,z_p)\right)\right]\right\} \qquad .(4.49)$$

with

$$P_1^{oth}(z) = \int v^2(z)\tanh^{-1}\left(\frac{w_m(y_o)}{B_n(x_q,z)}\right)dv; \quad P_2^{oth}(z) = \int \tanh^{-1}\left(\frac{w_m(y_o)}{B_n(x_q,z)}\right)dv \qquad (4.50)$$

The analytical solution of $P_1^{oth}(z)$ and $P_2^{oth}(z)$ is found in three steps. On the one hand, the change of variable $t = w_m^2(y_o)/B_n^2(x_q,z)$ is used, which transforms $P_1^{oth}(z)$ and $P_2^{oth}(z)$ respectively in

$$\begin{aligned} P_1^{oth}(z) &= -w_m^2(y_o)\int \frac{\tanh^{-1}(t)\sqrt{w_m^2(y_o)-Ct^2}}{t^4}dt \\ P_2^{oth}(z) &= -w_m^2(y_o)\int \frac{\tanh^{-1}(t)}{t^2\sqrt{w_m^2(y_o)-Ct^2}}dt \end{aligned} \quad . \tag{4.51}$$

with $C = w_m^2(y_o) + u_n^2(x_q)$ is used. Secondly, expressions in (4.51) are integrated by parts with $f(t) = \tanh^{-1}(t)$, $f'(t) = 1/(1-t^2)$. In the case of $P_1^{oth}(z)$, $g'(t) = \sqrt{w_m^2(y_o)-Ct^2}/t^4$, so that $g(t) = -\sqrt{(w_m^2(y_o)-Ct^2)^3}/(3w_m^2(y_o)t^3)$, whereas in the case of $P_2^{oth}(z)$, $g'(t) = 1/(t^2\sqrt{w_m^2(y_o)-Ct^2})$, thereby $g(t) = -\sqrt{(w_m^2(y_o)-Ct^2)}/(w_m^2(y_o)t)$. In both cases, $g(t)$ can be obtained from $g'(t)$ with the help of MAPLE™. In third place, the leftover integrals appearing in the integration by parts procedure is transform in a straightforward rational integrals through the transformation $s = \sqrt{(w_m^2(y_o)-t^2)/C}$. The closed solutions of $P_1^{oth}(z)$ and $P_2^{oth}(z)$ are obtained after some algebraic manipulations, which lead to

$$\begin{aligned} P_1^{oth}(z) &= \frac{v^3(z)}{3}\tanh^{-1}\left(\frac{w_m(y_o)}{B_n(x_q,z)}\right) + \frac{u_n^3(x_q)}{3}\tan^{-1}\left(\frac{w_m(y_o)v(z)}{u_n^2(x_q)B_n(x_q,z)}\right) \\ &\quad + \frac{w_m(y_o)}{6}\left[v(z)B_n(x_q,z) - (3u_n^2(x_q)+w_m^2(y_o))\tanh^{-1}\left(\frac{v(z)}{B_n(x_q,z)}\right)\right] \\ P_2^{oth}(z) &= v(z)\tanh^{-1}\left(\frac{w_m(y_o)}{B_n(x_q,z)}\right) + w_m(y_o)\tanh^{-1}\left(\frac{v(z)}{B_n(x_q,z)}\right) \\ &\quad - u_n(x_q)\tan^{-1}\left(\frac{w_m(y_o)v(z)}{u_n^2(x_q)B_n(x_q,z)}\right) \end{aligned} \tag{4.52}$$

The final analytical form of G^{oth} is obtained by simply replacing (4.52) in (4.49):

$$G^{oth}=\sum_{p=1}^{2}\sum_{q=1}^{2}(-1)^{p+q}\left\{\frac{1}{6}\left[v(z_p)\left(v^2(z_p)+3u_n^2(x_q)\right)\tanh^{-1}\left(\frac{w_m(y_o)}{B_n(x_q,z_p)}\right)\right.\right.$$
$$\left.+\frac{w_m(y_o)\left(3u_n^2(x_q)+w_m^2(y_o)\right)}{2}\tanh^{-1}\left(\frac{v(z_p)}{B_n(x_q,z_p)}\right)\right]$$
$$+\frac{1}{3}\left[v(z_p)w_m(y_o)B_n(x_q,z_p)-u_n^3(x_q)\tan^{-1}\left(\frac{w_m(y_o)v(z_p)}{u_n(x_q)B_n(x_q,z_p)}\right)\right]$$
$$\left.+\frac{w_m(y_o)\left(u_n^2(x_q)+w_m^2(y_o)\right)}{4}\ln\left(v(z_p)+B_n(x_q,z_p)\right)\right\}. \quad (4.53)$$

Notice that the trigonometric arctangent vanishes for $u_n(x_q)=0$ in (4.53). Finally, the integral over the observer patch of h^{oth}

$$H^{oth}=\int_{v(z_1)}^{v(z_2)}\int_{u_n(x_1)}^{u_n(x_2)}h^{oth}\left[u_n(x),v(z)\right]du_n dv \quad (4.54)$$

is provided. The inner integral in (4.54) is straight forward, inasmuch as it is formally the same as the inner integral of h^{pl} (4.35)-(4.36). Therefore,

$$H^{oth}=\sum_{q=1}^{2}(-1)^{q}\int_{v(z_1)}^{v(z_2)}\left[u_n(x_q)v(z)\tan^{-1}\left(\frac{u_n(x_q)w_m(y_o)}{v(z)B_m(x_q,y)}\right)\right.$$
$$\left.+v^2(z)\tanh^{-1}\left(\frac{w_m(y_o)}{B_m(x_q,z)}\right)\right]dv \quad (4.55)$$

The integral over the observer patch of the hyperbolic arctangent contribution (4.55) is the same as $P_1^{oth}(z)$ (4.52), while then contribution of the trigonometric arctangent needs the calculation of $P_3^{oth}(z)$. As consequence,

$$H^{oth}=\sum_{p=1}^{2}\sum_{q=1}^{2}(-1)^{p+q}\left[u_n(x_q)P_3^{oth}(z_p)+P_1^{oth}(z_p)\right] \quad (4.56)$$

With

$$P_3^{oth}(z)=\int v(z)\tan^{-1}\left(\frac{u_n(x_q)w_m(y_o)}{v(z)B_n(x_q,z)}\right)dv. \quad (4.57)$$

The primitive (4.57) is firstly broached by means of the variable transformation $t = u_n\left(x_q\right) w_m\left(y_o\right) \big/ v(z) B_n\left(x_q, z\right)$, which leads to

$$P_3^{oth}(z) = -\int \frac{u_n^2\left(x_q\right) w_m^2\left(y_o\right) \tan^{-1}(t)\, dt}{t^2 \sqrt{D^2 t + 4u_n^2\left(x_q\right) w_m^2\left(y_o\right)}}, \tag{4.58}$$

where $D = u_n^2\left(x_q\right) + w_m^2\left(y_o\right)$. Expression (4.58) is integrated by parts with $f(t) = \tan^{-1}(t)$, $f'(t) = 1 \big/ \left(1 + t^2\right)$, $g'(t) = 1 \Big/ \left(t^2 \sqrt{D^2 t + 4u_n^2\left(x_q\right) w_m^2\left(y_o\right)}\right)$. $g(t)$ is obtained from $g'(t)$ with the help of MAPLE™, which produces $g(t) = -\sqrt{\left(D^2 t^2 + 4u_n^2\left(x_q\right) w_m^2\left(y_o\right)\right)^3} \Big/ \left(4u_n^2\left(x_q\right) w_m^2\left(y_o\right) t\right)$. The last integral, which results from the integration by parts procedure, is easily transform in a rational integral via the change of variable $s = \sqrt{D^2 t^2 - 4u_n^2\left(x_q\right) w_m^2\left(y_o\right)}$. After solving this integral and applying some algebra

$$\begin{aligned} P_3^{oth}(z) = \frac{1}{4} \Bigg\{ & E_n\left(x_q, z\right) \tan^{-1}\left(\frac{u_n\left(x_q\right) w_m\left(y_o\right)}{v(z) B_n\left(x_q, z\right)} \right) \\ & - W_{nm}\left(x_q, y_o\right) \tan^{-1}\left(\frac{u_n\left(x_q\right) w_m\left(y_o\right) E_n\left(x_q, z\right)}{v(z) W_{nm}\left(x_q, y_o\right) B_n\left(x_q, z\right)} \right), \\ & + u_n\left(x_q\right) w_m\left(y_o\right) \Big[\ln\left| 2v(z) B_n\left(x_q, z\right) + E_n\left(x_q, z\right) \right| \\ & - \ln\left| 2v(z) B_n\left(x_q, z\right) - E_n\left(x_q, z\right) \right| \Big] \Bigg\} \end{aligned} \tag{4.59}$$

with $E_n\left(x_q, z\right) = 2v(z) + B_n\left(x_q, z\right)$ and $W_{nm}\left(x_q, y_o\right) = u_n^2\left(x_q\right) - w_m^2\left(y_o\right)$. Notice that the term involving the second trigonometric arctangent in (4.59) vanishes for $W_{nm}\left(x_q, y_o\right) = 0$, as well as the term involving the logarithms for $v(z) = 0$. It has to be also highlighted in expression (4.59) that precisely for $v(z) = 0$ the function exhibit a discontinuity of the type $\tan^{-1}\left(1 \big/ v(z)\right)$ coming from the second trigonometric arctangent. This provokes a casuistry in function of $u_n\left(x_q\right)$, $w_m\left(y_o\right)$ and $v(z)$, which is summarized in table 4.4 and has to be considered when using (4.59) within a definite integration framework. The analytical expression for (4.54) is found by replacing (4.52) and (4.59) in (4.56), which leads to

$W_{nm}(x_q, y_o)$	$v(z)$	$u_n(x_q)w_m(y_o)$	$\lvert u_n(x_q)\rvert - \lvert w_m(y_o)\rvert$	$4P_3^{oth}(z)/\pi$
$\neq 0$	0^+	≤ 0	>0	$-w_m^2(y_o)$
			<0	$-u_n^2(x_q)$
		>0	>0	$u_n^2(x_q)$
			<0	$w_m^2(y_o)$
	0^-	≤ 0	>0	$w_m^2(y_o)$
			<0	$u_n^2(x_q)$
		>0	>0	$-u_n^2(x_q)$
			<0	$-w_m^2(y_o)$
	0	≤ 0	>0	$-w_m^2(y_o)$
			<0	$-u_n^2(x_q)$
		>0	>0	$w_m^2(y_o)$
			<0	$u_n^2(x_q)$
0	0^+	≤ 0	0	$-w_m^2(y_o)$
		>0	0	$w_m^2(y_o)$
	0^-	≤ 0	0	$w_m^2(y_o)$
		>0	0	$-w_m^2(y_o)$
	0	≤ 0	0	$-w_m^2(y_o)$
		>0	0	$w_m^2(y_o)$

Table 4.4 *Casuistry linked to the usage of* $P_2^{oth}(z)$ *(4.59).* $0^{\pm}$ *stands for* $v(z) \to 0^{\pm}$.

$$H^{oth}=\sum_{p=1}^{2}\sum_{q=1}^{2}(-1)^{p+q}\left\{\frac{u_n(x_q)}{4}\left[E_n(x_q,z_p)\tan^{-1}\left(\frac{u_n(x_q)w_m(y_o)}{v(z)B_n(x_q,z_p)}\right)\right.\right.$$
$$-W_{nm}(x_q,y_o)\tan^{-1}\left(\frac{u_n(x_q)w_m(y_o)E_n(x_q,z_p)}{v(z)W_{nm}(x_q,y_o)B_n(x_q,z_p)}\right)$$
$$+u_n(x_q)w_m(y_o)\left(\ln\left|2v(z_p)B_n(x_q,z)_p+E_n(x_q,z_p)\right|\right.$$
$$\left.\left.-\ln\left|2v(z)B_n(x_q,z_p)-E_n(x_q,z_p)\right|\right)\right]+\frac{1}{3}\left[v^3(z)\tanh^{-1}\left(\frac{w_m(y_o)}{B_n(x_q,z_p)}\right)\right.$$
$$\left.+u_n^3(x_q)\tan^{-1}\left(\frac{w_m(y_o)v(z_p)}{u_n^2(x_q)B_n(x_q,z_p)}\right)\right]+\frac{w_m(y_o)}{6}\left[v(z_p)B_n(x_q,z_p)\right.$$
$$\left.\left.-\left(3u_n^2(x_q)+w_m^2(y_o)\right)\tanh^{-1}\left(\frac{v(z_p)}{B_n(x_q,z_p)}\right)\right]\right\} \tag{4.60}$$

Finally, the usage of (4.46), (4.53) and (4.60) in is set through a, and as

$$I_{oth}^{stc}=\sum_{m=1}^{2}\sum_{n=1}^{2}(-1)^{m+n}\left\{F^{oth}+G^{oth}+H^{oth}\right\} \tag{4.61}$$

sets the closed analytical expression of I_{oth}^{stc}. The validity of this expression is ascertained exactly in the same way as I_{pl}^{stc}. The only difference is that now the field cells are obtained by dividing a plate centered in the *XZ* plane in 21x21 cells, which measure L_x=1 x L_y=1/3 m. The relative error between (4.61) and the full numerical solution with regard to the normalized distance between the source cell center (X_c,Y_c) and the observer cell center (X,Y) is represented in Fig 4.6a, Fig 4.6b, Fig 4.6c, and Fig 4.6c respectively 2, 4, 8 and 16 integration abscissas in the numerical approach. As in the previous experiments in Fig 4.4 and Fig 4.5, it can be clearly appraised in Fig 4.6 that the numerical solution converges to (4.61). As expected, the relative error committed in the vicinity of the source cell is bigger, for the reason previously explained in section §4.5.1 As aforesaid only a qualitative comparison is targeted at this point. In section §4.6.3 and chapter §5, more detailed and rigorous experiments, which definitely confirm the validity of I_{oth}^{stc}, as well as I_{cp}^{stc} (4.22) and I_{pl}^{stc} (4.39) are exhibited.

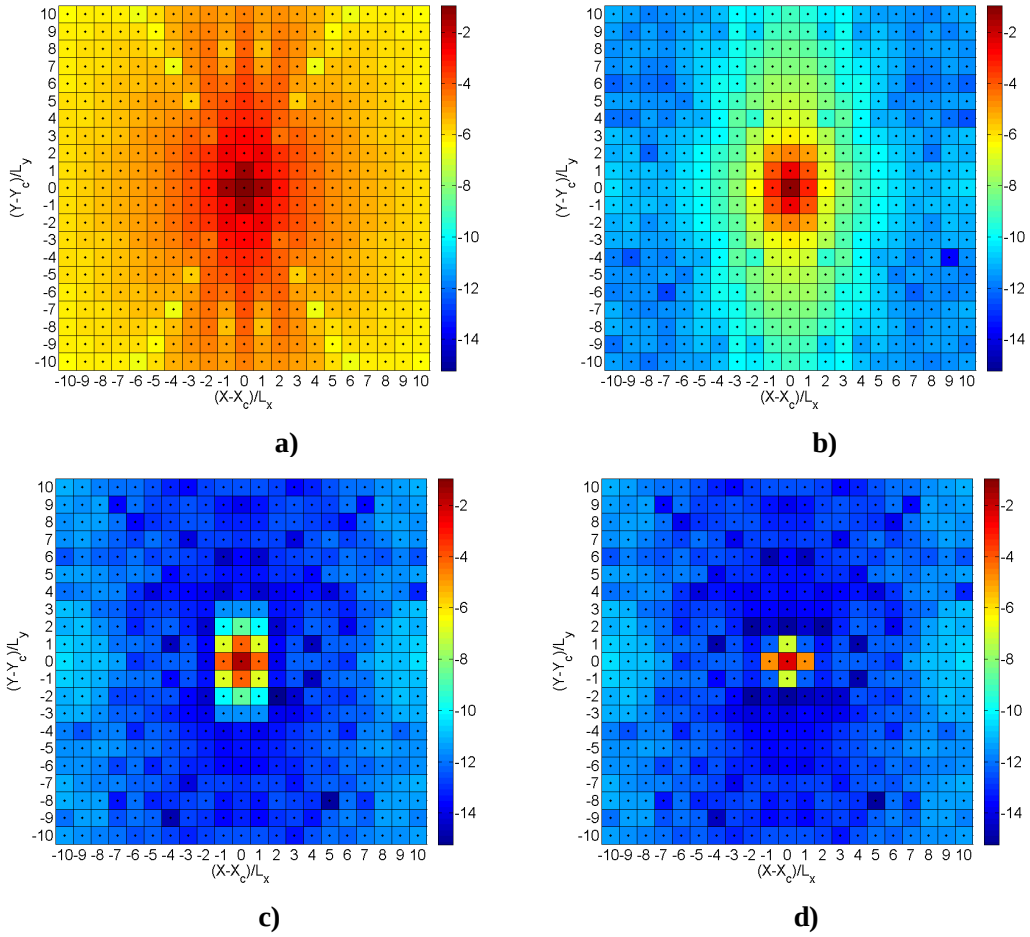

Fig 4.6 *Relative error between the analytic solution for the orthogonal scenario linked to (4.61) and the full numerical solution of (4.18), which is calculated with a) 2 b), 4 c), 8 and d) 16 integration points per dimensions. The observer cells are located in the XZ plane, whereas the source cell is centered at the origin of the XY plane.*

4.6 Hybrid Analytic-Numeric 4D Weakly MSI over Arbitrary Flat Polygons

As mentioned in section §4.4, the full analytical solution of the 4D weakly MSI of the free space static potential GF in a generic case is still an open problem. The reader is reminded, that excluding the expressions presented in the previous section, entire analytical forms of these MSI are only available for the self case (identical source and observer domains), in the case of triangular patches [23]-[24]. Nonetheless, this is not the situation in the general case and even less for other shapes like quadrangles, which are of obvious interest [27]-[29], or any arbitrary polygon. This last situation is solved by applying numerical integration techniques on the observer patch to the resulting analytical potential integral on the source patch, provided that a Galerkin strategy is used within a MoM framework.

This section is devoted to the deep analysis of the prior approach. Namely, the integral (4.14), which is recovered here

$$I^{stc} = \int_S \left[\int_{S'} \frac{1}{R} dS' \right] dS \tag{4.62}$$

as a matter of clarity, is solved via analytical techniques, which apply only to the 2D potential integral over the source patch S', and numerical techniques over the observer patch S. As depicted in Fig. 4.7a, a generic situation is tackled, that's to say, both source S' and observer S patches, which embrace respectively all the source points $\mathbf{r}'$ and all the observer points $\mathbf{r}$, are considered to be arbitrarily oriented flat polygons.

As indicated in section §4.4, analytical expressions, are available in literature for the inner integral in (4.62). Different analytical techniques have been used to obtain the close expression of this integral. In [21], the close form is attained for generic polygonal patches through Gauss integral theorems. Basically, the surface integral is transformed into an integral over the boundary of the polygon plus a residue calculated in the neighborhood of the singularity. A related procedure is used in [22] for the specific case of the triangle, whereas the same case is solved in [13] by utilizing some relations in [31]. In this thesis, an alternative technique, which stands out by its mathematical simplicity, is proposed to calculate the analytical expression of the potential integral. Just like in [13] and [21]-[22], the technique is based on a subdomain decomposition strategy. But on the contrary, the contribution of each subdomain is analytically calculated through an original transformation. It can be easily proved that the final expression presented in this paper is equivalent to those in [21]-[22], being also concise and suitable for numerical integration.

As aforesaid, the resulting analytical formulas correspond, physically to the scalar potential created by a uniform surface charge density distributed over a polygonal surface. Therefore, as predicted by classical potential theory, they must be continuous across the polygon boundaries. On the other hand, their derivatives will be discontinuous at these boundaries, as the electric fields generated by a uniform surface charge may be infinite on the surface edges. Consequently,

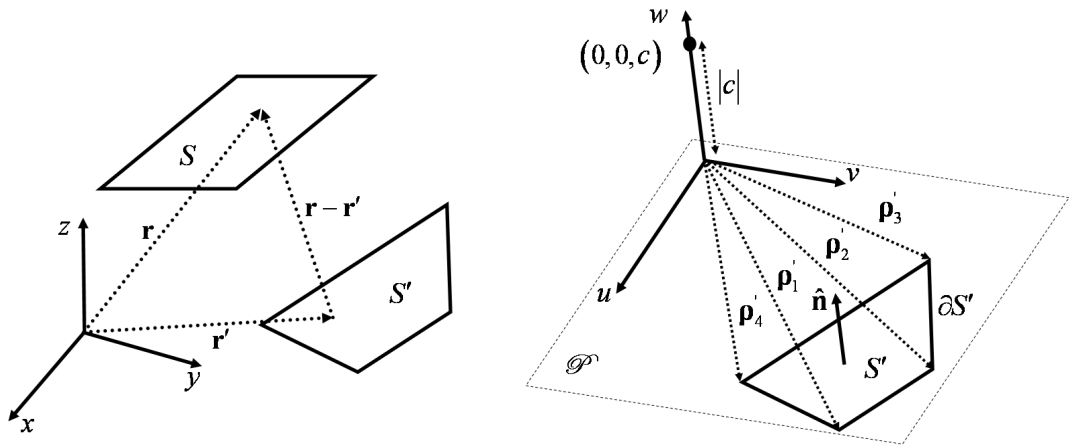

Fig. 4.7 *a) Polygonal source S' and observer S integration domains for generic static MSI and b) Auxiliary local frame defined in the plane $\mathscr{P}$ housing the source polygon to solve the static MSI.*

in weakly singular and weakly near singular scenarios, the problem of integrating a continuous function with infinite derivatives at the integration domain's boundaries has to be confronted. As introduced in previous sections and as it will be proven in section §4.6.3, standard (e.g. Gauss-Legendre) 2D quadratures, which are commonly used to perform the integration over the observer patch and are currently available in the literature, fail to produce accurate results in these scenarios. Here, after analytically showing the reason of this drawback, the problem is alleviated via the usage of numerical rules tailored to integrate functions with endpoint singularities as in [33]-[34]. In this section, these rules are applied to integrate the potential integral in several weakly singular and near singular scenarios of interest, whereas in chapter §5, problems within a SIE-MoM, where the impedance matrix is calculated via the integration of the potential integral through these rules, will be shown.

4.6.1 Alternative Analytical Approach to Evaluate the 2D Potential Integral

This subsection is only focused in presenting an alternative way, which is based on an original integral transformation, to solve the inner integral

$$V = \int_{S'} \frac{1}{R} dS' \tag{4.63}$$

in (4.62). Commonly, the mathematical complexity of this problem is reduced by solving the problem in an auxiliary local Cartesian frame (*u*,*v*,*w*). Here, this frame is located at $\mathbf{r_0} = \left(\mathbf{r} - \hat{\mathbf{n}} \cdot c\right)$, with $c = \left(\mathbf{r} - \mathbf{r}_n^{'}\right) \cdot \hat{\mathbf{n}}$ (for any *n*), so that $\hat{\mathbf{w}} \equiv \hat{\mathbf{n}}$ and the vectors $\hat{\mathbf{u}}$ and $\hat{\mathbf{v}}$ are within the plane $\mathscr{P}$ containing the polygon. Therefore, as exemplarily shown for a generic quadrangle in Fig. 4.7b, within the new local frame, the point represented by $\mathbf{r}$ is confined in the *w* axis with coordinates (*0*,*0*,*c*) and any point $\mathbf{r}^{'}$ can be expressed as (*u*,*v*,*0*). Consequently, the resolution of

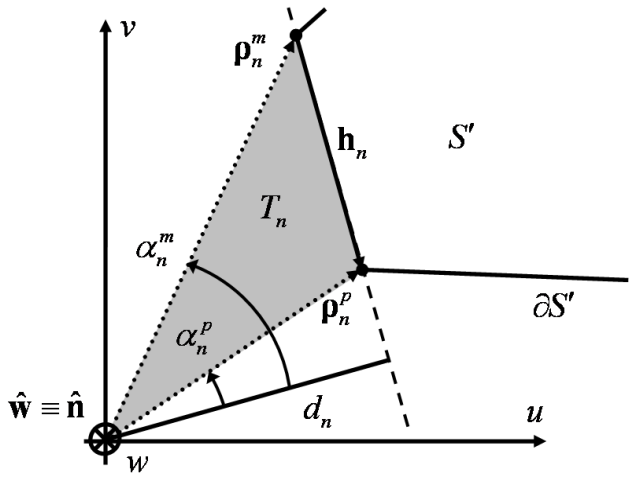

Fig. 4.8 *Geometrical description of a generic triangle T_n which is associated to the analytical resolution of V through a domain decomposition technique and a polar coordinate transformation.*

$$V = \int_{S'} \frac{1}{\sqrt{u^2 + v^2 + c^2}} dS' \tag{4.64}$$

in this frame is equivalent to solving (4.63) in the original coordinate system (*x*,*y*,*z*). Also in Fig. 4.7b, the vectors $\boldsymbol{\rho}_n' = \mathbf{r}_n' - \mathbf{r}_0$, lying in $\mathscr{P}$ and representing the position in the original Cartesian frame of the node $\mathbf{r}_n'$ from the origin $\mathbf{r}_0$ of the new local coordinate system, are shown.

The required analytical effort to solve (4.64) is usually tempered through the usage of a domain decomposition technique. Namely, the integral (4.64) over *S'* is expanded as a sum of *N* integrals over simpler domains as

$$V = \sum_{n=1}^{N} s_n \int_{T_n} \frac{1}{\sqrt{u^2 + v^2 + c^2}} dS' \tag{4.65}$$

These domains, denoted in (4.65) as T_n and described in Fig. 4.8, boil down to a set of *N* triangles which are enclosed by $\mathscr{P}$, whereas in [21]-[22] are the edges of the polygon. It is appreciated in Fig. 4.8, that T_n is built by means of the vectors $\mathbf{h}_n = \boldsymbol{\rho}_n^p - \boldsymbol{\rho}_n^m$, being $\boldsymbol{\rho}_n^m$ and $\boldsymbol{\rho}_n^p$ respectively either $\boldsymbol{\rho}_n'$ and $\boldsymbol{\rho}_{n+1}'$ for *n*=1..*N*-1 or $\boldsymbol{\rho}_N'$ and $\boldsymbol{\rho}_1'$ for *n*=*N*. Also in (4.65), $s_i = \mathrm{sgn}\left(\hat{\mathbf{n}} \cdot \left(\boldsymbol{\rho}_n^m \times \boldsymbol{\rho}_n^p\right)\right)$ is the sign of the contribution to *V* of each subintegral. Among the domain decomposition schemes described in literature, this choice permits a more intuitive, simple and robust computation of the sign associated to each contribution from orthogonal vectors to the polygon. Also note, that if $\mathbf{r}$ is in a polygon edge or its extension, which is the situation where $\boldsymbol{\rho}_n^m \parallel \boldsymbol{\rho}_n^p$, then the contribution linked to this edge vanishes.

A closed expression for (4.65) is only possible if its associated integrals are solved analytically. In this work, this has been done by starting with the use of a common polar coordinate transformation, typically used in a singularity cancellation context [13]. Therefore

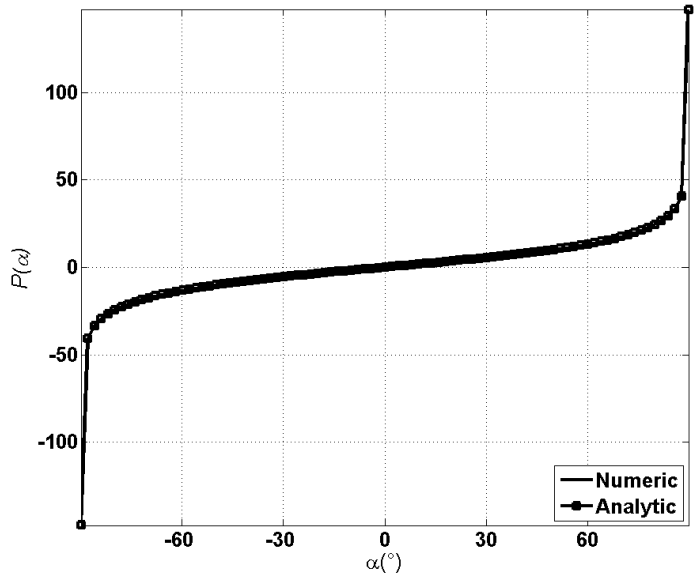

Fig. 4.9 *Analytic expression for P versus its numerical solution.*

$$V = \sum_{n=1}^{N} s_n \int_{\alpha_n^m}^{\alpha_n^p} \int_0^{\frac{d_n}{\cos(\alpha)}} \frac{\rho d\rho d\alpha}{\sqrt{\rho^2 + c^2}} \tag{4.66}$$

where all the involved geometric quantities can be inferred from Fig. 4.8 as $d_n = \left|\boldsymbol{\rho}_n^m \cdot \left(\hat{\mathbf{h}}_n \times \hat{\mathbf{n}}\right)\right|$, $\alpha_n^m = \tan^{-1}\left(\boldsymbol{\rho}_n^m \cdot \hat{\mathbf{h}}_n / d_n\right)$, $\alpha_n^p = \tan^{-1}\left(\boldsymbol{\rho}_n^p \cdot \hat{\mathbf{h}}_n / d_n\right)$, and $\hat{\mathbf{h}}_n = \mathbf{h}_n / |\mathbf{h}_n|$.

The first steps to solve (4.66) analytically are straightforward if the integral transformation $t = \rho^2 + c^2$ is employed in the inner integral. Therefore, (4.66) becomes

$$V = \sum_{n=1}^{N} s_n |c| \left[P\left(\alpha_n^p\right) - P\left(\alpha_n^m\right) - \Delta\alpha_n \right] \tag{4.67}$$

with $\Delta\alpha_n = \alpha_n^p - \alpha_n^m$ and $a_n = d_n / |c|$ and

$$P(\alpha) = \int \sqrt{1 + \left(\frac{a_n}{\cos(\alpha)}\right)^2}\, d\alpha \tag{4.68}$$

An original integral transformation, which is of the form

$$\gamma = \frac{\sin(\alpha)}{\sqrt{1 + \left(\frac{\cos(\alpha)}{a_n}\right)^2}} \tag{4.69}$$

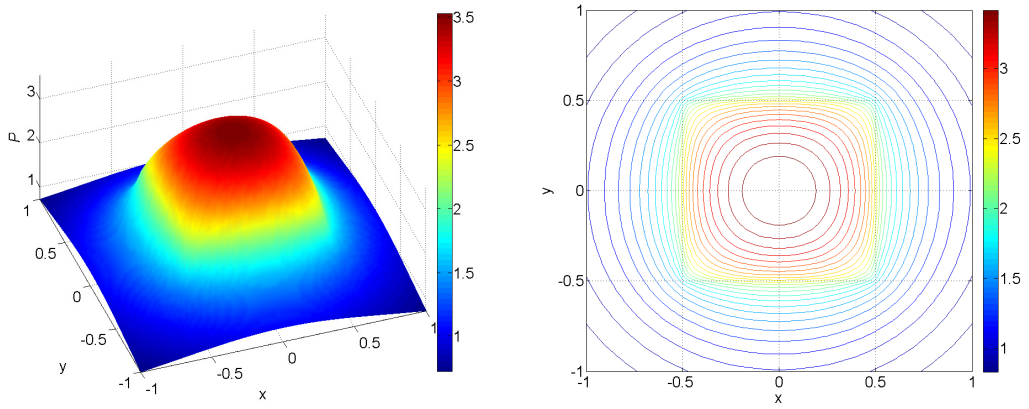

a) **b)**

Fig. 4.10 *a) 3D plot of V and b) the related isolines in the observer plane.*

is proposed to find the closed form of (4.68). Expression (4.69) has been obtained after combining three simpler changes of variable, which allow recursively solving (4.68) in three steps. These changes are $\beta^2 = 1+\left(a_n/\cos(\alpha)\right)^2$, $\eta = \beta^2 + b$ and $\gamma = \left(\eta/(\eta - b)\right)^{1/2}$, with $b = -\left(1+a_n^2\right)$. The transformation (4.69) can be directly utilized in (4.68), so that the integrand becomes a rational function. Therefore, after a classical fraction decomposition process, (4.68) is expressed as the sum of two integrals, whose analytical solution is really well known, thereby

$$P(\gamma) = a_n \int \frac{d\gamma}{1-\gamma^2} + \int \frac{d\gamma}{a_n\left(1+\dfrac{\gamma^2}{a_n^2}\right)} = a_n \tanh^{-1}(\gamma) + \tan^{-1}\left(\frac{|c|\gamma}{d_n}\right) \tag{4.70}$$

The validity of this expression can be appraised in Fig. 4.9, where (4.70) is compared with the numerical version of (4.68), which is calculated through the fundamental calculus theorem [35]. In this figure, the comparison is done for $-90^\circ < \alpha < 90^\circ$, since as it can be deduced from Fig. 4.8, α_n^p and α_n^m are always between this range. The use of (4.70) in (4.67) leads to the final analytical expression for V which is solution of (4.63),

$$\begin{aligned} V = \sum_{n=1}^{N} s_n \Bigg\{ & d_n \left[\tanh^{-1}\left(\gamma_n^p\right) - \tanh^{-1}\left(\gamma_n^m\right) \right] \\ & + |c| \left[\tan^{-1}\left(\frac{|c|\gamma_n^p}{d_n}\right) - \tan^{-1}\left(\frac{|c|\gamma_n^m}{d_n}\right) - \Delta\alpha_n \right] \Bigg\} \end{aligned} \tag{4.71}$$

noticeably with $\gamma_n^{(m,p)} = \sin\left(\alpha_n^{(m,p)}\right) \Big/ \sqrt{1+\left(\cos\left(\alpha_n^{(m,p)}\right)/a_n\right)^2}$. It has to be mentioned, as a matter of completeness and mathematical curiosity, that the inverse of (4.69) provides an alternative solution P_2 for P (also through fraction decomposition), being $P_2 = P + (2k+1)\pi/2$ with

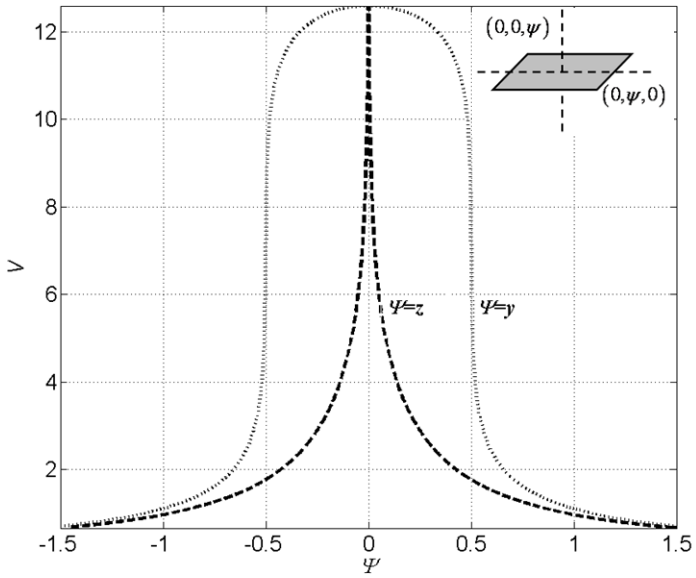

Fig. 4.11 *Resulting potentials after utilizing V for a rectangle lying on the XY plane, whose edges measure 0.01 m along x and 1 m along y. The observation points are* $\mathbf{r}_z$ *= (0, 0,* Ψ *) and* $\mathbf{r}_y$ *= (0,* Ψ*, 0) with = (−1.5 : 1.5).*

$k \in \mathbb{Z}$, which obviously leads also to (4.70), insomuch as $(2k+1)\pi/2$ vanishes when doing $P_2\left(\gamma_n^p\right) - P_2\left(\gamma_n^m\right)$.

As it has been mentioned, different analytical formulas exist in literature for (4.63). The present approach, summarized in (4.67), (4.69), (4.70) and (4.71), uses only elementary mathematics and is very well suited for being employed in numerical codes, since it is concise and easily programmable in function of clearly identifiable geometric quantities.

The last part of this section is devoted to verify (4.71) through some numerical experiments. These experiments are addressed to ascertain that this expression fulfils the physical properties bounded to the potential produced by a uniform charge distribution over a flat polygon. The selected source polygon is a rectangle lying on the *XY* plane, whose center is located at the coordinate origin. The rectangle edges, which are parallel to the coordinate axes *x* and *y*, measure respectively 0.01 m. along *x* and 1 m. along *y*. A total charge of $1\,C$ is assumed to be distributed over the polygon surface. On the one hand, the symmetry properties in the plane *XY* of (4.71) are validated through the 3D surface representation of the potential in Fig. 4.10a and more clearly in Fig. 4.10b, via the plot of the potential isolines linked to this surface. On the other hand, the behavior of V on the polygon's surface S' and its boundary $\partial S'$ is checked by computing (4.71) on the *z* and *y* with $\mathbf{r}_z = (0,0,\psi)$ and $\mathbf{r}_y = (0,\psi,0)$ as observation points, being $\psi = -1.5{:}1.5$. The resulting potentials are represented in Fig. 4.11, where it can be appraised that the basic classical potential theory predictions are verified. Firstly, the potential is symmetric and continuous in both S' and $\partial S'$. Secondly, the potential's directional derivative in a direction crossing S' and parallel to $\hat{\mathbf{n}}$ will be discontinuous on S', since V exhibits an angle point at $(0,0,0)$ in this case. Thirdly, this derivative will be singular on $\partial S'$ in a direction lying on the

plane $\mathscr{P}$ enclosing the polygon. This fact, which will be of relevance in the next section, can be inferred from Fig. 4.11, where the infinite value of the slope's tangents to V at $(0,-1/2,0)$ and $(0,1/2,0)$ is easily intuited.

4.6.2 Features of the Endpoint Singularities in the Potential Derivatives

As empirically inferred from Fig. 4.11, the derivatives of expression (4.71) will exhibit endpoint singularities on $\partial S'$ in a direction lying on the plane $\mathscr{P}$ housing the polygon. As aforementioned, this fact is totally coherent with classical potential theory, insomuch as these derivatives are connected to the electric field in $\mathscr{P}$, which is produced by a uniform surface charge distribution confined within a polygon and which is singular in the polygon boundary. In the enhancement of the numerical integration of (4.71), it is crucial to have a good knowledge of the analytical features inherent to the singularity which is being faced. This objective can be easily attained through the study of the potential in the plane confining the polygon, which boils down to particularize expression (4.71) for $c=0$. In this case, the use of the identity $\sin\left[\tan^{-1}(\tau)\right]=\tau/\sqrt{1+\tau^2}$ leads to $\gamma_n^{(m,p)}\big|_{c=0}=\boldsymbol{\rho}_n^{(m,p)}\cdot\hat{\mathbf{h}}_{\mathbf{n}}/\left|\boldsymbol{\rho}_n^{(m,p)}\right|$, with $\left|\boldsymbol{\rho}_n^{(m,p)}\right|=\sqrt{d_n^2+\left(\boldsymbol{\rho}_n^{(m,p)}\cdot\hat{\mathbf{h}}_{\mathbf{n}}\right)^2}$ easily deduced from Fig. 4.8. Consequently, after some basic algebraic manipulations, (4.71) for $c=0$ can be now expressed as

$$V_0=\sum_{n=1}^{N}s_n\left[d_n\ln\left(A_n^pA_n^m\right)-2d_n\ln\left(d_n\right)\right] \tag{4.72}$$

where $A_n^p=\left(\left|\boldsymbol{\rho}_n^p\right|+\boldsymbol{\rho}_n^p\cdot\hat{\mathbf{h}}_{\mathbf{n}}\right)$ and $A_n^m=\left(\left|\boldsymbol{\rho}_n^m\right|-\boldsymbol{\rho}_n^m\cdot\hat{\mathbf{h}}_{\mathbf{n}}\right)$. Direct inspection of (4.72) clearly reveals that, for any d_n extension, a $\ln(d_n)$ endpoint singular behavior is produced by $d_n\ln(d_n)$ in the directional derivative $\partial V_0/\partial d_n$ when $d_n\to 0$ (ergo for $\mathbf{r}$ in $\mathscr{P}$ and tending to $\partial S'$). This endpoint logarithmic singularity can be explicitly appraised in the expression of the electric field $\mathbf{E_0}$ produced by a polygonal uniform charge distribution when $c=0$, which invokes the calculation of the gradient of (4.72). The analytical expression of this field is

$$\mathbf{E_0}=\sum_{n=1}^{N}s_n\left\{2\mathbf{D}_n^d\left[\ln\left(d_n\right)-\ln\left(\sqrt{A_n^mA_n^p}\right)+1\right]-d_n\left[\frac{\mathbf{D}_n^p}{A_n^p}+\frac{\mathbf{D}_n^m}{A_n^m}\right]\right\} \tag{4.73}$$

where $\mathbf{D}_n^p=-\left[\hat{\mathbf{h}}+\boldsymbol{\rho}_n^p/\left|\boldsymbol{\rho}_n^p\right|\right]$, $\mathbf{D}_n^m=\left[\hat{\mathbf{h}}-\boldsymbol{\rho}_n^m/\left|\boldsymbol{\rho}_n^m\right|\right]$ and $\mathbf{D}_n^d=-\mathrm{sgn}\left[\boldsymbol{\rho}_n^m\cdot\left(\hat{\mathbf{h}}_n\times\hat{\mathbf{n}}\right)\right]\left(\hat{\mathbf{h}}_n\times\hat{\mathbf{n}}\right)$. In Fig. 4.12, the singular behavior of (4.73) is illustrated through the representation of $|\mathbf{E_0}|$ (Fig. 4.12a) and its related vectors (Fig. 4.12b), which are produced by a 1 *C* total charge uniformly distributed over a 1 m edge square lying in the *XY* and centered at the origin. In both figures, that (4.73) exhibits the biggest values in the vicinity of the polygon's boundary, aside from respecting the field symmetry properties in the *XY* plane. It has to be pointed the irrelevance of the shape of these boundaries. Namely, the same sort of singular behavior is expected for a polygonal contour, whose number of edges is either finite or, in the limiting case, infinite, as for instance a

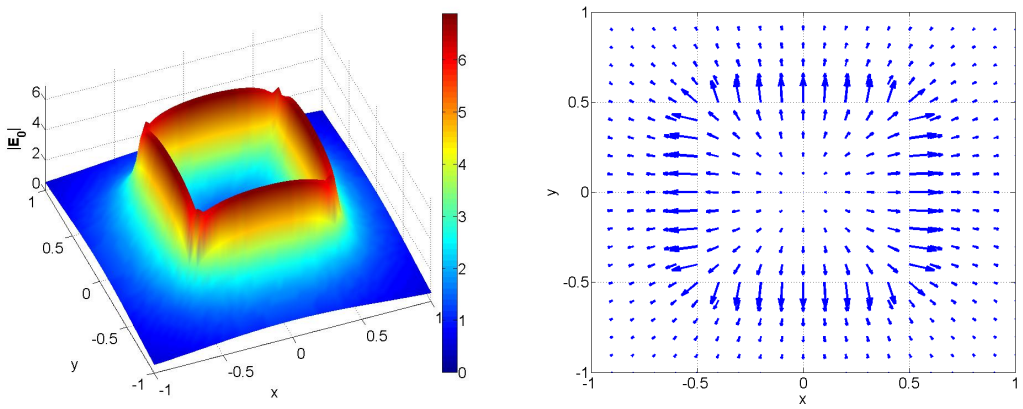

Fig. *4.12 a) Electric field* $\boldsymbol{E_0}$ *in the observer plane: magnitude and b) vector representation.*

circumference or a curved patch. This fact, which evinced in Fig. 4.13 and in 4.14, confirms mesh schemas based on curved contour patches [36] are not devoid of the inconveniences caused by these endpoint singularities. In these figures, the cut along x (x>0) of the fields' magnitude produced by a 1 C total charge uniformly distributed over the same square as in Fig. 4.12 and over a disk [37], which is inscribed within the square, are shown. Also in Fig. 4.13, it is exhibit the enhancement of the field singular behavior in the corners of a polygon boundary. This is done by also representing the cut along x (x>0) of the electric field bounded to the same 1 C total charge, which now is distributed over a rhombus which is inscribed in both square and disk, as the inset in Fig. 4.13 shows. On the other hand, the same experiment is presented in Fig. 4.14, but here, a surface charge density of $\sigma = 1\mathrm{C}/\mathrm{m}^2$ is assumed for the three different geometries. Notice as a matter of physical curiosity that, if the total charge is constant, then the three different singular behaviors can be clearly perceived inside the patch (x<0.5), being the corner case the one showing the fastest variation, while outside the patch the three singularities can be considered of the same degree. On the contrary, if the charge density is constant, corner and edge singularities can be properly discerned outside the patch (x>0.5), whereas inside the patch both fields exhibit the same variation. In the last scenario, it is also remarkable that the edge endpoint singularity of the disk is considerably mitigated with regard to the other two.

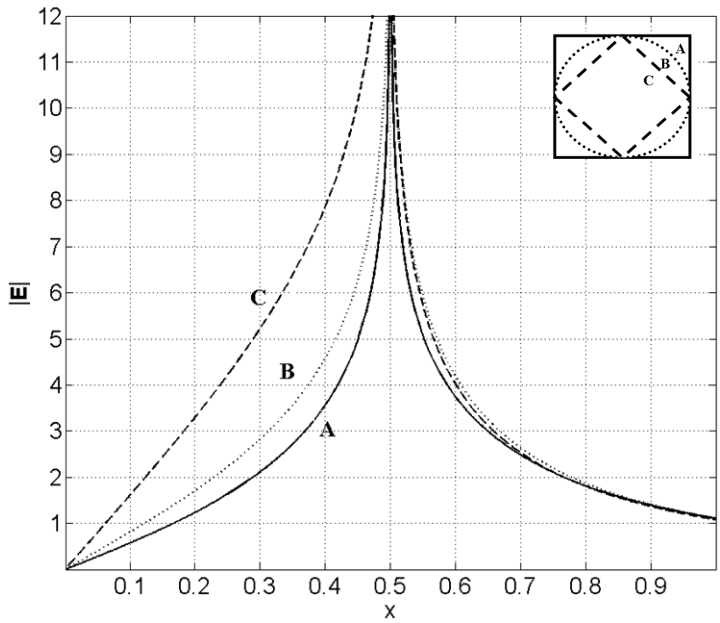

Fig. 4.13 *Computed electric field magnitudes along x (x > 0) for a1 C total charge uniformly distributed on a 1 m edge square, which lies in the XY plane and is centered at the origin, on a disk inscribed in the rectangle, and on a rhombus, which is inscribed in both disk and square.*

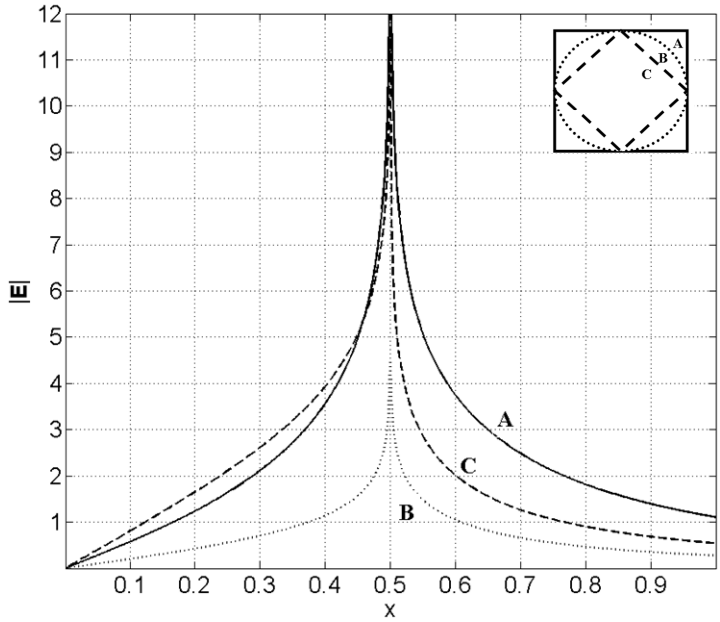

Fig. 4.14 *Computed electric field magnitudes along x (x > 0) for a 1 C/m^2 uniform charge density on a 1 m edge square, which lies in the XY plane and is centered at the origin, on a disk inscribed in the rectangle, and on a rhombus, which is inscribed in both disk and square.*

4.6.3 Numerical Integration of the 2D Observer Integral via DE Rules

Inside the MoM-Galerkin framework described in this thesis, the static contribution to the MoM matrix calls for the integration of (4.71) over the observer patch. Traditionally, expressions like (4.71) have been considered smooth enough to be integrated through standard Gaussian rules, as for instance Gauss-Legendre. These rules are tailored to numerically integrate truly smooth functions, namely, continuous functions with continuous derivatives. Although, this rules can produce accurate results in the smooth situations described in section §4.3, this is not the case in weakly singular and near singular scenarios. In these situations, the numerical integration over the observer patch is performed in a region, where logarithmic endpoint singular behavior of the integrand's derivatives in the patch boundary is magnified by the terms $d_n \ln(d_n)$ of the analytical potential integral, as illustrated in the previous section. Consequently as it will be shown in this section, the usage of Gaussian rules in these cases causes lacks of precision. Functions exhibiting this endpoint logarithmic singularity are accurately integrated through double exponential (DE) quadrature formula, which is tailored to attain this objective, in [33].

It is considered enriching and enlightening, to provide a brief explanation about some relevant historical and mathematical aspects associated to the DE formula. Interested readers are addressed to [33] in order to know more about this numerical rule. The discovery of the DE formula is totally linked to the proof given by Takahasi and Mori [38] about the optimality of the trapezoidal formula with an equal mesh size *h* to integrate analytic functions in $(-\infty,\infty)$. After obtaining the proof, the work of these authors was focused on finding an integral transformation $x=\phi(t)$, which is analytic for $-\infty<t<\infty$, and satisfy $\phi(-\infty)=-1$ and $\phi(\infty)=1$, so that the definite integral of any analytic function $f(x)$ between -1 and 1 can be mapped to the interval $(-\infty,\infty)$, and as consequence efficiently integrated via the trapezoidal rule with $2n+1$ abscissas. Namely,

$$If=\int_{-1}^{-1} f(x)\,dx=\int_{-\infty}^{\infty} f\left[\phi(t)\right]\phi'(t)\,dt \simeq h\sum_{k=-n}^{n} f\left[\phi(kh)\right]\phi'(kh) \tag{4.74}$$

Takahasi and Mori relied on the Euler-Mclaurin formula [39] to propose the following integral transformation

$$x=\phi(t)=\tanh\left(\frac{\pi}{2}\sinh(t)\right), \tag{4.75}$$

whose derivatives

$$\phi'(t)=\frac{\frac{\pi}{2}\cosh(t)}{\cosh^2\left(\frac{\pi}{2}\sinh(t)\right)} \approx O\left(e^{-\frac{\pi}{2}e^{|t|}}\right) \tag{4.76}$$

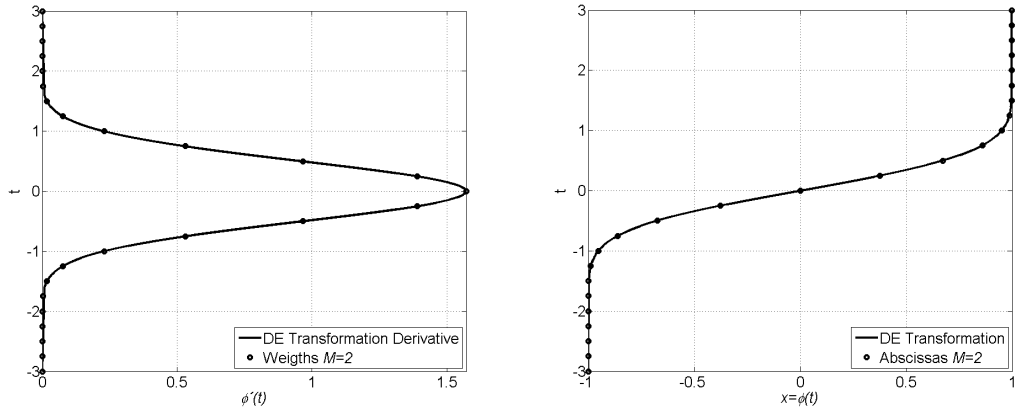

a) **b)**

Fig. 4.15 *a) DE transformation derivative (4.76) and weight distribution for the quadrature level M=2 and b) DE transformation itself (4.75) together with abscissas distribution also for M=2* .

exhibit a DE decay (hence the name of the quadrature) as $t \to \infty$, thereby the DE quadrature formula

$$If \approx h\sum_{k=-n}^{n} f\left[\tanh\left(\frac{\pi}{2}\sinh\left(t_k\right)\right)\right]\frac{\frac{\pi}{2}\cosh\left(t_k\right)}{\cosh^2\left(\frac{\pi}{2}\sinh\left(t_k\right)\right)} = h\sum_{k=-n}^{n} f\left(x_k\right)w_k\,, \quad (4.77)$$

is obtained by replacing (4.75) and (4.76) in (4.74). Obviously in (4.77), the abscissas $x_k = \phi\left(t_k\right)$ and the weights $w_k = \phi'\left(t_k\right)$ of the quadrature are respectively the sampled version of the integral transformation $\phi\left(t\right)$ and its derivative $\phi'\left(t\right)$ at $t_k = kh$, with *h* and *k* respectively the mesh size and the number of intervals of the trapezoidal rule.

The reason why the DE quadrature is highly suitable to integrate endpoint singular functions is illustrated with the help of Fig. 4.15. On the one hand in Fig. 4.15a, it can be appreciated that $\phi'\left(t\right)$ exhibits the DE decay shown in (4.76). In this figure, it can be even seen that the asymptotic behavior it is already reached for $\left|t\right|>1$, so that the weights $w_k = \phi'\left(t_k\right)$ will take values associated to this asymptotic zone for $\left|t_k\right|>1$. On the other hand, it can be easily inferred from Fig. 4.15b that the transformation $\phi\left(t\right)$ can map as much as values of the asymptotic zone as desired to the vicinity of the integration interval endpoints, being even possible to approach these endpoints as much as wanted. Namely, a theoretically infinite number of abscissas $x_k = \phi\left(t_k\right)$ can be placed near the endpoints interval [40]. Therefore, even if the integrand or its derivatives have a blow up singularity at an endpoint, it is possible to sum terms with abscissas very close to the endpoints until the rapidly decreasing weights overwhelm the large function values $f\left[x_k = \phi\left(t_k\right)\right]$ [33]. Noticeably, the number of abscissas and weights has to be truncated in order to code (4.77). As explained in [34], the most suitable parameterization for a generic integration propose is the one that results from truncating the series of abscissas and weights, which is generated for $n = 6\cdot 2^M$ and $h = 1/2^M$, where *M* is the so-called level of the quadrature rule. This series are truncated at a value *p*>0, so that $1 - x_{k=p} < eps$, where eps stands for the machine

OBSERVER PATCH VERTICES		$\mathbf{r}_1$	$\mathbf{r}_2$	$\mathbf{r}_3$	$\mathbf{r}_4$
Weakly Singular Scenarios	**Self**	$(1/2,-1/2,0)$	$(1/2,1/2,0)$	$(-1/2,1/2,0)$	$(-1/2,-1/2,0)$
	Adjacent Coplanar	$(1/2,1/2,0)$	$(1/2,3/2,0)$	$(-1/2,3/2,0)$	$(-1/2,1/2,0)$
	Adjacent Orthogonal	$(1/2,1/2,0)$	$(1/2,1/2,-1/2)$	$(-1/2,1/2,-1/2)$	$(-1/2,1/2,0)$
	Vertex	$(-1/2,1/2,0)$	$(-1/2,3/2,0)$	$(-3/2,3/2,0)$	$(-3/2,1/2,0)$
Weakly Near Singular Scenarios (*Parallel Patches separated by d m.*)	**Very Close**	$(1/2,-1/2,d_1)$	$(1/2,1/2,d_1)$	$(-1/2,1/2,d_1)$	$(-1/2,-1/2,d_1)$
	Close	$(1/2,-1/2,d_2)$	$(1/2,1/2,d_2)$	$(-1/2,1/2,d_2)$	$(-1/2,-1/2,d_2)$
	Far	$(1/2,-1/2,d_3)$	$(1/2,1/2,d_3)$	$(-1/2,1/2,d_3)$	$(-1/2,-1/2,d_3)$
	Very Far	$(1/2,-1/2,d_4)$	$(1/2,1/2,d_4)$	$(-1/2,1/2,d_4)$	$(-1/2,-1/2,d_4)$

Table 4.5 *Geometrical quantities for the experiments represented in figures 4.16 and 4.17. In the weakly near singular scenarios d_1=10 μm, d_2=1 mm, d_3=1 cm and d_4=10 cm.*

precision, ensuring that $1-x$ and $1+x$ are never equal to zero. Therefore, the final number of truncated points is equal to $N=2p+1$, which corresponds for levels (*M*) 0, 1, 2, 3, 4, 5, 6 and 7 respectively to (*N*) 7, 13, 25, 51, 101, 203, 405 and 809 integration points. Also in Fig. 4.15, the weights and abscissas distributions for *M*=2 are shown respectively in Fig. 4.15a and in Fig. 4.15b. It can be clearly appraised that the abscissas are mostly in the asymptotic zone, as well as their related weights, whose small values will impact on the large function values in the endpoint singular region.

The DE formula was introduced to the EM community in [33], where 2D generalized Cartesian product rules (GC) based on DE formula are used to numerically solve the integral observer triangular and quadrangular patches, respectively for the weakly MSI linked to the free space potential GF and the static free-space potential GF. In that reference, it is evinced that GC, which are built through the use of the DE formula in each of the dimensions, outperform Gaussian rules for some situations of interest. These situations are, weakly singular scenarios related to coincident domains and the near singular case associated to very close parallel cells. Here a more detailed study, which also includes the cases exhibited in [33] as a matter of completeness, is presented. This study consist of calculating the 4D weakly MSI for all the cases of interest described in section §4.3 by computing the 2D potential integral analytically via expression (4.71), whereas the observer integral is calculated via 2D GC based on either the DE formula or standard Gauss-Legendre (GL) rules. The quadrature levels utilized for the numerical integration are 0, 1, 2, 3, and 4, which respectively correspond to 7, 13, 25, 51 and 101 integration points per dimension. The 4D weakly MSI are performed, without loss of generality, over square source and observer patches, thereby the exact solutions of these 4D weakly MSI can be computed through the complete analytical formulas presented in section §4.5. This exact solution is taken as reference to compute the relative error committed in both cases, i.e. when using the DE formula or a GL rule to built the 2D GC, which on its turn, ascertain the validity of the expressions presented in §4.5 in a far more rigorous way. The source patch's nodes are $\mathbf{r}_1'=(1/2,-1/2,0)$, $\mathbf{r}_2'=(1/2,1/2,0)$, $\mathbf{r}_3'=(-1/2,1/2,0)$ and $\mathbf{r}_4'=(-1/2,-1/2,0)$, whereas the nodes of

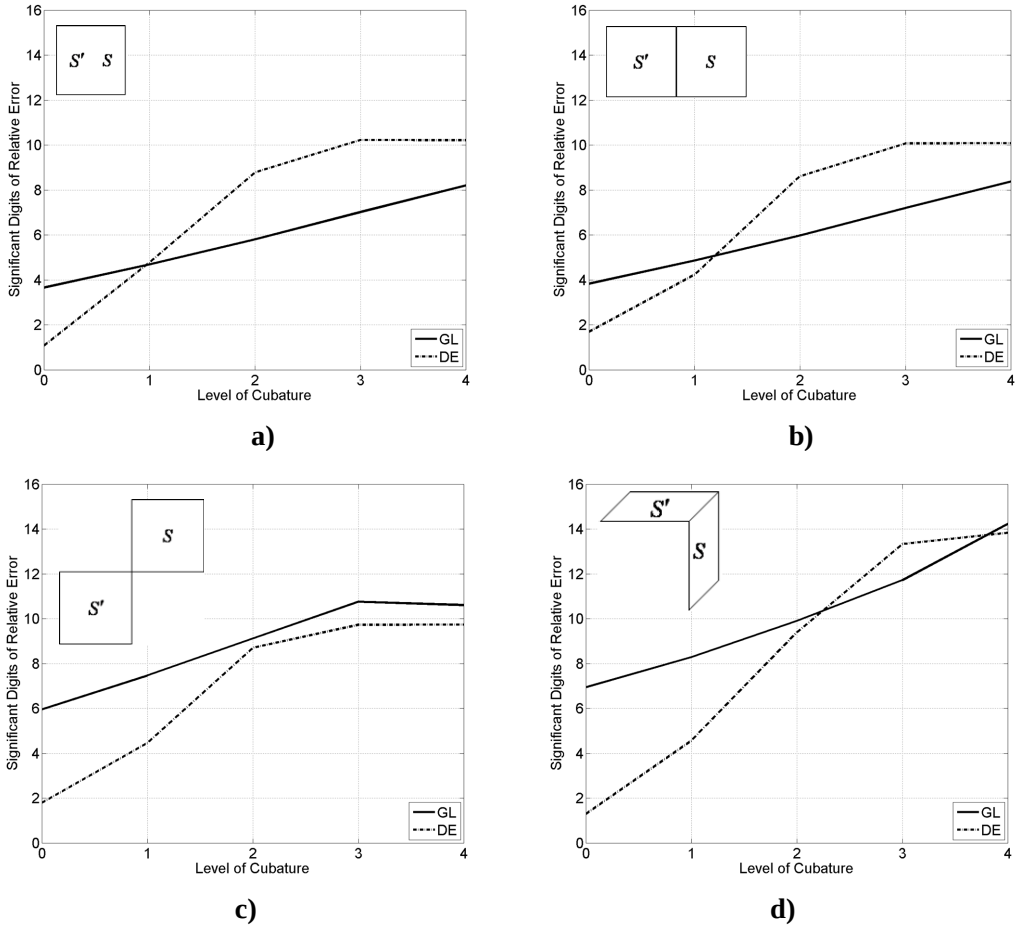

Fig. 4.16 *Relative errors in the weakly singular situations a) self b) adjacent c) vertex and d) adjacent orthogonal, when integrating (4.72) with 2D GC rules based either on the DE formula or on Gauss-Legendre quadratures.*

the observer patches for weakly singular and near singular scenarios are summarized in table 4.5. The resulting relative errors are presented in Fig. 4.16 and Fig. 4.17, respectively for weakly singular and weakly near singular scenarios. On the one hand, as appreciated in Fig. 4.16, DE based rules outperform Gaussian based schemes in weakly singular scenarios associated to self Fig. 4.16a and coplanar adjacent Fig. 4.16b cases, while for vertex Fig. 4.16c and orthogonal adjacent Fig. 4.16d situation they can be considered equivalent. It has to be pointed out that in a generic intermediate adjacent case, in which the angle formed by the two patches is different of 90°, one is tending either to the adjacent coplanar situation or to the self scenario. Therefore, it can be intuitively inferred from the inspection of Fig. 4.16 that in these cases the DE based schema will progressively outperform Gaussian rules, in other words, the closer to self or coplanar adjacent situation the scenario is, the worse the performance of GL based schemas is. Similar phenomena can be observed for weakly near singular scenarios, which correspond to two parallel patches separated a distance d, in Fig. 4.17. Here in Fig. 4.17a (d_1=10 μm) and in Fig. 4.17b (d_2=1 mm), it can be appraised, that when source and observer patches are considerably

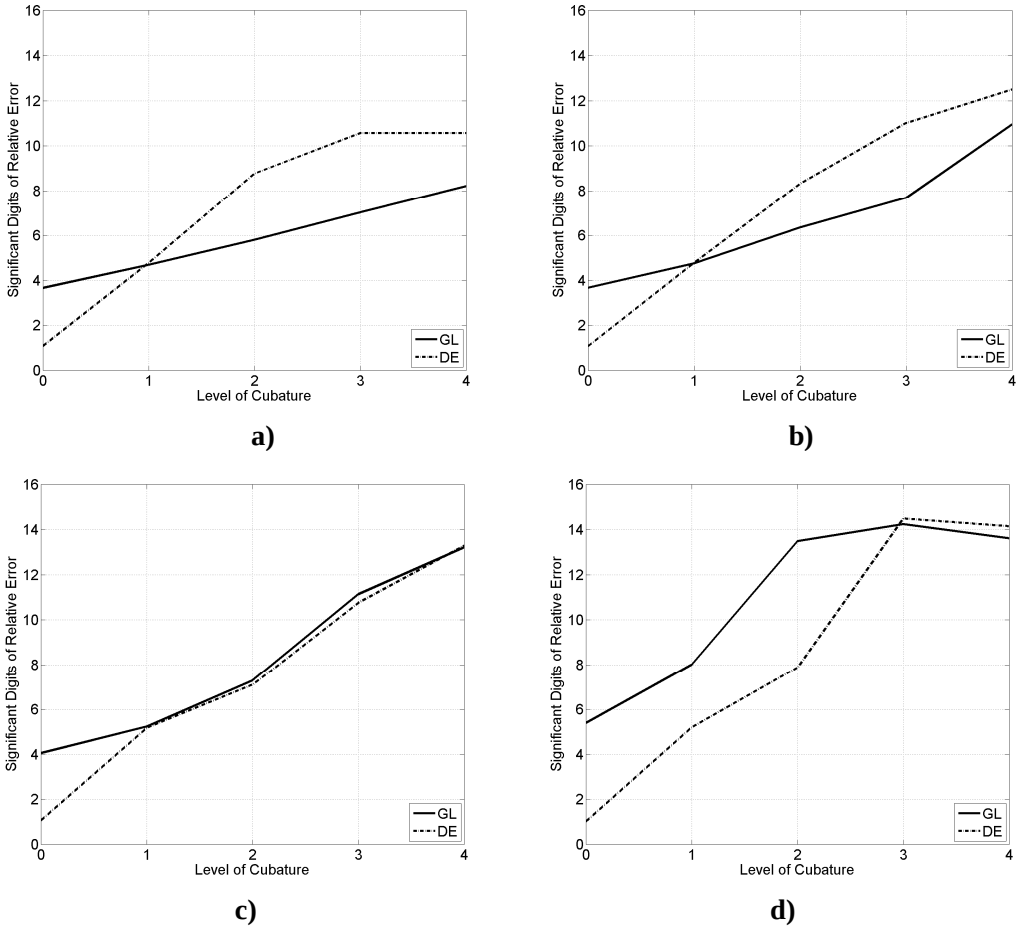

Fig. 4.16 *Relative errors in the parallel cells near weakly singular situations for a) d_1=10 μm, b) d_2=1 mm, c) d_3=1 cm and d) d_4=10 cm, when integrating (4.72) with 2D GC rules based either on the DE formula or on Gauss-Legendre quadratures.*

close DE based cubatures exhibit a better performance than GL bases schemes. However, the behavior of both techniques is almost the same for moderate distances between patches, as shown in Fig. 4.17c for d_3=1 cm. Finally, GL numerical rules are clearly better than DE ones when source and observer cells are substantially far, as it can be seen in Fig. 4.17d for d_4=10 cm. Although, these two last cases have been classified as weakly near singular, in fact they can be considered as smooth scenarios, as well as the corner weakly near singular situation. Both in these cases and in general smooth situation, most of the observer domain is located in a smooth variation region of the fields, so that the potential can be accurately integrated through Gaussian rules. On the contrary, in the rest of weakly singular situations, the observation patch can include a substantial part of the singular region of the fields. Consequently, Gaussian rules lose their accuracy in favor of DE based rules, which are addressed to work in this endpoint singular region of the potential derivatives. This fact is qualitatively illustrated by means of the representation of the integration abscissas for DE and GL based cubatures respectively in Fig. 4.18a and in Fig. 4.18b. These figures are related to the self weakly singular situation in Fig. 4.16a with order M=1. Notice that in Fig. 4.18a not all the abscissas associated to the GC-DE rule can be clearly

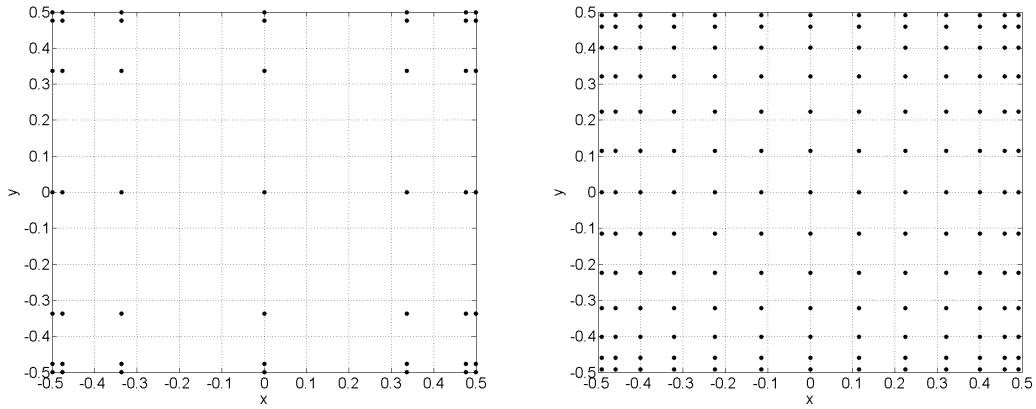

Fig 4.18 a) *Abscissas distribution when a 2D GC product rule is built via the DE formula or b) a standard Gauss-Legendre quadrature b).*

appraised, inasmuch as they are highly concentrated at edges and corners, being the distance between them very small, thereby it seems they overlap but this is not the case. Nonetheless in the GL case, this problem does not happen, since the distribution of the abscissas over the square is more uniform.

4.7 Conclusions

In this chapter, novel analytical expressions to calculate the quadruple integral of the weakly *1/R* static potential singularity are reported. These formulas are useful when using the MoM with rectangular cells and low order divergence constant basis functions to discretize potential SIEs within singularity subtraction context. All the topological scenarios of interest, namely weakly singular self, adjacent and vertex situations, as well as weakly near singular and smooth cases have been analytically solved for coplanar, parallel and orthogonal cells. Practical results involving the closed analytical expression reported here are presented in the next chapter for both, static problems and full-wave problems, which are solved via the MPIE.

As it has been explained in §4.4, it is not always possible to attain a full analytical solution for MSI involving the *1/R* static GFs, so that hybrid numerical-analytical techniques have to be applied to solve the MSI. An original strategy, which follows this schema is presented in §4.6. This strategy is based on a novel integral transformation, which is exhibit in §4.6.1 and is useful to calculate analytically weakly singular free space potential integrals associated to uniform sources distributed over arbitrarily shaped flat polygons. When compared with other existing techniques, this transformation eases considerably the mathematical effort and provides a concise, operative and accurate framework to the singularity subtraction procedures. The equivalency between the obtained expression with this alternative strategy and other existing formulas can be proven. Numerical integration drawbacks, bounded to the endpoints singularities in the

derivatives of the analytical potential integral, are alleviated through the usage of generalized Cartesian product rules based on the DE formula. It has been shown that the presented hybrid strategy is especially useful in both weakly self and adjacent situations, as well as in near singular situations, when source and observer cells are very close. Numerical examples showing these aspects within a SIE-MoM framework will be also provided in §5, demonstrating the interest of using the global approach presented in §4.6 for the double surface integrals appearing in Galerkin formulations.

The main findings of this chapter as shown in sections §4.5 and §4.6 have been reported in two peer reviewed journal papers.

References

[1] J. R. Mosig, "Arbitrarily shaped microstrip structures and their analysis with a mixed potential integral equation," *IEEE Trans. Microw. Theory and Techn.*, vol. 36, no. 2, pp. 314-323, Feb. 1988.

[2] T. Itoh (ed), *Numerical Techniques for Microwave and Millimeter-Wave Passive Structures*. USA: John Wiley & Sons, 1989.

[3] Jean Van Bladel, *Electromagnetic Fields*, USA: John Wiley & Sons, 2007.

[4] S. Rao, A. Glisson, D. Wilton, "Electromagnetic scattering by surfaces of arbitrary shape," *IEEE Trans. Antennas Propagat.*, vol. 30, no. 3, pp. 409–418, May 1982.

[5] Jerrold E. Marsden and Anthony J. Tromba, *Cálculo Vectorial*. Wilmington: Addison-Wesley Iberoamericana, 1991.

[6] Zbynec Raida. "Moment Method," *Modeling of Fields*. European School of Antennas. Prague, September 2006.

[7] A. G. Polimeridis and T. V. Yioultsis, "On the direct evaluation of weakly singular integrals in galerkin mixed potential integral equation formulations," *IEEE Trans. Antennas Propagat.*, vol. 56, no. 9, pp. 3011–3019, Sept. 2008.

[8] A. G. Polimeridis and J. R. Mosig, "Complete semi-analytical treatmet of weakly singular integrals on planar triangles via the direct evaluation method," *Int. J. Numer. Engng*. To appear.

[9] Michael G. Duffy, "Quadrature over a pyramid or cube of integrands with a singularity at a vertex," SIAM J. Numer. Anal., wol. 19, no. 6 Dec 1982.

[10] J. C. F. Telles,"A self-adaptive co-ordinate transformation for efficient numerical evaluation of general boundary element integrals," Int. J. Numerical Methods Eng., vol. 24, pp. 959-973, 1987.

[11] R. D. Graglia, "Static and dynamic potential integrals for linearly varying source distributions in two- and three-dimensional problems ," IEEE Trans. Antennas Propag., vol. 35, no. 6, pp. 662-669, June 1987.

[12] C. Schwab and W. L. Wendland, "On numerical cubatures of singular surface integrals in boundary element methods," Numer. Math., vol. 62, pp. 343-369, 1992. [22] R. Klees, "Numerical calculation of weakly singular surface integrals," J. Geodesy., vol. 70, pp. 781-797, 1996.

[13] L. Rossi and P. J. Cullen, "On the fully numerical evaluation of the linear-shape function times the 3-D Greens function on a plane triangle," *IEEE Trans. Microw. Theory Tech.*, vol. 47, no. 4, pp. 398–402, Apr. 1999.

[14] W. Cai, Y. Yu, and X. C. Yuan, "Singularity treatment and high-order RWG basis functions for integral equations of electromagnetic scattering," Int. J. Numerical Methods Eng., vol. 53, pp. 31-47, 2002.

[15] A. Herschlein, J. v. Hagen, and W. Wiesbeck, "Methods for the evaluation of regular, weakly singular and strongly singular surface reaction integrals arising in method of moments," ACES Journal, vol. 17, no. 1, pp. 63-73, Mar. 2002.

[16] M. A. Khayat and D. R. Wilton, "Numerical evaluation of singular and near-singular potential integrals," *IEEE Trans. Antennas Propag.,* vol. 53, no. 10, pp. 3180–3190, Oct. 2005.

[17] S. M. Seo and J. -F. Lee, "Accurate integration of the weakly singular integrals from EFIE," CEFC Conference on Electromagnetic Field Computation, Miami FL, USA, Apr. 2006.

[18] W. -H. Tang, and S. D. Gedney, "An efficient evaluation of near singular surface integrals via the Khayat-Wilton transform ," Microwave Opt. Tech. Lett., vol. 48, no. 8, pp. 1583-1586, Aug. 2006.

[19] M. S. Tong, and W. C. Chew, "Super-hyper singularity treatment for solving 3D electric field integral equations," Microwave Opt. Tech. Lett., vol. 49, no. 6, pp. 1383-1388, June 2007.

[20] R. D. Graglia and G. Lombardi, "Machine precision evaluation of singular and near-singular potential integrals," *IEEE Trans. Antennas Propag.,* vol. 56, no. 4, pp. 981–998, Apr. 2008.

[21] D. R. Wilton, S. M. Rao, A. W. Glisson, D. H. Schaubert, O. M. AL-Bundak, and C. M. Butler, "Potential integrals for uniform and linear source distributions on polygonal and polyhedral domains," *IEEE Trans. Antennas Popag.,* vol. 32, no. 3, pp. 276-281, Mar. 1984.

[22] R. D. Graglia, "On the numerical integration of the linear shape functions times the 3-D Green's function or its gradient on a plane triangle," *IEEE Trans. Antennas Popag.,* vol. 41, no. 10, pp. 1448-1455, Oct. 1993.

[23] T. F. Eibert and V. Hansen, "On the calculation of potential integrals for linear source distributions on triangular domains," *IEEE Trans. Antennas Popag.,* vol. 43, no. 12, pp. 1499-1502, Dec. 1995.

[24] P. Arcioni, M. Bressan, and L. Perregrini, "On the evaluation of the double surface integrals arising in the application of the boundary integral method to 3-D problems," *IEEE Trans. Mcrw. Theory Tech.,* vol. 45, no. 3, pp. 436-439, Mar. 1997.

[25] S. Järvenpää, M. Taskinen, and P. Ylä-Oijala, "Singularity subtraction technique for high order polynomial vector basis functions on planar triangles," *IEEE Trans. Antennas Propag.*, vol. 54, no. 1, pp. 42-49, Jan. 2006.

[26] J. S. Asvestas and H. J. Bilow, "Line-integral approach to computing impedance matrix elements," *IEEE Trans. Antennas Propag.*, vol. 55, no. 10, pp. 2767-2772, Oct. 2007.

[27] T. Adams and J. Singh, "A nonrectangular patch model for scattering from surfaces," *IEEE Trans. Antennas Propag.*, vol. 27, no. 4, pp. 531-535, Jul. 1979.

[28] P. Tulyathan and E. H. Newman, "A surface patch model for polygonal plates," *IEEE Trans. Antennas Propag.*, vol. 30, no. 4, pp. 588-593, Jul. 1982.

[29] B. M. Kolundzija, "On the locally continuous formulation of surface doublets," *IEEE Trans. Antennas Propag.*, vol. 46, no. 12, pp. 1879-1883, Dec. 1998.

[30] J. R. Mosig and J. M. Rius, "Macrobasis functions and Multilevel algorithms for printed structures," in *Proc. IEEE Trans. Antennas Propag Int. Symp..*, vol. 2, pp. 44-46, Boston, USA, Jul.. 2001.

[31] I. S. Gradshteyn and I. M. Ryzhik, *Tables of Integrals, Series and Products*. New York: Academic, 1980.

[32] Herbert Bristol Dwight, Tables of Integrals and other Mathematical Data. New York: The MacMillan Company, 1961.

[33] D. H. Bailey, K. Jeyabalan and X. S. Li "A comparison of three high-precision quadrature schemes," *Experimental Mathematics*, vol. 14, no. 3, pp. 317-329, 2005.

[34] A. G. Polimeridis and J. R. Mosig, "Evaluation of weakly singular integrals via generalized Cartesian product rules based on the double exponential formula," *IEEE Trans. Antennas Propag.*, to appear.

[35] K. G. Binmore, *Mathematical Analysis a straightforward approach*. United Kingdom: Cambridge, 1982.

[36] B. M. Notaros, "Higher Order frequency-domain computational electromagnetics," *IEEE Trans. Antennas Propagat.*, vol. 56, no. 8, pp. 2251–2276, August 2008.

[37] E. Durand, *Électrostatique : I Les Distributions*. Paris: Masson et C^{ie}, 1964, pp. 247–248.

[38] H. Takahasi and M. Mori, "Double exponential formulas for numerical integration," *Publ. RIMS, Kyoto Univ.*, no. 9, pp. 721-741, 1974.

[39] A. R. Krommer and C. W. Ueberhuber, Computational integration. SIAM, 1998.

[40] M. Mori, "Quadrature formulas obtained by variable transformation and the DE-rule," *J. Comput. Appl. Math.*, no. 112, pp. 119-130, 1985.

5 Applications

"Hell, there are no rules here; we're trying to accomplish something."

Thomas A. Edison

"I tried a dozen different modifications that were rejected, but they all served as a path to the final design."

Mikhail Kalashnikov

5.1 Introduction

This chapter is devoted to exhibit several numerical examples and practical applications of the theoretical results developed in previous sections. The solutions to all the presented electromagnetic (EM) problems are obtained within the framework of potential surface integral equations (SIE) discretized through the Method of Moments (MoM). The SIE-MoM technique is applied both in static and full-wave situations, tackling in both scenarios open and close problems.

In the first section of this chapter, the performance of the formulation developed in §4 is shown within a SIE-MoM context. This is done via the resolution of static problems, which are tackled either by means of the hybrid analytic-numeric integration technique, that is based on the novel integral transformation (4.69) shown in §4.6.1 and on double exponential (DE) rules (4.6.3), or through the original total analytical expressions, which are related to the 4D integrals presented in §4.5.

Secondly, the SIE-MoM strategy is utilized to study the effects of metallic shields on the EM response of metallic scatterers. In first place, the structure under study is analyzed in free space, which invokes the usage of free-space Green functions (GF) within the SIE-MoM framework. Then, the same analysis is implemented but enclosing the structure inside a perfect electric conducting (PEC) rectangular cavity. Advantageously, the usage of a SIE-MoM strategy permits to implement this second analysis by simply changing the free space GF by a cavity GF. The cavity GF developed in chapter §3 are utilized in this second analysis. In both cases (free space and cavity), singularity subtraction techniques are used to fill in the MoM matrix. In addition to

allow the derivation of several relevant scientific conclusions, this study has also a major applied impact. Indeed, it has been used to ascertain the good behavior of all the tools needed in the development of a proof of concept (POC) software, which is being implemented in the framework of several European Space Agency (ESA) project. The objective of this software is to show the ability of the use of the mixed potential integral equation together with the MoM (MPIE-MoM) to analyze combline resonators in waveguide/cavity technology.

In the final section of this chapter, some practical results, which have been obtained with the aforementioned POC software in the context of combline filters, are shown. The typical structures used in this kind of filters, that's to say tuning posts and mushrooms, as well as the most common excitation techniques, namely coaxial, magnetic and dumbbell, are simulated within a single resonator context. Finally, results for a combline filter, where the coupling between resonators is done via a full opening window are shown. All the results are ascertained through the comparison with commercial software.

5.2 Static Problems

As aforesaid, this section is devoted to show the performance of the formulation and techniques described in chapter §5 through the resolution of static problems. The reader is reminded that a singularity subtraction technique consist basically of extracting a static problem from a complete full-wave problem. Namely, the GF static part, which includes the GF spatial singular behavior, is separated from the GF dynamic part and processed severally. Consequently, the computation of a static MoM impedance matrix is invoked. Therefore, it can be concluded that a good knowledge of the static interactions in the structures under study is mandatory, inasmuch as they are not only relevant for the zero frequency case; on the contrary, they play a very important role in the whole spectrum.

5.2.1 Performance of 2D GC-DE rules within a SIE-MoM Framework

In first place, the suitability in using 2D Cartesian product rules based on DE formula, instead of Gauss standard quadratures, to integrate potentials as (4.71) (§4.6.1) to compute the Galerkin-MoM matrix static interactions in the cases of interest described in §4.3 within a SIE-MoM framework is shown. The resolution of two very simple static problems is only required to achieve the objective. To this goal, two simple static problems have been selected, consisting of the computation of the charge appearing in the surface of two polyhedrons at constant unit potential 1 V. The first polyhedron is a 3D trapezohedron, which is shown in the inset in Fig. 5.1a Bottom and top trapezohedron's sides are parallel squares, which separated by 0.5 m and centered at z axis. The lengths of the squares' edges are respectively 1 m for the bottom side and 0.5 m for the top one. The second polyhedron, which is depicted in the inset of Fig. 5.1b is a cube, which is also centered at the coordinate origin and whose edges measure 1 m. In both cases the SIE to solve is

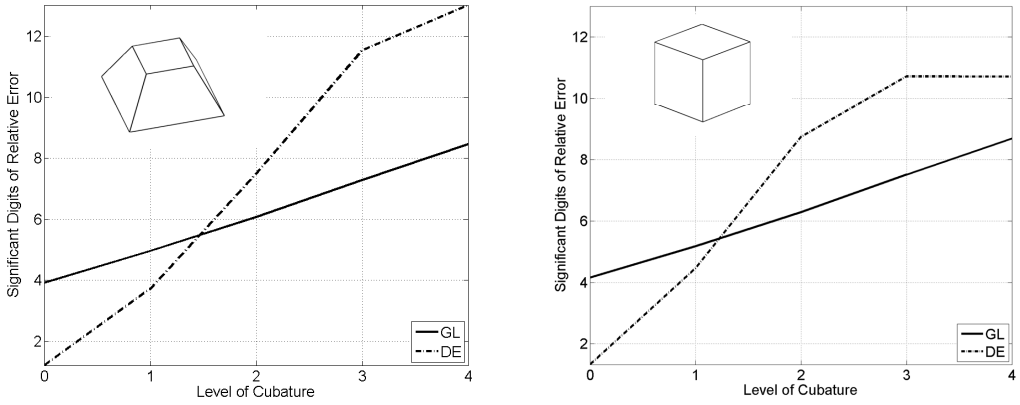

a) **b)**

Fig. 5.1 *a) Relative error in calculating the total charge in a trapezohedron and b) in a cube, both at 1 V. In the case of the trapezohedron the MoM matrix related to (5.1) has been calculated through the usage of (4.69) and DC-DE rules, whereas in the case of the cube the MoM matrix is absolutely filled thanks to the analytical formulas in§ 4.5.*

$$\int_{S'} \frac{\sigma_{s'} dS'}{R} = 1 \tag{5.1}$$

where S' is the surface of the polyhedron and $\sigma_{s'}$ the surface charge density, which is expanded by means of uniform basis functions on each cell. All the needed MoM matrix integrals are related to the weakly and near singular interactions previously described in section §4.3. It has to be pointed out that the static MoM matrices, which are associated to the MPIE full-wave analysis of the same structures, can be built from the MoM matrices required here, if low order basis functions are used. Both for the trapezohedron and for the cube, these matrix elements are computed by integrating (4.71) through 2D generalized Cartesian product rules based on the DE and Gauss-Legendre rules, for levels 0, 1, 2, 3 and 4 in both cases. The relative errors in the resulting total charge are shown in Fig. 5. The reference solution for this error in the case of the trapezohedron is computed though 2D generalized Cartesian product rules based on the DE quadrature with level 6 (405 points per dimension), whereas in the case of the cube, the full closed expression presented in section §4.5 are utilized to compute this reference. It can be clearly appraised in Fig. 5.1a and Fig. 5.1b, that the joint use of (4.71) and DE-based rules outperform Gaussian rules within a complete SIE-MoM framework. Obviously, this hybrid analytic-numeric technique should be used in absentia of the total analytical solution. This fact can be easily evinced from the computational times related to the problem solved in Fig. 5.1b The total time in the obtention of the solution when filling the MoM matrix analytically is of 0.012 s, whereas 40 s are needed in the case of the hybrid approach (level 3, 51 points per dimensions), where it can be considered that the solution has already converged. These cases have been run in a PC with a 2.66 GHz processor and 3.87 Gb of RAM.

5.2.2 Numerical Static Potential GFs

Although, the IE-MoM strategy is considered one of the most powerful techniques to solve EM problems, its usage is commonly limited by the mathematical difficulty in the obtention of the GF linked to the problem under study. Commonly, this GF can be obtained via analytical mathematical techniques in the case of canonical geometries, as for example rectangular (chapter §3), cylindrical [1], spherical [2] cavities or waveguides whose section is also rectangular [3], cylindrical [1]. In a generic scenario, the obtaining analytic expression of the GF will not be available. However in these cases, it is possible to calculate numerically the GF from the free space GF by means of the MoM of moments. This numerical technique invokes for the meshing of the whole structure under test, what can lead to an expensive computational cost, if the MoM matrix is computed also through numerical techniques. In the past, this fact has meant that this technique has not been deeply explored in the framework of the IE-MoM procedures. Nevertheless, the analytical computation of the MoM matrix elements can mitigate this issue.

In this subsection, the numerical procedure to obtain a GF via the MoM is illustrated via the calculation of static potential GF of a PEC rectangular cavity. Even though as shown in chapter §3, there are other alternatives to calculate the GF of this geometry, this benchmark is considered enlightening, since it is very a well known result, whose ascertainment is straightforward. The static GF of a PEC rectangular cavity is solution of the Poisson's equation

$$\nabla^2 G\left(\mathbf{r}-\mathbf{r}'\right)=\delta\left(\mathbf{r}-\mathbf{r}'\right), \tag{5.2}$$

with Dirichlet boundary conditions (G=0). Obviously in (5.2), G is the static GF and δ represents an electric unitary charge q located at $\mathbf{r}'$. Physically, G boils down to the electrostatic potential in the volume enclosed by the cavity walls S'. Therefore, for an arbitrary position of q inside the cavity $\mathbf{r}'=\mathbf{r}_q$, G can be expressed as

$$G\left(\mathbf{r},\mathbf{r}_q\right)=\frac{1}{\left|\mathbf{r}-\mathbf{r}_q\right|}+\int_{S'}\frac{\sigma_{s'}\left(\mathbf{r}'\right)}{\left|\mathbf{r}-\mathbf{r}'\right|}dS'. \tag{5.3}$$

The first adding term in (5.3) represent the potential produced by q itself, whereas the second one is the potential produced by the induced surface charge density by q $\sigma_{s'}\left(\mathbf{r}'\right)$ at the cavity walls. In Fig. 5.2a, the problem is represented for $\mathbf{r}_q$ the center of the cavity. Noticeably, the targeted GF in (5.3) requires knowing $\sigma_{s'}\left(\mathbf{r}'\right)$, whose closed expression is not available a priori. Nonetheless, a discrete version of the induced charge can be calculated for any position $\mathbf{r}_q$ through the MoM. This calls for solving the IE

$$\left.\frac{1}{\left|\mathbf{r}-\mathbf{r}_q\right|}+\int_{S'}\frac{\sigma_s\left(\mathbf{r}'\right)}{\left|\mathbf{r}-\mathbf{r}'\right|}dS'=0\right|_{\forall\mathbf{r}\in S'} \tag{5.4}$$

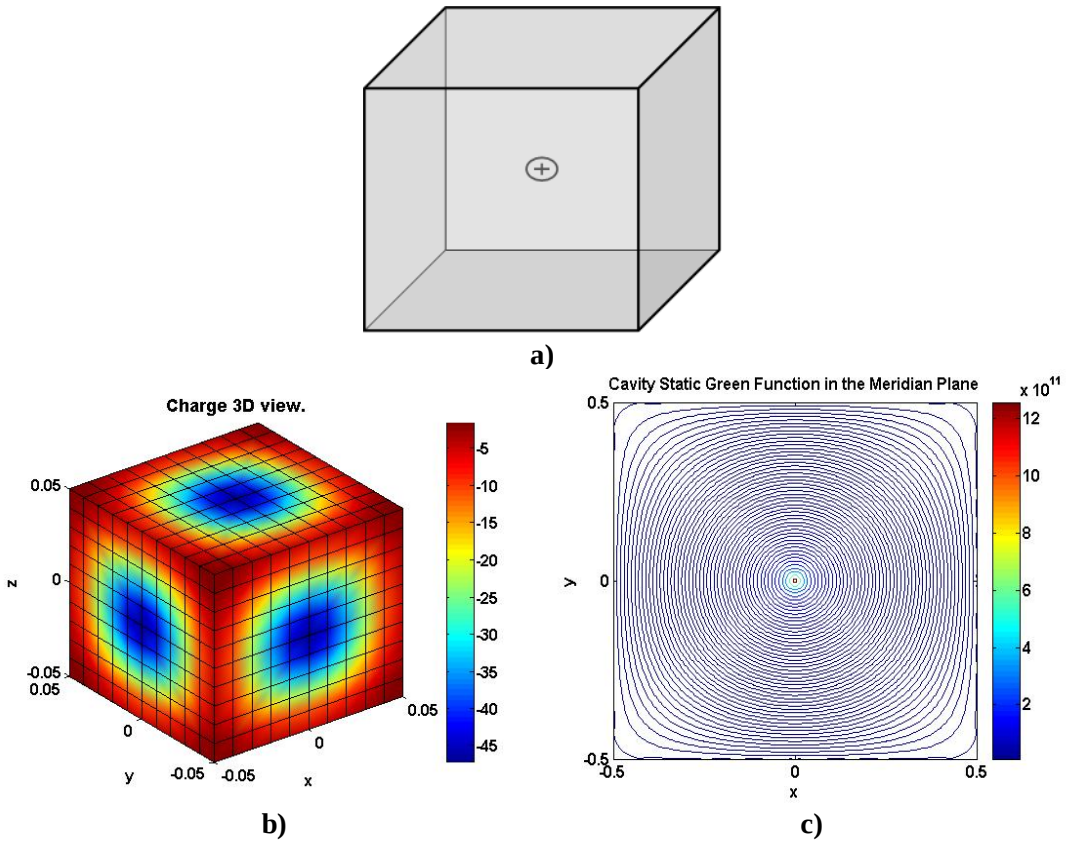

Fig 5.2 *a) Enclosed unitary electric charge by a PEC cuboid of 100 mm size. b) Induced charge density at the cuboid's walls by the enclosed charge, which is obtained after solving (5.4) via the MoM. c) This induced charge density is used in (5.3) to compute the cavity static GF isolines in the cavity meridian plane.*

which arises from imposing the Dirichlet boundary conditions (G=0) for the potential at the cavity walls. In Fig. 5.2b, the resulting $\sigma_{s'}(\mathbf{r}')$, which correspond to the solution of (5.4) through the MoM for a cavity of 0.1 m. per side and $\mathbf{r}_q$ the center of the enclosure, is presented. The cavity has been uniformly meshed with 600 square cells, over which sub-domain pulse basis functions are defined. It can be observed in Fig. 5.2b, that the result is fully coherent with theory since the charge distribution is symmetrically distributed, is concentrated in the center of the enclosure walls and has negative sign. An excellent check of the numerical accuracy achieved is the fact that the resulting total value of charge on the shield is of -1.003 C, so that the relative error is of 0.3% which it is a good result in terms of precision. All the needed integrals to fill in the MoM matrix to solve (5.4) have been analytically computed via the expressions presented in §4.5. The problem has been solved reaching a speed of 14758 integrals/s (processor Intel Pentium IV at 3.2 GHz, 1 GB of RAM), which allow stating that the reported formulation in §4.5 is also competitive in terms of efficiency.

Finally, the numerical version of the GF solution of (5.2) is obtained after solving the potential integrals, which result of replacing the samples of the discrete version of $\sigma_{s'}(\mathbf{r}')$ derived from (5.4), in (5.3). These integrals are also solved analytically by using the expressions in

chapter §4. The numerical version of *G* in the meridian plane of the cavity containing a centered *q* is shown in Fig. 5.2c. These values have been calculated by replacing the discrete version of $\sigma_{s'}(\mathbf{r}')$ shown in Fig. 5.2b, in (5.3). In this figure, it is appreciated that the isolines of *G* have symmetry of revolution rounding the point $\mathbf{r}' = \mathbf{r}_q$ and match the boundary condition on the cavity walls. Besides also Fig. 5.2c, it is observed that the singular phenomenon at $\mathbf{r}' = \mathbf{r}_q$ is fulfilled. These facts allow stating that the physical GF behavior, which was explained in chapter §3, is well recovered.

Several facts have to be pointed out regarding this method. In first place, the method is highly flexible, insomuch as the GF of any geometry can be numerically inferred. Secondly in regard to the efficiency, it has to be noticed that the MoM matrix has to be computed only once (at least in the static case, otherwise a MoM matrix is needed for each frequency), that's to say, the same MoM matrix is valid for all the possible values of $\mathbf{r}_q$. The computation of this matrix can be efficiently performed if analytical formulas are available for the interaction integrals. Obviously, the accuracy of the method can be improved by increasing the number of unknowns to compute $\sigma_{s'}(\mathbf{r}')$, what can produce a lack of efficiency. However, this drawback can be solved via the incorporation of fast solvers [4]-[5] for MoM. Finally, notice that the final step in the obtaining of the GF only calls for the computation of potential integrals, which have analytical solution at least for the static case.

It must be pointed out that here we use a fast IE to determine the required GF. Once this GF is known and properly approximated, the charge density $\sigma_{s'}(\mathbf{r}')$ induced in any metallic object of surface S existing inside the cavity would be obtained through the solution of a second IE, namely

$$U = \int G(\mathbf{r}, \mathbf{r}_q) \sigma_s(\mathbf{r}_q)\, dS \tag{5.5}$$

5.3 Impact of PEC Enclosures in the EM Response of Shielded Structures

The analysis of enclosed structures is a common problem in many electromagnetic researching areas. For example, the use of shielded housings is a typical electromagnetic compatibility (EMC) technique to protect equipment of unwanted effects. In filter design, structures are also boxed to protect them, to keep radiation inside and even to improve their behavior [6]-[8]. Also, for antenna measurement purposes, a scatterer is shielded to determine its response. In this section, the frequency response of a whole system, including both the shield and the boxed scatterer effects, is studied. It is very complex to understand how these two effects are combined to produce the resulting frequency response of the whole system. Depending on several parameters, this frequency response can be seen as the alteration of the box's response due to the structure inside or vice versa.

The study has been implemented by choosing a simple system, which consists of two front to front strongly coupled metallic strips. In this direction, some interesting results using thin wire approximations together with Pocklington and Hallen integral equations are found in literature

[9]-[10]. These results are related to EMC problems and are limited to wire scatterers, but they represent a good starting point to broach the problem. Although this is a very simple structure, the physical phenomena inherent to highly coupled structures are of relevance in more complex systems as for example combline filters, where the gaps between shielded elements are used to tune the frequency response of the filter's resonators, as it will be shown in §5.4. This study is split into two parts: firstly, the objects are analyzed in free space to discern their intrinsic frequency response; subsequently, the scatterer is shielded with a PEC cavity to study the effects of the enclosure on the aforesaid frequency response. Several numerical experiments are presented to determine the influence of the cavity on the free space response of the scatterer, especially in terms of matching, coupling and resonances. All the different physical phenomena embedded in the set cavity plus enclosed object can be described from the previous results.

In the aforementioned free-space and cavity scenarios, the obtained frequency response is summarized by the S parameters linked to the structure under analysis, which are obtained through an MPIE-MoM strategy (chapter §2). The strongly coupled structure under analysis have been meshed with rooftop basis functions defined over rectangular cells (section §4.2) and a δ-gap generator (references in §2) has been used to model the excitation. The utilization of a MPIE-MoM strategy allows analyzing the same structure in both scenarios by simply changing the free-space GF by a cavity GF, while the other features associated to the analysis remain unchanged. The free-space analysis has been implemented by means of home-made (HM) software envisioned to analyze open problems, whereas the cavity problem has been analyzed through a POC software developed in the framework of [11]. Both codes follow the classical IE-MoM chain presented in §2, using the POC software the GFs developed in chapter §3. As mentioned in §5.1, singularity subtraction techniques are used to compute the MoM matrix elements, so that the GFs are expressed as the sum of a dynamic and a static part. Obviously in the free space case, this static part is free space static GF. In the cavity scenario, the GF static part is inferred from this the free space static GF by means of image theory, as explained in section §3.4. All the MoM interaction integrals associated to these static GFs are computed via the closed analytical formulas, which are solution of the 4D integrals presented in section §4.5.

As mentioned above the study presented in this section has a foreseen application range from EMC problems to accurate determination of cavity combline filter performance. Specifically, this study helps to ascertain that the POC code based on the MPIE-MOM strategy is able to properly recover the frequency response associated to enclosed high coupled structures. This allows setting a strong basis to broach the analysis of more complex shielded systems, as it will be shown in the next section.

5.3.1 The Coupled Strips Antenna in Free Space

This study starts with the analysis of two strongly coupled strip-like antennas, whose geometry is shown in Fig. 5.3a. In this figure, *L* and *w* are respectively the length and the width of the strips, while *d* is the separation between them. As aforementioned, this system is relatively simple to model by using a free space Green function and a standard MPIE-MoM implementation. In the same figure, it is shown the rectangular cell mesh to apply MoM and the port definition in the centre of the strips. This ports are modeled using a tension δ-gap generator

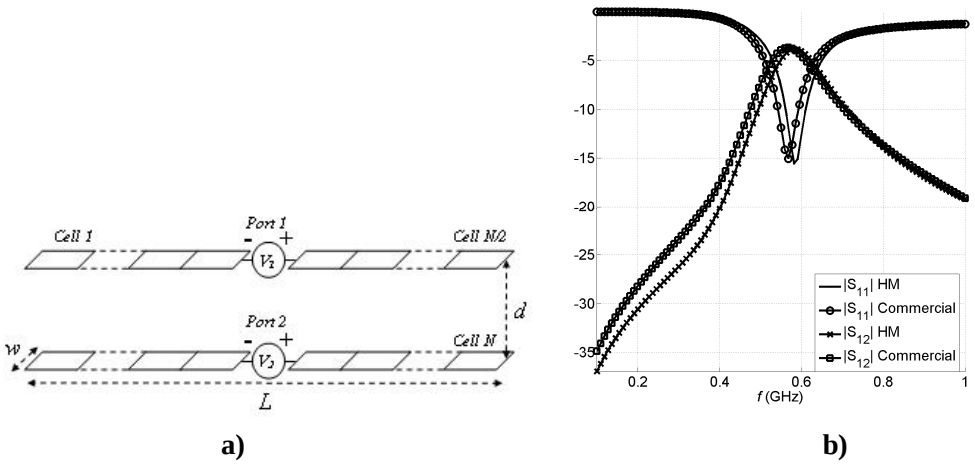

a) **b)**

Fig. 5.3. *a) Coupled strips geometry under study. b) S Parameters comparison between the HM software and HFSS^{TM} for L = 240 mm, w = 20 mm and d = 50 mm .*

with values $V_1 = V_2 = 1$ V. Also as aforesaid, the free space experiments are implemented with HM MPIE-MoM software. In 5.3b, the good agreement of this software with the commercial code HFSS^{TM} is shown. This figure is related to a couple of strips with $L = 240$ mm, $w = 20$ mm and $d = 50$ mm. Here, it is observed that nearby 0.58 GHz the resonance is produced. The electrical length of the strips at this frequency is approximately $0.464 \cdot \lambda$. This is coherent with the theory, as expected in a capacitive loaded system. Other interesting phenomenon is the lump in S_{12} near 0.39 GHz. At this frequency the strips are $0.304 \cdot \lambda$. This lump, not apparent in S_{11} is only seen here as a slight change in the curvature of the S_{12} response. However it will play a significant role in the following numerical experiments.

In Fig. 5.4a, $|S_{11}|^2$, $|S_{12}|^2$ and $|S_{11}|^2+|S_{12}|^2$ for the previous configuration are shown. Here, three points are defined in order to study some interesting phenomena, which will appear in our numerical experiments. The first point is R_M that is related to the minimum of $|S_{11}|^2+|S_{12}|^2$. Therefore, there is a maximum in the radiated power in R_M. The other two points are M_T and m_r, which are respectively related to the maximum of $|S_{12}|^2$ and to the minimum of $|S_{11}|^2$. It is seen that these three points are perfectly aligned nearby 0.58 GHz in this original situation, namely when the strips are $0.464 \cdot \lambda$. In the same figure, the lump is not observed. This basically happens because of the linear scale. Now, the effect of the coupling on the S parameters is studied. To do this, the strips are moved nearer. Results are presented in Fig. 5.4b, where several phenomena can be appreciated. Firstly, it is observed that the level in m_r slightly varies, namely, the reflected power is almost the same. In second place, the level in M_T rises considerably, that is to say, the coupling is increased. With regard to R_M an increment of the level is also observed, thus, the radiated power decreases. It can be noted that the rise of R_M is less significant when the strips are really close. It is also worth mentioning the frequency shifts of R_M, M_T and m_r. It is even observed that these three points are no more located at the same frequency. A slight frequency shift towards left it is seen for m_r. In the case of M_T a more significant rightwards shift happens. In relation to R_M a leftwards displacement is observed. All this can be viewed as an increment of the maximum transmitted power at cost of a diminution of the maximum radiated power, while the minimum of the reflected power remains. Besides, the closer the strips are, the more moved away

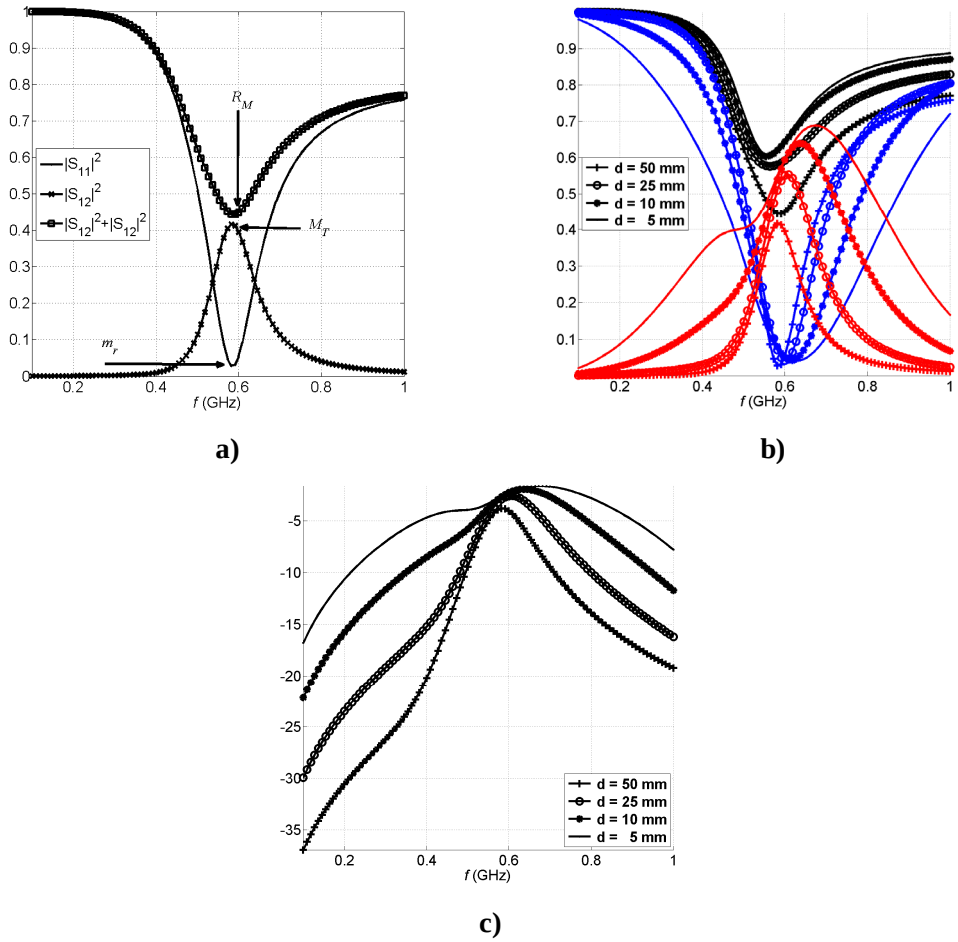

Fig 5.4. *a) Confrontation of $|S_{11}|^2$, $|S_{12}|^2$ and $|S_{11}|^2+|S_{12}|^2$ for coupled strips with L = 240 mm, w = 20 mm and d = 50 mm . b) Variation with d of $|S_{11}|^2$ (blue), $|S_{12}|^2$ (red) and $|S_{11}|^2+|S_{12}|^2$ (black). c) Variation with d of $|S_{12}|$ (dB) to observe the lump in all the cases c).*

the three phenomena are. In Fig. 5.4b the lump in S_{12} is only observed for d = 5 mm. To closely observe this phenomena $|S_{12}|$ in dB is shown in Fig. 5.4c. Here, it can be noted that the lump is present in all the simulations. Moreover, it is observed that this phenomena shifts in frequency towards left.

5.3.2 The Coupled Strips Antenna inside a Cavity

In this subsection the structure shown in Fig 5.3a is shielded with a rectangular cavity of dimensions *a*, *b* and *c* respectively in *x*, *y* and *z*. As previously mentioned, the numerical experiments in this subsection are implemented with a POC MPIE-MoM code which has been developed in the framework of an ESA-ESTEC contract [11] and uses the GFs described in chapter §3. The only difference with regard to the analysis presented in the previous subsection is precisely these GFs. In Fig 5.5a, the resulting S parameters for shielded coupled strips with *L* =

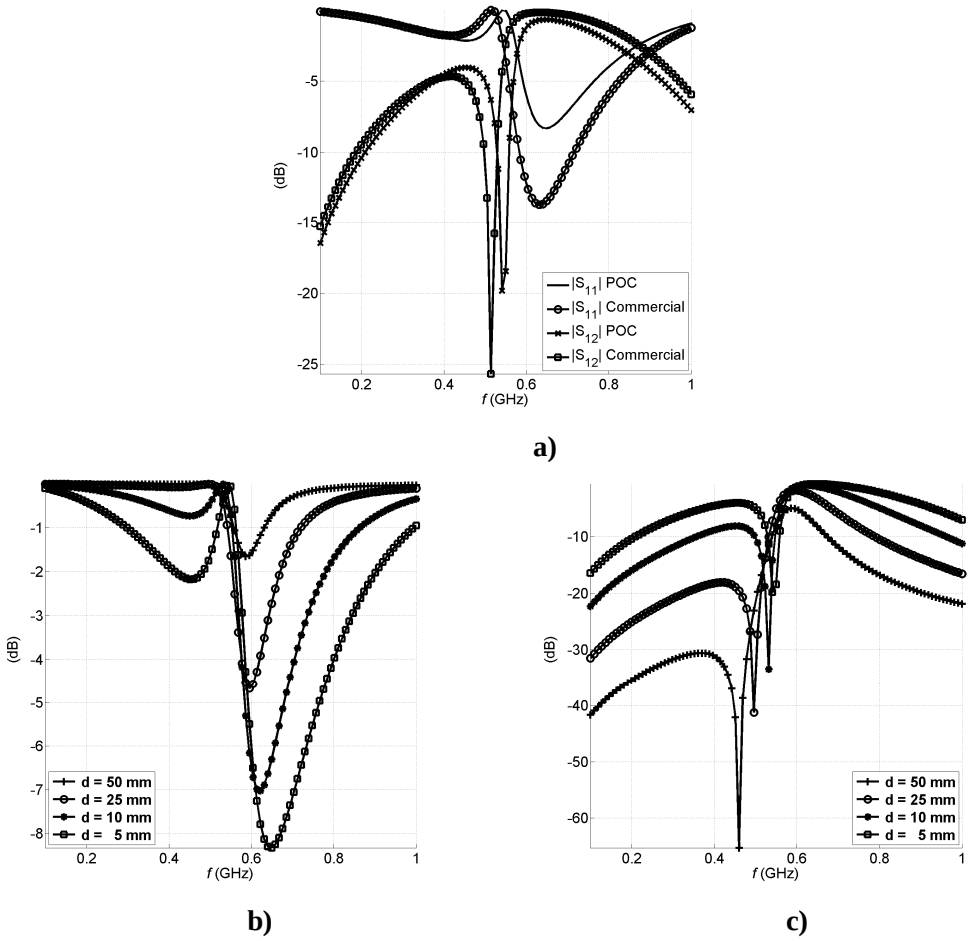

Fig 5.5 *a) Comparison between POC code and HFSS^{TM} for coupled strips with L = 240 mm, w = 20 mm and d = 50 mm within a rectangular cavity with a = 270 mm, b = 150 mm and c = 100mm. b) Variations of $|S_{11}|$ and c) of $|S_{12}|$ with d.*

240 mm, w = 20 mm and d = 50 mm are presented. The strips are inside a cavity of dimension a = 270 mm, b = 150 mm and c = 100mm. The cavity dimensions have been selected in order to have initially the resonance of our free space antenna with all the cavity modes at cut-off. The simulation is implemented in the range 0.1-1 GHz, where no cavity modes are present. Therefore, cavity resonances are not expected in the resulting S-parameters, as noticed in Fig. 5.5a. In this figure, the results of our MPIE-MoM algorithm are compared with HFSS^{TM} Both methods agree qualitatively and recover the same physical phenomena.

Firstly, the effect of the coupling between the strips within a cavity is studied. Namely, the study of §5.3.1 is done again, by simply replacing the free space GF by the cavity GF. The dimensions of the cavity are the same as in Fig. 5.5a. The resulting $|S_{11}|$ and $|S_{12}|$ are respectively shown in Fig. 5.5b and Fig. 5.5c. It is noted in Fig. 5.5b that the structure resonates nearby the same frequencies as in free space. The frequency shift trend observed in free space is also maintained, but now, the maximum of $|S_{12}|$ and the minimum of $|S_{11}|$ happen at the same

frequency. In Fig. 5.5c, it is noticed that a deep transmission zero in $|S_{12}|$ appears at the frequency where a lump was observed in the free space case. This zero keeps also the same shifting trend as in free space. In Fig. 5.5b, full reflection is observed in $|S_{11}|$ at the frequencies where the transmission zero happens in $|S_{12}|$. It is also noticed in Fig. 5.5b and Fig. 5.5c, that the closer are the strips, the better is the coupling.

The second implemented experiment consists of varying the size of the cavity by keeping the enclosed structure unchanged. The size of the strips remains the same and *d* is set to 5 mm. The dimensions of the cavity are obtained from the previous experiment by equally increasing *a*, *b* and *c* by a 0%, 50%, 95% and 175% of the original size. There are no cavity modes in the simulation band for the first enclosure, while in second, third and fourth shields 2, 7 and 16 modes are respectively present. In Fig. 5.6a and Fig. 5.6b the resulting $|S_{11}|$ and $|S_{12}|$ are respectively shown. Here, it is observed that the curves follow the free space response in absence of cavity modes, except in the zone where the lump was. In this area, the full reflection and the transmission zero appear respectively in $|S_{11}|$ and $|S_{12}|$. This happens there where the lump was in free space. The relation between the transmission zero and the lump can be specially noted in Fig. 5.6b between 0.4 and 0.6 GHz. An increase of the cavity size causes a leftwards frequency shift of these phenomena as can be also appreciated in this figure. As expected, it is observed in Fig. 5.6b that when cavity modes are present some of them can be excited, what can change dramatically the free space response as it can be noticed from the dotted curves in Fig. 5.6. It is very difficult to determine which modes are excited in this case. To do this, the shielded structure should be really smaller compared to the cavity size. Studies in this direction can be found in [9]-[10].

The most interesting phenomenon found in this study is the potential relationship between the lump in free space and the transmission zero in the cavity. Although, further research is needed in this topic to set a conclusive reason for this relationship, some guidelines can be set at this moment. As aforementioned, the only difference between free-space and cavity simulations is the utilized GF, thereby it make sense to look at these GFs to try to discern the causes of this relationship. Other possibility is to analyze the MoM matrix, inasmuch as the same conclusions can be derived, since the MoM matrix elements boil simply down to the integral of the GFs. In Fig. 5.7 a column of the MoM matrix is shown both for free space and for the cavity. The simulation frequency is 0.55 GHz, which is nearby the transmission zero. The dimensions of the strips are the same as in the previous experiments and $d = 5$ mm. In this figure it is observed that the imaginary part of the Green function is almost the same in both scenarios. The real part of the Green function is zero inside cavity (it does not appear in Fig. 5.7 because of the logarithmic scale), while in free space is different of zero. Therefore, it can be preliminarily stated that the lump is a phenomenon linked to the Green function real part. In absentia of this part the cavity catalyses this phenomenon putting a transmission zero and this at a frequency where all the unperturbed cavity modes are at cut-off. It is expected that the GFs and the methodology original methodology introduced in this chapter will allow future researchers to set more conclusive reasons.

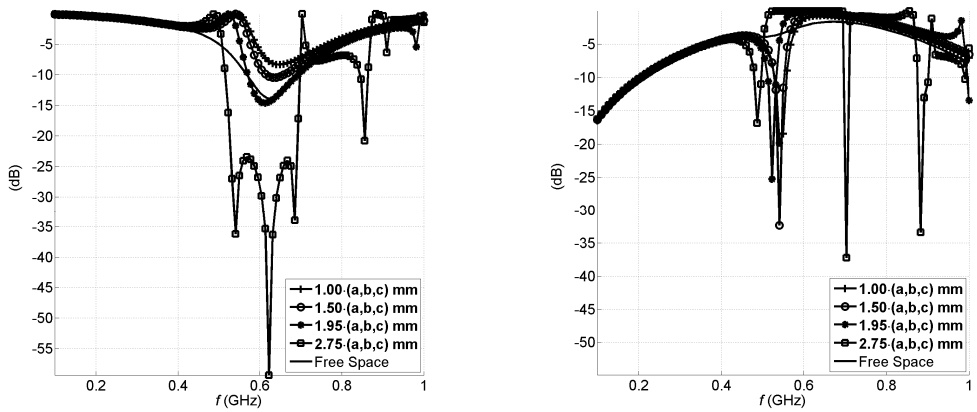

Fig. 5.6 *a) Variation of $|S_{11}|$ and b) $|S_{12}|$ with the size of the cavity. A coupled strips structure with L = 240 mm, w = 20 mm and d = 5 mm is the enclosed structure. The dimensions of the cavity are obtained by equally increasing a = 270 mm, b = 150 mm and c = 100mm by a 0%, 50%, 95% and 175%.*

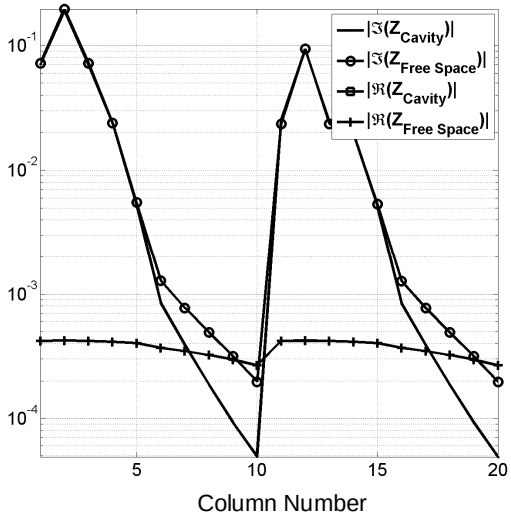

Fig. 5.7 *Plot of a MoM matrix columns both for free space and for a cavity. Two coupled strips, whose dimensions are L = 240 mm, w = 20 mm and d = 5 mm, enclosed in a rectangular cavity with dimension a = 270 mm, b = 150 mm and c = 100mm, are simulated at f = 0.55 GHz nearby the transmission zero.*

Fig. 5.8 *a) Half-Rooftop and b) Broken-Rooftop basis functions.*

5.4 Analysis of Combline Type Shielded Structures

Nowadays, waveguide microwave filters, transitions and multiplexer are key components in the communication payload of satellite systems, where their presence is ubiquitous. They appear in the input front-end, where they usually must achieve low-loss performance and in the transmitter output end, where they must withstand high power levels. In the most commonly encountered situation, where the information is globally sent through a common unique antenna, filters with very sharp frequency behaviors must be used, and combined to create diplexers and multiplexers, allowing the channelization of the information into a series of RF transponders. The ability to produce very specific frequency transfer functions stabilized in frequency and satisfying rather astringent requirements in matching, isolation and rejection are therefore of paramount relevance

It is well-known that combline filters can match these specifications. These filters consist essentially of metallic cavities whose access ports are rectangular waveguides or circular coaxial waveguides, and they have typically metallic and/or dielectric obstacles inside. Actually, it exist a continuous effort to create and improve software capable of analyzing and optimizing these kind of structures, trying to avoid the problems that the actual tools have, like for example the incapacity of modeling the effect of specific coaxial-post configurations or of achieving the required delicate balance between geometrical flexibility and accuracy in frequency.

As aforesaid, this section is devoted to exhibit several of the obtained results with a POC software, which has been developed in the framework of the research activities associated to the ESA-ESTEC project [11]. The software is envisioned to show the capabilities of a MPIE-MOM strategy to match the above-mentioned specifications in terms of flexibility and accuracy when simulating combline type shielded structures. This POC code attains this objective by just using the theory and results obtained in §3 and §4 to simulate 3D PEC structures of rectangular section (this sort of geometry has been also used by other authors [12]-[14]), which are housed by a PEC rectangular cavity, which on its turn, is excited via coaxial techniques. The simulation of enclosed dielectric objects or waveguide excitations will require the computation of additional GFs, which are not described in this work. The coaxial excitation is modeled by using δ-gap generators (references in §2), whereas all the equivalent electric currents on the enclosed structures are expanded via rooftop basis functions defined over rectangular cells (§4.2). Two special rooftop types are also utilized: on the one hand the connections with the PEC shield are modeled via half-

rooftop basis functions (Fig. 5.8a); on the other hand, broken-rooftops (Fig. 5.8b) are used to model the current flow through the edges of the enclosed structure. The flexibility of the MPIE-MoM strategy is proven through the simulation of the most common shielded structures and combinations of them as well as the most frequently used excitation techniques.

As previously introduced, the utilized GFs to describe the EM behavior within the empty cavity are expressed as the sum of a dynamic part and a static part. These parts are respectively represented by a 2D modal expansion and by a 3D image series, as shown in §3. As also described in that chapter, this technique allows perfectly recovering both the frequency and spatial behavior of the GF. The reader is reminded that a good representation of the spatial behavior is crucial, especially when the gap either between the shielded structures or between the enclosed items and the cavity walls is small. In these cases, a very good model of the static type GF singularity is required, since this is the quantitative dominant part of the phenomena to be modeled. This good model is achieved by inferring the GF static part from the static free space GF as a 3D image expansion, insomuch as the mathematical expression of the singularity appears explicitly in the GF formulation. In the previous section, it has been shown, through the analysis of a very simple system, that all the physical phenomena, which are within a strong static coupling scenario, are properly recovered by using image theory to compute the GF static part. On the other hand, a modal expansion of the GF dynamic part helps to properly model both the interactions between far shielded structures and the sharp cavity resonances. The accurate computation of these GFs together with the usage of the analytic expressions derived in §4.5 to integrate the GF static part result in a MPIE-MoM POC code, which correctly detects the cavity resonances and moreover, properly predicts the resonant frequency shift due to the coupling between the cavities and the enclosed structures. Noticeably, the GF dynamic part should be also analytically integrated to compute the MoM matrix elements, but this represents a minor problem, since these integrals only involve trigonometric and hyperbolic functions, whose analytical integration is straightforward.

This section is organized in two parts. Firstly, several numerical experiments involving the most common 3D structures utilized in combline filters, namely, single posts, tuning posts and mushrooms are presented. Also in this part, the performance of the MPIE-MoM strategy is shown when using either a magnetic or dumbbell excitation techniques are used to couple with the enclosed item. This subsection will be concluded with results related to a combination of some the previous structures and excitation techniques. Secondly, a filter with two resonators coupled by using a full opening window will be analyzed. Here, the performance in the case of strong and weak coupling between shielded structures will be studied in several scenarios. The accuracy of the results is ascertained in all the presented numerical experiments by comparing with the results provided by the commercial software HFSS^{TM}, which is based on a finite elements method (FEM) approach.

5.4.1 Single Combline Resonator Study

Typically, a filter is built through the combination of several resonators. In the case of combline filters, these resonators can be built either by means of planar technology [15]-[16] or by loading cavities with 3D structures [17]-[25]. Here, the last scenario will be analyzed through

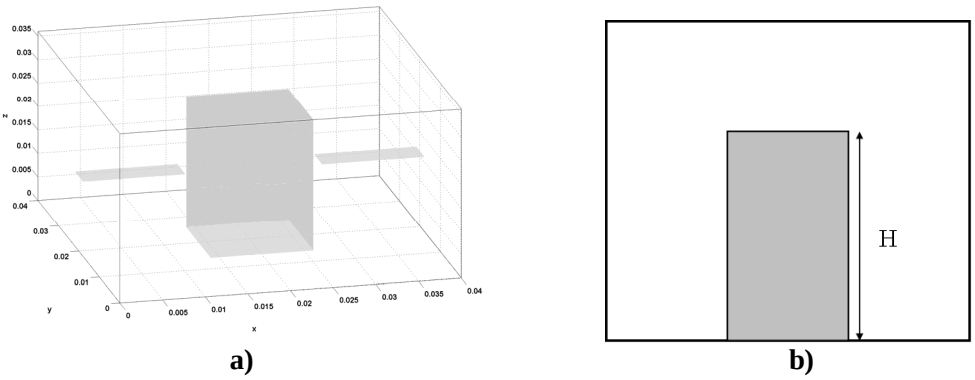

Fig. 5.9 *a) Single shielded post and b) varying quantities for the numerical experiments.*

several parametric studies involving the most common shielded PEC structures in these resonators. All the presented numerical experiments are performed by using a PEC rectangular cavity, whose dimensions in *x*, *y* and *z* are respectively set to 40 mm, 40 mm and 36 mm. As aforesaid, coaxial techniques are only considered to excite the cavity. This external excitation will couple the fields within the enclosed volume through the use of probes, which will be modeled via two strips of 12 mm in *x* and 4 mm in *y*, that on its turn are centered at the cavity walls. As aforesaid, the coaxial excitation is modeled via a δ-gap tension generator, which is defined along the edge of the strips touching the cavity wall. Two ports are considered, so that the resulting biport's S_{11} and S_{12} will be presented. These S parameters are obtained via the utilization of the expressions in [26], which infer the S parameters from the biport admittance matrix, which is calculated from the induced currents on the half rooftops modeling the connection between the strips and the cavity walls.

The simplest 3D combline resonator consists of a single post shielded by a cavity as shown in Fig. 5.9a, where it can be also appreciated the previously described excitation probes. This structure behaves as a conventional coaxial resonator [24]. The height of the post is strongly linked to the resonant frequency of the system [21], so that this height is varied to reduce or to increase the gap between the post and the uppermost lid of the cavity. The capacitive coupling appearing in this gap makes the resonant frequency shift, thereby the smaller the gap, the smaller the resonant frequency is as well [21], as in conventional coaxial resonator happens. Now, a parametric study addressed to show this phenomenon is presented. As in the study presented in [12] or in the practical realization shown in [13], a post of rectangular section is considered to implement this numerical experiment. In Fig. 5.9b, the varying parameters within the experiment, which are the height (H) of the post and consequently the gap between the post and the top cavity wall, are shown. The resulting $|S_{11}|$ are exhibited in Fig. 5.10, respectively for H=20 mm (Fig. 5.10a), H=24 mm (Fig. 5.10b), H=28 mm (Fig. 5.10c) and H=32 mm (Fig. 5.10d), which respectively implies gaps between the post and the uppermost lid of the cavity of 16mm, 12mm, 8mm and 4mm. The related $|S_{12}|$ are shown in Fig. 5.11 also for H=20 mm (Fig. 5.11a), H=24 mm (Fig. 5.11b), H=28 mm (Fig. 5.11c) and H=32 mm (Fig. 5.11d). In this figures and more clearly in Fig. 5.12a for $|S_{11}|$ and in 5.12b for $|S_{12}|$, it can be clearly appraised that the basic underlying physical phenomena is properly recovered by the MPIE-MoM POC code, since the higher is the

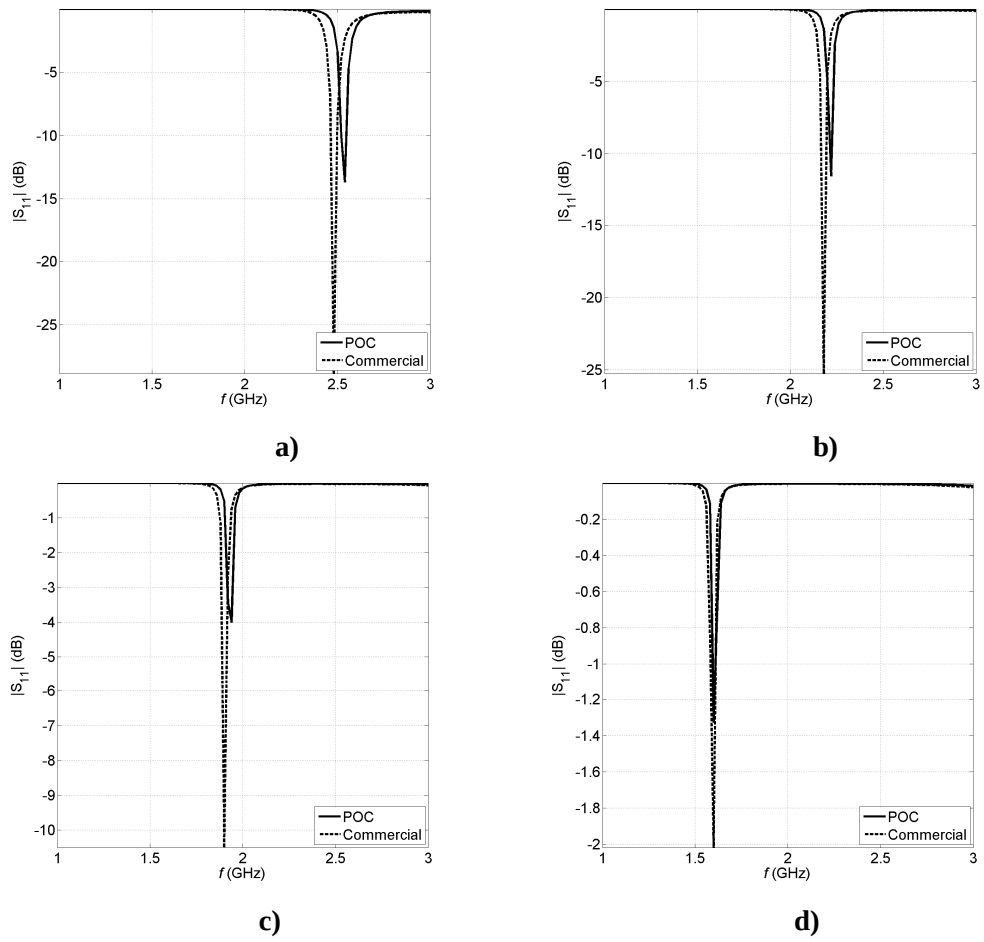

Fig 5.10 *Resulting $|S_{11}|$ with both HFSS^{TM} and the POC code for a) H=20mm, b) H=24mm, c) H=28mm and d) H=32mm.*

post the smaller is the resonant frequency. The downwards evolution of this frequency with the post height H is explicitly shown in Fig. 5.13a. Also in Fig. 10 and in Fig. 11, it can be appreciated that the results produced by the POC software exhibit a very good agreement with the commercial tool HFSS^{TM}. The accuracy of the MPIE-MoM approach is evaluated by computing the frequency deviation Δf at the resonance frequency between two softwares as

$$\Delta f = \frac{|f_2 - f_1|}{f_2 + f_1}, \tag{5.6}$$

where f_1 and f_2 are respectively the resonance frequencies produced by the commercial software and the POC code. The values of (5.6) for the current experiments (H=20 mm, 24mm, 28 mm and 32 mm) is presented in Fig. 13b, where it can be seen that Δf is always smaller than 1.2%, which can be considered satisfactory.

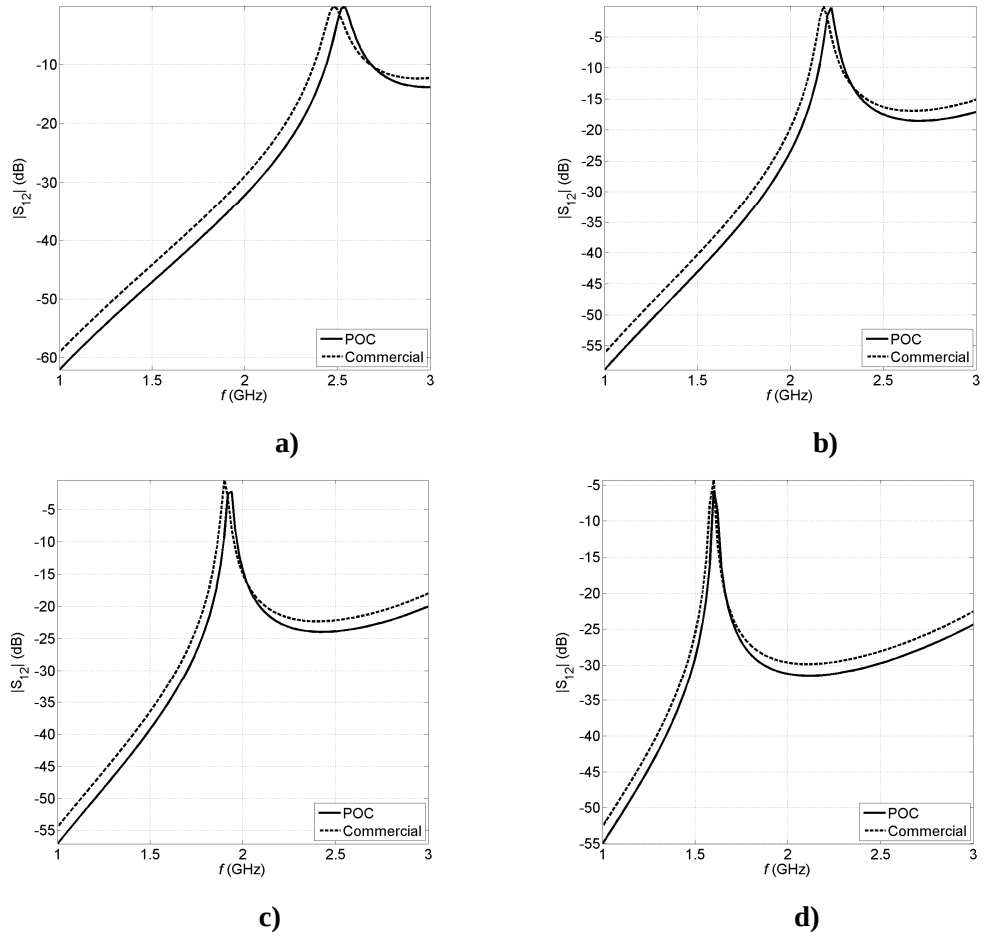

Fig 5.11 *Resulting $|S_{12}|$ with both HFSS^{TM} and the POC code for a) H=20mm, b) H=24mm, c) H=28mm and d) H=32mm.*

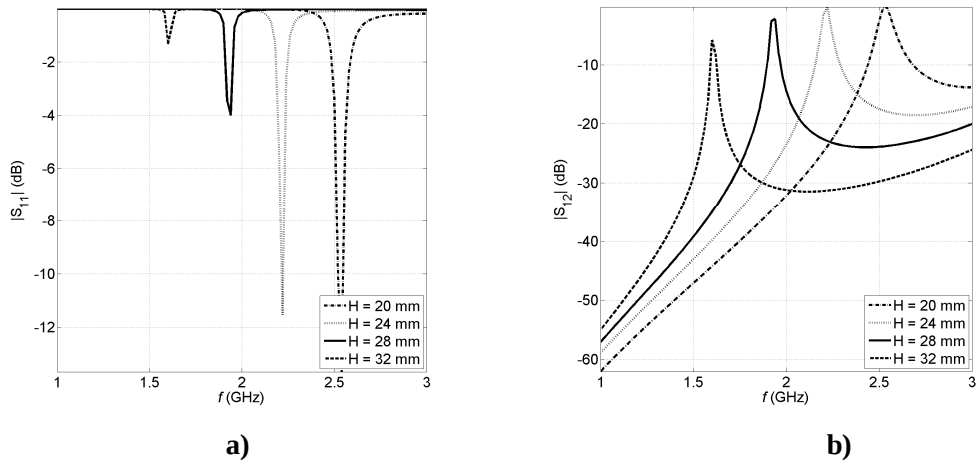

Fig. 5.12 *a) $|S_{11}|$ and b) $|S_{12}|$ variation with the post height H.*

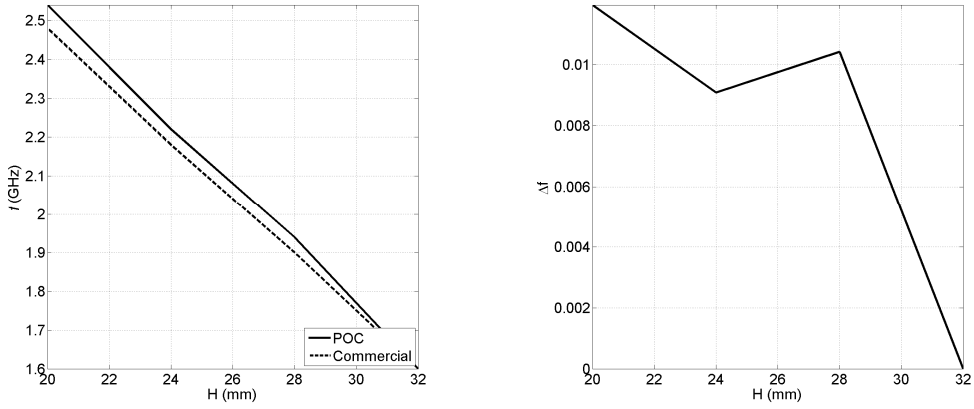

a) **b)**

Fig. 5.13 *a) Resonance frequency evolution with H and b) Δf, also with H, between the MPIE-MoM approach and HFSS^{TM} at this resonance frequency.*

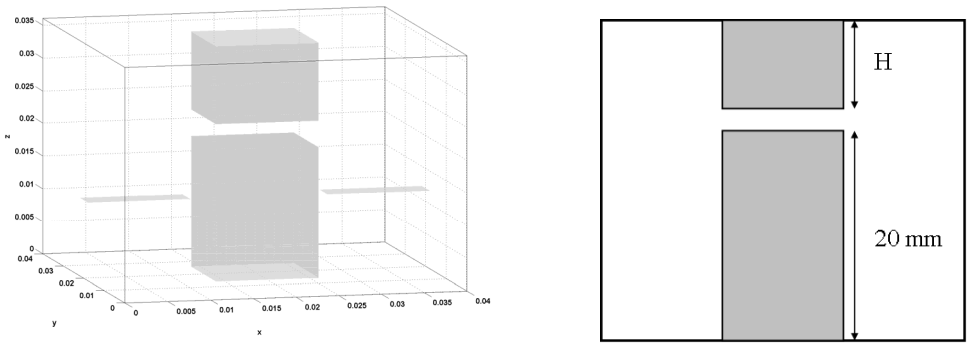

a) **b)**

Fig. 5.14 *a) Two shielded posts and b) varying quantities for the numerical experiments.*

Another possibility to build a combline coaxial-like resonator requires the usage of two aligned post [17] as shown in Fig. 5.14a. One post is fixed, whereas the second one is moveable post in order to change the gap between both posts. The capacity appearing in this gap is used as before to tune the resonator, so that an increment of this capacity makes also the resonant frequency shift downwards. This fact is illustrated through a numerical experiment in the same direction as the previous one. A fixed post of the same section as the post in Fig. 5.9 but with the height set to 20 mm, and a moveable post or tuning post with also the same rectangular section as the fixed one, are used. A cut of the geometry under study is shown in Fig. 5.14b. The heights of the second post are set to H = 4mm, 8mm and 12 mm, so that the gap between two post are respectively 12 mm, 8 mm and 4 mm. Notice also in Fig 5.14a, that the probe excitation is kept. The obtained $|S_{11}|$ for the aforesaid values of H are respectively shown in Fig. 5.15a, Fig. 5.15b and Fig. 5.15c, while the resulting $|S_{12}|$ are also respectively exhibit in Fig. 5.16a, Fig. 5.16b and Fig. 5.16c. As before, it can be appreciated in these figures that a very good agreement between POC and commercial software is obtained. In Fig. 5.17a and Fig5.17b respectively for $|S_{11}|$ and $|S_{12}|$, it can be clearly seen that the fundamentals of the physical phenomenon are correctly

recovered by the POC code. Namely, there is frequency shift of the resonating frequency downwards when the capacity between posts is increased, as it was expected. Notice in these figures, that the situation, in which there is no tuning post (Fig 5.10a and Fig. 5.11a) has been also represented, which has been done to show that the gap between posts has to be considerably diminished to produce a significant resonance shift with regard to the scenario without post. This can be explicitly appraised Fig. 5.18a, where evolution of the resonance with the gap size is represented. As explained in [17], the need of such small gap limits the tunability of the resonator, what can be solved through the usage of a conductor post insert reentrant resonator. Although, this sort of resonators are not object of this study, interested readers can consult [17] for further information. Besides, it has also to be remarked, that unlike the previous experiment (Fig. 5.13a), now the resonance shift is not lineal. Finally in Fig. 5.18b, the frequency deviation at the resonance (5.6) is presented. Here, Δf is always smaller than 1.3% in all the experiments, which can be considered very good in terms of accuracy, as well.

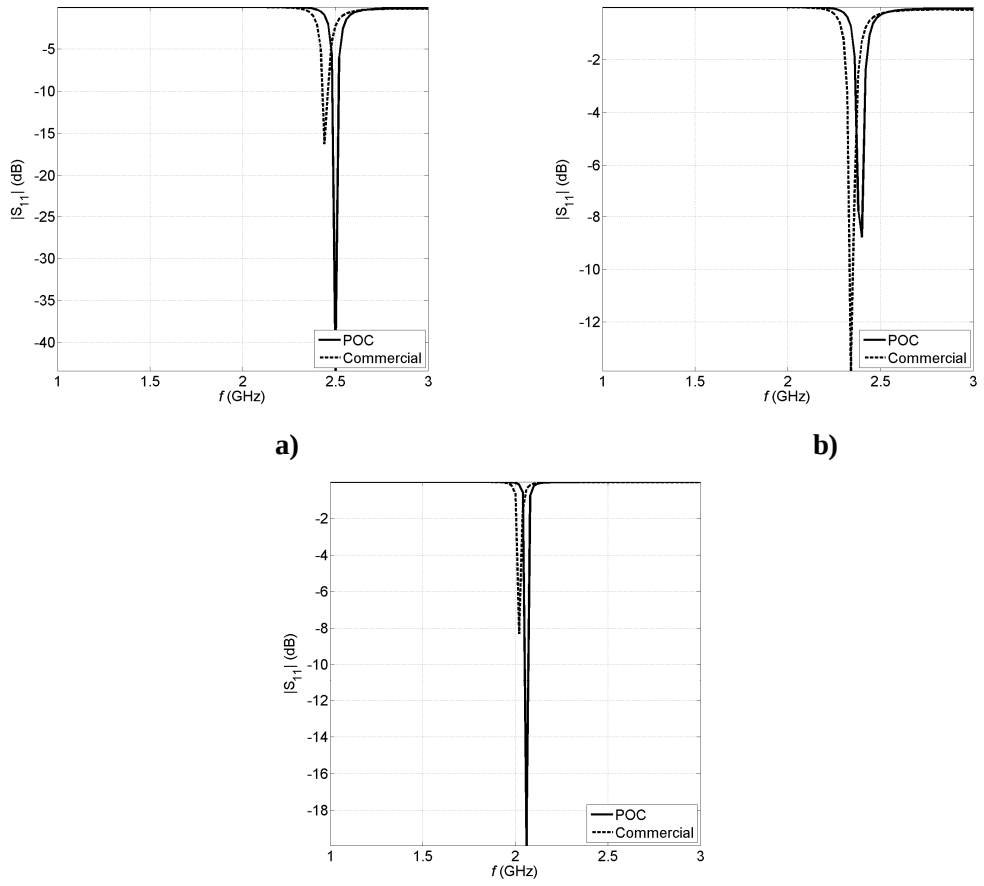

Fig 5.15 *a) Resulting $|S_{11}|$ with both HFSS^{TM} and the POC code for tuning post height H=4 mm, b) H=8 mm, c) H=12mm.*

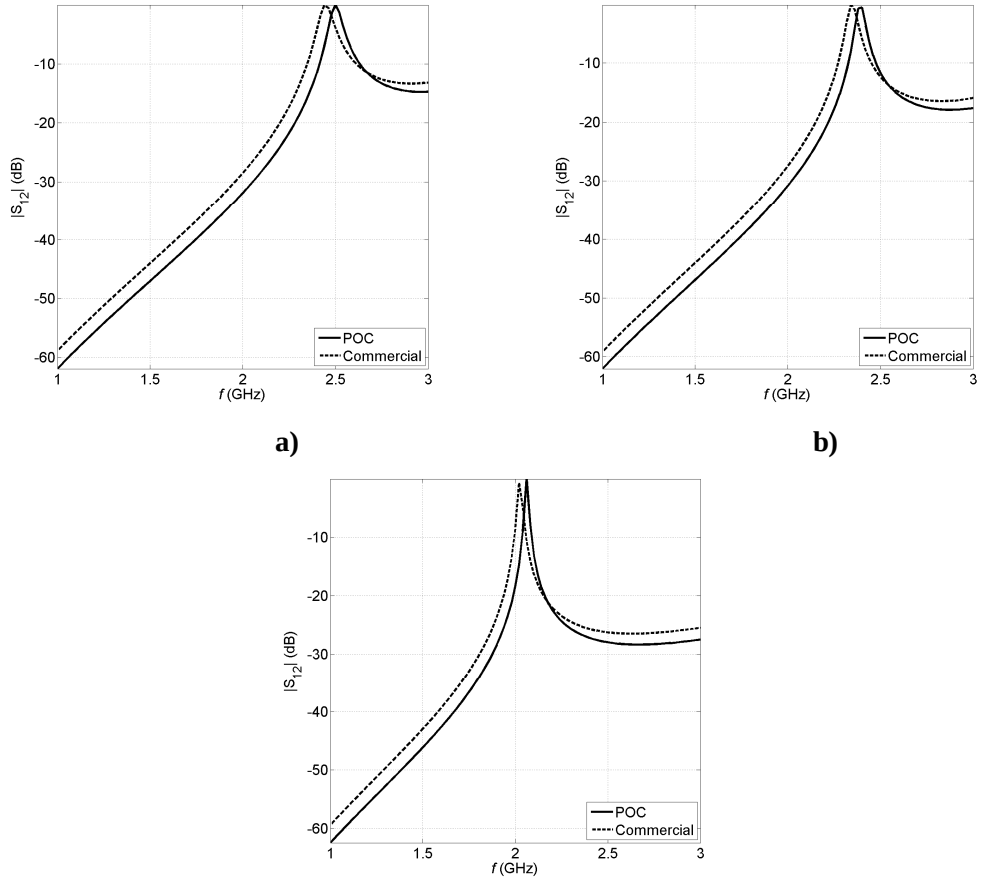

Fig 5.16 *Resulting $|S_{12}|$ with both HFSS^{TM} and the POC code for tuning post height a) H=4 mm, b) H=8 mm, c) H=12mm.*

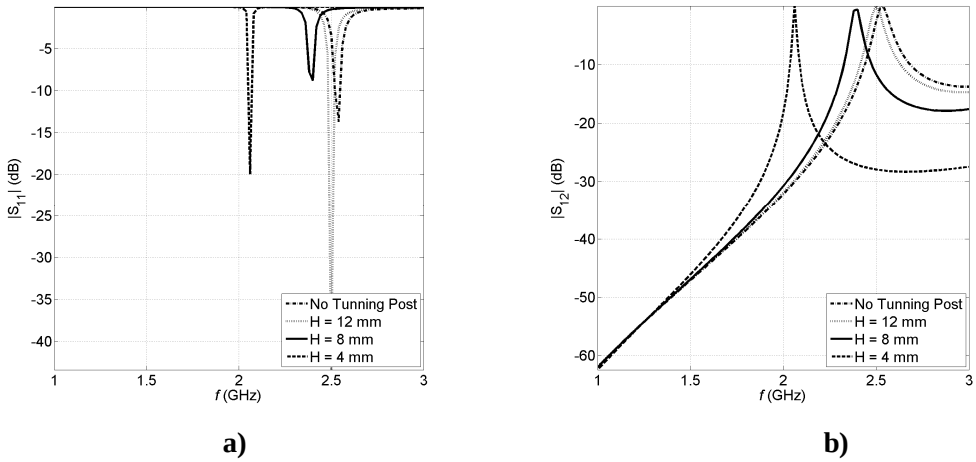

Fig. 5.17 *a) $|S_{11}|$ and b) $|S_{12}|$ variation with the tuning post height H.*

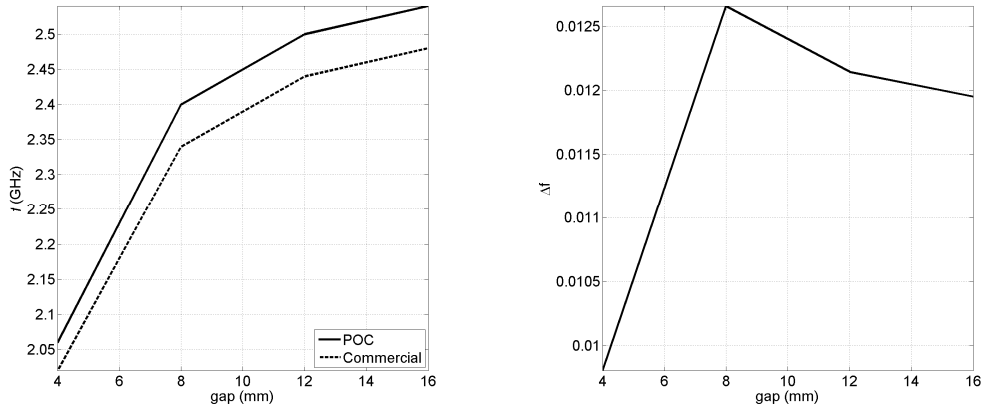

a) **b)**

Fig. 5.18 *a) Resonance frequency evolution with the gap between post and b) ∆f, also with this gap, between the MPIE-MoM approach and HFSS™ at this resonance frequency.*

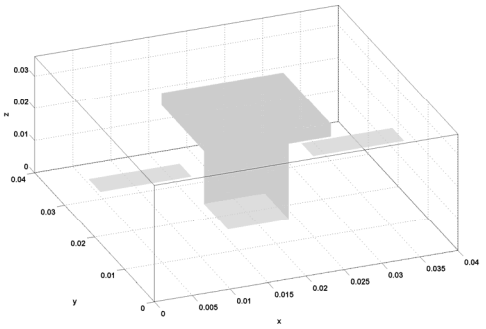

a)

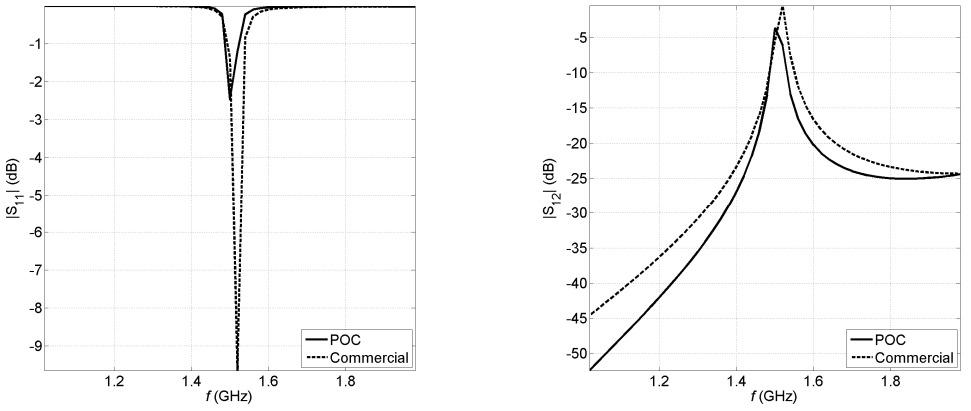

b) **c)**

Fig 5.19 *a) Cavity housing a mushroom. Comparison between the resulting b) |S11| and c) |S12| provided by HFSS and the POC code.*

The last structure under study, which typically appears in 3D combline coaxial-like resonators, is the mushroom [24]. As shown in Fig. 5.19a for a mushroom of rectangular section, this structure consists of a post, above which it is placed the mushroom's cap, whose perimeter is bigger than the post one. The greater area of the uppermost cap's surface allows enhancing the capacitive effects with the cavity top lid, or in general, with any other shielded structure, so that more significant resonance frequency shifts can be produced. At this point, it is only presented a numerical experiment involving this structure, since later in this subsection, the mushroom will be used a more complete parametric study. The dimensions of the simulated structure shown in Fig. 5.19a are 8 mm x 8 mm x 16 mm for the post, whereas the cap measures 16 mm x 16 mm x 4 mm. As also appreciated in this figure, the cavity is still excited through two probes, which are located in the same position and have the same dimensions as in the previous experiments. The resulting S parameters are presented in Fig 5.19b ($|S_{11}|$) and Fig. 5.19c ($|S_{12}|$), where it can be appraised the good agreement between commercial and POC software (Δf=0.068%). As expected, it can be also observed in these figures that the system is resonating at a considerably low frequency (1.55 GHz), even if the gap between the mushroom and the uppermost cavity wall is big (20 mm). In the single post case (Fig. 5.9 - Fig. 5.11), it is proven that this gap has to be very narrow (4 mm) to produce a similar resonance frequency. As aforesaid, this is because the bigger area of the uppermost surface of the mushroom helps to obtain similar capacitive effects with big gaps to the ones produced with posts, whose gap with the cavity top wall is very small.

Until this moment, the shown coaxial-like resonators have been exited via the usage of simple probes. Now, two techniques, which are also commonly used when utilizing a coaxial to insert energy in the resonator, will be studied. The first technique consists of bending the probe and connecting it to ground, that's to say to the cavity wall ([18] and [23]). Therefore, a loop, which aims to excite the magnetic field within the resonator [23], is created. For this reason, this technique is also known as *magnetic coupling*. There are several ways of creating this loop, for instance, the probe can be bended and attached to the same wall [23], in which the coaxial port is placed, or simply, an elbow of 90° is created from the probe, so that its termination is directly connected to the cavity bottom wall. Here, the effects on the combline resonator performance produced by this last strategy will be studied, by simply connecting to ground one of the probes of the resonators exhibit in Fig. 5.9a and 5.14a. The new geometries under study are shown in Fig. 5.20a and 5.20b which respectively corresponds to the 28 mm height single post resonator and to the two post resonator having a gap of 8 mm between posts. The resulting $|S_{11}|$ and $|S_{12}|$ for the structure depicted in Fig. 5.20a are respectively shown in Fig. 5.20b and Fig. 5.20d, while in Fig. 5.20c and Fig. 5.20e, the $|S_{11}|$ and $|S_{12}|$, corresponding to the geometry in Fig.5.20b, are exhibit. As it can be appreciated in these figures a very good agreement between POC and commercial software is also obtained for this sort of excitation. Specifically, the attained frequency deviations Δf (5.6) are 0.5% and 0.8% respectively for the single post and the double post resonators. The physical effects of this type of coupling are deduced for Fig. 5.21, where the scenarios related to the single probe excitation and the ground connection are compared. In Fig. 5.21a and Fig. 5.21c, the comparison between the $|S_{11}|$ and the $|S_{12}|$ is respectively exhibit in the single post case, whereas the same comparison is shown in Fig. 5.21b and Fig. 5.21d for the double post resonator. It can be inferred by inspecting these figures that the effects produced by

the ground connected probe boil simply down to a shift of the resonant frequency upwards together with an increase of the resonator's bandwidth.

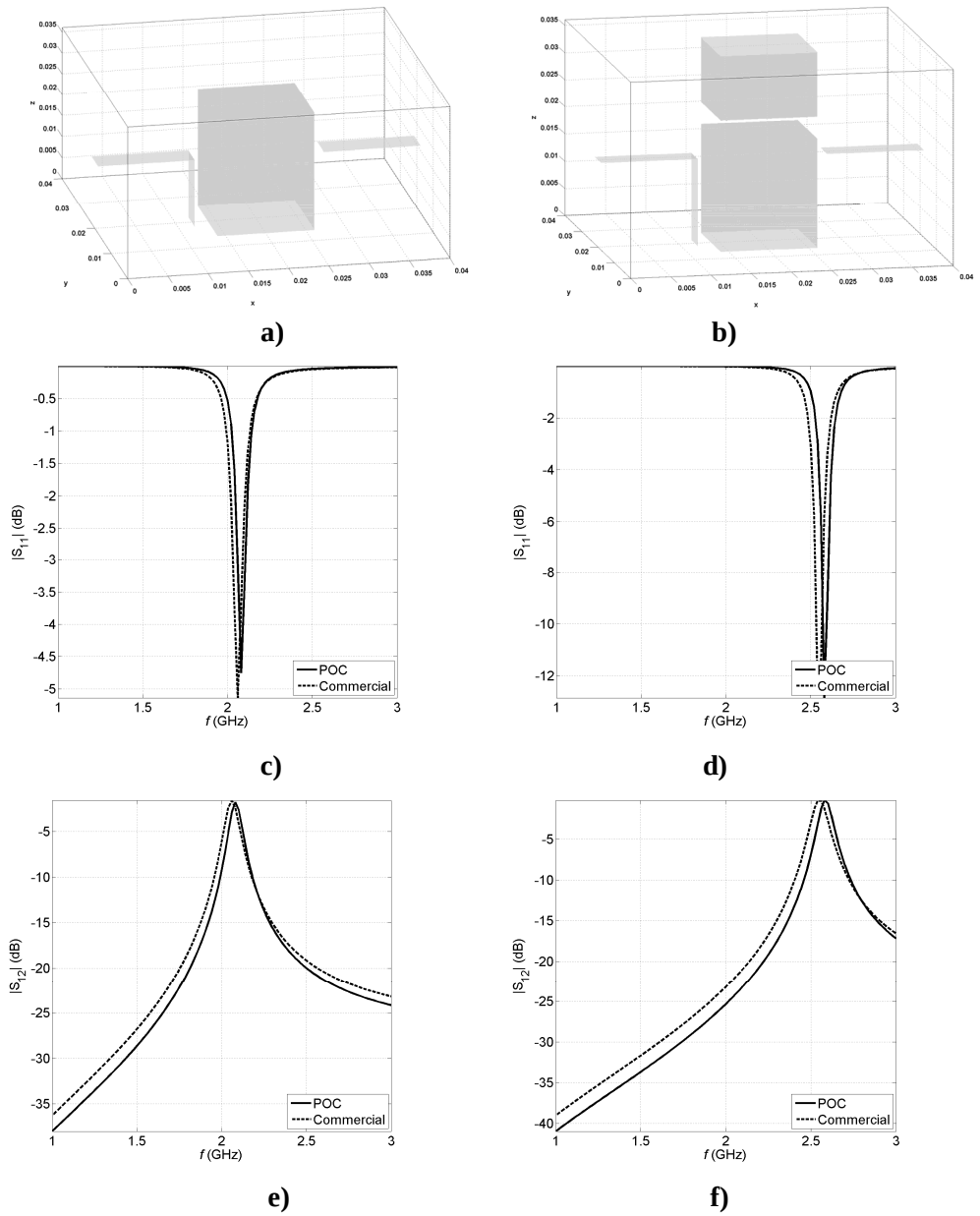

Fig 5.20 *a) Single post resonator and b) double post resonator excited via a ground connected probe. $|S_{11}|$ Comparison between HFSS^{TM} and the POC code for c) the single post scenario and d) the double post situation. Same comparison for $|S_{12}|$ e) (single post) and f) (double post).*

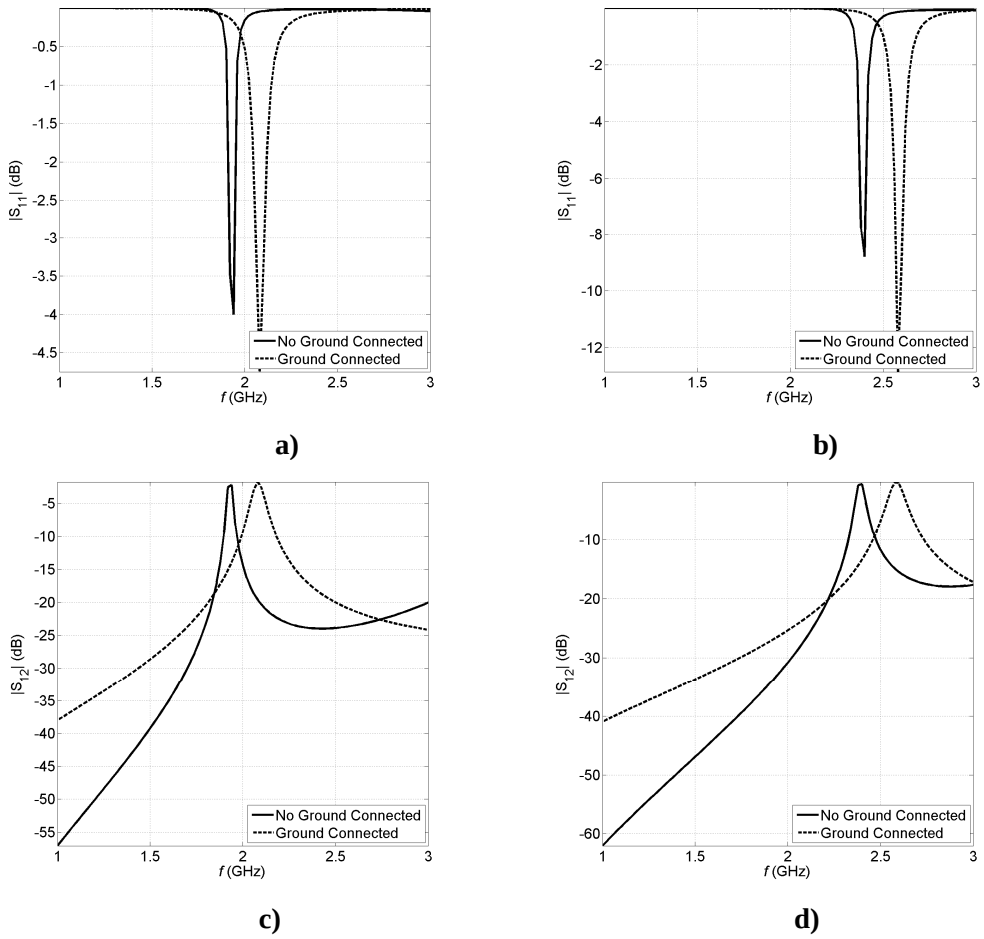

Fig 5.21 *$|S_{11}|$ responses comparison between the non ground connected probe and the ground connected probe excitation for a) the single post resonator and b) double post resonator. Same comparison for $|S_{12}|$ in the case of c) single post and d) double post.*

The second coaxial excitation technique under study, which is also commonly used within the combline resonator framework, dumbbell coupling ([12] and [24]). This technique consists basically of connecting a plate to an excitation probe, so strong capacitive phenomena appear between this system and the shielded structure. This type of excitation is also known as *capacitive coupling*. In Fig. 5.22a, a resonator, which is excited via this strategy and is loaded with a post of 28 mm height (the same post used in previous experiments), is shown. The dumbbell has been performed by connecting a plate, which measures 12 mm along *x* and 8 mm along *y*, to a probe of 4 mm. The resulting S parameters for this configuration are shown in Fig. 5.22b ($|S_{11}|$) and Fig. 5.22c ($|S_{12}|$), where it can be appraised that the results provided by the POC code agree very well with the ones obtained with HFSS^{TM}. The effects of this type of excitation on the resonator performance are studied through a parametric study, which consists of computing the resonator's S parameters for different lengths (l) of the probe. These S parameters are respectively presented in Fig. 5.23b ($|S_{11}|$) and Fig. 5.23c ($|S_{12}|$). In these figures, it can be firstly observed that, for a small length of the probe (l = 4 mm), the same response as in the case of a single probe of 12 mm

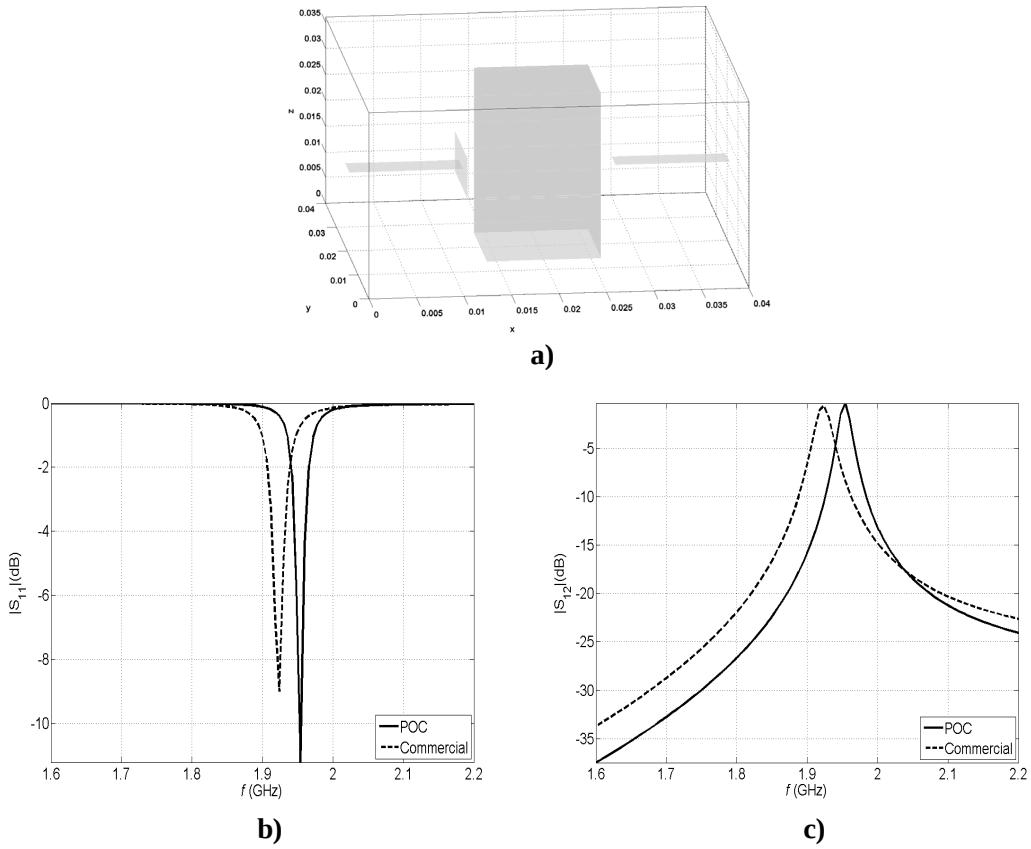

Fig 5.22 *a) Single post resonator excited via a dumbbell technique. b) Resulting $|S_{11}|$ and c) $|S_{12}|$ for resonator excited via a dumbbell technique, measuring the probe 4 mm and the plate 12 mm x 8 mm. In both b) and c), the results are compared with HFSS™.*

length (Fig. 5.10c and Fig. 5.11c respectively for $|S_{11}|$ and $|S_{12}|$) is almost obtained. Namely, the dumbbell allows the usage of smaller probes, inasmuch as the appearing capacitive phenomena produce the same resonator's response as with deep penetrating probes. Secondly, if the probe length is made progressively bigger, so that the gap between the dumbbell's plate and the post is smaller, then the performance of the resonator can be totally lost.

The final numerical experiment, which is presented in this section within the framework of single combline resonator, involves several of the structures and techniques previously studied. Hence, it can be considered a definitive test to judge the fitness of our approach and its good matching to the specifications initially defined in this research project. The geometry associated to this experiment is presented in Fig. 5.24, where it can be observed a coaxial-like resonator, which is loaded with a mushroom and a tuning post and is excited via a ground connected probe through one of its ports. The dimensions of the mushroom are the same as the one exhibit in Fig. 5.19a, whereas the post measures 12 mm along both *x* and *y*. The bended probe has also the same dimensions as the one in Fig. 5.19a and Fig. 5.19b. In the first tackled scenario the mushroom is simulated in absence of post. The S parameters related to this situation are presented in Fig. 5.25a ($|S_{11}|$) and in Fig. 5.25b $|S_{12}|$. In Fig. 5.25c and Fig. 5.25d, the resulting $|S_{11}|$ and $|S_{12}|$ after adding a tuning post of 4 mm height to the previous scenario, are respectively exhibit. Finally, the S

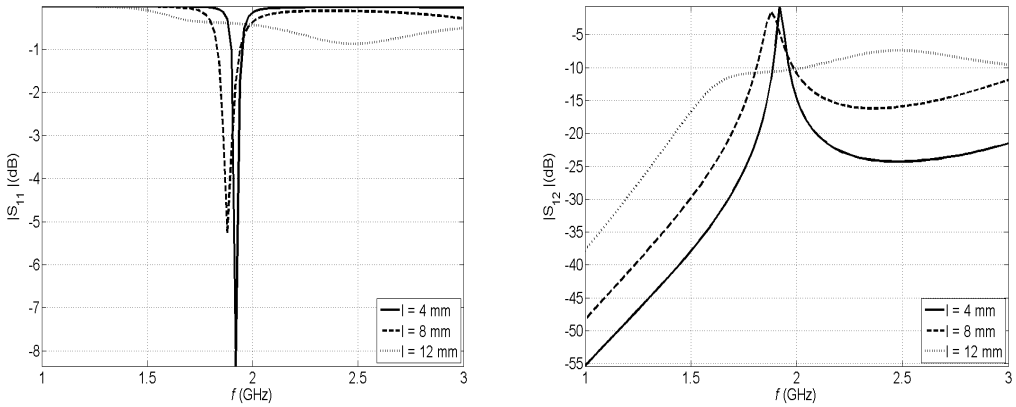

a) **b)**

Fig. 5.23 *Resulting a) $|S_{11}|$ and b) $|S_{12}|$ for several lengths of dumbbell's probe.*

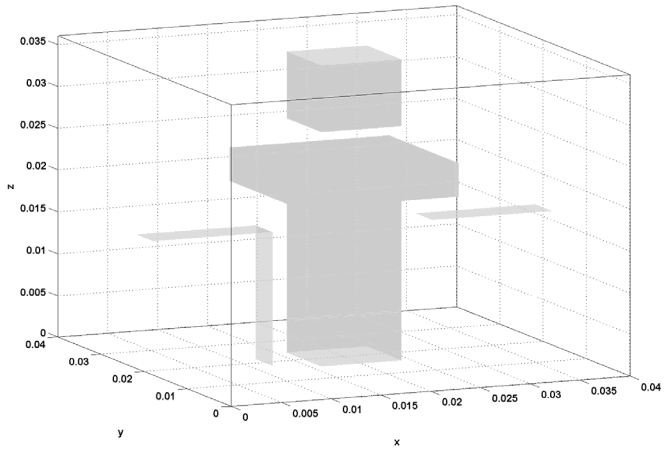

Fig. 5.24 *Resonator loaded with a mushroom, a tuning post and excited through a ground connected probe in one of its ports.*

parameters for a tuning post, which height is of 8 mm, are presented in Fig. 5.25e ($|S_{11}|$) and Fig. 5.25f ($|S_{12}|$). The obtained frequency deviations Δf (5.6) between the POC and commercial software are 0.65%, 0.66% and 1.35% for the scenarios respectively related to absence of tuning post, presence of 4 mm and 8 mm height tuning posts, which is very good in terms of accuracy. Besides, it can be easily appraised from direct inspection of Fig. 5.26a for $|S_{11}|$ and in Fig. 5.26a for $|S_{12}|$ that the physical behavior is properly recovered. The addition of ground connected probe represents an increment of the resonator bandwidth and a upwards shift of the resonant frequency with regard to situation exhibited in Fig. 5.19a, where a simple probe is used to excite the resonator. On the other hand, if a small tuning post is added then a slight downwards shift of the resonance is produced. This shift is more significant when the tuning post is made bigger, since the capacitive effects in the smaller gap appearing between post and mushroom are also bigger.

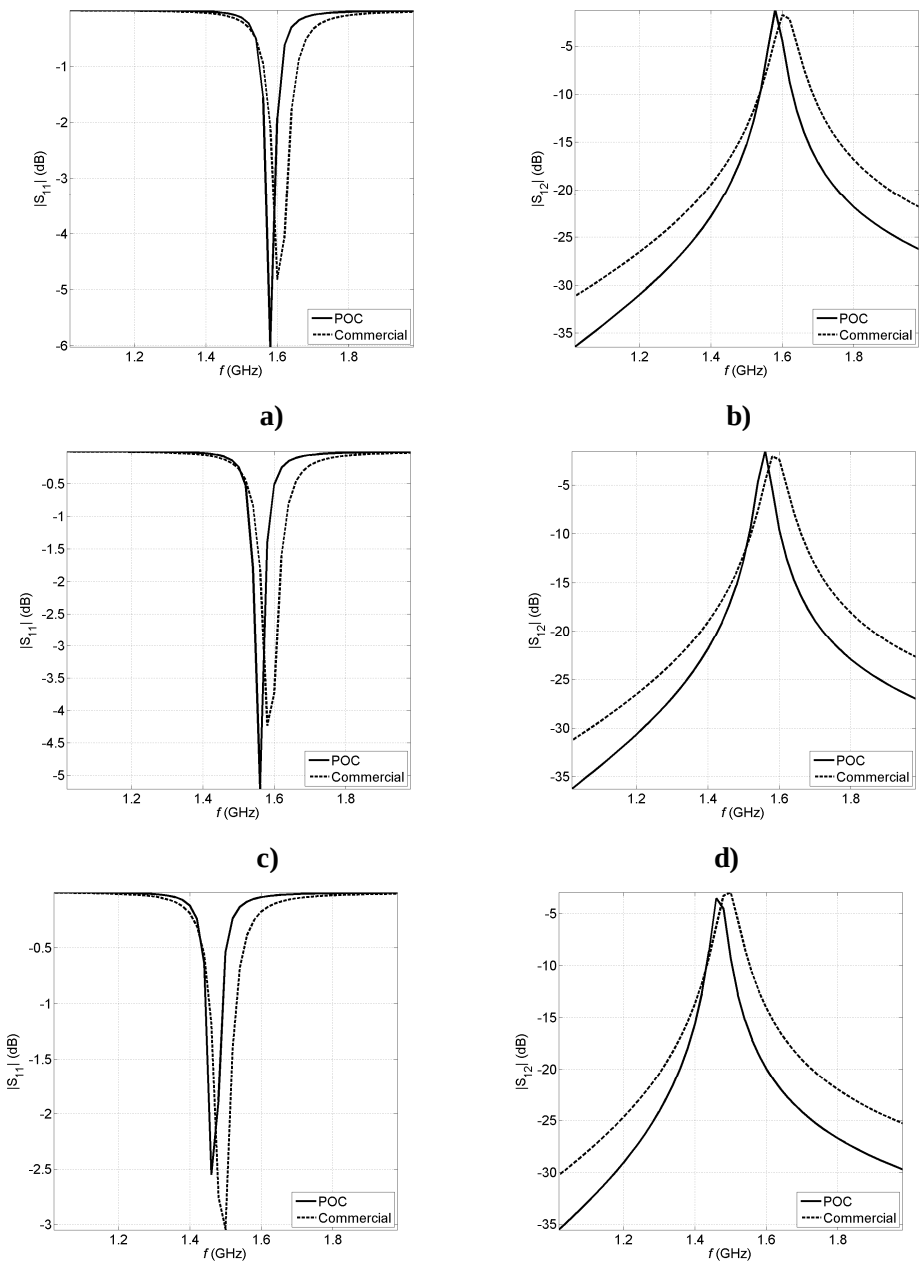

Fig 5.25 *Comparison between the S parameters provided by both the POC code and HFSS™ for: a) $|S_{11}|$ and b) $|S_{12}|$ associated to the single mushroom without tuning post; c) $|S_{11}|$ and d) $|S_{12}|$ linked to the mushroom with a 4 mm height tuning post; e) $|S_{11}|$ and f) $|S_{12}|$ related to the mushroom with a 8 mm height tuning post.*

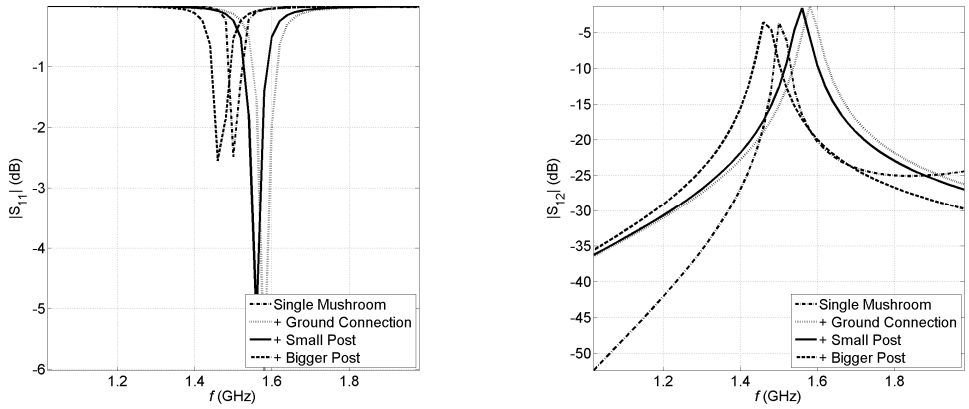

a) **b)**

Fig 5.26 *Evolution of a) $|S_{11}|$ and b) $|S_{12}|$ from the situation exhibit in Fig. 5.19a (resonator loaded with a mushroom and excited via two probes) to the scenario shown in Fig. 5.24, which is related to a resonator loaded with a mushroom and a tuning post of 8 mm height (Bigger Post). The intermediate steps consist of connecting one probe to ground (Ground Connection) and adding a small tuning post (Small Post).*

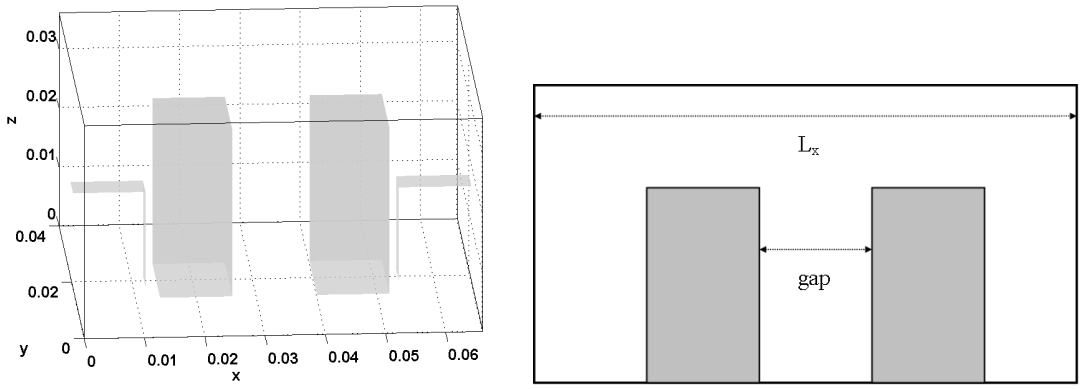

a) **b)**

Fig. 5.27 *a) Two post combline filter under study and b) varying quantities in the parametric study.*

5.4.2 Combline Filter Study

In this subsection, two parametric studies, which involve two poles combline filters, are presented. The filters are implemented via two coaxial like resonator, which uses a single post of rectangular section, that measure 12 mm x 12 mm x 28 mm. The coupling between these resonators is done through a full opening window, so that the whole filter can be considered as a single cavity enclosing two posts. Therefore as in the previous subsection, only the GFs presented in §3, which relate electric currents and electric fields, are needed to perform the analysis.

The geometry associated to the first parametric study is presented Fig. 5.27a, where it can be seen that the two ports of the filter use ground connected probes as excitation technique. The study consists of analyzing the effects in the S parameters when increasing the coupling between

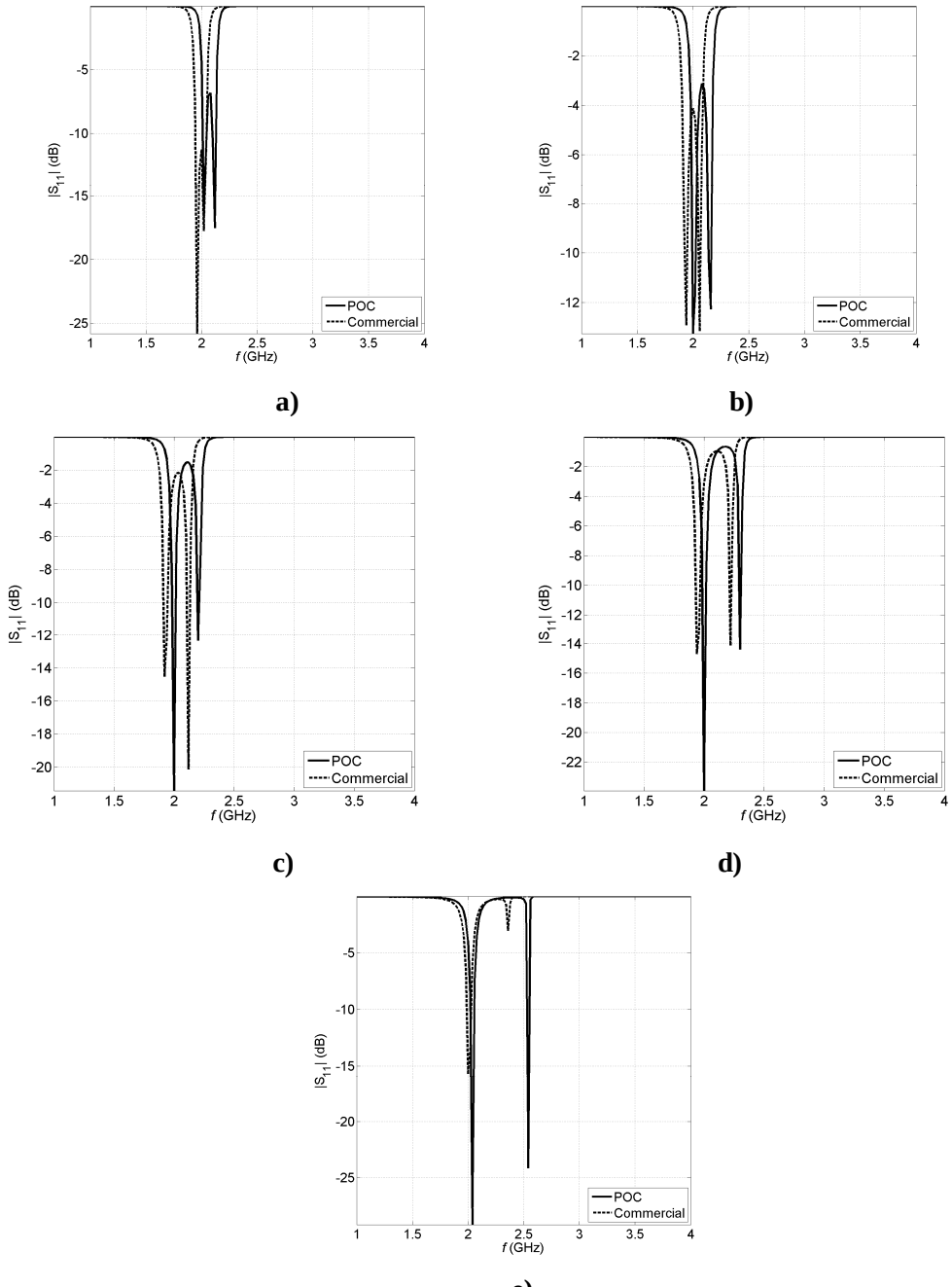

Fig 5.28 *$|S_{11}|$ comparison between POC and HFSS^{TM} when simulating the filter in Fig. 27a with a gap between post a) 28 mm (L_x = 80 mm), b) 21 mm (L_x = 73 mm), c) 14 mm (L_x = 66 mm), d) 7 mm (L_x = 59 mm) and e) 1 mm (L_x = 53 mm).*

posts while keeping the coupling of these posts with the excitation probes. This is done by reducing the size of the cavity in the *x* direction, so that the gap between posts diminishes. The varying geometric quantities can be appreciated in Fig. 5.27b. A cavity of L_x x 40 mm x 36 mm is used, where L_x subsequently is set to 80 mm, 73 mm, 66 mm, 59 mm and 53 mm. As

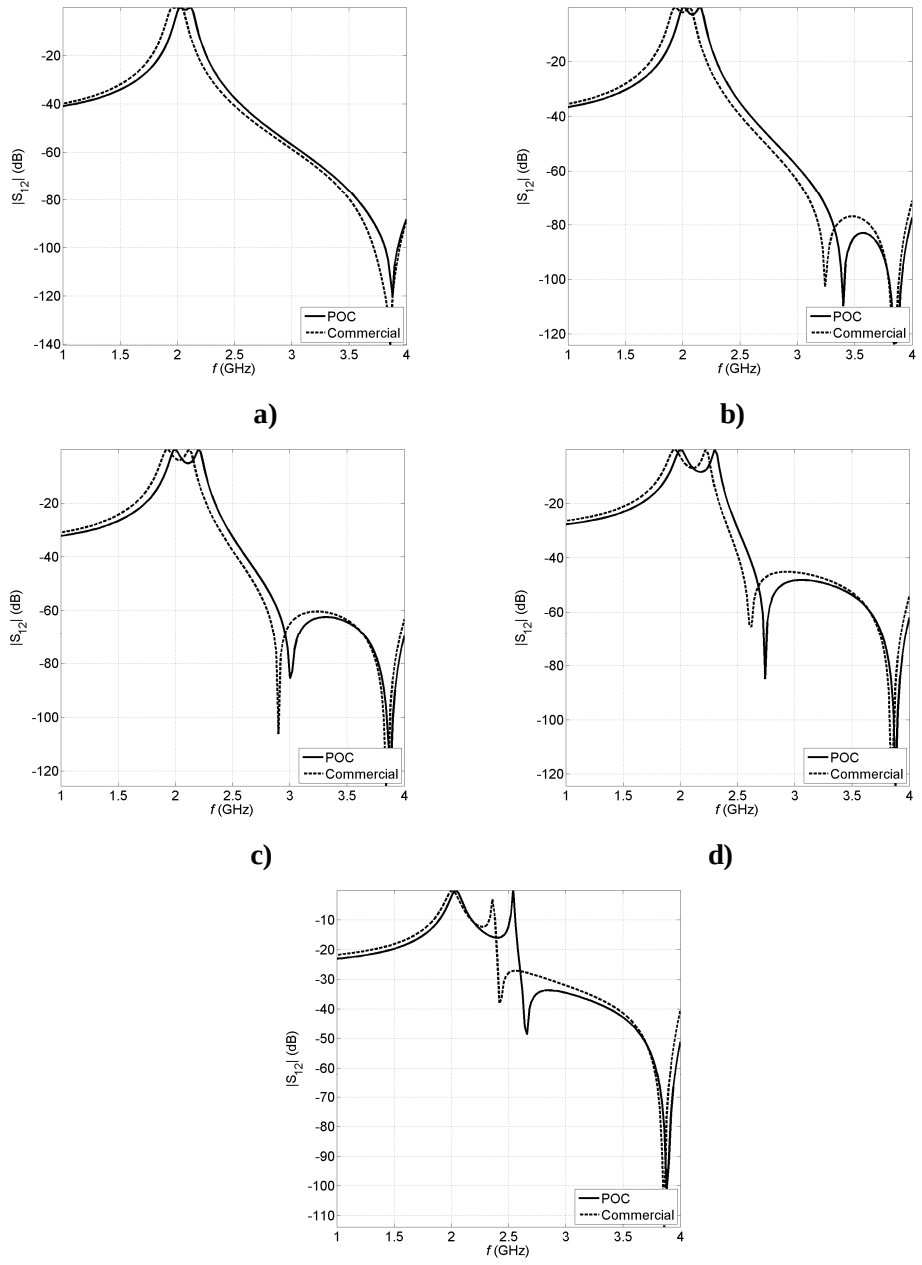

Fig 5.29 *$|S_{12}|$ comparison between POC and HFSS^{TM} when simulating the filter in Fig. 27a with a gap between post a) 28 mm (L_x = 80 mm), b) 21 mm (L_x = 73 mm), c) 14 mm (L_x = 66 mm), d) 7 mm (L_x = 59 mm) and e) 1 mm (L_x = 53 mm).*

consequence, the gaps between posts are 28 mm, 21 mm, 14 mm, 7 mm and 1 mm. The $|S_{11}|$ and $|S_{12}|$ bounded to the filters, which exhibit these gaps between posts are respectively presented in Fig. 5.28 and Fig. 5.29. As in §5.4.1 these S parameters have been computed with the POC software and they have been ascertained through a comparison with the commercial tool HFSS^{TM}. Fig. 2.28a, Fig. 2.28b, Fig. 2.28c, Fig. 2.28d and Fig. 2.28e are respectively related to $|S_{11}|$ when

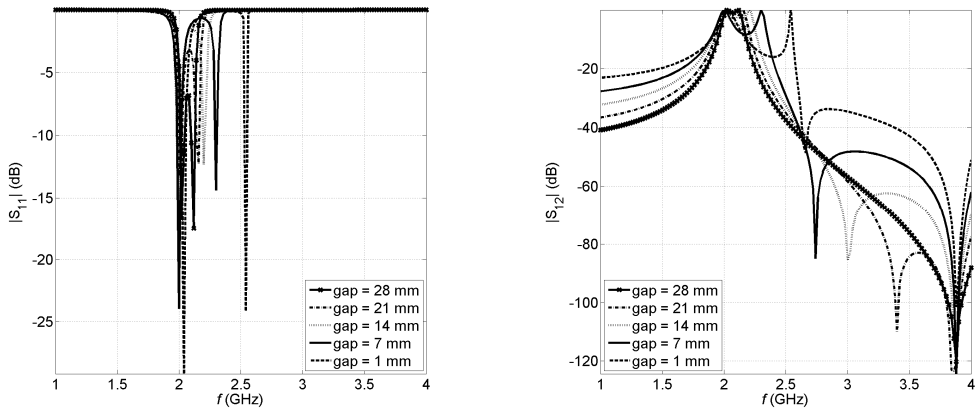

a) **b)**

Fig. 5.30 *Evolution of a) $|S_{11}|$ and b) $|S_{12}|$ with the gap between posts.*

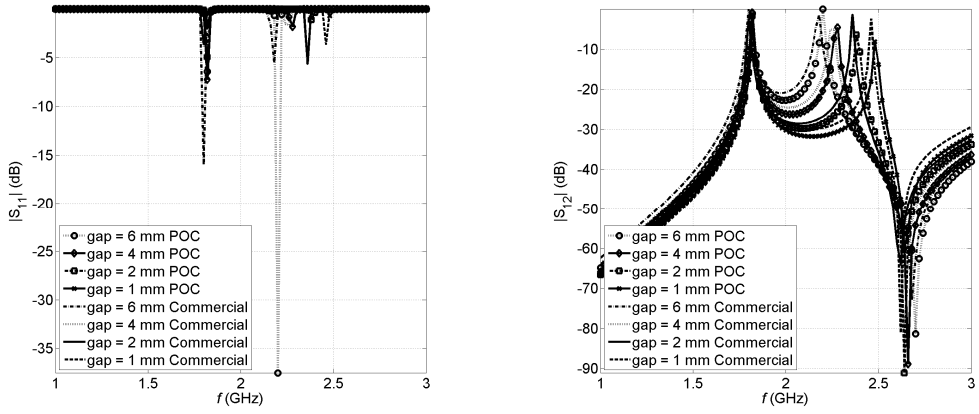

a) **b)**

Fig. 5.31 *Evolution of a) $|S_{11}|$ and b) $|S_{12}|$ when diminishing the gap between posts by moving the second post to the second one. In this case the filter is excited via simple probes. The results provided by HFSS™ are also shown.*

the gap between posts is 28 mm, 21 mm, 14 mm, 7 mm and 1 mm, whereas Fig. 2.29a, Fig. 2.29b, Fig. 2.29c, Fig. 2.29d and Fig. 2.29e are also respectively linked to these gaps but for $|S_{12}|$. In all this figures, it can be appraised that the agreement between POC and commercial codes is very good when simulating this kind of filters. The evolution of $|S_{11}|$ and $|S_{12}|$ with the gap between posts are respectively shown in Fig. 5.30a and Fig. 5.30b. The physical implications of reducing this gap can be inferred from these figures. It can be seen in Fig. 5.30a that the first resonance of the filter remains almost unchangeable when making the gap smaller, whereas the second one shifts toward higher frequencies. On the other hand, it is observed in Fig. 5.30b that the first transmission zero in $|S_{12}|$ shifts downwards in frequency, while the second one stays invariant.

The second parametric study, which concludes this section, basically involves the same filter as in the one shown in Fig. 5.27a. However now, the energy is introduced inside the filter by

means of simple probes instead of using the ground-connection. As before, the gap between posts is diminished, but now this is done by moving the second post towards the first one along the *x* direction, so that the coupling between the second post and the second port decreases as well. Namely, the dimensions of the cavity, which are 58 mm x 40 mm x 36 mm, remain unchangeable. The resulting $|S_{11}|$ and $|S_{12}|$ are respectively shown in Fig 5.31a and Fig. 5.31b for gaps of 6 mm, 4 mm, 2 mm and 1 mm. It is appraised in this figures that the displacement of the second post towards the first one basically implies a shift of the second resonance towards higher frequencies and a decrease in the level of $|S_{12}|$. In the same figures, it can be also appreciated that both HFSS^{TM} and the POC code agrees.

5.5 Conclusions

This chapter has dealt with several practical applications involving the theoretical concepts and results exhibited in §2-§4 have been shown in this chapter, the results presented here having been published in several conference papers. In §5.2.1, it has been proven than the hybrid technique based on the original transformation presented in §4.6.1 and the use of generalized Cartesian product rules based on the DE formula §4.6 outperform standard Gaussian integration techniques within a SIE-MoM framework. Numerical examples showing these aspects have been presented are within a SIE-MoM framework, demonstrating the interest of using the presented global approach presented for the double surface integrals appearing in Galerkin formulations. Although, this technique improves the accuracy of the results, they can not overwhelm closed analytical formulations in terms of efficiency. This has also been shown in §5.2.1, where it has been proven that an analytical filling of the MoM matrix clearly outperforms a computation of the elements of this matrix via the proposed hybrid integration method to fill the MoM matrix with a total analytical. The analytical filling has been done through the original analytical expressions to calculate the quadruple integral of the *1/R* potential singularity reported in §4.5, which have also been applied to compute numerically static cavity GFs in §5.2.2.

In §5.3, an empirical study of two front to front highly coupled strips has been undertaken. The structure has been simulated in two scenarios by using an MPIE-MoM strategy. The first scenario is a free space environment. Here it has been noted how the minimum of reflection and maximums of radiation and transmission obviously vary in function of the separation of the strips. These points can happen at different frequencies for a fixed structure. Besides, an interesting anomalous behavior has been observed as a “lump” in the frequency behavior of $|S_{12}|$. The second scenario is the interior of a PEC rectangular cavity. Here the same study as in free space has been performed. It has been seen that the minimum of $|S_{11}|$ and the maximum of $|S_{12}|$ shift in frequency in a coherent way. A transmission zero has been found at the free space frequency where the lump was. Finally, a study varying the cavity size and keeping the enclosed structure unchanged has been done. It has been noted how the cavity modes can affect the free space response when they are present in the simulation band. The transmission zero in $|S_{12}|$ has been also found in the zone where the lump was in free space. The relation between the transmission zero in the cavity and the lump in free space is the most interesting phenomenon found. At present we know that this phenomenon is strongly correlated with the Green function’s real part in the frequency range of the lump. We conclude empirically that the cavity can enhance

this free space phenomenon. It is expected the presented methodology will help in future studies to set more conclusive statements.

The results in §5.4 have been obtained in the framework of the scientific activities of an ESA project. One of the goals of this project is to explore the capabilities of the MPIE-MoM strategy to analyze combline filters. The results in this section have been obtained with a non-optimized but performing enough POC code, which is envisioned to attain this objective and uses the results in §3 and §4. Several satisfactory results, which involve the simulation of combline type structures, in terms of accuracy have been presented and compared with highly optimized commercial tools. There is plenty of room for enhancing the performance in terms of efficiency of our strategy, particularly in the image series expansion and in the treatment of the GF modal series. Therefore, prospects are strong for improving its accuracy while reducing the computer time. With the strong analytical preprocessing introduced in this paper, our surface based approach should be really competitive.

References

[1] K. Moshe, "The dyadic green's functions for cylindrical waveguides and cavities," *IEEE Trans. Microw. Theory and Techn.*, vol. 28, no. 8, pp. 894-898, Aug. 1980.

[2] C. Phongcharoenpanich, M. Krairiksh and J-I Takada, "Dyadic green's functions of the concentric conducting spherical cavity," in Proc. Asia Pacific Microwave Conference, pp. 757-770, Dec. 1997.

[3] C-t. Tai, *Dyadic Green Functions in Electromagnetic Theory*. USA: Intext Educational Publ., 1971.

[4] A.Heldring, J. M. Rius, J. M. Tamayo, J. Parrón and E Úbeda, "Fast direct solution of method of moments linear system," *IEEE Trans. Antennas Propagat.*, vol. 55, no. 11, pp. 3220–3228, Nov. 2007.

[5] A.Heldring, J. M. Rius, J. M. Tamayo and J. Parrón, "Compressed block-decomposition algorithm for fast capacitance extraction," *IEEE Trans. Comput.-Aided Design Integr. Circuits Syst.*, vol. 27, no. 2, pp. 265–271, Feb. 2008.

[6] P. Crespo-Valero, M. Mattes, I. Stevanovic, and J. R. Mosig, "Analysis of multilayer boxed printed circuits," in *13th IEEE Mediterranean Electrotechnical Conference (MELECON 2006)*, Torremolinos, Málaga, Spain, May 16-19, 2005, pp. 206-209.

[7] P. Crespo-Valero, M. Mattes and J. R. Mosig, "MAMBO: An implementation of an efficient method for the simulation of multilayered packaged printed circuits," in *Microwave Technology and Techniques Workshop*, ESA-ESTEC, Noordwijk, the Netherlands, May 15-16, 2006.

[8] P. Crespo-Valero, M. Mattes and J. R. Mosig, "Full-wave simulation of multi-layered boxed printed circuits," in *Proc. International Workshop on Microwave Filters (IWMF 2006)*, CNES, Toulouse, France, Oct. 16-18, 2006.

[9] F. Gronwald, "Calculation of mutual Antenna coupling within rectangular enclosures," *IEEE Trans. On Electromagnetic Compatibility*, vol. 47, no. 4, pp. 1021-1025, Nov. 2005.

[10] F. Gronwald and E. Blume, "Reciprocity and mutual impedance formulas within lossy cavities," Advances in Radio Science, vol. 3, pp. 91-97, 2005.

[11] ESA-ESTEC Activity 16332/02/NL/LvH.

[12] C. Wang and K. A. Zaki, "Full-wave modeling of electric coupling probes in comb-line resonators and filters," *IEEE Trans. Microw. Theory and Techn.*, vol. 48, no. 12, pp. 2459-2464, Dec. 2000.

[13] Fritz Arndt, Vali Catina, Joern Brandt, "Efficient Hybrid EM CAD and Optimization of a Comprehensive Class of Advanced Microwave Filters,", in *Microwave Technology and Techniques Workshop*, ESA-ESTEC, Noordwijk, the Netherlands, May 15-16, 2006.

[14] F. D. Quesada Pereira, V. E. Boria Esbert, J. Pascual García, A. Vidal Pantaleoni, A. Alvarez Melcón, J. L. Gomez Tronero and B. Gimeno, "Efficient análisis of arbitrarily shaped inductive obstacles in rectangular waveguides using a surface integral-equation formulation," *IEEE Trans. Microw. Theory and Techn.*, vol. 55, no. 4, pp. 715-721, Apr. 2007.

[15] G. L. Mattahaei, "Comb-line band-pass filters of narrow or moderate bandwidth,", The microwave journal, pp. 82-91, Aug. 1963.

[16] G. L. Mattahei, L. Young and E. M. T. Jones, Microwave filters, impedance-matching networks, and coupling structures. USA: McGraw-Hill, 1964.

[17] K-L. Wu, R. R. Mansour and H. Wang, "A full wave analysis of a conductor posts insert reentrant coaxial resonator in rectangular waveguide combline filters," *IEEE MTT-S Digest*, 1996.

[18] D. Kajfez, and P. Guillon (ed), *Dielectric Resonators*. Norwood: Artech House, 1986.

[19] A. Borji and S. Safavi-Naeini, "Fast full-wave analysis of conductor-loaded rectangular cavity resonators using surface integral equation and moment method," ,in *Proc. IEEE AP-S*, vol. 2, pp. 1187-1190, 2004.

[20] I. Hunter, *Theory and design of microwave filters*, Stevenage: The Institution of Electrical Engineers, 2001.

[21] M. El Sabbagh, K. A. Zaki, H-W. Yao and M. Yu, "Full-wave analysis of coupling between combline resonators and its application to combline filters with canonical configurations," *IEEE Trans. Microw. Theory and Techn.*, vol. 49, no. 12, pp. 2384-2393, Dec. 2001.

[22] V. Catina, F. Arndt and J. Brandt, "Hybrid surface integral-equation/mode-matching method for the analysis of dielectric loaded waveguide filters of arbitrary shape," *IEEE Trans. Microw. Theory and Techn.*, vol. 53, no. 11, pp. 3562-3567, Nov. 2005.

[23] R. S. Kashyap, "Waveguide resonators,", Term paper report, Dept. of Electrical Engineering, Indian Institute of Technology, Bombay.

[24] R. J. Cameron, C. M. Kudsia and R. R. Mansour, *Microwave Filters for Communication Systems*. Hoboken: John Wiley & Sons, 2007.

[25] C. A. Valagiannopoulos and N. K. Uzunoglu, "Rigorous analysis of a metallic circular post in a rectangular waveguide with step discontinuity of sidewalls," *IEEE Trans. Microw. Theory and Techn.*, vol. 50, no. 8, pp. 1673-1684, Aug. 2007.

[26] D. M. Pozar, *Microwave Engineering*. USA: John Wiley & Sons, 1988.

6 Thesis Assessment

"Begin thus from the first act, and proceed; and, in conclusion, at the ill which thou hast done, be troubled, and rejoice for the good."
Pythagoras

"Like the old soldier of the ballad, I now close my military career and just fade away, an old soldier who tried to do his duty as God gave him the light to see that duty. Goodbye."
Douglas McArthur

The presented work has been mainly focused on the calculation and evaluation of the GFs, as well as the integration of its singularity, within a Mixed Potential Integral Equation-Method of Moments (MPIE-MoM) context. Most of the results presented here have been obtained in the framework of an ESA project, whose aim is to explore the capabilities of MPIE-MoM strategy to the simulation of shielded structures.

As in the case of any other integral equation technique (IE) technique, the use of the MPIE requires a good knowledge of the GFs of the shield, which in this thesis, is a PEC rectangular cavity. GF evaluation techniques based on image series, modal expansions and combination of both, have been presented in §3. It has been shown that the strategy, which attains a good representation of both the boundary conditions (BC) at the cavity walls and the singular behavior inherent to the GF, as well as a good model of the cavity resonances, consists of splitting the GF in two parts. The first part is the GF dynamic part, which is calculated as a 2D modal series, whereas the second part is the GF static part, which contrarily, is based on an image series representation. The good behavior in frequency has been ascertained through a method based on a classification of the modes of the cavity, which allows setting the link between GF component, resonant frequency and excited mode a priori, which permits a faster validation of the GF. Albeit, the aforesaid link has been set for cavity GFs obtained via the Lorentz's gauge, studies in the same direction can be performed with GFs, which are calculated through the Coulomb gauge.

Also in §3, a novel method to compute the GF static part has been presented. This method was proposed by J. M. Tamayo from the Polytechnic University of Catalonia (UPC) during a successfully collaboration during his stay at LEMA/EPFL, being the author of this thesis instrumental in the numerical implementation and analysis of the procedure. This method is also based on a hybrid representation via image and modal expansions. Very promising preliminary results have been obtained, since in the convergence rate of the presented strategy is comparable to Ewald's one. However, the optimal values of several parameters associated to the method are

still to be determined. Oppositely to the Ewald technique, a potential advantage of the presented approach is that it can be analytically integrated via existing techniques, so that a more efficient evaluation of the MoM matrix elements can be attained.

Original analytical formulas associated to the 4D integrals of the potential GFs' weak singularity, have been reported in §4. This formulas apply within a singularity subtraction method The reader is remind that this kind of methods extract the static term of the GF and deal with it separately, just as it has been done in §3. Several scenarios of interest related to weak and singular situations, as well as smooth cases, have been analytically solved. Nevertheless, the obtention of a formula to perform the analytical integration of this singularity in a generic situation (the 4D integral of *1/R* over two arbitrarily oriented polygons) is still and open problem. Here, this generic situation has been solved via the usage of a hybrid numeric-analytic integration technique which is based on a novel integral transformation and the usage direct exponential (DE) rules. Basically, the potential integral is analytically integrated, whereas the problems, which linked to the numerical integration of the singularities in the derivatives of the resulting potential, are tempered via the use of the DE rules, since they are tailored to integrate this sort of functions. This feature inherent to the DE rules, makes us to think in the possibility of applying then to other numerical methods, which require of this capabilities as for instance the Nyström method. This would be an interesting future research topic.

Most of the theory and results exhibited in §3 and §4 have been used to solve several practical problems in §5. It has been shown how the hybrid numeric-analytical integration technique proposed in §4 overwhelm schemas based on classical Gaussian numerical integration rules. However, as expected, it can not beat full analytical techniques. In the same chapter it has been found the relationship between a lump in free space and a cavity transmission 0 in the S parameters related to high coupled structures. Conclusive reasons for this interesting anomalous behavior are still to be provided. Also in §5 the result to several benchmarks proposed by ESA during the development of the aforementioned project are shown. These results have been obtained with a non optimized proof of concept (POC) code, which aims to exhibit the capabilities of the MPIE-MoM strategy to simulate combline type structures, especially when gaps between enclosed structures are very small. Although, several efficient commercial tools are available to efficiently solve these problems, the results obtained in this chapter allow envisioning the future development of a competitive MPIE-MoM tool. Therefore, prospects are strong for improving its accuracy while reducing the computer time. With the strong analytical preprocessing introduced in this thesis, the MPIE-MoM surface based approach should be really competitive.

CV

Sergio López Peña was born on October 19, 1976 in Barcelona, Spain. He received the Ingeniero de Telecomunicación degree from the Escuela Tècnica Superior d'Enginyeria de Telecomunicació Barcelona (ETSETB), Universitat Politècnica de Catalunya (UPC), in 2003. In February 2006, he started PhD studies at the Laboratoire d'Electromagnétisme et d'Acoustique (LEMA), Ecole Polytechique Fédérale de Lausanne (EPFL).

In June 2003, he obtained in UPC his final diploma project with honors for a work entitled "Aplicacion del método de Nyström a problemas electrostáticos 2D y 3d" where he performed an exhaustive study of the capabilities of this method to the resolution of static problems. In February 2005, he joined LEMA where he is currently Research and Teaching Assistant. He has been active research member in the following projects:

- "Integrated planar and waveguide simulation tool". Responsible for the design of a POC code to show the capabilities of the IE-MoM strategy to analyze combline structures. ESA/ESTEC Contract No. 16332/02/NL/LvH. European Space Agency Project (January 2006-Mai 2008).

- "Polaris". Responsible for the characterization and design of the basic elements of a P-Band ice sounder radar. ESA/ESTEC Contract No. 19307/05/NL/JA. European Space Agency Project.

Among his teaching activities he has assisted in the exercises for the courses of Electromagnetics I and II and Antennas and Propagation, graded exams, and proposed and supervised several student semester and final diploma projects.

List of Publications

REFEREED JOURNAL PAPERS

1. S. López-Peña and J.R. Mosig, "Analytical evaluation of the quadruple static potential integrals on rectangular domains to solve 3D electromagnetic problems," *IEEE Transactions on Magnetics*, vol. 45, no. 3, pp. 1320 - 1323, 2009.
2. S. López-Peña, A.G. Polimeridis and J.R. Mosig, "On the analytic-numeric treatment of weakly singular integrals on arbitrary polygonal domains," submitted to *IEEE Transactions on Antennas and Propagation*, 2010.
3. J.M. Tamayo, S. López-Peña, M. Mattes, A. Heldring, J.M. Rius, and J.R. Mosig, "A hybrid acceleration technique for static potential Green's functions of a rectangular cavity combining image and modal series," submitted to *IEEE Transactions on Microwave Theory and Techniques*, 2010.

REFEREED CONFERENCE PAPERS

1. S. López-Peña, M. Mattes and J.R. Mosig, "Relevance of the resonances of the Green's functions when solving shielded combline filters with an MPIE strategy," in *Proc. 1st European Conference on Antennas and Propagation (EuCAP 2006)*, Nice, France, November 2006.
2. S. López-Peña, M. Mattes and J.R. Mosig, "Towards an efficient software tool for combline filters based on a IE-MOM strategy," *Microwave Technology and Techniques Workshop Enabling Future Space Systems*, ESA-ESTEC (Noordwijk), The Netherlands, May 2006.
3. S. López-Peña, M. Mattes and J.R. Mosig, "Simple scheme to analyze posts in rectangular cavities using an IE-MoM strategy," in *Proc. V Iberic Meeting of Computational Electromagnetism (V-EIEC)*, Aiguabalva (Gerona), Spain, April 2007.
4. S. López-Peña, M. Mattes and J.R. Mosig, "The impact of metallic scatterers on the performance of a class of shielded structures," in *Proc. 2nd European Conference on Antennas and Propagation (EuCAP 2007)*, Edinburgh, UK, November 2007.

5. S. López-Peña, M. Mattes and J.R. Mosig, "Quadruple static potential integrals for uniform source distributions on rectangular domains," in *Proc. VI Iberian Meeting on Computational Electromagnetism (VI-EIEC)*, Chiclana de la Fontera (Cádiz), Spain, October 2008.
6. S. López-Peña and J.R. Mosig, "Analytical evaluation of the quadruple static potential integrals on rectangular domains to solve 3D electromagnetic problems," in *Proc. 13th Biennal IEEE Conference on Electromagnetic Field Computation (CEFC 2008)*, Athens Greece, May 2008.
7. F. J. Herraiz-Martínez, S. López-Peña, J.R. Mosig, L. E. García-Muñoz and D. Segovia-Vargas, "Analysis of Patch Antennas Partially Filled with LH cells using the MPIE-MoM Approach," *COST ASSIST Workshop on Antenna Systems & Sensors for Information Society Technologies*, Dublin, Ireland, October 2008.
8. S. López-Peña and J.R. Mosig, "Analytical form of the quadruple static potential integrals for uniform source distributions on rectangular domains and their application to the resolution of 2D and 3D antenna problems," in *Proc. 3rd European Conference on Antennas and Propagation (EuCAP 2009)*, Berlin, Germany, March 2009.
9. J.A. Herrero, J.M. Rius, J.M. Tamayo, A. Heldring, E. Ubeda, J. Parron, S. López-Peña, A.G. Polimeridis, J.R. Mosig, H. Espinosa and A. Boag, "Software framework for integration of method of moments kernel with direct or iterative fast solvers," in *Proc. 4th European Conference on Antennas and Propagation (EuCAP 2010)*, Barcelona, Spain, April 2010.
10. S. López-Peña, J.-F. Zürcher, R. Torres, A.G. Polimeridis and J.R. Mosig, "Modeling and manufacturing of a series of identical antennas for a P-band ice sounder," in *Proc. 4th European Conference on Antennas and Propagation (EuCAP 2010)*, Barcelona, Spain, April 2010.
11. S. López-Peña, A.G. Polimeridis and J.R. Mosig, On the double potential integrals arising in the method of methods and their analytic-numeric hybrid treatment," in *Proc. 4th European Conference on Antennas and Propagation (EuCAP 2010)*, Barcelona, Spain, April 2010.

TECHNICAL REPORTS

1. S. López-Peña and M. Mattes, and J. R. Mosig, "Analysis of combline filters by using an IE-MoM strategy. Numerical thecniques and mathematical formulation"Validation and verification of the electromagnetic kernel," Technical Notes TN401-Updating TN301, ESA-ESTEC Activity 16332/02/NL/LvH : Planar and waveguide simulation tools, Sep. 2007.
2. S. López-Peña and M. Mattes, and J. R. Mosig, "Cofresito. Code verification and documentation," Technical Note TN304, ESA-ESTEC Activity 16332/02/NL/LvH : Planar and waveguide simulation tools, Sep. 2007.

3. S. López-Peña and M. Mattes, and J. R. Mosig, “Analysis of combline filters. Code verification and documentation” Technical Notes TN302-402, ESA-ESTEC Activity 16332/02/NL/LvH: Planar and waveguide simulation tools, Apr. 2008.
4. S. López-Peña and M. Mattes, and J. R. Mosig, “Evaluation of EM approach, losses in metallic enclosures, losses in metallic post,” Technical Notes TN404, TN601-2 and TN602-2, ESA-ESTEC Activity 16332/02/NL/LvH: Planar and waveguide simulation tools, Apr. 2008.

…